NASA CONTRACTOR REPORT

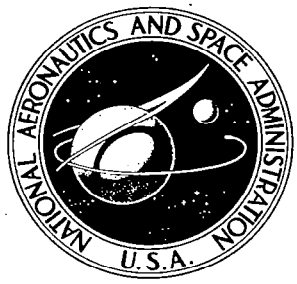

NASA CR-812

VAPOR-CHAMBER FIN STUDIES

TRANSPORT PROPERTIES AND BOILING CHARACTERISTICS OF WICKS

by H. R. Kunz, L. S. Langston, B. H. Hilton, S. S. Wyde, and G. H. Nashick

Prepared by
PRATT & WHITNEY AIRCRAFT
West Hartford, Conn.
for Lewis Research Center

NATIONAL AERONAUTICS AND SPACE ADMINISTRATION • WASHINGTON, D. C. • JUNE 1967

NASA CR-812

VAPOR-CHAMBER FIN STUDIES

TRANSPORT PROPERTIES AND BOILING CHARACTERISTICS OF WICKS

By H. R. Kunz, L. S. Langston, B. H. Hilton,
S. S. Wyde, and G. H. Nashick

Prepared under Contract No. NAS 3-7622 by
PRATT & WHITNEY AIRCRAFT
Division of United Aircraft Corporation
West Hartford, Conn.

for Lewis Research Center

NATIONAL AERONAUTICS AND SPACE ADMINISTRATION

For sale by the Clearinghouse for Federal Scientific and Technical Information
Springfield, Virginia 22151 – CFSTI price $3.00

FOREWORD

This report describes the work conducted by Pratt & Whitney Aircraft Division of United Aircraft Corporation under NASA Contract 3-7622 and was originally issued as Pratt & Whitney Report PWA-2953, November 1966. The experimental work was performed by J. F. Barnes and the authors. Martin Gutstein of the Space Power Systems Division, NASA-Lewis Research Center, was the Technical Manager.

ABSTRACT

The purpose of this paper is to define and present the wicking material properties that are considered to be important to the operation of a vapor-chamber fin or a heat pipe.

Three classes of wicking materials are studied: sintered metal screens, sintered metal powders, and sintered metal fibers. The porosity of these sintered materials ranges from 47.7 to 91.8 per cent.

Two characteristics of the wicking material are considered to limit the operation of the heat pipe, 1) the capillary pumping characteristics of a wick, and 2) the evaporative heat transfer characteristics of a liquid-saturated wick.

To evaluate the effect of capillary pumping characteristics, a simplified analysis of a planar-wick heat pipe is made. The result of this analysis gives the maximum operating length of a planar-wick model in terms of the external boundary conditions, the heat pipe fluid properties, and the capillary pump characteristics of the wicking material. The capillary pump characteristics are found to be proportional to the equilibrium height to which the heat pipe liquid will rise in the wicking material, divided by the wicking material friction factor, when net body forces are zero. The latter is the reciprocal of the permeability for the wicking material. When gravity effects cannot be neglected, then the equilibrium height to which the heat pipe liquid will rise in the wicking material becomes another distinct factor.

The results of wick equilibrium height experiments and wick permeability experiments run on the three classes of wicking materials are presented. Both water and Freon 113 are used as working fluids in these experiments. These results are combined to yield the capillary pumping characteristics of wicking materials.

To evaluate the effect of the evaporative heat transfer characteristics of wicks, experimental data on porous samples selected from the three classes of wicking materials is presented. This data results from evaporative heat transfer experiments run on planar-wick samples using water and Freon 113. Comparison of results with the heat transfer characteristics of a flat plate submerged in water indicate that equivalent or superior performance can be obtained with wick covered surfaces. However, the data also indicates that the entrapment of vapor bubbles in the wick matrix may cause premature film boiling in the porous material at relatively low heat fluxes, depending on the structure of the wicking material. The heat transfer characteristics of Freon 113 were poorer than those exhibited by water.

TABLE OF CONTENTS

TABLE OF CONTENTS (Cont'd)

I. SUMMARY

This report summarizes the work performed to obtain the capillary pumping and evaporative heat transfer characteristics of wicks with respect to vapor-chamber fin or heat pipe operation.

To determine the capillary pumping characteristics which affect the operation of a vapor-chamber fin, a simplified analysis of a planar-wick geometry was made. The simplified analysis indicates that the maximum height to which a liquid will rise in a vertical wick, ℓ_m, and the wick friction factor, K_1, are important parameters in determing the capability of a capillary pump in a heat pipe. The larger the value of the capillary pump parameter, ℓ_m/K_1, the better the capillary pump, when head effects due to gravity are negligible. If an application involves operation at a condition in which a capillary pump must work against gravity, consideration must be given to both the value of ℓ_m/K_1 and of ℓ_m itself. The important fluid properties for capillary pumping are also indicated by the simplified analysis.

The equilibrium height of liquid rise in a vertical wick was experimentally determined for 10 different wick samples with water as the test fluid. Equilibrium heights of six samples were also determined with Freon 113. Three classes of wicking materials were studied: sintered metal screens, sintered metal powders, and sintered metal fibers. The porosity of these sintered materials ranged from 47.7 to 91.8 per cent. The wick friction factor was determined for thirteen different samples with water as the test fluid. Tests were repeated on four of these samples with Freon 113 as the test fluid. The friction factor of each sample was found to be essentially constant over a range of mass velocities and temperatures for the two fluids tested when they were deaerated. When the test fluid was aerated water, the wick friction factor was found to increase with time.

The experimentally determined capillary pumping characteristics of the three classes of materials indicated that as a class the sintered fiber samples were best, followed by the sintered powder samples. The sintered screen samples demonstrated the lowest potential as capillary pumps.

The evaporative heat transfer characteristics of six different samples from the three general classes were determined experimentally. The effects of orientation, thickness of sample, degree of submergence of the sample in the test fluid, test fluid and wick surface modifications were determined. Some of these porous materials provide high values of heat transfer coefficients and limiting heat transfer rates for boiling when adequate paths for vapor escape from within the wick are provided. Other samples which do not provide vapor removal paths result in values of heat transfer coefficients significantly lower than those of a bare flat surface. Three sintered fiber samples were determined to have the best heat transfer characteristics of those tested, followed by a sintered powder sample and sintered screens.

II. INTRODUCTION

The work of Grover, et al[1], and other investigators [2, 3] has shown that the heat pipe is a heat transfer device that can exhibit an extremely high effective thermal conductivity, much greater in fact than any known homogeneous material. The heat pipe consists of a long closed container in which vaporization and condensation of a fluid take place. Heat added at one end of the container causes evaporation of liquid into vapor. Condensation of the vapor along the length of the container maintains the surface at a nearly constant temperature. The resulting condensate is returned to the heated end of the container by the action of capillary forces in the liquid layer which is contained in a wick lining the inside of the cavity.

A parametric study done by Haller, Lieblein, and Lindow[4] indicates that the heat pipe might be used as a "vapor-chamber fin" in reducing the weight of a radiator for a Rankine-cycle space powerplant. Such a fin is shown in cross-section in Figure 1. Possible vapor-chamber fin configurations for use in a space radiator are shown in Reference 4.

An investigation was begun under Contract NAS 3-7622 to explore and define the mechanisms of fluid and heat transport in vapor-chamber fins or heat pipes, to provide design information for space radiators and other applications. The investigation is divided into three parts, 1) wicking studies, 2) boiling studies, and 3) steady-state fin operation. This report summarizes the accomplishments of the first two parts of the program.

In order to obtain an understanding of fin operation, wicking and boiling studies were conducted in order to evaluate the capillary and frictional forces associated with the wicking materials and the boiling heat transfer characteristics of wicks to be used in the fin. The mechanistic model and simplified analysis of fin operation presented in Section III of this report indicate the need for this information. Section IV lists and explains the selection of wicking materials and fin fluids which were tested. The wicking material studies are treated in Sections V, VI and VII, where an explanation and description of the equations and experimental apparatus necessary to evaluate the forces acting on a liquid flowing in a wick are given. The test program to measure the boiling and evaporation heat transfer properties of a liquid in a wicking material is discussed in Section VIII.

---

[1] See Appendix 1 for numbered references

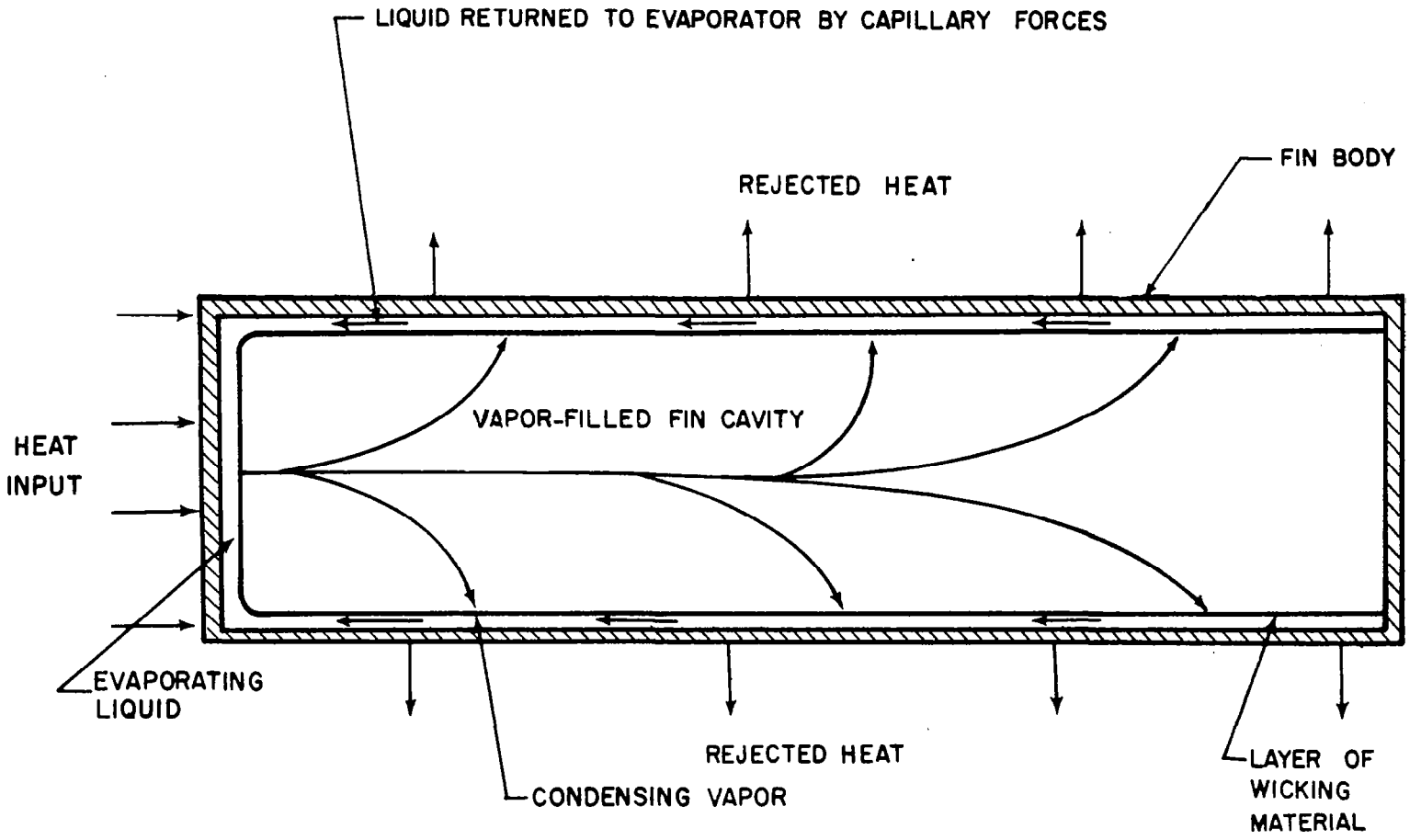

Figure 1 Vapor-Chamber Fin in Operation

III. ANALYSIS OF VAPOR-CHAMBER FIN

A. Vapor-Chamber Fin Operation

The various mechanisms that control the operation of the vapor-chamber fin can be discussed by considering the schematic diagram of the fin shown in Figure 2. This diagram illustrates the fact that the vapor-chamber fin is similar to a heat engine consisting of an evaporator, a condenser, and a pump. Although there is no net work output, pumping work is provided by capillary forces in transporting the liquid from the condenser to the evaporator.

In the evaporator section of the fin, heat must be conducted from the source of heat through the metal wall of the fin and the composite layer of liquid and wicking material in contact with the wall. This energy transfer results in evaporation of the liquid at the liquid-vapor interface.

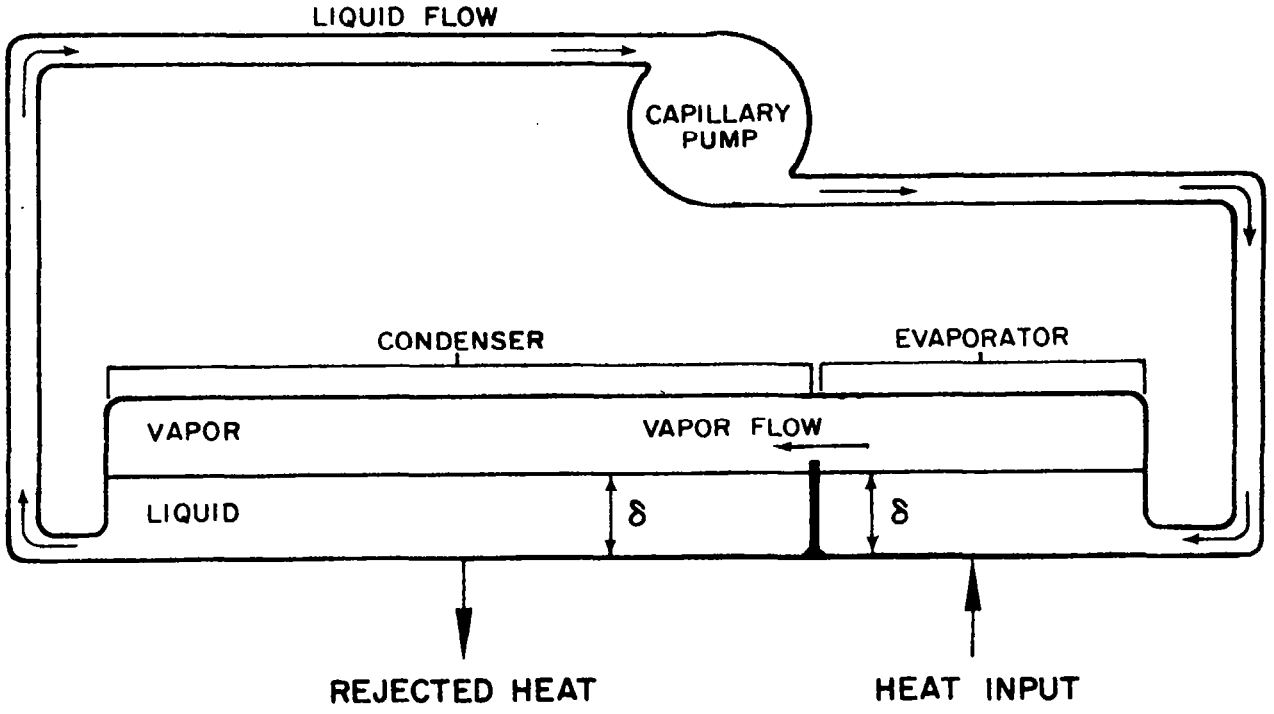

Figure 2 Mechanistic Model of Vapor-Chamber Fin

In the condenser section of the fin the reverse process to that in the evaporator occurs. Vapor condenses at the liquid-vapor interface, liberating its latent heat of vaporization. This energy is then conducted through the composite liquid-wick layer to the fin wall, then through the fin wall itself, from which it is rejected to the environment of the fin. Radiation is the mode of heat rejection from the fin in a space-radiator application.

The capillary pump serves the function of returning the condensed liquid to the evaporator. The pump may consist of a wicking material, the pores of which are small enough to provide capillary forces of sufficient magnitude to cause the liquid to flow back to the evaporator. The differences in the radius of curvature of the liquid-vapor interface in the condensing and evaporating sections of the fin provide the driving force of the pump. The details of this capillary pumping will be discussed in Section III C below.

When the various transport processes that occur during fin operation are analyzed, it is found that there are essentially two possibly interrelated phenomena which limit the maximum rate of energy that the fin can transfer. They are:

1) The heat flux at which apparent film-boiling occurs in the wick of the evaporator, and

2) The maximum liquid flow rate that the capillary pump can provide to the evaporator.

There may be other limiting phenomena, depending on the particular application in which the fin is used. For example, the thermal conductivity of the liquid-wick layer may be of such a magnitude as to provide a significant resistance to heat flow. But for the present study in which conventional liquids and space-radiator geometries will be studied, the film-boiling heat flux and the maximum capillary pump output seem to be the two limitations of most importance. Thus, although other factors that influence the operation of the fin will be taken into account in this program, these two phenomena will be studied separately and in greater detail.

It is unfortunate that these two limiting phenomena depend on the wick; for in the near zero-gravity environment of a space radiator, it is conceivable that a vapor-chamber fin wick would not be needed. The liquid would simply wet the walls of the fin cavity and due to changes in the radius of curvature at the liquid-vapor interface, would flow back to the evaporator section of the fin. In the present study all tests will be run in a 1-g environment, thereby necessitating the use of a wicking material in any fin models tested in order to make the capillary forces large relative to the gravitational force. However, even in an

actual vapor-chamber fin space radiator, a wick of some form would probably be used to ensure that the radiator would work in a force field such as gravity. In all discussions that follow it is assumed that the fin is in a gravitational field.

When either of the two limiting phenomena occurs, the result should be the same: any attempt to increase the net heat input to the fin would result in a large temperature rise at the base of the fin. This temperature increase, shown in the plot of Figure 3, is probably caused by an insufficiency of liquid at the liquid-wick-solid interface in the evaporator of the fin.

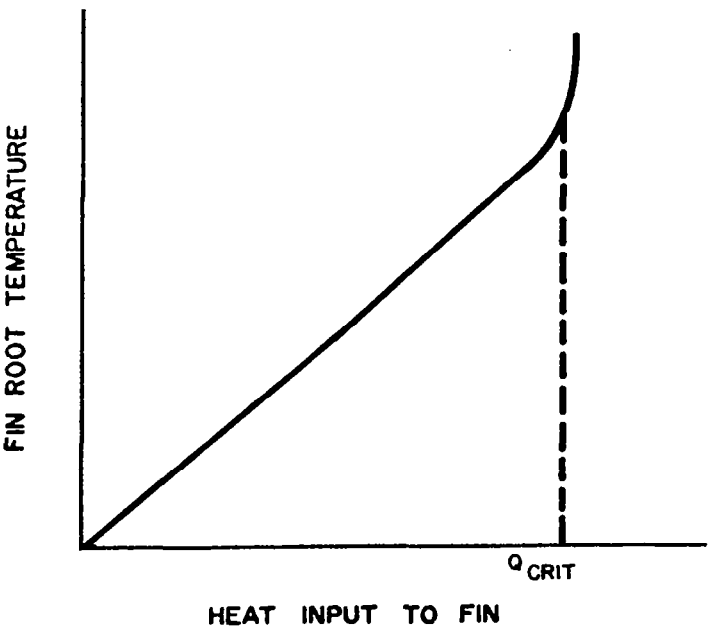

Figure 3 Idealized Performance of Vapor-Chamber Fin as Function of Heat Input

Thus, when the performance of a vapor-chamber fin falls off as the heat input is increased, the question arises as to which of the two limiting phenomena is responsible, wick film-boiling or insufficient capillary pump output. In order to answer the question a separate evaluation of each of these two possible causes of fin failure is needed. The following two sections discuss each possibility.

B. Limitation Due to Wick Boiling

An evaluation of the first of the limiting phenomena listed in the preceding section involves a study of the process of boiling of a liquid in a wick.

The actual process occurring in the evaporator section of the fin can be visualized in the following manner. As heat is initially added in the evaporation region, the heat will be conducted through the fin wall and the wick-liquid composite to the liquid-vapor interface where evaporation will take place. As the heat input to an operating fin is increased, it is presumed that the liquid-wick-solid interface temperature will rise to the point where the adjacent liquid is sufficiently superheated to cause nucleate boiling at the interface. If an equilibrium condition is to occur without excessive superheat, the capillary and/or buoyancy forces must be great enough to cause convection of the resulting vapor bubbles through the wick to the vapor cavity of the fin and supply fresh liquid to the heating surface at a sufficient rate. The buoyancy forces will be dependent upon the gravitational field in which the fin is operating. If vapor does not leave the interface at the rate at which it is produced, liquid will be excluded from the interface, causing film-boiling to set in. The effects of such a process are shown in Figure 3, as a sharp increase in temperature at the base of the fin, causing the fin to eventually become ineffective.

Because of the limited success with theoretical models of the simpler case of pool boiling, an attempt to evaluate boiling heat flux limits analytically in a relatively complicated wick structure appears unpromising. Thus, an experimental program to study boiling in wicks was conducted and will be described in Section VIII.

C. Limitation Due to Capillary Pump

The second major limitation on fin operation is the maximum output of the capillary pump. Stated differently, it is a matter of the wicking forces of the wick material overcoming the frictional and gravitational forces to provide sufficient flow rate.

To analyze the action of the wick as a capillary pump, the simplified model of the vapor-chamber fin shown in Figure 4 can be considered. The liquid pres-

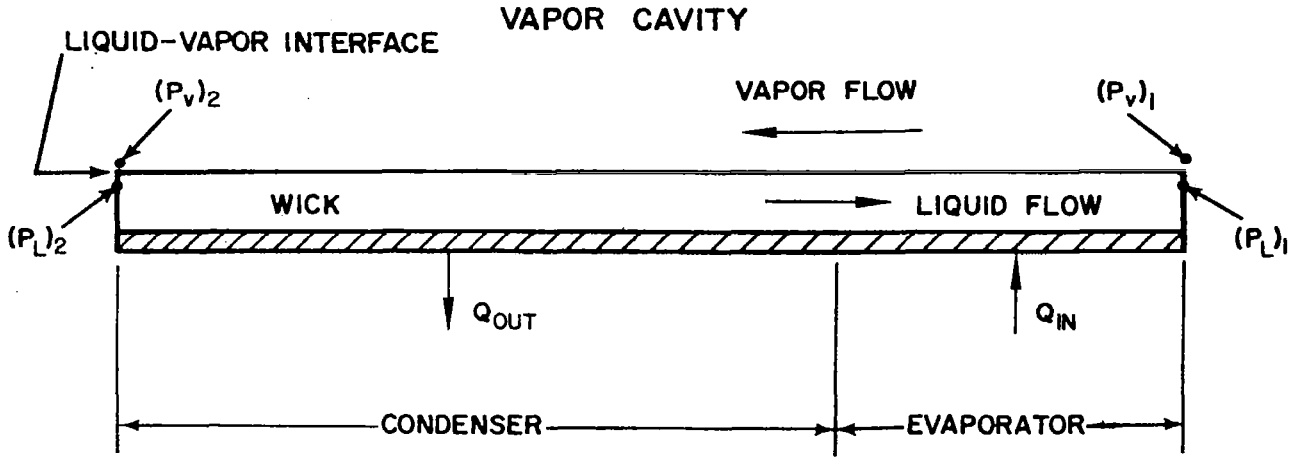

Figure 4 Two-Dimensional Model of Vapor-Chamber Fin

sures at the ends of the fin are $(P_L)_1$ and $(P_L)_2$, while the vapor pressures at the ends directly above the liquid are $(P_V)_1$ and $(P_V)_2$ respectively. In all of the following discussions it is assumed that no boiling takes place.

For the fin to operate, there must be a liquid flow from 2 to 1. Therefore, to overcome frictional forces and momentum changes

$$(P_L)_2 > (P_L)_1 \tag{1}$$

Similarly, there must be a counter vapor flow from 1 to 2, so that

$$(P_V)_1 \geq (P_V)_2 \tag{2}$$

If the system in Figure 4 is at steady state, the sum of the pressure changes that a given fluid particle experiences as it leaves the evaporator and returns again, is zero, or

$$[(P_V)_1 - (P_V)_2] + [(P_V)_2 - (P_L)_2] + [(P_L)_2 - (P_L)_1] + [(P_L)_1 - (P_V)_1] = 0 \tag{3}$$

As the liquid flows in the wick or the gas in the cavity, the pressure changes are balanced by frictional and inertial forces. These pressure drops due to friction, rate of change of momentum, etc., can be defined as

$$(\Delta P)_d \equiv (\Delta P_V)_d + (\Delta P_L)_d \equiv (P_V)_1 - (P_V)_2 + (P_L)_2 - (P_L)_1 \tag{4}$$

where, in general:

$$(\Delta P_V)_d \geq 0 \text{ and } (\Delta P_L)_d > 0 \tag{5}$$

These terms are usually positive since they consist primarily of the frictional components.

At any vapor-liquid interface there is some radius of curvature of the resulting surface, whether it be a very small value or infinity. The Laplace-Young equation of capillarity[5] shows that there is a pressure change across an interface, given by

$$\Delta P = \sigma \left(\frac{1}{R} + \frac{1}{R'} \right) \tag{6}$$

where ΔP is the pressure difference across the surface, σ is the liquid-vapor surface tension, and R and R' are the two radii of curvature necessary to describe any three-dimensional surface. The highest pressure is always on the concave side of the interface when R and R' have identical signs. When it is not clear which is the concave side (e.g., a saddle-shaped interface) the higher pressure is on the side of the smaller radius.

If the liquid wets the wick, that is, if the contact angle is less than 90°, and if it is assumed that the condenser and evaporator vapor-liquid interfaces can each be characterized by a single radius of curvature, the remaining terms in Equation (3) become

$$(P_V)_2 - (P_L)_2 = \frac{2\sigma}{R_2}$$

$$(P_L)_1 - (P_V)_1 = \frac{-2\sigma}{R_1} \tag{7}$$

where σ is the liquid-vapor surface tension and R_1 and R_2 are the radii of curvature describing the liquid-vapor interfaces in the evaporator and condenser regions.

Since the fin operates at a nearly constant temperature, any temperature-dependent variation of σ can be neglected. Combining Equations (3), (4), (5) and (7) yields

$$(\Delta P)_d = \frac{2\sigma}{R_1} - \frac{2\sigma}{R_2} > 0 \qquad (8)$$

This means that

$$R_1 < R_2$$

Thus, the capillary pump, that is, the wick, overcomes the frictional and inertial forces in the vapor-chamber fin by allowing a larger radius of curvature to form in the condenser than in the evaporator. Of course, the liquid must wet the wick for this to be true.

Physically this means that vapor condensing out on the wick causes a large interfacial radius of curvature to form as the liquid tends to flood the wick. However, the heat added to the evaporator makes the vapor-liquid interface retreat into the matrix of the wick, causing a smaller interfacial radius of curvature, a radius probably characteristic of the size of the pores in the wick itself and the contact angle. These differences in radii of curvature at different locations along the wick make the porous medium of the wick act as a capillary pump.

At first it might be thought that to increase the capacity of the pump it would be best to decrease the size of the pores in the wick, thereby decreasing R_1 in Equation (8). However, this also tends to increase the frictional forces in the wick. The relationship between the capillary forces, frictional forces, and inertial forces will be derived in the next section.

The upper limit on the frictional and inertial pressure drops in both the vapor and liquid can be calculated using the above expressions. The upper limit on the pressure drop through the vapor is obtained by using Equations (4), (5) and (8) and assuming that the liquid pressure drop is zero to get the inequality

$$(P_V)_1 - (P_V)_2 < 2\sigma \left(\frac{1}{R_1} - \frac{1}{R_2} \right) \qquad (9)$$

The right side is maximized when the condenser is completely flooded, that is, when $R_2 \rightarrow \infty$. Hence, for the fin to operate

$$(P_V)_1 - (P_V)_2 < \frac{2\sigma}{R_1} \tag{10}$$

Values of the right-hand side can be obtained by considering the minimum effective pore size in the wick, which for most wicking materials considered yields

$$\frac{2\sigma}{R_1} \approx 5 \text{ to } 20 \text{ inches of } H_2O$$

By similar reasoning it can be shown that the maximum pressure drop in the liquid is bounded by this same value.

It has been demonstrated that the shape of the liquid-vapor interface is critical to the operation of the capillary pump. In particular, the radii of curvature in the evaporator section are most crucial, for as long as the evaporator supplies sufficient vapor and the fin is sufficiently charged with liquid, the radii of curvature in the condenser will be large, making the pump term in Equation (8) strongly dependent on R_1.

It is not apparent what the actual shape or position of the entire liquid-vapor interface is in the fin evaporator. Three possible positions are shown in Figure 5.

The situation pictured in (a), where the interface has retreated only slightly into the wick matrix, is a correct representation for lower heat-input rates (assuming that the wick has been initially saturated with liquid). However, the situation cannot be so easily visualized while the wick is providing liquid flows at higher heat-input rates, for under such conditions, the liquid-vapor interface is certain to retreat further into the wick. At still higher values of heat input, the wick will no longer be able to supply sufficient liquid to be evaporated. The wick matrix will then dry and the interface could assume the position shown in (b) or (c), or be a combination of these. Whatever the interfacial position, when the maximum flow rate of the pump is exceeded the evaporator will dry and the base temperature will rise, as shown in Figure 3, causing eventual loss of fin effectiveness.

Because it is not clear what the shape and position of the evaporator liquid-vapor interface will be at high heat-input rates, it is essential that an isotropic wicking material be used in the present study of the vapor-chamber fin (the term isotropic will be clarified in Section IV A). In this way any limitation in fin operation due to the maximum flow rate provided by the capillary pump cannot be attributed to the directional properties of the wick.

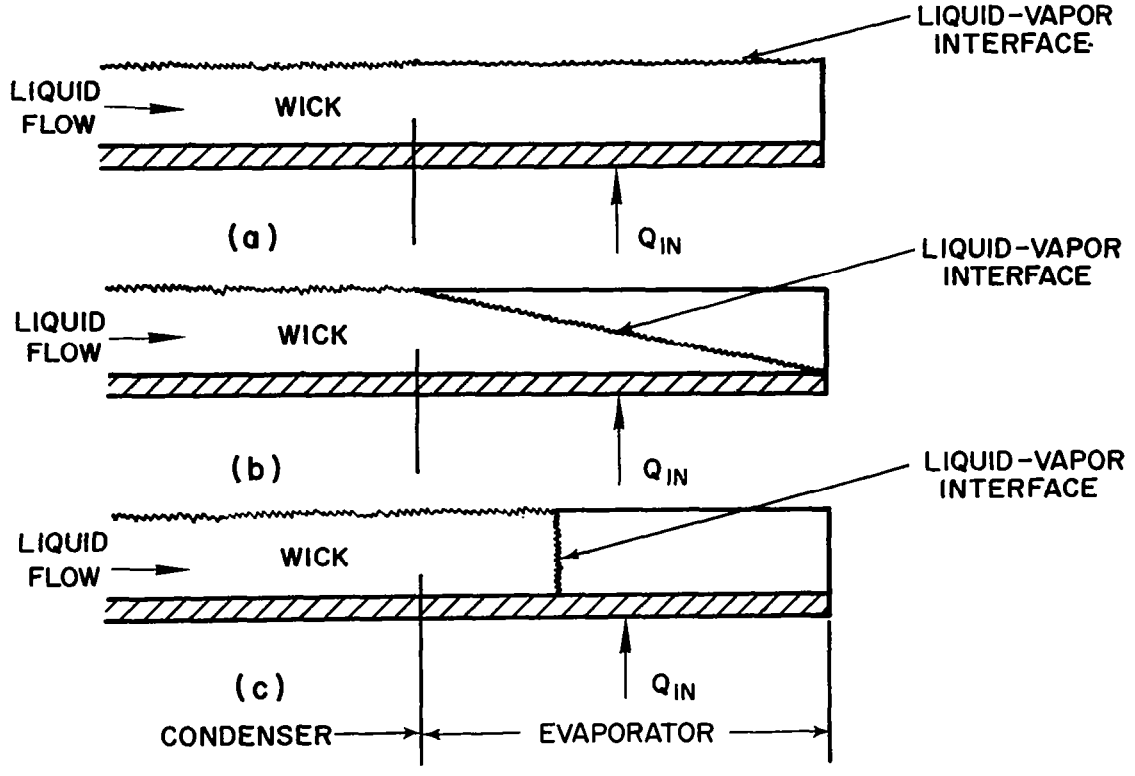

Figure 5 Simplified Picture of the Liquid-Vapor Interface in the Evaporator Section of the Fin

So far it has been shown how the capillary pump functions qualitatively. In the next section a simplified analytical model of the fin will be derived, based entirely on the limitations imposed by the capillary pump. For the present it will be assumed that the evaporator section is sufficiently small compared to the condenser section so that the pressure drop of the liquid in the evaporator section may be neglected. It will also be assumed that the evaporator heat flux is below the film boiling value.

With the help of some simplifying assumptions, an expression will be derived that will show what effect the capillary pump capability has on the maximum size of a vapor-chamber fin for a given heat input, or conversely, what effect the pump has on the maximum heat input that a fin of a given size can accept.

D. Simplified Model of Vapor-Chamber Fin

This section contains the derivation of a simplified model of the vapor-chamber fin. An analytical model of the heat pipe has been formulated by Cotter [6]. The purpose of this model of the vapor-chamber fin is to discover the parameters necessary to adequately describe the mechanism of the fin. Within the framework of the assumptions made in its derivation, the model includes the effects of rate of change of momentum, surface tension forces, and the frictional forces in the body of the wicking material.

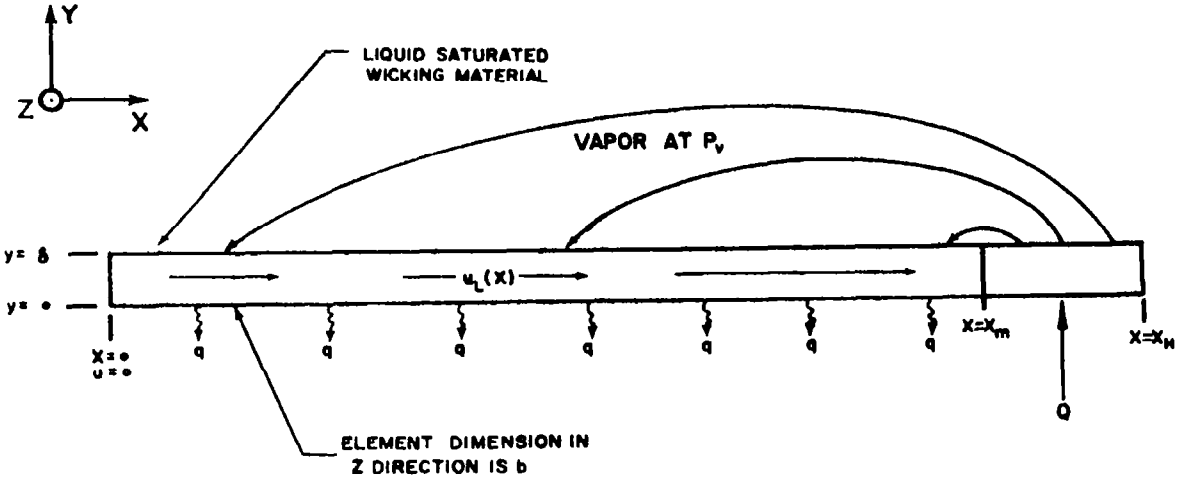

Figure 6 Simplified Model of Vapor-Chamber Fin

Figure 6 shows a simplified model of the vapor-chamber fin that is rejecting heat at a specified heat flux density q. The fin width in the z-direction is b and the heat rejecting length is x_m. Because limiting boiling heat fluxes are not being considered, the evaporator section, from $x = x_m$ to $x = x_T$, is assumed to be of sufficient size to provide enough vapor to meet the requirements set by the specified value of the condenser rejection flux density q. In addition, the following assumptions are made concerning the model shown in Figure 6:

1) The wicking material is rigid, is of constant thickness δ, and is saturated with a wetting liquid along the entire condenser length x_m. Also the wicking material is considered to be isotropic, so that at any given cross-section of the wick, the pore area, A_p, and the total area of the cross-section, A_T, are related by

$$\frac{A_p}{A_T} = \epsilon \tag{11}$$

where ϵ is the porosity of the material. This relation is derived in Section IV B.

2) The vapor and the liquid are at the same constant temperature from $x = 0$ to $x = x_m$. This assumes no subcooling of the liquid. It follows that the vapor pressure P_V is also constant along this length, and that there is little conducted energy or variation in convected energy in the x or z directions within the wicking material.

3) The vapor that condenses on the liquid-vapor interface has a velocity u_V in the y-direction. This velocity has no x or z components; thus there are no momentum contributions in these directions.

4) The effects of gravity are not considered.

5) At any given point, the liquid-vapor interface can be characterized by one radius of curvature, R.

6) The velocity of the liquid in the wicking material, u_L, has an x component only, and is uniform across the wick thickness δ. This velocity is considered to be an average velocity in the pores of the wick.

7) Any terms containing differentials raised to the second or higher powers are neglected.

8) The heat flux is considered constant with length.

Figure 7 shows the forces and momentum fluxes associated with a differential element of the saturated wicking material at a given x in the heat rejecting portion of the fin.

Applying the continuity equation for the element of Figure 7, the relationship between the liquid flow rate w_L and the vapor flow rate w_V is obtained

$$(w_L)_x + w_V = (w_L)_{x+dx} \tag{12}$$

Because

$$(w_L)_x = \rho_L \epsilon (\delta b) u_L \tag{13}$$

and

$$(w_L)_{x+dx} = \rho_L \epsilon (\delta b)\left(u_L + \frac{du_L}{dx} dx\right) \tag{14}$$

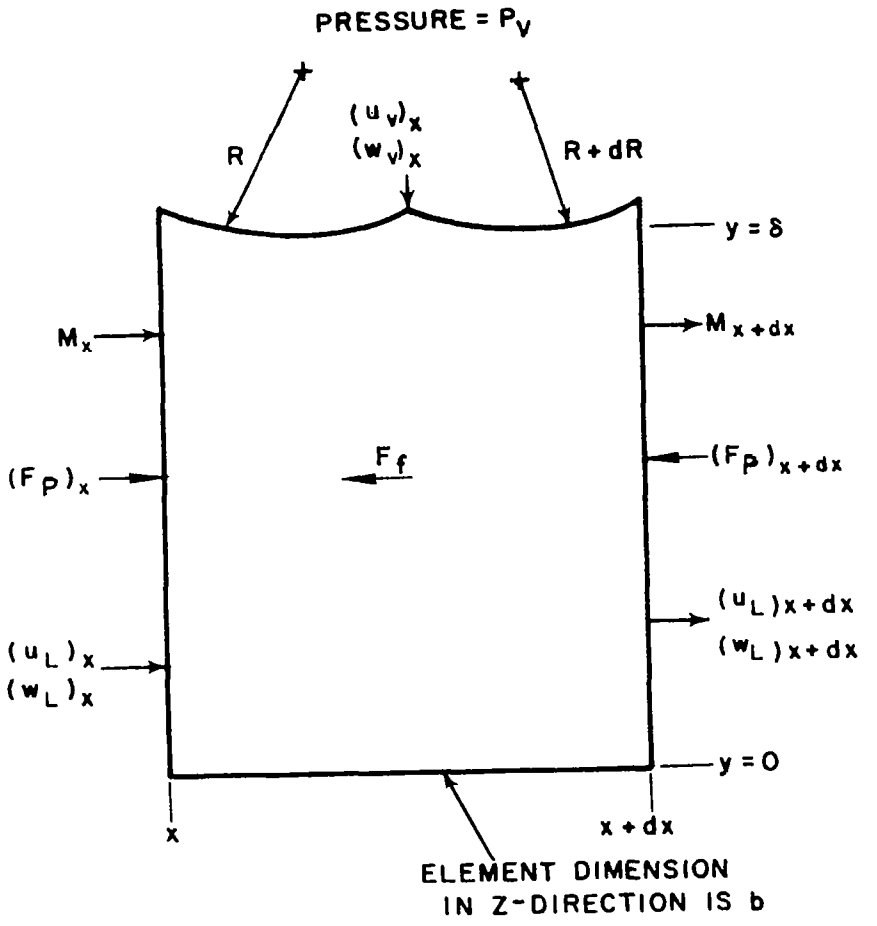

Figure 7 Differential Element of Wicking Material for Momentum Equation

where ρ_L is the liquid density, it follows that

$$w_V = \rho_L \frac{du_L}{dx} \, dx \, \epsilon \, (\delta \, b) \tag{15}$$

where

$$w_V = \rho_V \, u_V \, (bdx) \tag{16}$$

and ρ_V is the vapor density.

The momentum equation in the x-direction for the element in Figure 7 is

$$\Sigma F_x = M_{x+dx} - M_x \tag{17}$$

The momentum terms are

$$M_x = \frac{\rho_L}{g_o} u_L^2 \epsilon (b \delta) \tag{18}$$

$$M_{x+dx} = \frac{\rho_L}{g_o} u_L^2 \epsilon (b \delta) + \frac{\rho_L}{g_o} \frac{d(u_L^2)}{dx} dx \epsilon (b \delta) \tag{19}$$

where g_o is the proportionality constant in Newton's second law. It should be noted that because of Assumption 3 there is no momentum contribution to Equation (17) by the vapor as it enters the top of the element. Calculations show that when such a momentum term is included, it is negligible compared to the other terms in Equation (17). In addition, the presence of the rigid wick at the liquid-vapor interface interferes with the interaction of the liquid and vapor with respect to momentum, and thus makes the inclusion of such a term doubtful in the analysis of an actual vapor-chamber fin.

Two forces make up the force term in Equation (17): the pressure force due to the differences in radius of curvature at x and x + dx, and the frictional force F_f acting on the liquid as it flows through the porous medium of the wick. Thus

$$\Sigma F_x = (F_p)_x - (F_p)_{x+dx} - F_f \tag{20}$$

The pressure force F_p is obtained by use of the Laplace-Young equation, Equation (6). Because of Assumption 5 this reduces to

$$\Delta P = \frac{2\sigma}{R} \tag{21}$$

where ΔP is the pressure drop across the liquid-vapor interface at x, σ is the liquid-vapor surface tension, and R is the radius of curvature of the interface at x. Thus the pressure forces at x and x + dx are

$$(F_p)_x = \left(P_V - \frac{2\sigma}{R}\right) \epsilon (\delta b) \tag{22}$$

$$(F_p)_{x+dx} = \left(P_V - \frac{2\sigma}{R + dR}\right) \epsilon \, (\delta b) \tag{23}$$

where the vapor pressure P_V is constant, by Assumption 2.

The net pressure force on the element is found by adding Equations (22) and (23) vectorially to get

$$(F_p)_x - (F_p)_{x+dx} = - \epsilon \, (\delta b) \, (2\sigma) \, \frac{dR}{R^2} \tag{24}$$

where RdR has been neglected when it is compared to R^2.

Because of the low flow rates and velocities encountered with capillary flow in wicks, the flow produced by the net capillary force in Equation (24) can be assumed to be both laminar and relatively free from inertia effects. As pointed out by Scheidegger[7], both of these conditions must be met if Darcy's law[7] for flow through porous media is to apply. Darcy's law can be stated as

$$\left(\frac{dP}{dX}\right)_f = K_1 \left(\frac{\mu_L}{\rho_L}\right) \frac{w_L}{A_T} \tag{25}$$

where

$\left(\frac{dP}{dX}\right)_f$ = pressure gradient in the porous medium due to frictional forces

μ_L = liquid viscosity

ρ_L = liquid density

A_T = total cross-sectional area of flow (i.e., the sum of the pore area and the area of the solid at a given cross-section through the porous material)

w_L = liquid mass flow rate

The term K_1 is a constant of proportionality. This constant is particularly important in the evaluation of wicking materials. It is dependent on the geometry and dimensions of the passages in the wicking material and could possibly be described adequately if an equivalent passage diameter, the wick tortuosity, and porosity of the material were all known functions. Since this is usually not the case, K_1 can be determined experimentally by passing a known flow rate of liquid through the wicking material and measuring the resulting pressure drop across the sample. Then K_1, which will be called the wick friction factor, can be calculated from Equation (25). The constant K_1 has the dimensions of $(\text{length})^{-2}$ and is the reciprocal of permeability.

The frictional force on the fluid element shown in Figure 7 is given by

$$F_f = \left(\frac{dP}{dx}\right)_f \quad dx \quad [\epsilon (\delta \quad b)] \tag{26}$$

By combining Equations (13), (25), and (26), an expression for the friction term in Equation (20) is given by

$$F_f = K_1 \epsilon^2 (\delta b) \mu_L u_L dx \tag{27}$$

Combining Equations (17), (18), (19), (20) (24), and (27) results in the differential momentum equation

$$- 2 \sigma \frac{dR}{R^2} - \epsilon K_1 \mu_L u_L dx = \frac{\rho_L}{g_o} \frac{d (u_L)^2}{dx} dx \tag{28}$$

The remaining relationship necessary to describe the operation of the fin is the energy equation. Figure 8 shows the energy fluxes associated with a differential wick element at some x in the condenser portion of the fin, where Q is the energy

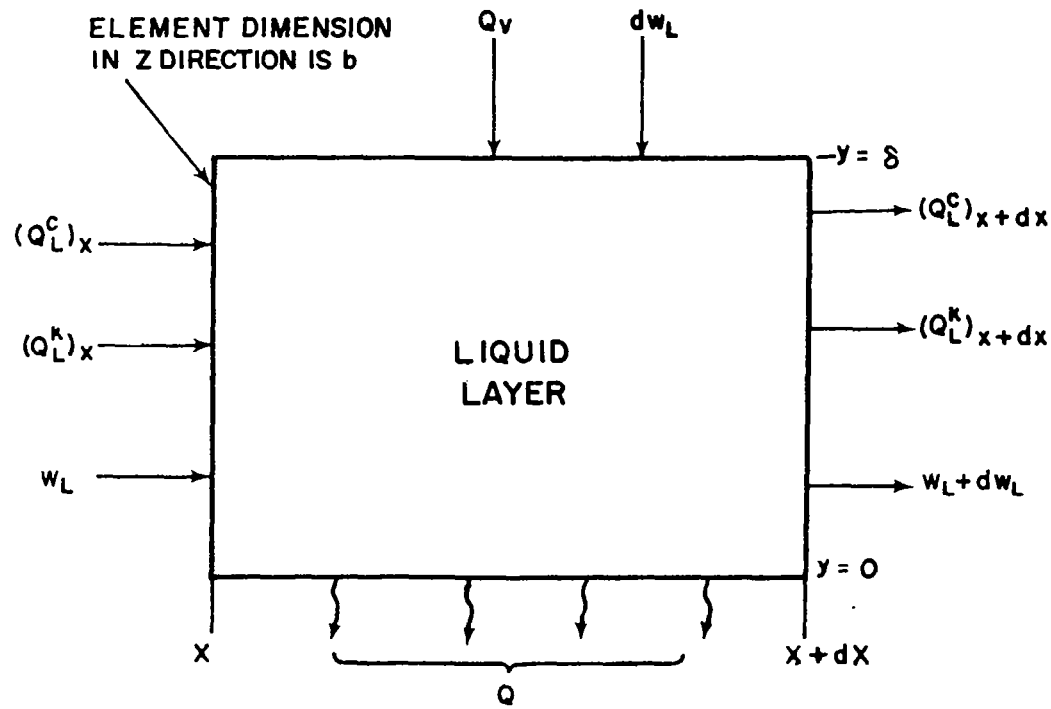

Figure 8 Differential Element of Wicking Material for Energy Equation

transferred per unit time, the superscripts c and k refer to convection and conduction, and L and V refer to liquid and vapor.

Neglecting changes in kinetic energy, the individual terms in Figure 8 are given by

$$\underline{\text{in}} \qquad\qquad \underline{\text{out}}$$

$$\left.\begin{aligned} Q_V &= Q_V^c + Q_V^k & (Q_L^c)_{x+dx} &= w_L h_L + \frac{d(w_L h_L)}{dx}\, dx \\ (Q_L^c)_x &= w_L h_L & (Q_L^k)_{x+dx} &= -k_L (\delta b)\left[\frac{dT_L}{dx} + \frac{d^2 T_L}{dx^2}\, dx\right] \end{aligned}\right\} \quad (29)$$

$$(Q_L^k)_x = -k_L (\delta b)\, \frac{dT_L}{dx} \qquad\qquad Q = q\,(b\ dx)$$

where h is enthalpy and k_L is the thermal conductivity of the liquid-wick combination.

Because of Assumption 2 all of the conduction terms in Equation (29) are zero. Thus the energy equation for the element in Figure 8 is

$$Q_V^c + (Q_L^c)_x = (Q_L^c)_{x+dx} + Q \qquad (30)$$

The energy entering the top surface of the element is

$$Q_V = Q_V^c = w_V h_V \qquad (31)$$

Combining this with the continuity equation, Equation (15), results in

$$Q_V^c = h_V \rho_L \frac{du_L}{dx}\, dx\, \epsilon\, (\delta b) \qquad (32)$$

Putting Equations (32), (29) and (13) into Equation (30) yields the combined energy-continuity differential equation

$$u_L \rho_L \frac{dh_L}{dx} - (h_V - h_L) \rho_L \frac{du_L}{dx} + \frac{q}{\delta \epsilon} = 0 \tag{33}$$

But for an incompressible liquid where internal energy is a function of temperature only, the enthalpy variation with x is expressed as

$$\frac{dh_L}{dx} = C_L \frac{dT_L}{dx} + \frac{1}{\rho_L} \frac{dP_L}{dx} \tag{34}$$

where C_L is the specific heat of the liquid. As shown in Section III C , the pressure drop in the liquid is very small, so that

$$\frac{dP_L}{dx} \approx 0 \tag{35}$$

Also by Assumption 2

$$\frac{dT_L}{dx} = 0 \tag{36}$$

Thus

$$\frac{dh_L}{dx} \approx 0 \tag{37}$$

so that Equation (33) becomes

$$\frac{du_L}{dx} = \frac{q}{h_{VL} \delta \epsilon \rho_L} \tag{38}$$

where h_{VL} is the latent heat of vaporization of the liquid.

Integrating Equation (38) and using Assumption 8 yields the combined energy-continuity equation

$$u_L = \frac{q}{h_{VL} \delta \epsilon \rho_L} x \tag{39}$$

showing that the liquid velocity varies linearly with x. The liquid flow rate then becomes

$$w_L = \frac{qb}{h_{VL}} \quad x \tag{40}$$

Finally, Equations (39) and (28) can be combined to give an energy-continuity-momentum integral equation

$$-\int_{R_{x=o}}^{R_{x=x_m}} 2\sigma \frac{dR}{R^2} - \int_{o}^{x_m} K_1 \frac{q}{h_{VL}\delta} \frac{\mu_L}{\rho_L} x\,dx = \int_{o}^{x_m} \frac{2q^2 x\,dx}{g_o h_{VL}^2 \rho_L \epsilon^2 \delta^2} \tag{41}$$

where, as shown in Figure 6, x_m is the length of the heat rejection portion of the fin.

To evaluate the maximum output of the capillary pump, Equation (40) shows that x_m must be a maximum. In Equation (41) it is seen that to maximize x_m the limits of integration on the surface tension must contain both minimum and maximum values of R. In Section III C it was shown that at x = 0, R can be very large and can be considered to approach an infinite value for optimum fin operation. Similarly, as shown by Equation (8) the radius of curvature in the evaporator must be at some minimum radius of curvature, R_{min}. To calculate the maximum value of x_m, the assumption is made that at

$$x = 0, \; R \rightarrow \infty$$

and that at (42)

$$x = x_m, \; R \rightarrow R_{min}$$

where R_{min} is the minimum radius of curvature that the wicking material can support. It is further assumed that the entire evaporator liquid-vapor interface can be characterized by R_{min}, although no assumption has to be made about the position of the interface in the evaporator.

Using the above limits for R, Equation (41) can be integrated and solved for x_m to obtain

$$x_m = \left\{ \frac{\rho_L h_{VL} \sigma}{\mu_L} \left[\frac{\frac{2}{R_{min}}}{\frac{qK_1}{2\delta}\left(1 + \frac{2q}{g_o \mu_L h_{VL} \delta \epsilon^2 K_1}\right)} \right] \right\}^{1/2} \tag{43}$$

If a range of representative values is substituted for the quantities in the non-unity term in the denominator of Equation (43), it is found that

$$\frac{2q}{g_o \mu_L h_{VL} \delta \epsilon^2 K_1} \ll 1 \tag{44}$$

This term represents the contribution of the rate of change of liquid momentum, and can be neglected when compared to unity. Thus the expression for the maximum length of the heat rejection portion of the fin is given by

$$x_m = 2 \left(\frac{\rho_L h_{VL} \sigma}{\mu_L} \right)^{1/2} \left(\frac{\delta}{K_1 q R_{min}} \right)^{1/2} \tag{45}$$

In Equation (45) the liquid properties enter as the dimensional parameter

$$N = \frac{\rho_L h_{VL} \sigma}{\mu_L} \tag{46}$$

To maximize the performance of the fin, a liquid should have as large a value of N as possible. N for conventional liquids ranges roughly from 1 to 350 Btu hr lb_f/ft^3 lb_m. By way of contrast, the liquid metal bismuth has a value of N = 2097 Btu hr lb_f/ft^3 lb_m at 1300°F. Other values of N are listed in Section IV D.

The only quantity in Equation (45) that is not readily measurable is R_{min}. Because a maximum value of x_m is desired, R_{min} is assumed to be the smallest radius of curvature that the wick can support. The method used to determine an effective minimum radius of curvature in a wicking material was to observe the maximum height to which the liquid rises in a vertical sample of the wicking material. If the pores in the vertical wick through which the liquid rises can be thought of as single capillary tubes of an equivalent diameter, the effective minimum radius of curvature is

$$R_{min} = \frac{2 g_o \sigma}{\rho_L g \ell_m} \tag{47}$$

where ℓ_m is the maximum height of the liquid in the vertical wick when exposed to a gravity field, g. Equation (47) is obtained from a static force balance on the liquid in a capillary tube. See Section V A for the derivation of Equation (47). R_{min} in Equation (47) is termed the effective minimum radius of curvature because in actuality the smaller pores in a wicking material are not single capillaries but are interconnected with pores of larger size. However,

Equation (47) should still be an effective measure of R_{min} for a vapor-chamber fin application. This will be demonstrated in Section V A.

By combining Equations (47) and (45) it is seen that the final expression for the maximum length of the condenser section of the fin is given by

$$x_m = \left[2 \left(\frac{\rho_L \, h_{VL} \sigma}{\mu_L} \right) \left(\frac{\delta}{q} \right) \left(\frac{g \, \rho_L}{g_o \, \sigma} \right)_{WR} \frac{\ell_m}{K_1} \right]^{1/2} \qquad (48)$$

where
- σ = surface tension
- g = acceleration of gravity
- g_o = Newton's second law proportionality constant
- ρ_L = liquid density
- h_{VL} = liquid latent heat of vaporization
- δ = liquid - wick thickness (constant)
- ℓ_m = equilibrium height of liquid rise in vertical wick
- μ_L = liquid viscosity
- q = specified rejection heat flux
- K_1 = wick friction factor

and where the subscript WR refers to wicking-rise test conditions.

Thus, x_m is maximized when the wicking parameter ℓ_m/K_1 is large. It should be emphasized that gravity effects have not been considered in Equation (48) and that g, the acceleration of gravity, enters only through the separate process of determining R_{min} from Equation (47).

Equation (48) can be expressed in terms of the maximum total fin heat input Q_{max}. Thus, instead of solving for x_m and specifying a heat rejection flux q, the problem can be restated to get

$$Q_{max} = 2 \left(\frac{\rho_L \, h_{VL} \sigma}{\mu_L} \right) \left(\frac{b \, \delta}{x_m} \right) \left(\frac{g}{g_o} \frac{\rho_L}{\sigma} \right)_{WR} \left(\frac{\ell_m}{K_1} \right) \qquad (49)$$

where b is the fin width in the z-direction. This is the maximum total heat input that can be transferred to a vapor-chamber fin with a condenser of length x_m.

A plot of Equation (48) is shown in Figure 9 for water at 350°F and a wick thickness of $\delta = 0.1$ inch. This plot shows the maximum size of the heat rejection portion of the fin of Figure 6 for various heat rejection rates

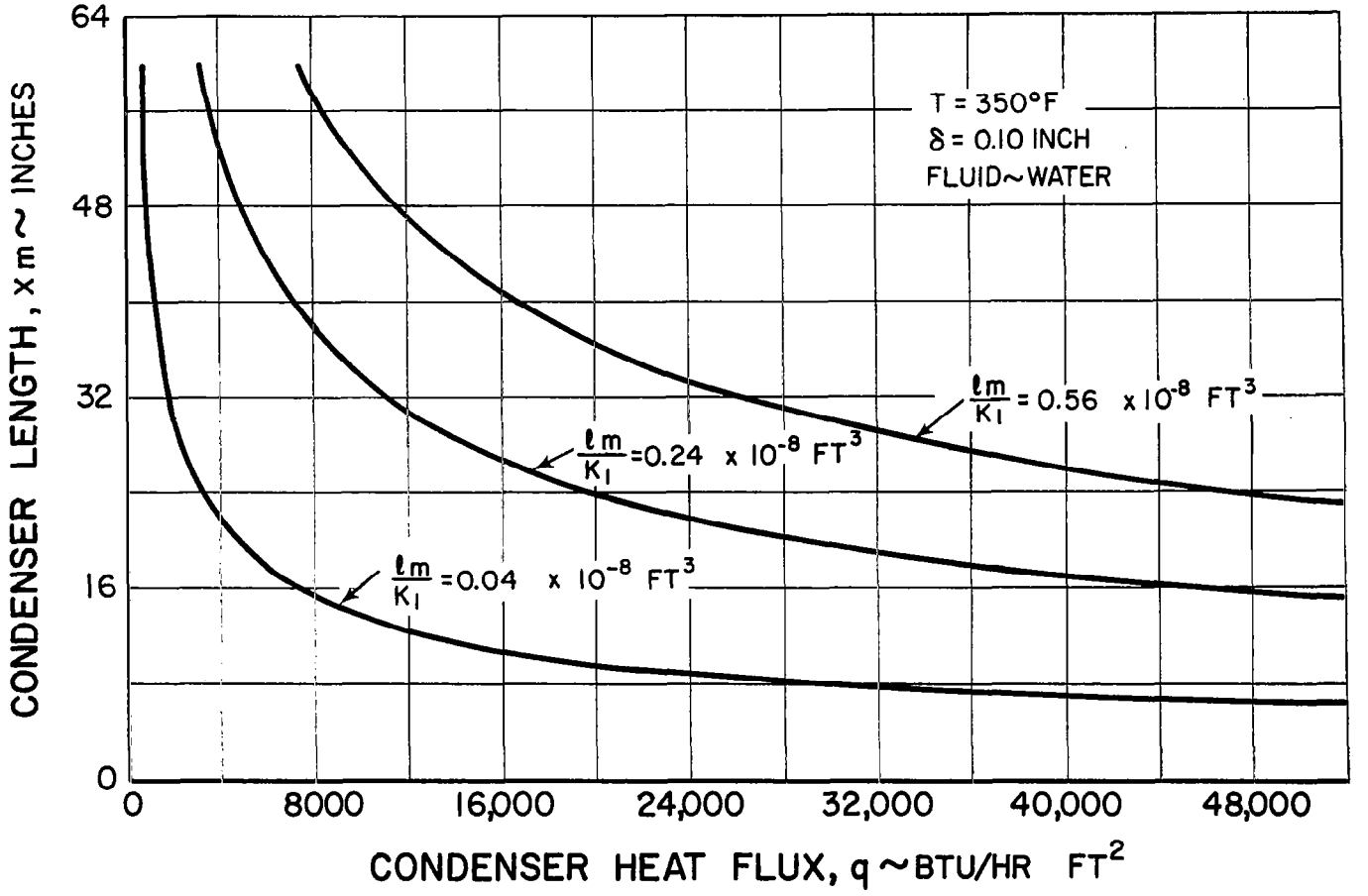

Figure 9 Condenser Length as Function of Condenser Heat Flux and Wick Properties Computed from Equation (48)

as a function of the capillary pumping parameter ℓ_m/K_1. Again it must be remembered that neither gravity nor the evaporator section size are considered.

If the effects of gravity are included in the analysis, then the maximum total heat input that can be transferred is given by the following equation (see Appendix 3 for the derivation).

$$Q_{max} = \left[\left(\frac{2\rho_L h_{VL} \sigma}{\mu_L} \right) \left(\frac{b\,\delta}{x_m} \right) \left(\frac{g}{g_o} \frac{\rho_L}{\sigma} \right)_{WR} - \frac{2\rho_L^2 h_{VL}}{\mu_L} \frac{g}{g_o} \left(\frac{\delta\, b}{\ell_m} \right) \sin\theta \right] \frac{\ell_m}{K_1} \tag{50}$$

In most applications of the vapor-chamber fin, the evaporator section is small in area compared to the condenser section and may be assumed to have no effect on the condenser, as long as the limiting heat flux is not reached. However, if it is inherent in a heat-rejection problem to have low evaporator heat flux, the evaporator may be of significant length when compared to the condenser. The following equation includes the effects of liquid pressure drop in the evaporator (see Appendix 3 for the derivation) and gravity.

$$Q_{max} = \left[\left(\frac{2\rho_L h_{VL} \sigma}{\mu_L} \right) \left(\frac{b\,\delta}{X_T} \right) \left(\frac{g}{g_o} \frac{\rho_L}{\sigma} \right)_{WR} - \frac{2\rho_L^2 h_{VL}}{\mu_L} \frac{g}{g_o} \left(\frac{b\,\delta}{\ell_m} \right) \sin\theta \right] \frac{\ell_m}{K_1} \tag{51}$$

The simplified analytic model of the vapor-chamber fin presented in this section illustrates the need for a separate wicking study to determine the value of ℓ_m/K_1 for various wicking materials. The results of such a study are outlined in the next sections.

E. Summary

In the present study of the vapor-chamber fin for use in space-radiator applications, the two key factors in the operation of the fin as a heat rejection device seem to be:

1) The heat flux at which apparent film-boiling occurs in the wick of the evaporator section of the fin, and

2) The maximum liquid flow rate that the capillary pump can provide to the evaporator section of the fin.

Due to the complicated nature of the phenomenon of boiling itself, a separate experimental program was conducted to evaluate the limits imposed on fin operation by the onset of boiling in wicks.

To evaluate the effect of the capillary pump on fin operation, a simplified analytic model has been derived in which it was found that the output of the capillary pump depends on the liquid parameter

$$N = \frac{\rho_L \, h_{VL} \, \sigma}{\mu_L} \tag{52}$$

and the capillary pumping parameter ℓ_m/K_1 when net body forces are zero.

Both of these parameters should be large to maximize the performance of the vapor-chamber fin.

The capillary pumping parameter is the ratio of the maximum capillary forces to the frictional forces on a liquid flowing in a wick. The constant ℓ_m is a measure of the magnitude of the capillary forces associated with the liquid-wick combination. Physically, ℓ_m is the equilibrium height to which the liquid will rise in a vertical sample of the wick.

The constant K_1 is a measure of the magnitude of the frictional forces associated with a flow of the liquid through the wick under conditions where Darcy's law applies. This constant is obtained by measuring the pressure drop across a wicking material sample through which a given amount of liquid is flowing.

Thus to study the effect of the capillary pump on the operation of the fin, a separate wicking materials study was conducted to measure values of ℓ_m and K_1.

IV. WICKING MATERIALS AND TEST FLUIDS

A. Description of Wicking Materials

A wick can be defined as a porous material whose pores are of such size that a liquid can be moved through it by the action of capillary forces. The pores must also be highly interconnected rather than separate and discrete. The pore sizes should fall into a range where a favorable balance exists between the capillary forces and the frictional forces associated with the motion of a liquid.

The wicking materials considered in this study for use in vapor-chamber fins were narrowed down to three classes of metallic porous materials. They are:

1) sintered screen materials
2) sintered powder materials
3) sintered fiber materials

The reasons for selecting these materials, which are outlined below, include ease of fabrication, dimensional stability, isotropy and thermal conductivity.

1) Wetting Properties

For a porous material to act as a wick, it must be wetted by the liquid. With average care in eliminating contaminants, nickel forms a wetting surface with the conventional liquids used in this study. Nickel oxide is even more likely to form a smaller contact angle than pure nickel, because of its higher surface energy (see Figure 38).

Because stainless steel is also wetted by most liquids, it was employed as a second choice. However much greater care must be taken with a stainless steel surface to insure that no contaminants are present to prevent wetting. The need to keep stainless steel especially clean has been pointed out by Fox, Hare, and Zisman[8].

2) Chemical Activity

Nickel, stainless steel, and their oxides are inert with respect to the working fluids of this study.

3) Fin Fabrication

Any sample tested may eventually be installed in a fin model. All of the porous materials listed are capable of being attached to the metal surface of the fin cavity and are capable of being fabricated in a variety of shapes.

4) Dimensional Stability

As shown by the analytic model of the last section, the wick dimensions must be known with some accuracy. All of the above materials are sufficiently rigid so that they will maintain their dimensions when saturated with a liquid. This is not true of soft fibrous and woven materials such as Fiberglas, textile fabrics, etc. The latter materials may either swell upon absorbing liquid or become compressed by capillary forces at a liquid-solid-vapor interface.

Sample rigidity also allows the pore size distribution to be determined, since there are no experimental techniques for measuring this quantity in nonrigid porous materials.

5) Isotropy

As pointed out in Section III C, it is essential that an isotropic wicking material be used. By isotropic, it is meant that the wicking material has the same pore size distribution in any given direction. Thus, by using isotropic wicks, the operation of the capillary pump can be studied without complications caused by wick directional properties.

The porous materials listed are essentially isotropic, with the obvious exception of the metallic screen layers. An analysis of the latter shows that for a square weave structure, the departure from isotropy is not great.

6) Wick Thermal Conductivity

The thermal conductivity in the liquid-wick layer is a factor in fin performance. The effective thermal resistance of this layer is reduced if a wicking material of relatively high thermal conductivity is used.

This is shown by considering the two limiting cases of heat conduction in a porous medium as presented by Gorring and Churchill[9]. The lower limit on the effective conductivity of a two-phase porous medium is found by assuming that the two phases conduct heat in series. The resulting expression is

$$\left(\frac{k}{k_s}\right)_{min} = \frac{1}{1 + \epsilon\left(\frac{k_s}{k_L} - 1\right)} \qquad (53)$$

where k is the effective thermal conductivity, ϵ is the porosity, and k_S and k_L are solid and liquid conductivities respectively. To maximinize k, k_S should be as large as possible.

The upper limit on the effective heat conductivity would occur if both phases conducted heat in parallel. This yields

$$\left(\frac{\bar{k}}{k_s}\right)_{max} = 1 - \epsilon\left(1 - \frac{k_L}{k_s}\right) \tag{54}$$

Again, k_S should be as large as possible to maximize k, the effective conductivity.

Hence, from the standpoint of wick thermal conductivity, metal porous materials will be superior to other more conventional wicking materials, due to their inherently higher conductivities.

The following is a detailed description of each class of porous material.

1. Sintered Screen Materials

The four sintered nickel screen samples that have been studied are listed in Table 1.

TABLE 1

Sintered Screen Samples

Sample No.	Mesh Size, (wires per inch)	Wire Diameter, inches
M7	50	0.0090
M8	100	0.0045
M9	150	0.0030
M10	200	0.0022

The sintered screen samples consist of layers of nickel screen that have been pressed against a nickel foil backing and sintered together at points of contact in a furnace with an ammonia atmosphere. The mesh referred to is the number of wires per linear inch in either the warp wire direction or the woof wire direction. The wire diameter given is that of both the warp and woof wires.

A typical screen sample (in this case 100 mesh) is shown in cross-section in Figure 10 and in plan in Figure 11. The solid structure at the bottom of the sample in Figure 10 is the nickel backup foil to which the screens are sintered. The porous material of this sample is 0.0675 inch thick and the backup foil is 0.0248 inch thick. These photomicrographs exhibit a number of features of sintered screens as porous materials. For instance, as the screens are stacked in Figure 10, it would probably be incorrect to characterize the pore size of the material based solely on the spacing of the wires in one layer of screen. The photomicrographs show that screen layers (at least in the two top layers) are stacked in such a way that alternate layers are displaced from one another by one-half a wire spacing. This means that wherever there is a square opening (or pore) formed by two warp and two woof wires in one screen layer, there is a crimped wire elbow protruding into the center of the opening from the screen layer immediately below the first. This results in a smaller pore size and a denser structure. Also noteworthy is the lack of any relatively large pores that are continuous from the backup foil to the free surface of the porous material.

Comparison of Figures 10 and 11 also shows that sintered screen samples are not strictly isotropic. However, because of the interlocking of the screen layers, (i.e., the displaced stacking discussed above) the departure from isotropy is not great.

2. Sintered Powder Materials

The six sintered nickel powder samples investigated are listed in Table 2.

TABLE 2

Sintered Powder Samples

Sample No.	Powder Size Range, Microns
M1	150-297
M2	150-297
M3	297-841
M4	297-841
M5	297-841
M6	297-841

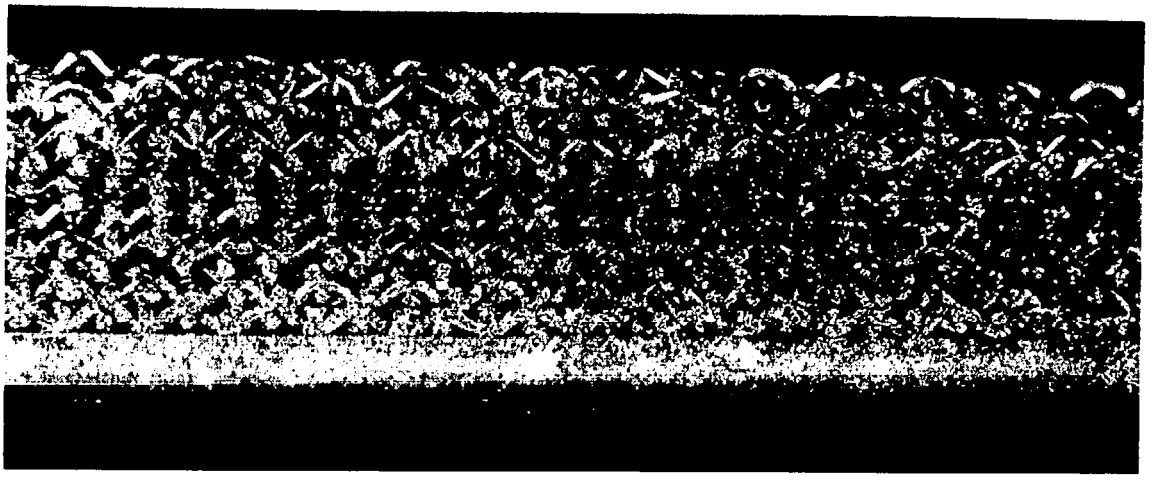

Mag:21X

Figure 10 Cross-Sectional View of 100-Mesh Sintered Nickel Screen Sample M8

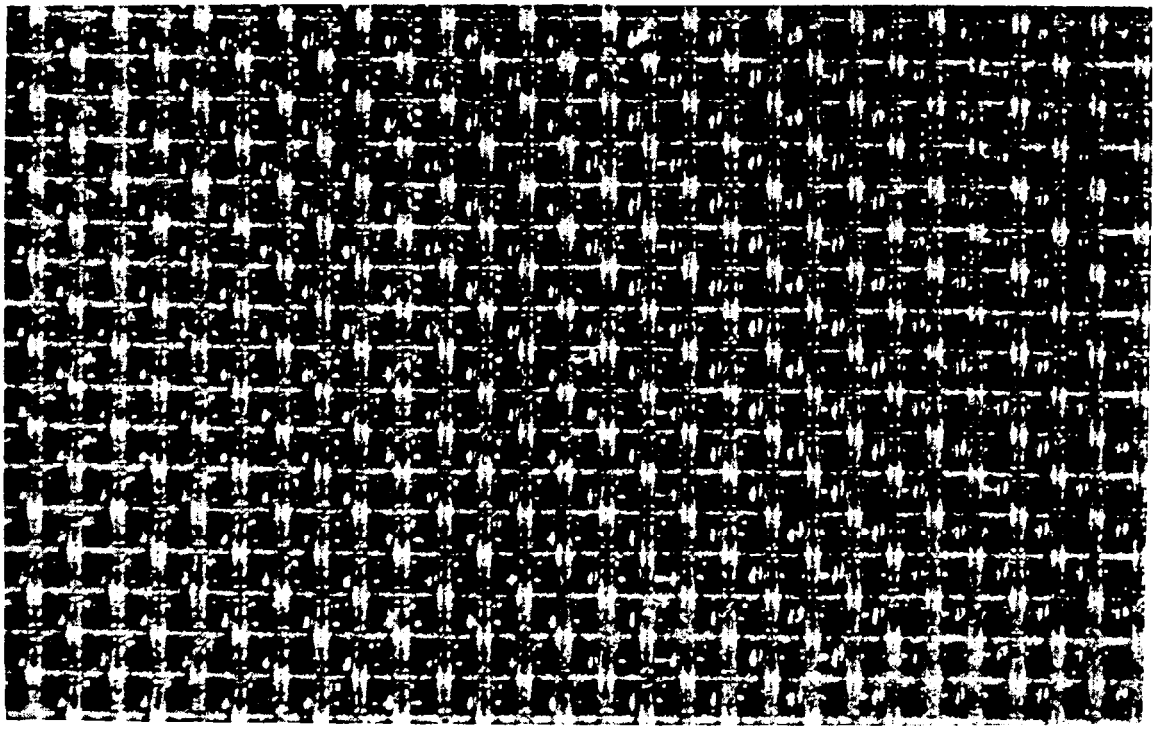

Mag:21X

Figure 11 Top View of 100-Mesh Sintered Nickel Screen Sample M8

These samples were made by compressing the nickel powder against a nickel backup foil, using a die. This "green" material was then placed in a furnace with an ammonia atmosphere, where the nickel powder was sintered to itself and to the nickel backup foil. The nickel powder used to make each sample is termed an irregular powder, irregular in that the nickel particles in the powder were more needle-like than spherical. The length-to-diameter ratio of these needle-like particles is typically 4 or less.

In an irregular powder with its needle-like particles, the porosity can be varied over a fairly wide range from sample to sample. However, if a spherical powder is used; the porosity is restricted to fairly narrow limits. There are two regular patterns in which spheres of equal diameter can be packed together stably, cubic and rhombohedric. The porosities of these packings are 47. 84 and 25. 95 per cent respectively. By using irregular powders rather than spherical regular powders, the porosity of sintered powdered samples can be greater than the 47. 84 per cent that a spherical powder might impose.

One of the sintered powder samples, M4, is shown in cross-section in Figure 12 and in plan in Figure 13. The solid structure at the bottom of the sample in Figure 12 is the nickel backup foil. The porous sintered nickel powder is 0. 0873 inch thick and the nickel backup foil is 0. 0248 inch thick.

The irregularity of the pore structure shown in Figures 12 and 13 is in contrast to the relatively regular structure exhibited by the sintered screen samples. At some locations the powder seems to have melted in sintering and coalesced into large globules.

The range of pore sizes is apparently greater in Sample M4 than for the sintered screens. As shown in Figure 13, the pores on the surface range from voids of dimensions comparable to the diameter of the smallest powder used, to large voids that could more aptly be termed craters. Figure 12 also shows that there is a significant number of large interconnected pores of relatively low tortuosity running from the backup foil to the free surface of the porous material. Such a pore geometry is necessary for good boiling heat transfer characteristics, as will be shown in Section VIII.

Mag:21X

Figure 12 Cross-Sectional View of Sintered Nickel Powder Sample M4

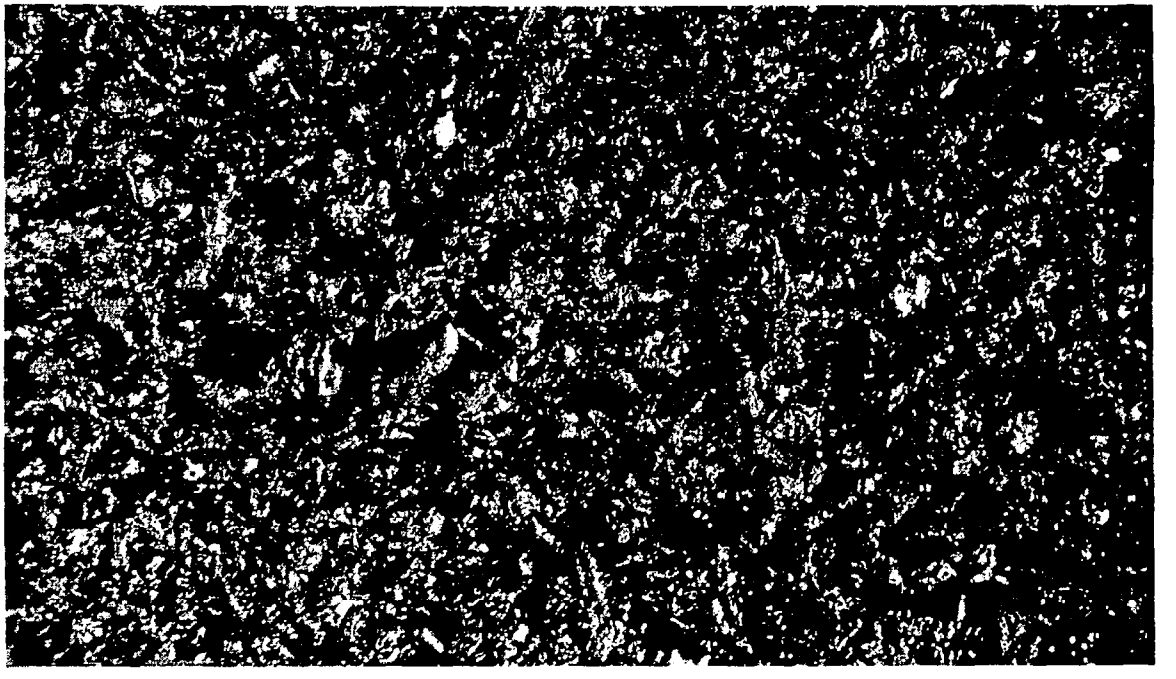

Mag:21X

Figure 13 Top View of Sintered Nickel Powder Sample M4

3. Sintered Fiber Materials

The thirteen sintered metal fiber samples studied are listed in Table 3.

TABLE 3

Sintered Fiber Samples

Sample No.	Material	Mean Fiber Diameter, Inches
H1	nickel	0.0004
H2	nickel	0.0004
H3	nickel	0.0004
H4	nickel	0.0004
H5	nickel	0.0006
H6	nickel	0.0006
H7	nickel	0.0006
H8	nickel	0.0006
H9	nickel	0.0006
H10	nickel	0.0006
H11	430 stainless steel	0.0013
H12	430 stainless steel	0.0013
H13	430 stainless steel	0.0030

As shown in the table, these sintered fiber samples were made from nickel or stainless steel. In each case the backup foil to which the porous material is sintered was the same material as the porous structure.

The metallic fibers making up the porous material had a length-to-diameter ratio in the range of 10 to 1000. The fibers were felted to produce a randomly interlocked structure. The latter was pressed against a backup foil and then sintered in a controlled-atmosphere furnace to produce bonds at points where the fibers touch one another and the foil backing.

A sintered nickel fiber sample, H1, is shown in cross-section in Figure 14 and in plan in Figure 15. The nickel fiber structure is 0.0825 inch thick and the nickel backup foil is 0.0218 inch thick.

Photomicrographs of a sample (H12) composed of stainless steel fibers of a much larger diameter are shown in Figures 16 and 17. In this case, the stainless steel fiber structure shown is 0.0991 inch thick and the stainless steel backup foil is 0.0218 inch thick.

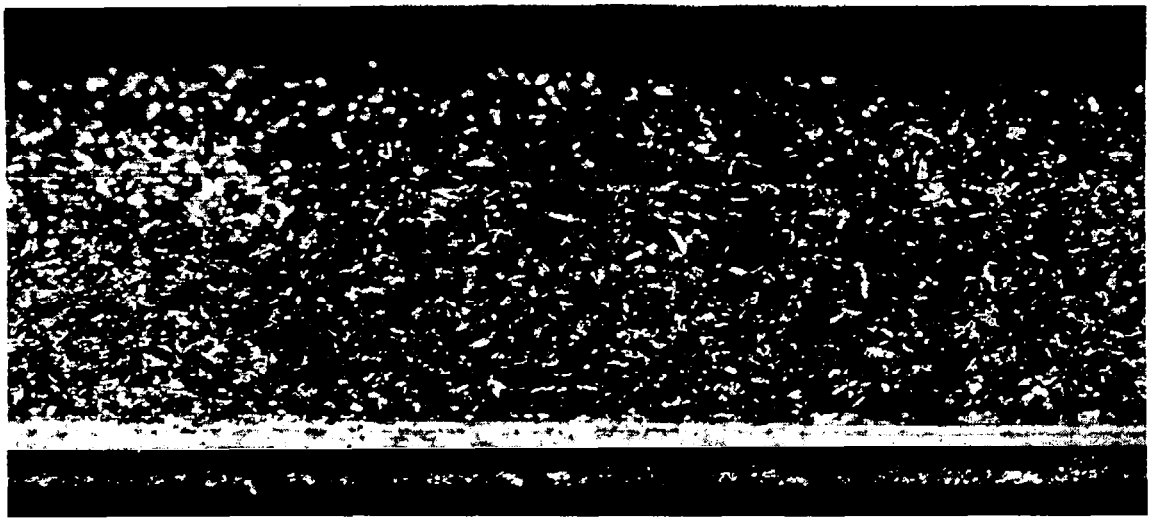

Mag:21X

Figure 14 Cross-Sectional View of Sintered Nickel Fiber Sample H 1

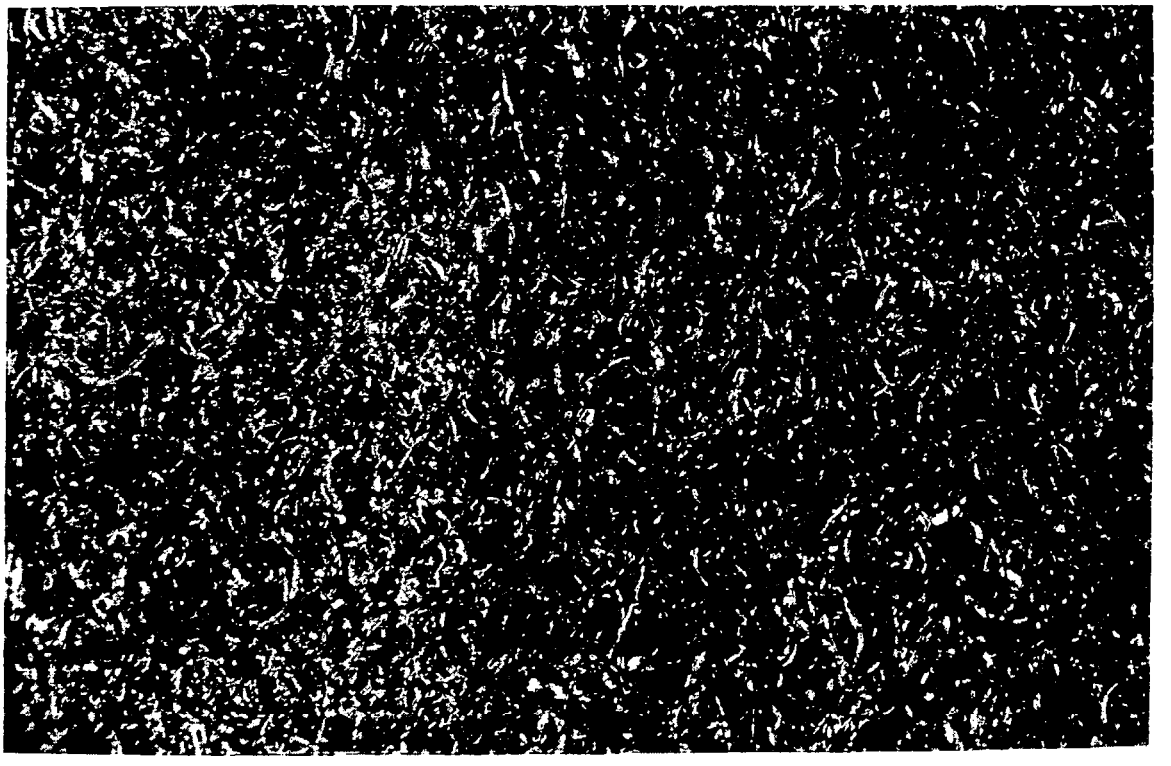

Mag:21X

Figure 15 Top View of Sintered Nickel Fiber Sample H1

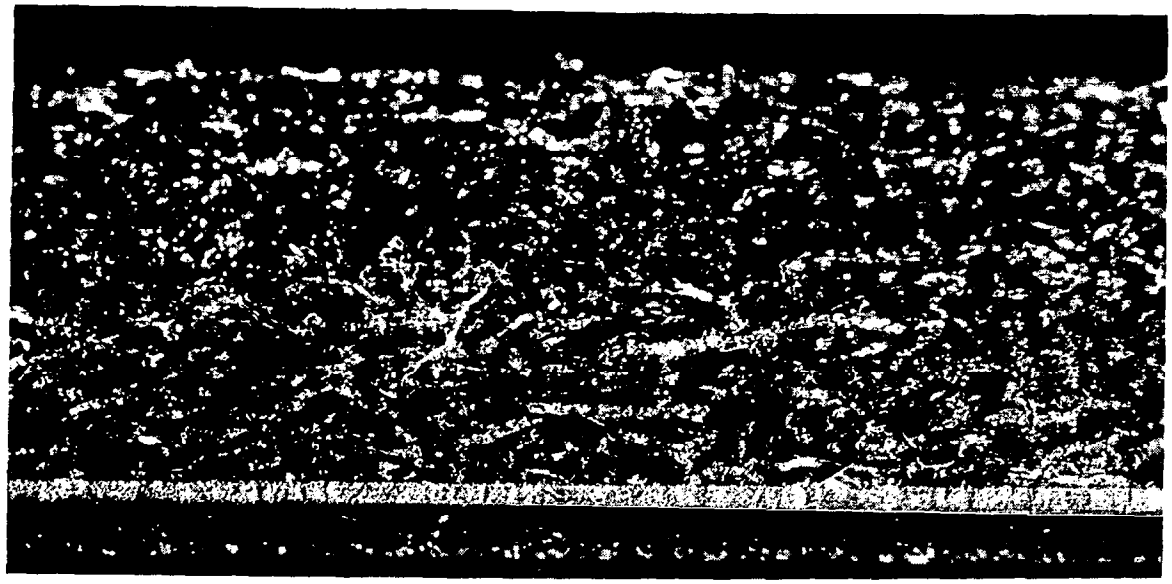

Mag:21X

Figure 16 Cross-Sectional View of Sintered Nickel Fiber Sample H12

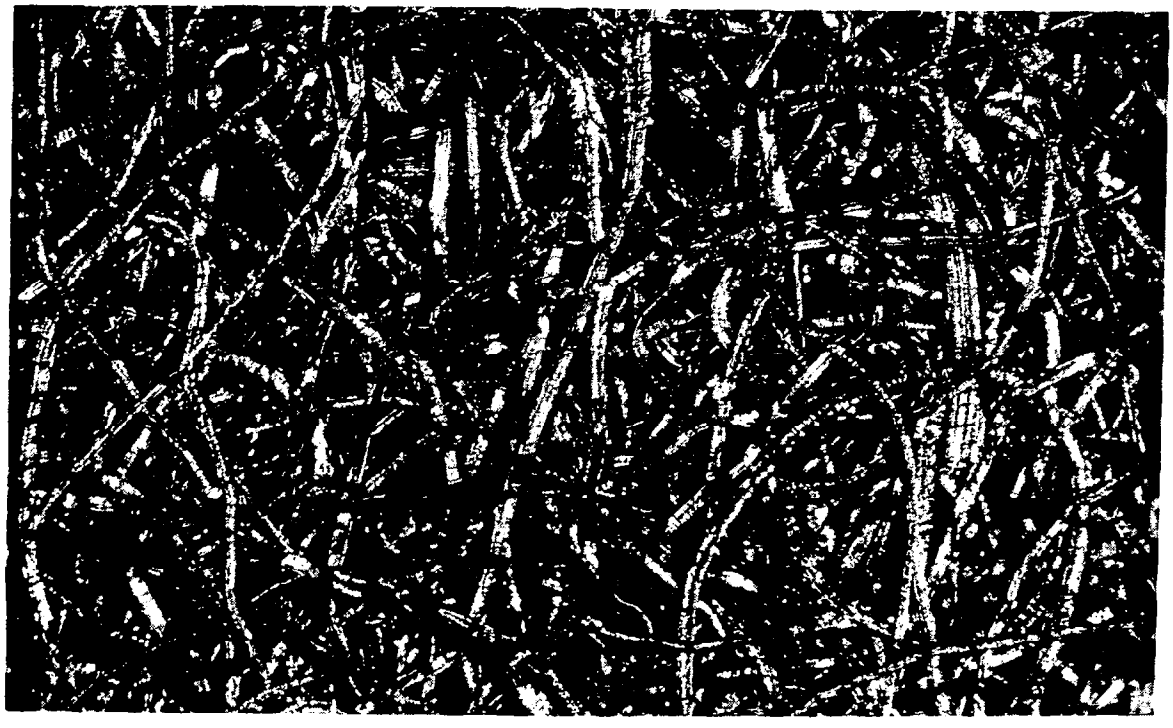

Mag:21X

Figure 17 Top View of Sintered Nickel Fiber Sample H12

An examination of the photomicrographs in Figures 14 through 17 shows that there is an abundance of pores present in the fiber mat. In addition, there is a large degree of interconnectiveness associated with the pore structure. Because of their structure the sintered fiber metals offer the widest range of pore sizes and porosity of any of the porous materials that have been considered so far.

B. Properties of Wicking Materials

Knowledge of the porosity and the way in which the pore space is distributed through a porous solid is essential to any study of porous material. A description of the quantities necessary to evaluate the porosity, the pore size distribution, and the free-flow area ratio is presented in the following sections.

1. Porosity

The porosity, ϵ, of a material is defined as the total pore volume of a sample divided by the total volume of the sample itself. Thus a porosity of zero per cent denotes a solid substance containing no pores or voids, while one of 100 per cent denotes a complete void. While the porosity accounts for all pores or voids in a sample, the effective porosity is based upon the interconnected (as opposed to separate or noninterconnected) pore space within the sample.

The study of the flow of a fluid through a pore system in a material should be based on the effective porosity rather than the porosity. By examining Figures 10, 11, 14 and 15 it can be seen that the pores of both the sintered screens and the sintered fibers are for the most part interconnected. Thus the effective porosity of each of these materials can be taken as equal to the porosity.

The powders used in making the sintered powder samples were composed of solid particles that contained no voids. However, in compacting the powder, isolated voids can form. This compacting was kept to a minimum during the fabrication of the sintered powder samples, represented by Figures 12 and 13, by compressing the powder before sintering as little as possible. Thus, in all samples considered in this study, the effective porosity will be taken as equal to the porosity, ϵ.

The porosity of each of the samples described in Section IV A was measured and is tabulated in Table 4.

TABLE 4

Porosity of Porous Material Samples

	Sample No.	Porosity, %		Sample No.	Porosity, %
Sintered Powder Samples	M1	59.7	Sintered Fiber Samples	H1	86.8
	M2	65.8		H2	82.5
	M3	47.7		H3	68.9
	M4	54.0		H4	62.8
	M5	69.1		H5	91.8
	M6	69.6		H6	88.0
Sintered Screen Samples	M7	62.5		H7	82.0
	M8	67.9		H8	82.8
	M9	67.8		H9	62.6
	M10	67.6		H10	70.9
				H11	91.6
				H12	80.8
				H13	82.2

In calculating the porosity values listed in Table 4 the basic definition of porosity was used in the form

$$\epsilon = \frac{V_T - W_T/\rho_S}{V_T} \tag{55}$$

where V_T = total wick volume
W_T = total weight of wick
ρ_S = density of the solid (8.90 gm/cc for nickel and 7.70 gm/cc for 430 stainless steel)

The weight of each sample was determined by using a triple-beam balance, while the volume was determined by taking many measurements of the dimensions of each sample with micrometers. In all measurements and computations, the fact that the samples were backed with a solid nickel or stainless steel foil was taken into account. The maximum uncertainty of the per cent porosity (confidence interval based on odds of 20 to 1) for any of the sintered screen samples was calculated to be ±1.6 while that of the sintered powder and sintered fiber samples was ±1.3. These measured porosity values not only provide a measure of the total pore space in a given sample, but also tell something about the structure of the porous material. For instance, if the sintered powder samples were composed of perfectly spherical powders, the maximum porosity that each sample could have would be

47.84 per cent. However, the substantially higher values of porosity listed in Table 4 show that the combined effect of irregular powders and loose packing leads to a structure that is less dense than an equivalent spherical packing.

The maximum porosity that a perfectly stacked screen structure can assume was calculated to be about 61 per cent. This configuration was termed a square stacking. The measured porosity values of Table 4, ranging from 62.5 to 67.9 per cent, indicate that the screen samples in this study probably approximate the square stacking. Although Figure 10 shows that many of the layers follow the square configuration, there are many layers that are much more closely stacked. The higher porosity values that were measured indicate that some of the screen layers may be imperfectly sintered, thus producing a greater void volume in the sample.

The sintered fibers have a much higher porosity than the other two classes of porous material, due to their structure. In one case the randomly interlocked fiber structure produced a porosity of 91.8 per cent. This is about the practical upper limit on rigid sintered fiber materials, for this sample (H5) tended to deform easily. The porosity of any of these samples, be they sintered screen, powder, or fiber, could be decreased by rolling and compressing the sample.

2. Pore Size Distribution

The manner in which the pore space is distributed in a porous material is given by the pore size distribution function. This function, $\alpha(r)$, is defined by the equation

$$dV = -\alpha(r)dr \qquad (56)$$

where dV is the volume of the pores with radius between r and r + dr. For purposes of the following discussion, V itself will be defined as the volume of all pores with radius equal to or greater than r.

The porous materials described in Section IV A have pore diameters falling in the range of 0.1 to 1000 microns. For this range of pore diameters the best method available for determining the pore size distribution function is to use a mercury intrusion porosimeter. This instrument employs the injection of non-wetting mercury into the pore system of a sample, and recording the pressure necessary to accomplish the injection. By measuring the volume of the mercury in the porous material as a function of pressure, the pore size distribution can be calculated. An explanation of the operation of the device is presented in the following paragraphs.

When a liquid is introduced into the pore system of a porous material, the liquid will form menisci whose curvature is determined by the shape and size of the pores in the material. If the liquid is a non-wetting fluid such as mercury, a positive pressure will be necessary to force the liquid into the pore system. For a given size of pore, this positive pressure is given by the Laplace - Young equation

$$\Delta P = \sigma \left(\frac{1}{R_1} + \frac{1}{R_2} \right) \tag{57}$$

where ΔP is the pressure drop across the liquid-vapor interface, σ is the liquid-vapor surface tension, and R_1 and R_2 are the two principle radii of curvature necessary to describe the liquid-vapor interface. If the pore system has been evacuated prior to the introduction of the liquid and if the vapor pressure of the liquid is small (e.g., mercury at room temperature), then

$$P \approx \Delta P \tag{58}$$

where P is the pressure of the liquid.

It is assumed here that R_1 and R_2 completely describe the entire liquid-vapor interface in the pore. Up to now the terms pore radius and pore diameter have been used without precise definition. An examination of the photomicrographs, Figures 10 to 17, shows that it would be quite unrealistic to assume that the pores are cylindrical in the materials under study. Their pore shape and structure are quite irregular. However an equivalent pore radius can be defined as

$$r_e = 2 \left(\frac{\text{cross-sectional area of pore}}{\text{perimeter of pore}} \right) \tag{59}$$

In fluid mechanics terminology this equivalent pore radius can also be called a hydraulic radius. As r_e is defined, Equation (59) reduces to the radius of a cylinder for the case of a cylindrical pore. Hereafter the term pore radius and r will be taken as equivalent to the definition given by Equation (59).

Using Equation (58), a force balance on the meniscus in the pore yields

$$(F_\sigma)\,(\text{perimeter of pore}) = (P)\,(\text{cross-sectional area of pore}) \tag{60}$$

where F_σ is the surface tension force per unit length of interfacial boundary. The latter is given by

$$F_\sigma = \sigma \cos \phi \tag{61}$$

where σ is the surface tension and ϕ is the contact angle.

Combining Equations (59), (60) and (61) yields

$$Pr = 2\sigma \cos \phi \tag{62}$$

For constant values of surface tension and contact angle, this equation directly relates r, the pore radius, to P, the measured pressure necessary to force the non-wetting liquid (in this case mercury) into the pore. It should be noted that the expression is independent of the measured volume of liquid, V. If ϕ and σ are constant, Equation (62) can be differentiated to obtain

$$rdP + Pdr = 0 \tag{63}$$

By combining Equations (56), (62) and (63) an expression for the pore size distribution function is obtained

$$\alpha(r) = \frac{P^2}{(2\sigma \cos \phi)} \frac{dV}{dP} \tag{64}$$

where $\alpha(r)$ = pore size distribution function

P = pressure required to force mercury into evacuated pores of radius r

V = volume of all pores in the sample with radius equal to or greater than r

σ = surface tension

ϕ = contact angle

Thus to evaluate $\alpha(r)$ for a given porous material, both P and V must be measured. This is done with the mercury intrusion porosimeter by measuring the pressure, P, necessary to force a given volume, V, of mercury into the evacuated sample. Knowing this $\alpha(r)$ can be calculated from Equation (64) and r can be found from Equation (62), where σ is taken to be 473 dynes/cm for mercury at 70°F and the contact angle is 130 degrees. The latter value has been found to be valid for most mercury-metal systems. The derivative dV/dP is calculated by taking the slope of a plot of P vs V.

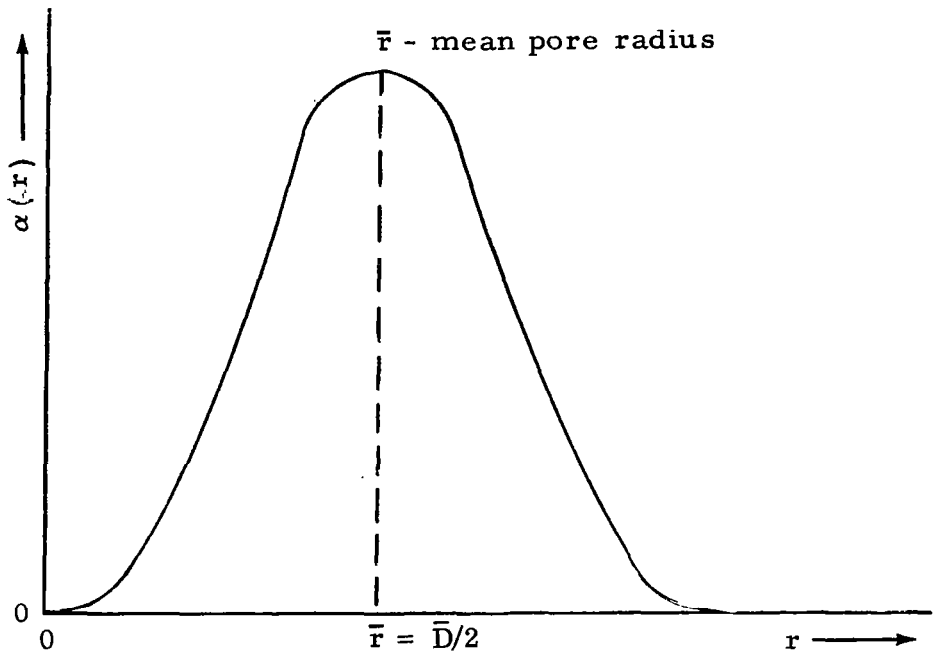

Figure 18 Pore Size Distribution Curve

A typical pore size distribution curve is shown in Figure 18, where $\bar{r}$ is defined as the mean pore radius, i. e., the pore size that occupies more of the total pore volume than any other pore size. It should also be noted that as defined, $\alpha(r)$ is dependent on the actual size of the sample.

The V-P data to calculate $\alpha(r)$ was obtained for twelve of the most promising porous material samples described in Section IV A. These were samples H1, H2, H3, H6, H10, H11, H12, H13, M2, M4, M6, and M8. At least two pieces of each porous material sample were tested in a mercury intrusion porosimeter made by the American Instrument Company. Each sample was placed in the porosimeter container which was evacuated before the mercury was introduced into the sample. All samples were cleaned using the procedure outlined in Section V C. The most complete V-P curve for each of twelve samples is shown in Figures 19 through 30. These plots show volume as a function of pressure and volume as a function of pore diameter. From Equation (62) the pore diameter is given by

$$D = \frac{4\sigma \cos\phi}{P} \tag{65}$$

where

D = diameter of pore, i.e., twice the pore radius given by Equation (59)

P = pressure required to force mercury into a pore of diameter D

σ = surface tension of mercury = 473 dynes/cm at 70 °F

ϕ = contact angle between mercury and solid material = 130 degrees

Figures 19 through 30 present essentially the same information that a plot of the pore size distribution would show, for they illustrate the measurable range of pore sizes in each sample and the volume occupied by each pore size. To replace the mean pore radius $\bar{r}$ in Figure 18, the median pore diameter has been chosen to characterize the pore space of each sample. The median pore diameter D_{med} is defined as the pore size at which 50 per cent of the connected pore space is filled with mercury.

Fairly complete pore spectra were obtained for samples H1, H2, H3, H6 and M10, with pore diameters falling between 0.5 and 100 microns (Figures 19 to 23). These samples were four of the sintered fiber samples of finest fiber and one sintered powder sample. The range of pore sizes that occupies the greatest portion of the total pore volume occurs in the region of the maximum slope of the V-P curve. For sample H3 (Figure 21) this portion of the total volume occurs for pore sizes between 20 and 30 microns. For this sample the median pore diameter D_{med} can be calculated by noting that at a pore volume of 0.08 cc (equal to 50 per cent of the connected pore volume) the pressure as read from the V-P curve of Figure 21 is about 6.6 psia. Using Equation (65), or using the pore diameter scale in Figure 21, D_{med} is found to be 26.5 microns. Figure 21 also shows that the pore diameters ranging from 10 to 34 microns contain 90 per cent of the connected pore volume of the sample. Similar conclusions can be drawn from Figures 19, 20, 22 and 23.

Because of the construction of the mercury intrusion porosimeter, pressures less than 2.5 psia could not be read. This pressure, using Equation (65), corresponds to a pore size of 70 microns. Thus, if a sample had pore

structure in which most of the pore space was contained in pores of diameter greater than 70 microns, a complete pore spectrum could not be measured by this method.

Such was the case in the remainder of twelve selected materials, samples H11, H12, H13, M2, M4, M6 and M8. They constitute the more porous sintered fiber samples, two sintered powder samples and one sintered screen sample. The V-P curves for these samples are shown in Figures 24 to 30. In all of these cases the median pore diameter is greater than 70 microns. However, because of the shape of the V-P curves shown in Figures 24 to 30, the value of the lower bound estimate on median pore size can be increased. For example, sample M8 can be interpreted to have a median pore size greater than 100 microns.

TABLE 5

Pore Space Distribution of Twelve Selected Porous Materials

Sample No.	Measured Median Pore Diameter, microns	Pore Diameter Range of 90% of Pore Space, microns
M2	>70	-
M4	~80	-
M6	>80	-
M8	>100	-
M10	~50	43.4-57.8
H1	43.8	19.4-54.2
H2	35.0	13.3-48.9
H3	26.5	10.3-34.0
H6	40.7	15.5-59.3
H11	>80	-
H12	>70	-
H13	>80	-

The pore space distribution data presented by Figures 19 to 30 is summarized in Table 5. The median pore diameter is listed for each sample. Also tabulated for five of the twelve samples is the pore diameter range that represents 90 per cent of the pore volume in any given sample. In all cases the term pore diameter is defined as twice the radius defined by Equation (59).

3. Free-Flow Area Ratio

The free-flow area ratio is defined as the area available to flow the fluid

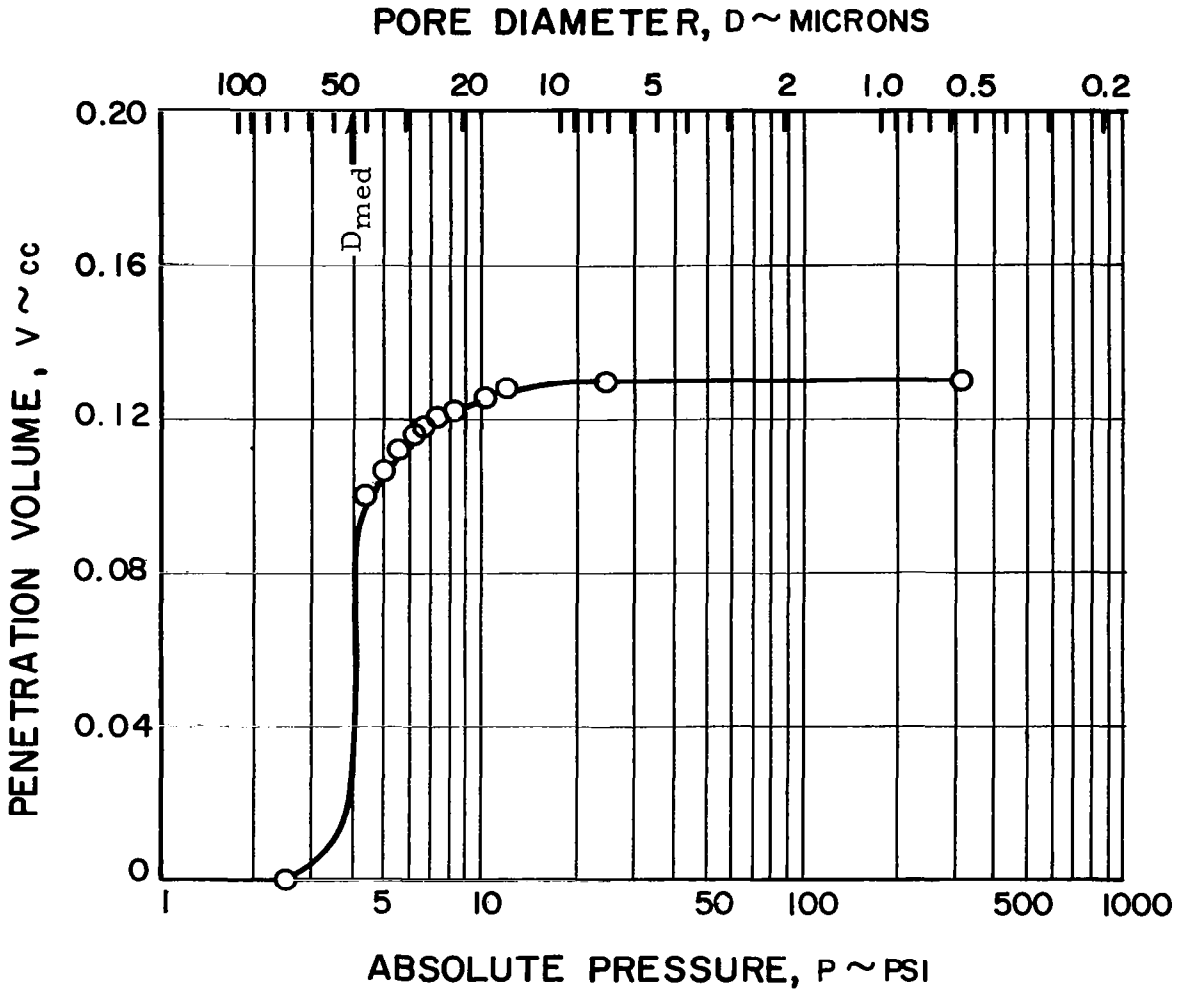

Figure 19 Mercury Intrusion Porosimeter Curve for Sample H1

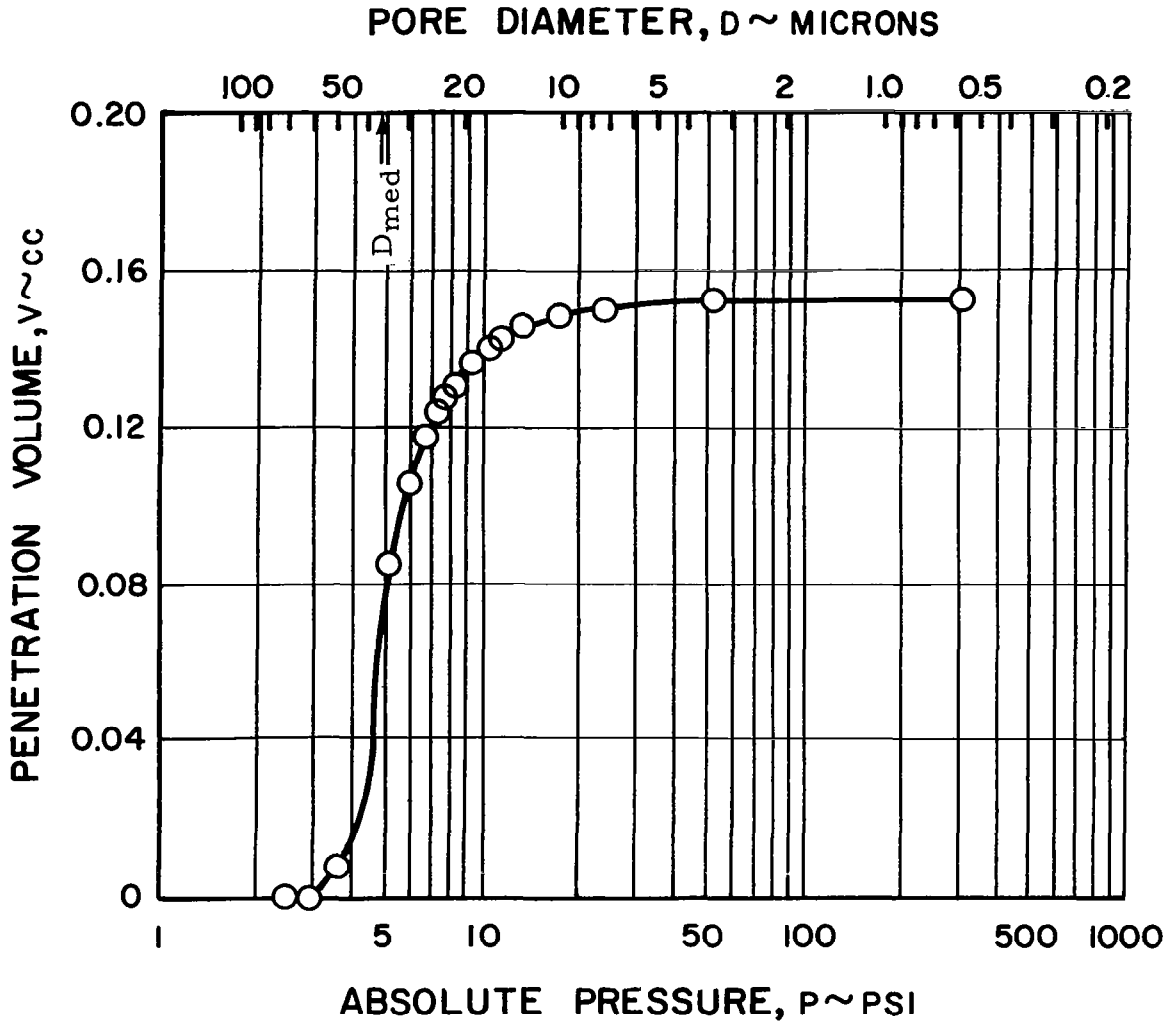

Figure 20 Mercury Intrusion Porosimeter Curve for Sample H2

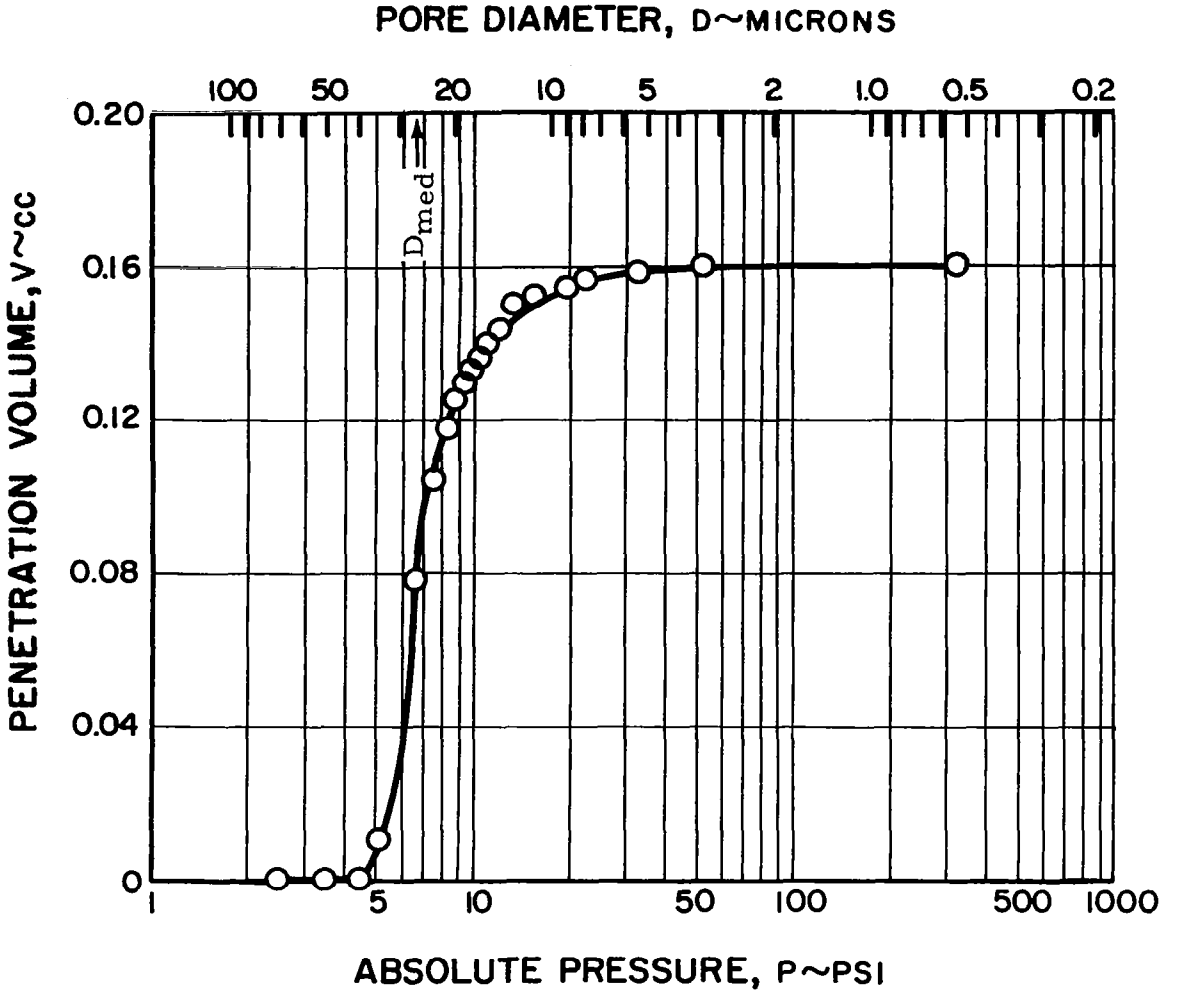

Figure 21 Mercury Intrusion Porosimeter Curve for Sample H3

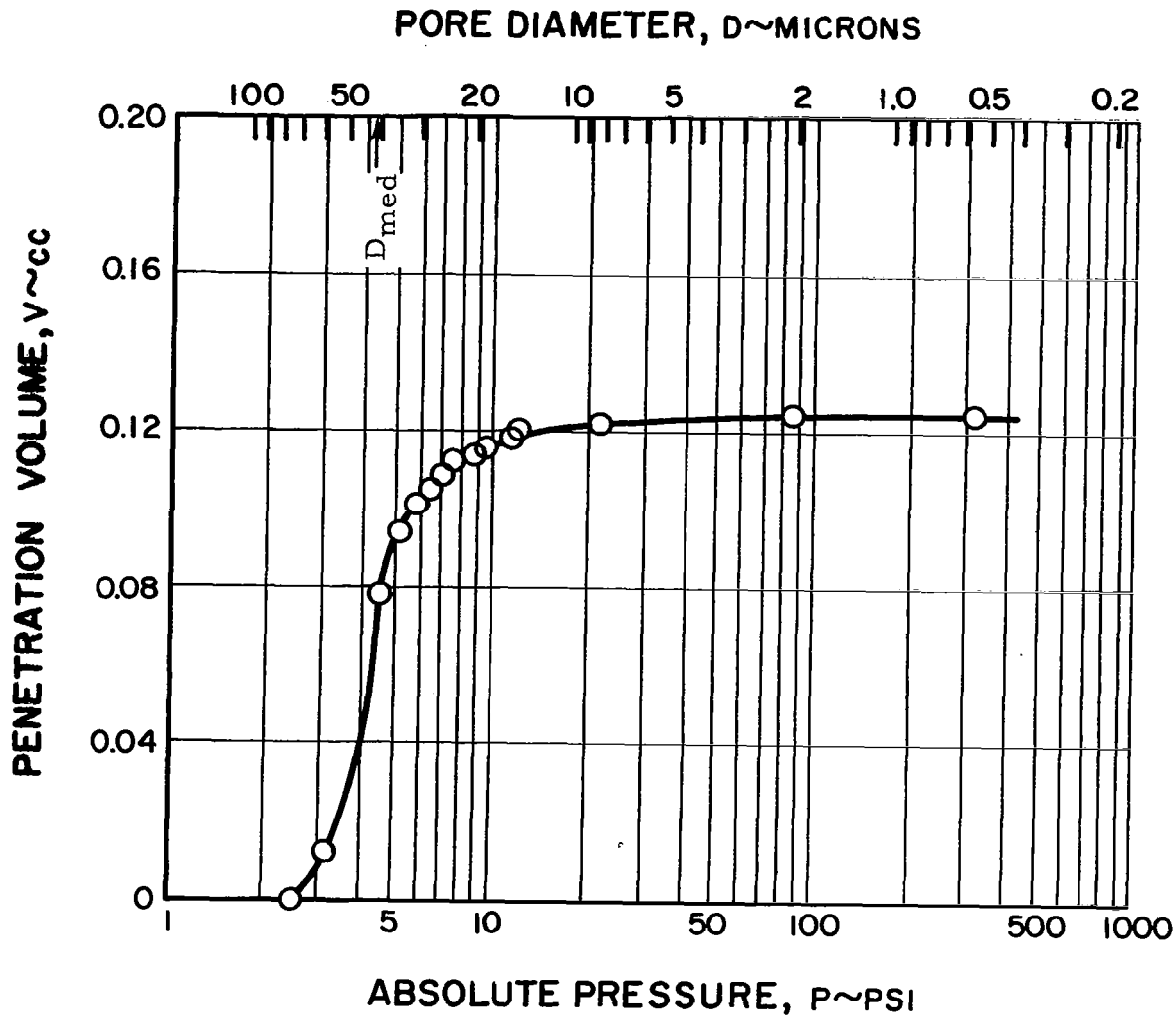

Figure 22 Mercury Intrusion Porosimeter Curve for Sample H6

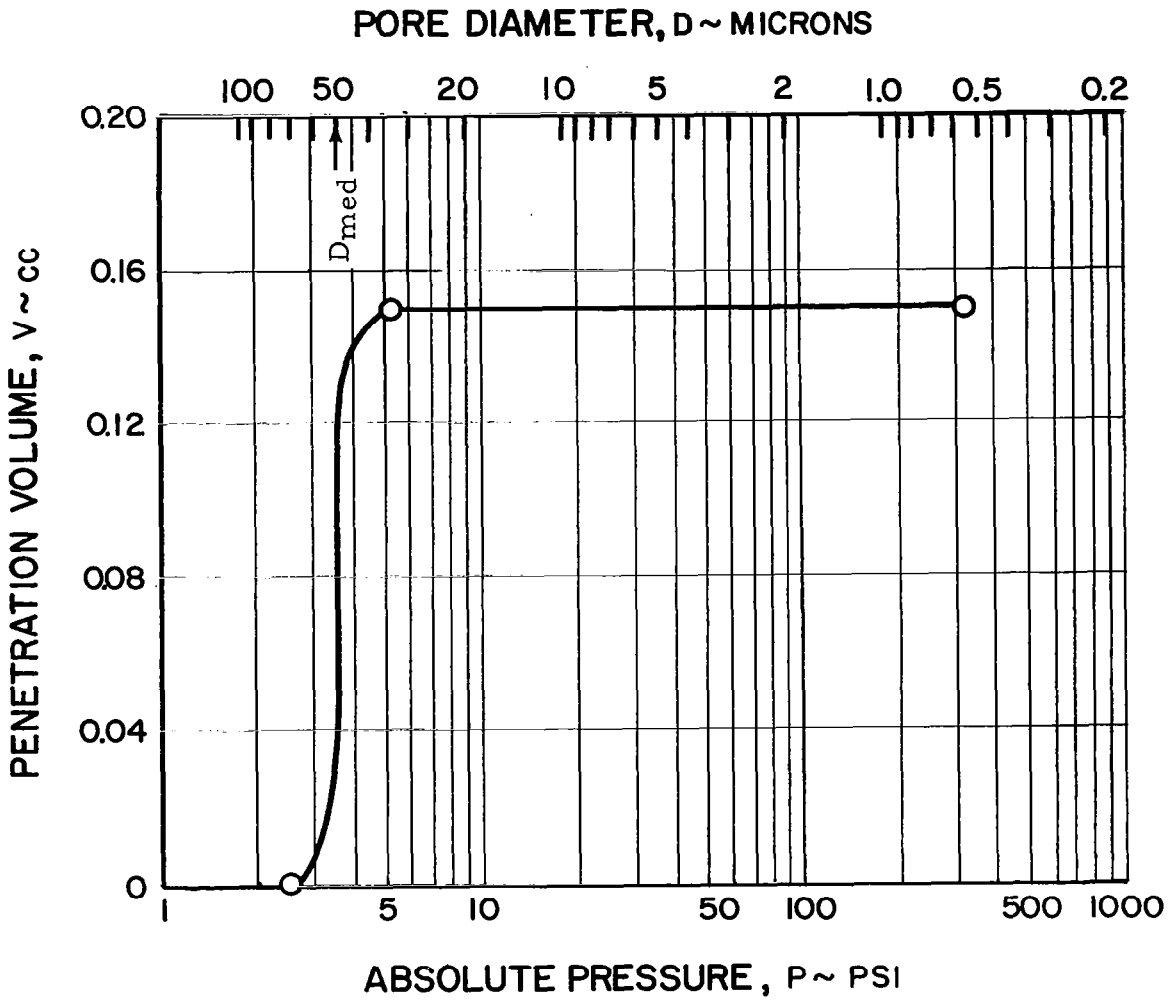

Figure 23 Mercury Intrusion Porosimeter Curve for Sample M10

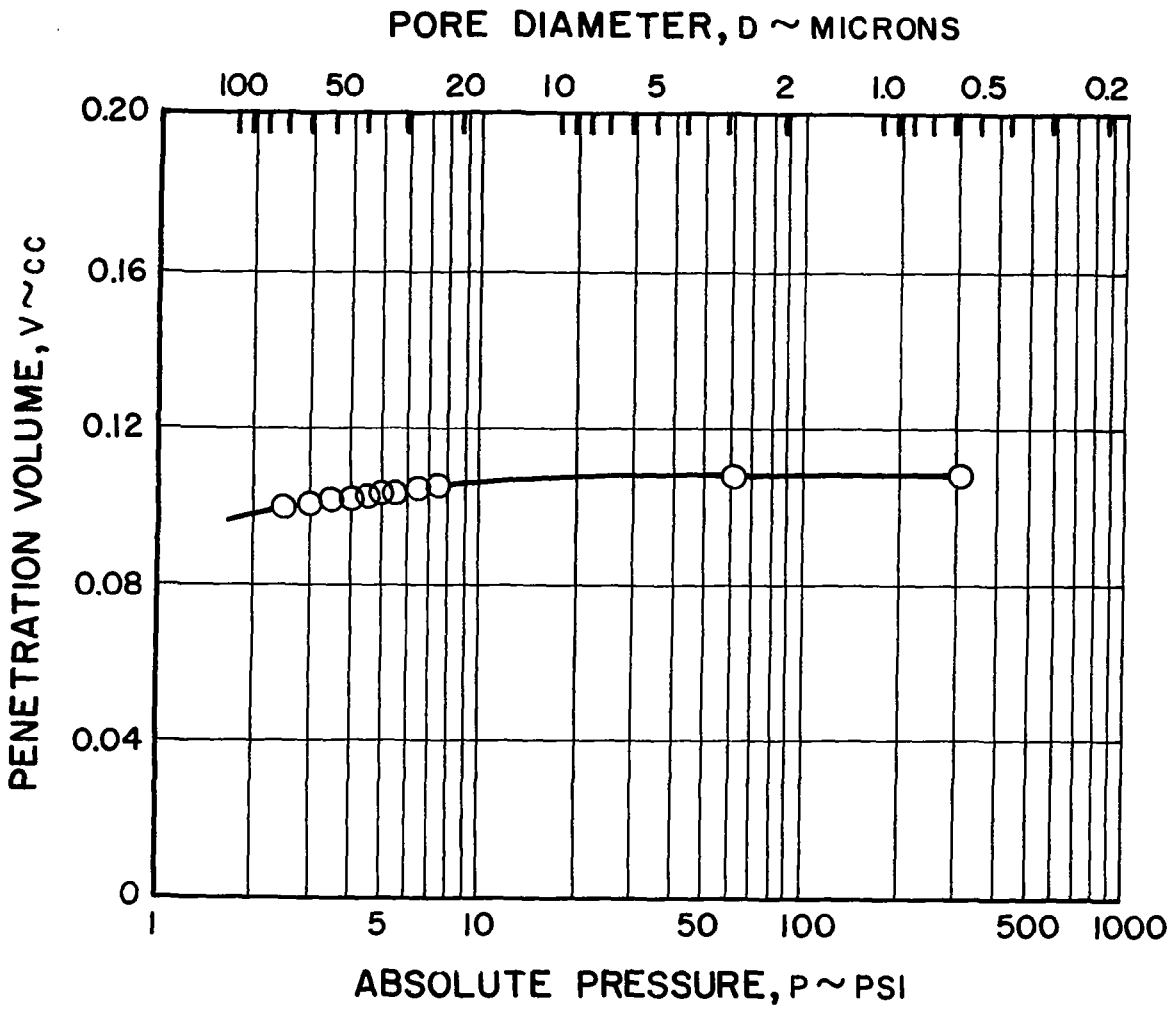

Figure 24 Mercury Intrusion Porosimeter Curve for Sample H11

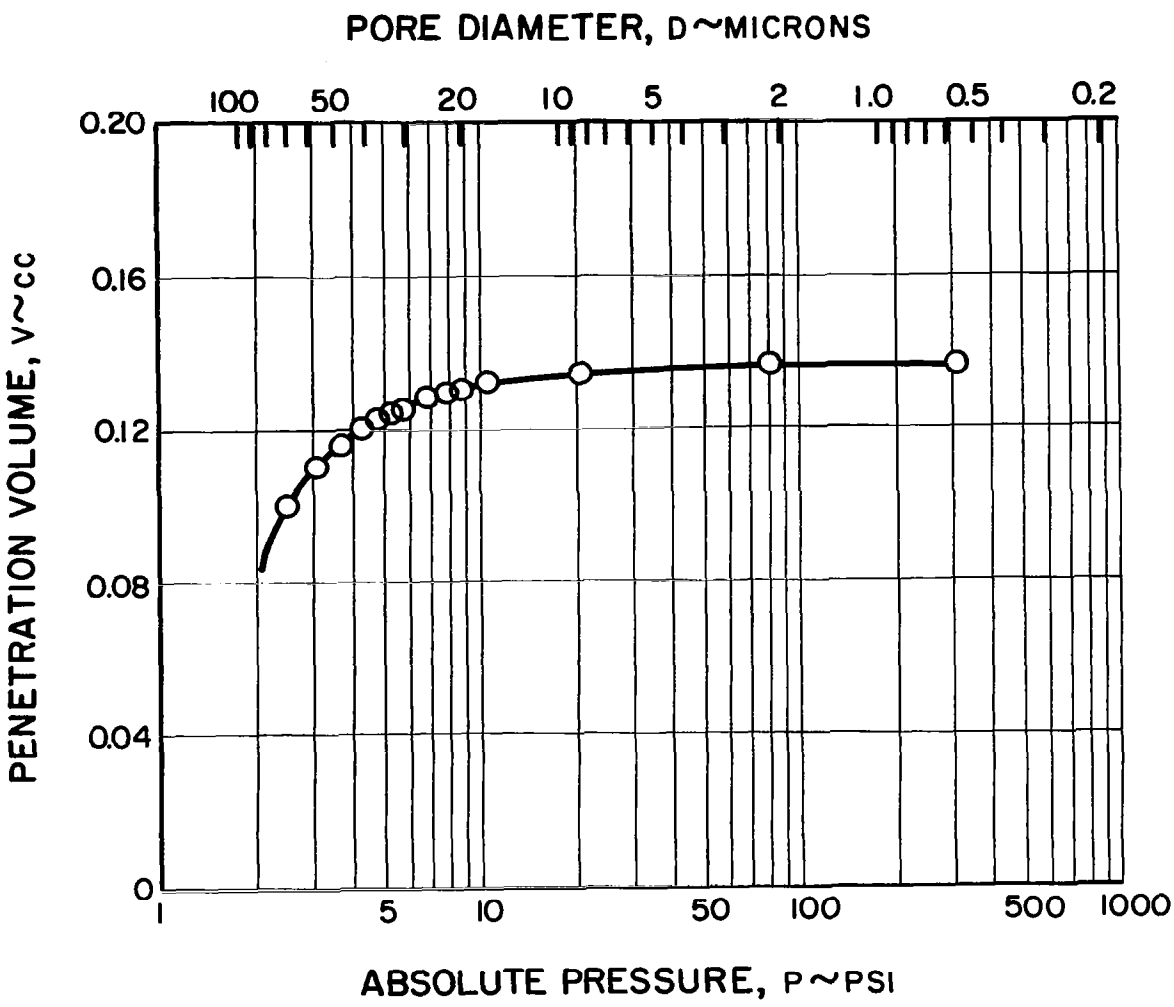

Figure 25 Mercury Intrusion Porosimeter Curve for Sample H12

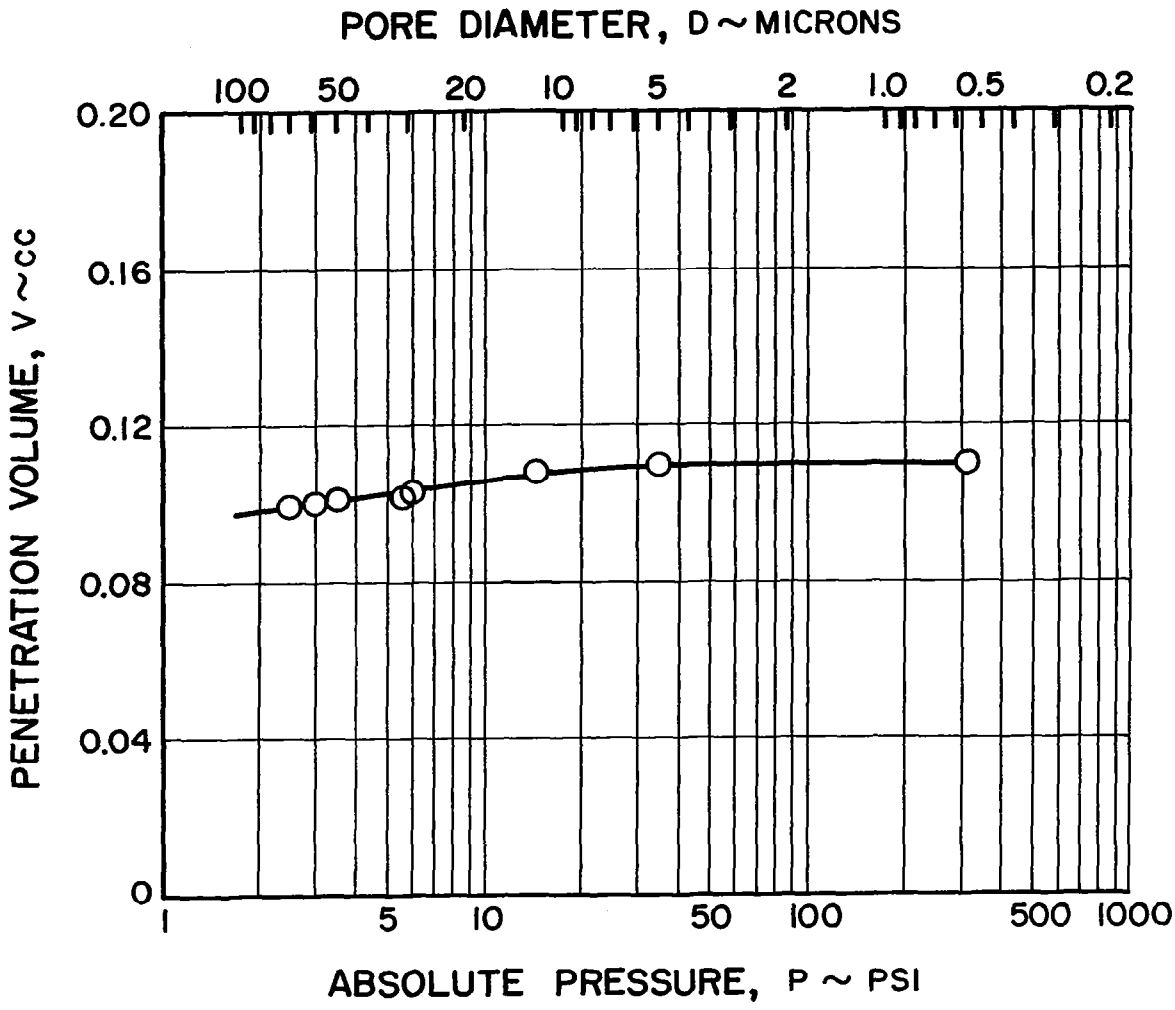

Figure 26 Mercury Intrusion Porosimeter Curve for Sample H13

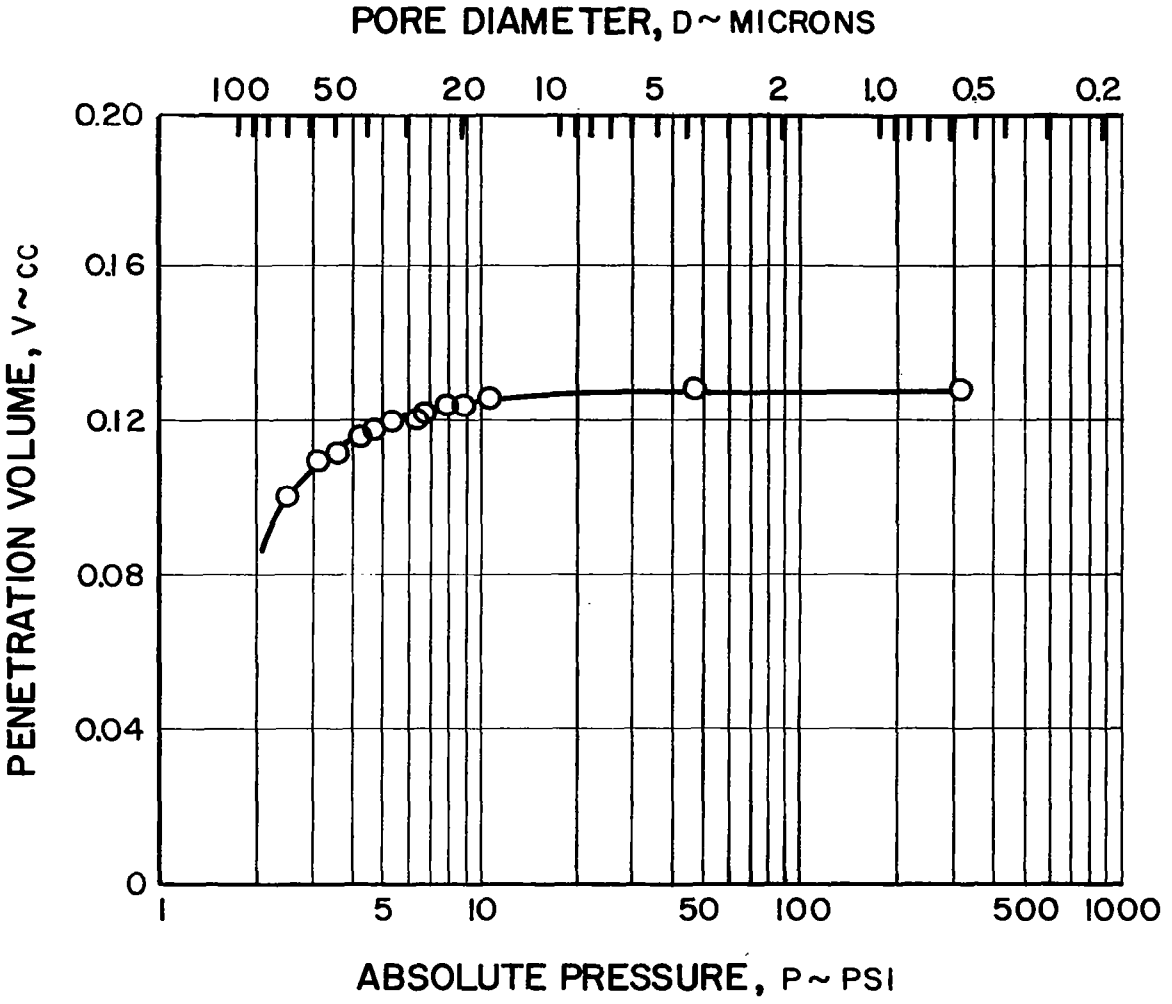

Figure 27 Mercury Intrusion Porosimeter Curve for Sample M2

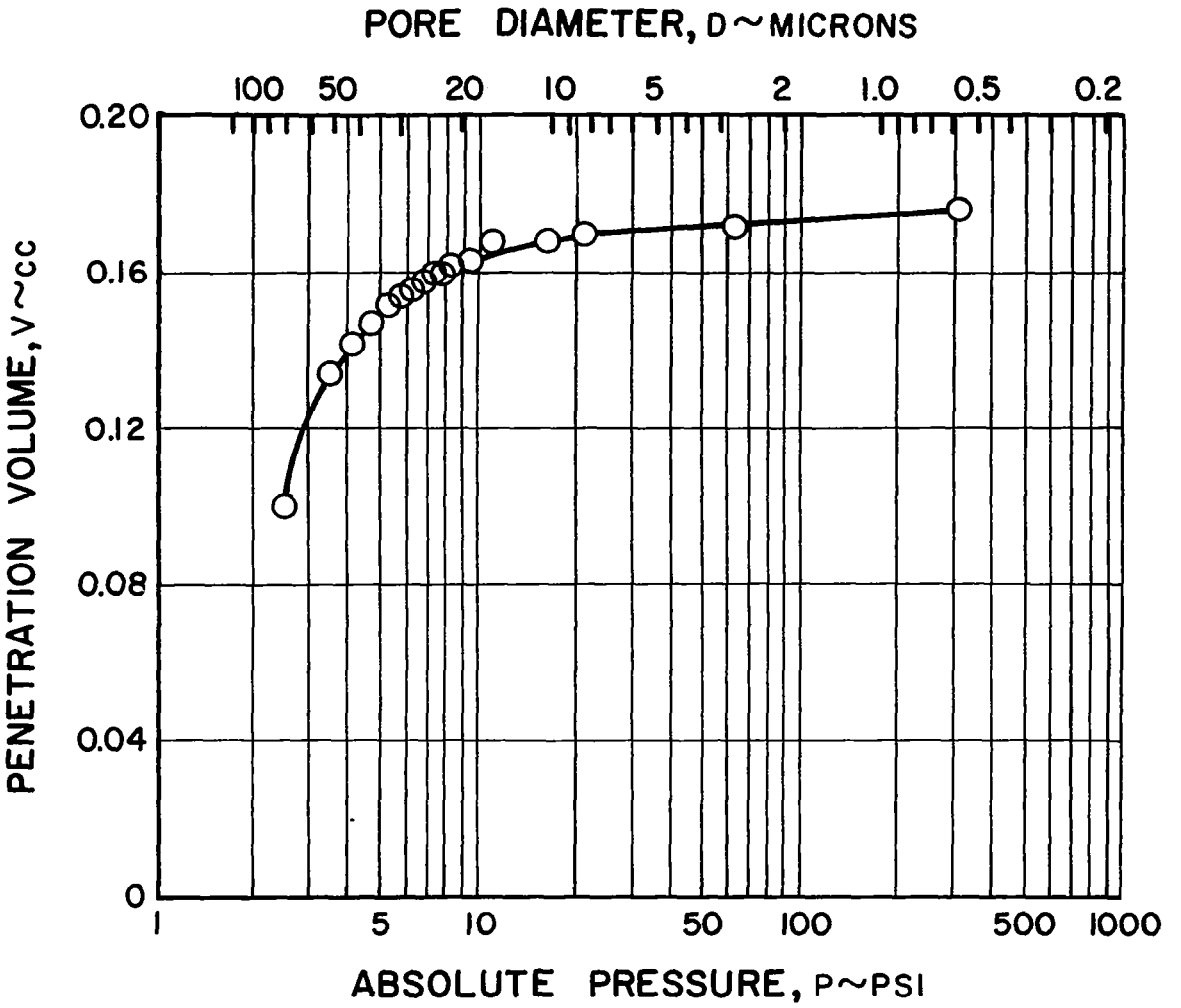

Figure 28 Mercury Intrusion Porosimeter Curve for Sample M4

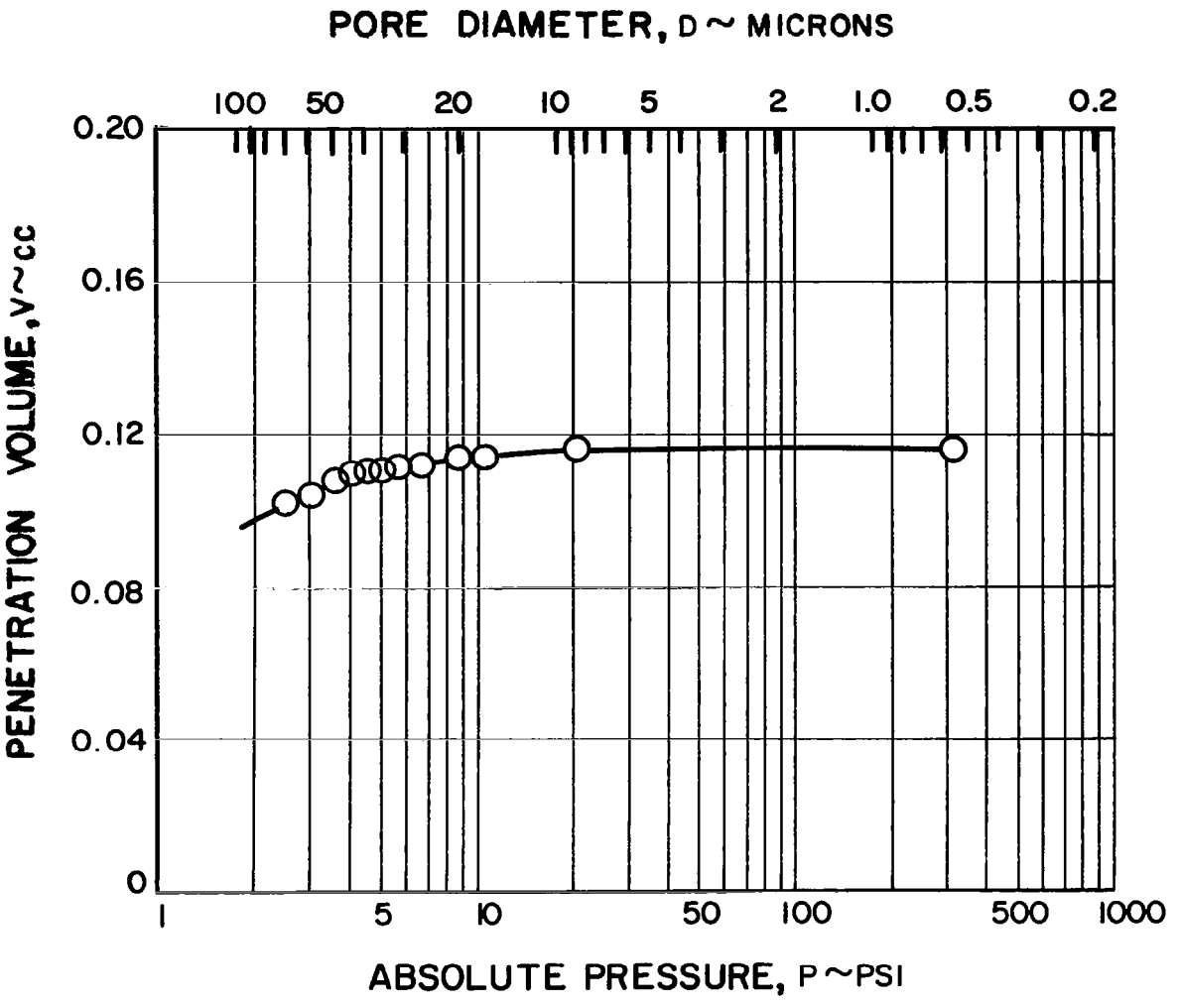

Figure 29 Mercury Intrusion Porosimeter Curve for Sample M6

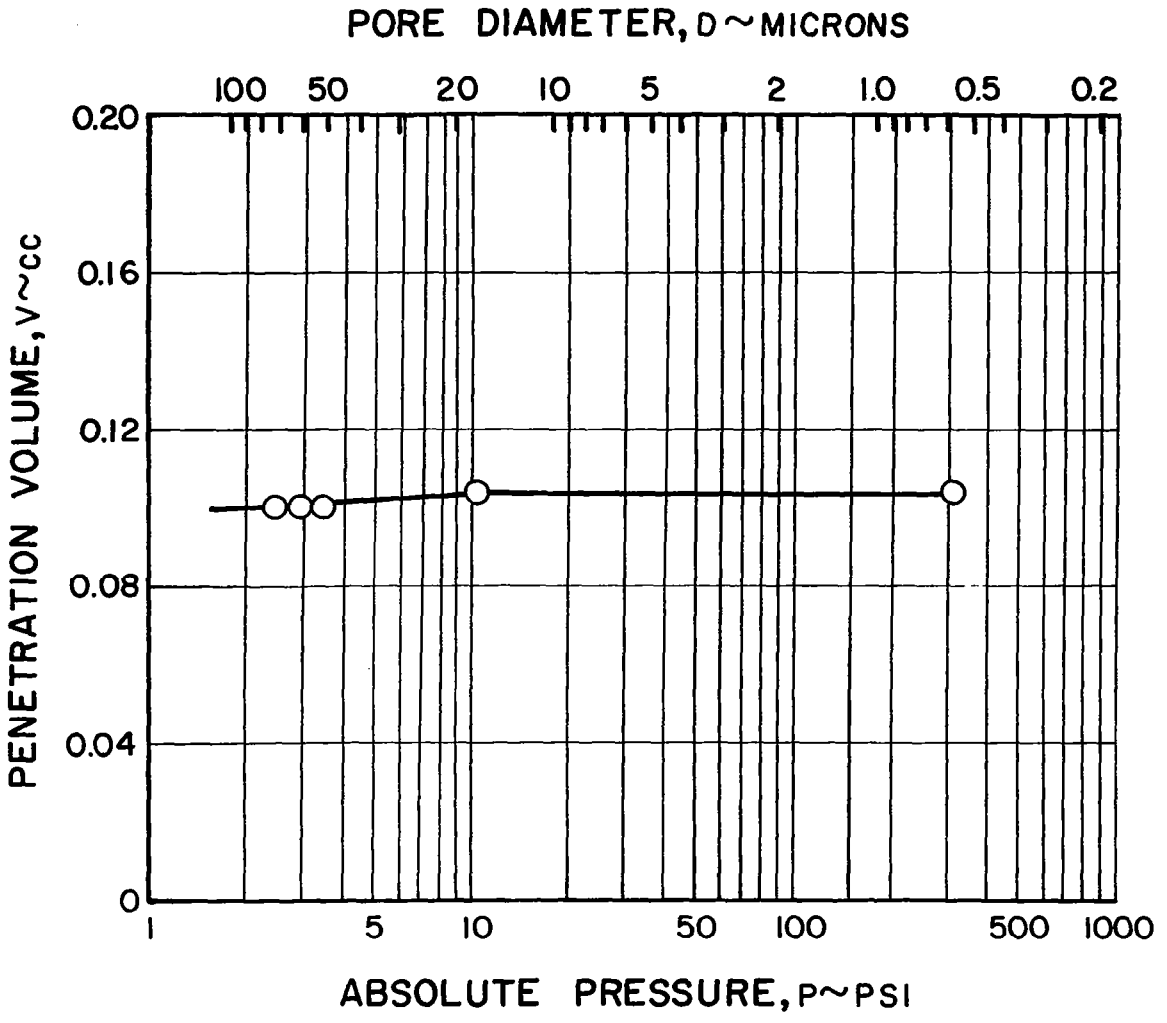

Figure 30 Mercury Intrusion Porosimeter Curve for Sample M8

at any given cross-section of the porous material, divided by the total cross-sectional area. In accordance with this definition, the free-flow area ratio is a measure of the actual cross-sectional area available to the flow of a fluid in any given porous material.

An expression for F_{AR} that is based solely on considerations of isotropy can be derived as follows. In a given porous material, a body of any shape can be considered so that its smallest dimension is much greater than the largest pore size. The body will be considered to be x_1 units long in some chosen x-direction and to have a cross-sectional area normal to the x-direction of A_T, where A_T is some known function of x.

By definition, the free-flow area ratio at a given x for the body of porous material is given by

$$F_{AR} = \frac{A_P}{A_T} \tag{66}$$

or

$$A_P = F_{AR} A_T \tag{67}$$

where A_T is the total cross-sectional area at x, F_{AR} is the free-flow area ratio, and A_P is the total pore area contained in A_T.

The porosity of the body is given by

$$\epsilon = \frac{V_P}{V_T} \tag{68}$$

where ϵ is the porosity, V_T is the total volume of the body of porous material, and V_P is the total volume of the pore space in the body. The total volume can be calculated by integrating in the x-direction to get

$$V_T = \int_0^{x_1} A_T \, dx \tag{69}$$

Similarly, by using Equation (67) for A_P, the pore volume is given by the integral

$$V_P = \int_0^{x_1} F_{AR} \, A_T \, dx \tag{70}$$

Combining Equations (68), (69), and (70), it is seen that

$$\epsilon = \frac{\int_0^{x_1} F_{AR}\ A_T\ dx}{\int_0^{x_1} A_T\ dx} \tag{71}$$

As stated above, A_T is some known function of x. Now, if it is assumed that the porous material is truly isotropic and that the pore space is randomly distributed, the value of the free-flow area ratio as given by Equation (66) at any given x will be a constant, if the dimensions of A_T are large compared to the largest pore sizes. Thus, since F_{AR} is not a function of x, Equation (69) reduces to

$$F_{AR} = \epsilon \tag{72}$$

subject to the conditions of isotropy and a randomly distributed pore space. Hence, for an isotropic porous material with a randomly distributed pore space, the free-flow area ratio is equal to the porosity. This result agrees with a similar conclusion given by Carman[10].

The photomicrographs of Figures 12 to 17 indicate that the assumptions of isotropy and a randomly distributed pore space apply reasonably well to sintered powder materials and sintered fiber materials. However, the structural regularity exhibited by the sintered screen sample shown in Figures 10 and 11 indicates that Equation (72) is at best an approximation to a mean value of F_{AR} for these porous materials. The interlocking of the screen layers discussed in Section IV A will help both assumptions.

The values of the free-flow area ratio are useful in computing actual fluid flow velocities, Reynolds numbers, and an equivalent flow pore diameter.

C. Porous Material Machining

One of the problems encountered when dealing with porous materials was that of cutting or machining a sample without disturbing the porous structure in the region adjacent to the cutting plane. A minimum of disruption is necessary to insure that there are no end effects at the edges of the samples used for the wick permeability and boiling studies.

Normal cutting techniques such as band-sawing, shearing, grinding and cutting with a torch were found to both deform the porous material sample itself and

smear the cut surface. Such a surface is shown in Figure 31, a photomicrograph of a cross-section sample H4, a sintered nickel fiber material. The machined surface shown was produced by cutting the sample with a rotating rubber wheel charged with diamond dust. The nickel backup foil (0.0218 inch thick) is at the bottom of the cross-section, with porous structure (0.0982 inch thick) above it. It can be seen that almost the entire pore space has been smeared over and sealed off by the machining process. Such a surface would exhibit a relatively high resistance to flow during a permeability test.

The porous structure can be preserved during cutting by filling the sample with some supporting material such as a wax or a salt. The filler material can be removed after the machining operation by melting or leaching. However, it is difficult to determine whether the filler is completely removed or that it has not changed the wetting characteristics of the porous material.

Figure 32 shows a photomicrograph of the same sample H4 where the material was cut by electro-discharge machining (EDM). EDM is a process of metal removal brought about by an electrical spark jumping a gap between the workpiece and an electrode. A dielectric liquid flows between the electrode and the workpiece, both to cool the work and to remove the spark-eroded particles as they come off the workpiece.

As seen by the cross-sectional view of Sample H4 in Figure 32, this machining method tends to produce a rough edge. The electrical discharges tend to erode the solid backup foil unevenly, producing a pitted surface. When examined under a microscope the porous material near the cut surface can be seen to be disrupted and opened up just the reverse of the situation shown in Figure 31.

The cutting process finally chosen was electrochemical machining (ECM). A cross-sectional view of Sample H4 cut in this manner is shown in Figure 33. Electrochemical machining is essentially metal removal by controlled electroplating in reverse. The workpiece and a shaped tool form a pair of electrodes.

An electrolyte (usually an ordinary salt solution) is pumped between the workpiece and the tool, and a voltage is applied to them. The material of the workpiece is then removed by electrolysis, duplicating the shape of the tool. The electrolyte sweeps away the metal ions so that they cannot deposit out on the tool, which acts like an anode. This cutting process occurs at the temperature of the electrolyte so that there are no excessive temperatures at the cut surface. Also, because of the electrolysis process, all chemical reactions take place right at or near the cut surface rather than in the matrix of the porous material.

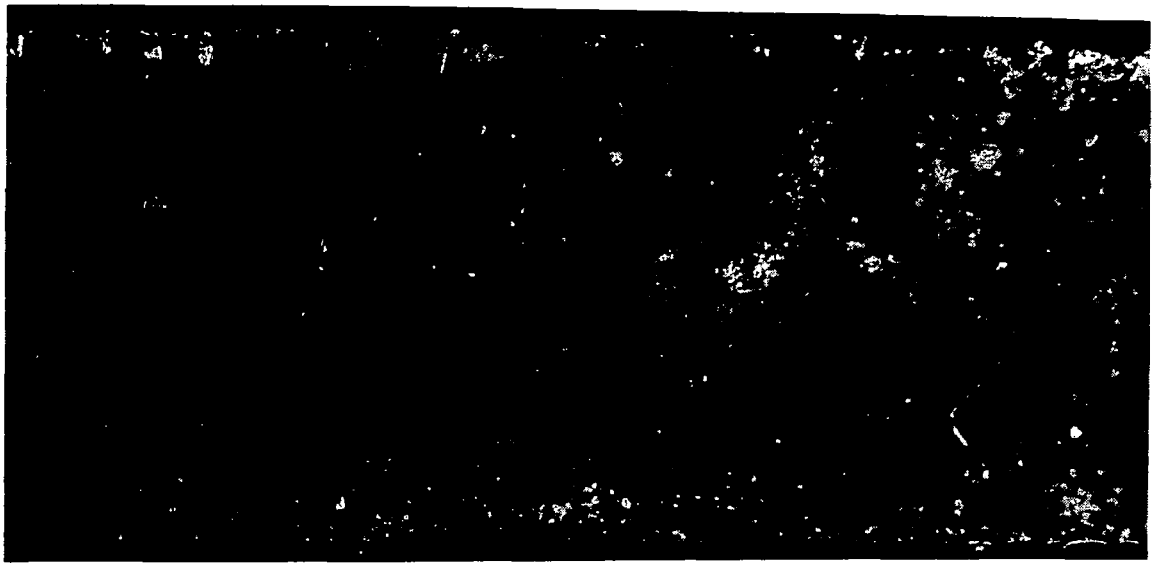

Mag:21X

Figure 31 Cross-Sectional View of Sintered Nickel Fiber Sample H4 Cut by Grinding Method

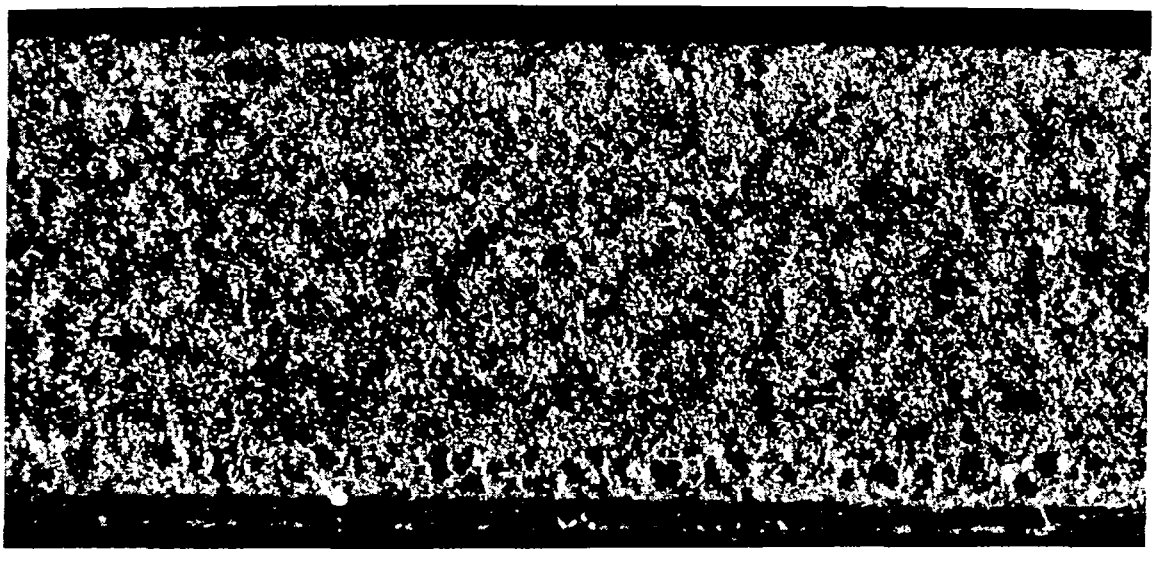

Mag:21X

Figure 32 Cross-Sectional View of Sintered Nickel Fiber Sample H4 Cut by Electrical Discharge Method

Figure 33 shows that both the porous material and the backup foil of Sample H4 were cut cleanly and with a minimum of disruption. As will be shown in Section VI D , samples cut by the ECM method show no observable end effects. The machined surfaces shown in Figures 10, 12, 14 and 16 were all produced by the electrochemical machining process.

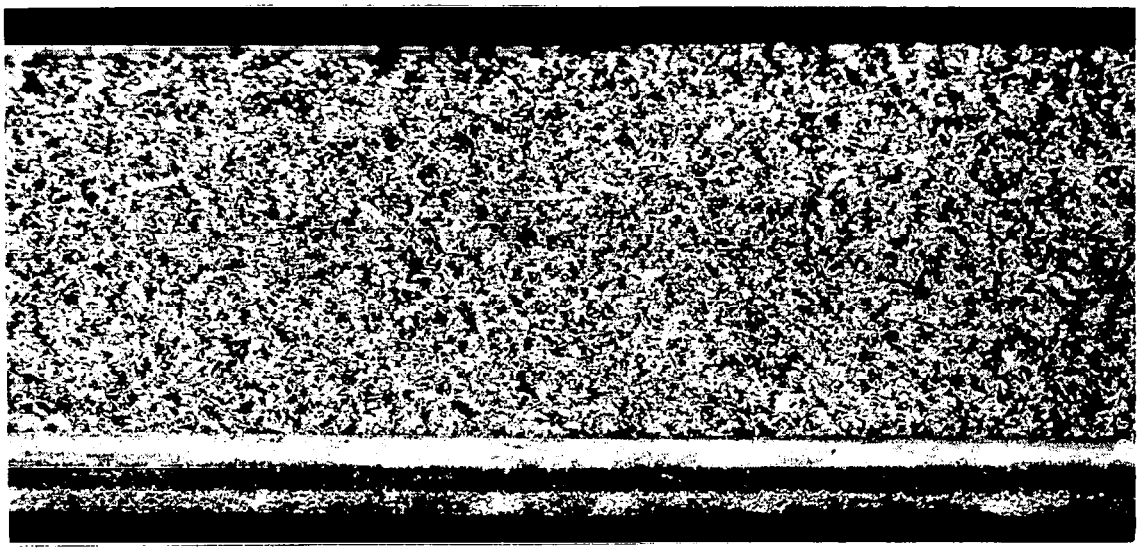

Mag:21X

Figure 33 Cross-Sectional View of Sintered Nickel Fiber Sample H4 Cut by Electrochemical Machining Method

D. Test Fluids

As shown by Equation (45), the liquid properties enter into the operation of the vapor-chamber fin as the dimensional parameter N, defined as

$$N = \frac{\rho_L \, h_{VL} \, \sigma}{\mu_L} \tag{73}$$

where ρ_L is the liquid density, h_{VL} is the latent heat of vaporization, σ is the liquid-vapor surface tension, and μ_L is the liquid viscosity.

To maximize the heat transport properties of the fin, N should be as large as possible. Also, the test liquid should have a vapor pressure significantly higher than the vapor pressure drop in the vapor-chamber fin. In this way the temperature of the vapor-chamber fin can be maintained nearly uniform, resulting in an efficient device. Also, the chamber pressure should not be too high, or the fin will become a pressure vessel with prohibitively thick walls.

Values of N for a number of liquids are listed in Table 6.

TABLE 6

Properties of Various Liquids

Liquid	Normal Boiling Point, °F	Vapor Pressure, psia at 70°F	Vapor Pressure, psia at 1300°F	N*, Btu hr lbf/ft^3 lbm at 70°F	N*, Btu hr lbf/ft^3 lbm at 1300°F	N*, Btu hr lbf/ft^3 lbm at B. P.
Metal						
bismuth	2875	-	$<10^{-2}$	-	2097	2360
lead	3169	-	$<10^{-2}$	-	2007	-
sodium	1630	-	2.0	-	1983	2016
mercury	674	-	760	-	-	1253
potassium	1395	-	9.0	-	406	411
Non-metal						
water	212	0.36	-	138	-	336
methyl alcohol	150	-	-	25.1	-	-
acetone	136	3.77	-	17.9	-	-
ethyl alcohol	173	-	-	9.9	-	19.2
Dowtherm E	352	< 5.0	-	9.8	-	-
carbon tetrachloride	-	1.8	-	7.3	-	-
Freon 112	199	-	-	-	-	5.7
Freon 12	-21.6	84	-	5.2	-	-
Freon 113	118	5.5	-	4.8	-	5.2
Freon 114B2	117	5.5	-	4.2	-	4.4
Dowtherm A	496	< 0.2	-	2.9	-	-
FC-75	216	0.4	-	1.15	-	1.21
sulfur	832	-	245	-	-	0.17

* approximate values

The values listed in this table show water to have one of the highest values of N for conventional liquids, in addition to having a favorable vapor pressure - temperature relationship for testing. Hence water was selected as the primary test fluid.

To evaluate the effect of the variation of N on the heat transfer properties of the fin, one other liquid was selected. The second fluid must satisfy the conditions given above and have a value of N significantly lower than that of water,

although not low enough to drastically reduce the heat input to the fin, see Equation (49),and thereby cause the experimental uncertainties to become too high. Also the fluid should have a fairly complete tabulation of properties and be compatible with the wicking material. Because it was to be tested in the atmosphere during the wicking and boiling tests it must be relatively nonreactive and nontoxic.

Of the liquids listed in Table 6, Freon 113 seems to best satisfy these requirements and thus was used as the second fluid to evaluate the effect of N on the operation of the vapor-chamber fin.

E. Summary

A total of 23 porous materials was selected, representing three classes of porous materials: sintered metal screens, sintered metal powders, and sintered metal fibers. Each sample was composed of either nickel or 430 stainless steel.

The porosity of all the samples was measured and was found to vary between 47.7 and 91.8 per cent.

A mercury intrusion porosimeter was used to measure the pore size distribution function of twelve of the twenty-three porous material samples. A complete pore spectrum was found for five of the twelve samples. The median pore diameter for these five ranged from 26.5 to 50.0 microns.

The free-flow area ratio, useful for computing Reynolds number and effective flow velocities in a given porous material, was found to be equal to the porosity. Thus the free-flow area ratio ranged from 47.7 to 91.8 per cent for the twenty-three samples.

A study of the machining of porous materials was made. It was found that the best method available was that of electrochemical machining and therefore this method was used in fabricating all samples used in subsequent testing.

Water was selected as the primary test fluid since analysis indicated that it is one of the best conventional fluids for use in a vapor-chamber fin. Freon 113 was selected as the secondary test fluid since its properties fall in the desired range and are significantly different from those of water.

V. WICKING RISE TESTS

A. Objective

The purpose of the wicking rise tests was to determine the maximum height to which a liquid will rise in a given vertical wicking material sample and thereby obtain a measure of the minimum liquid-vapor interfacial radius of curvature that the material will support. As shown in the derivation of the fin model in Section III D , the value of this curvature, R_{min}, is needed to evaluate the maximum pumping force produced by the wicking material. This maximum pumping force, expressed as a differential pressure is

$$\Delta P = \frac{2\sigma}{R_{min}} \tag{74}$$

Thus by evaluating R_{min} for a given wicking material, the maximum pumping force of the wick is evaluated. The frictional forces associated with the liquid flow caused by the pumping force are evaluated in the permeability tests described in Section VI.

The wicking rise test is a simple method of determining the effective minimum radius of curvature that a wicking material can support. As an explanation, the wick and liquid reservoir shown in Figure 34 can be considered.

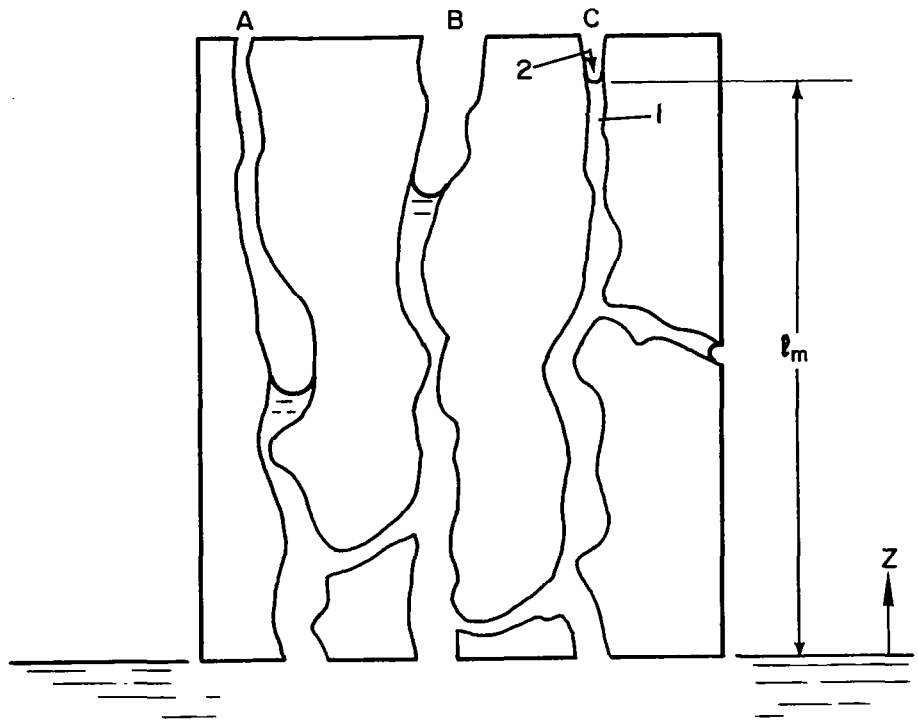

Figure 34 Equilibrium Condition for Three Selected Pores in Saturated Wick

In the porous material shown in Figure 34, only three connected pores are pictured out of the many that actually contain liquid. It is assumed that the material of this wick is one of those listed in Section IV A. Thus, due to the properties of isotropy and homogeneity, at any given height z in the wick, all pore sizes from the smallest to the largest will be represented.

In Figure 34 the liquid has risen to an equilibrium height in each of the pores and it is observed that the liquid front in the wick has risen in some pores to a maximum height ℓ_m represented by pore C. It has been noticed that in a wicking rise test, the degree of wick saturation decreases with increasing z. This is probably due to the smaller fraction of pores (i.e. those with sufficiently small radii) being able to overcome the increased liquid head as z increases. In other words, as z increases, more and more of the larger pores are unable to support the liquid head.

By employing the laws of hydrostatics in the equilibrium situation pictured, the pressure in the liquid of pore C at point 1 just under the meniscus is

$$P_1 = P_a - \frac{\rho_L g}{g_o} \ell_m \tag{75}$$

where P_a is the pressure on the liquid reservoir at z = 0. Equation (75) holds no matter what the shape and size of pore C is, or how many connections it has with other pores and the free surface of the wick.

If the very small vapor head between z = 0 and point 2 just above the meniscus is neglected, then

$$P_2 = P_a \tag{76}$$

The pressure difference across the meniscus in pore C is then

$$P_2 - P_1 = \frac{\rho_L g}{g_o} \ell_m \tag{77}$$

But the Laplace-Young equation (see Section III D) gives the pressure difference across the meniscus as

$$P_2 - P_1 = \frac{2\sigma}{R_c} \tag{78}$$

where it is assumed that pore C can be characterized by one value of the radius of interfacial curvature, R_c.

By equating Equations (77) and (78) it is seen that

$$R_c = \frac{2g_o \sigma}{\rho_L g \ell_m} \tag{79}$$

Since ℓ_m is a maximum for the sample and all pore sizes are present at any given z

$$R_c = R_{min} \tag{80}$$

where R_{min} is the minimum radius of curvature that the wicking material can support. Thus the wicking tests are a means of determining R_{min}.

The above assumes that the liquid wets the porous material of the wick, i.e., has a contact angle $0 \leq \phi < 90°$. The wicking test is not a measure of the minimum pore size of the wicking material, because a definite value of the contact angle would have to be known to calculate this. It merely permits an evaluation of the maximum capillary forces that a given liquid-wicking material combination will produce.

Thus two wicking materials with exactly the same pore structure but made of different materials would probably have different equilibrium heights with a given liquid, due to differences in their wetting characteristics. Also if a given wick is considered with two different liquids, the minimum radius of curvature, R_{min}, of each wick-liquid combination could be different due to differences in the wetting characteristics.

The result of the wicking rise tests is an equilibrium height yielding a measure of the maximum capillary pumping force for the wick-liquid combination tested. The pumping forces are functions of both the wetting characteristics of the wick-liquid combination and the pore size and structure of the wick.

B. Description of Wicking Rise Apparatus

The test apparatus consists of glass tubes with a 60 mm inside diameter which are attached in a vertical position to a metal framework as shown in Figure 35. Each tube encloses a wicking sample and is open at the bottom with a rubber stopper on the top. The stopper has two openings in it to receive a valve assembly, used in venting the tube before the start of a test, and a fitting which allows the sample height to be adjusted. The sample is suspended in the glass tube by

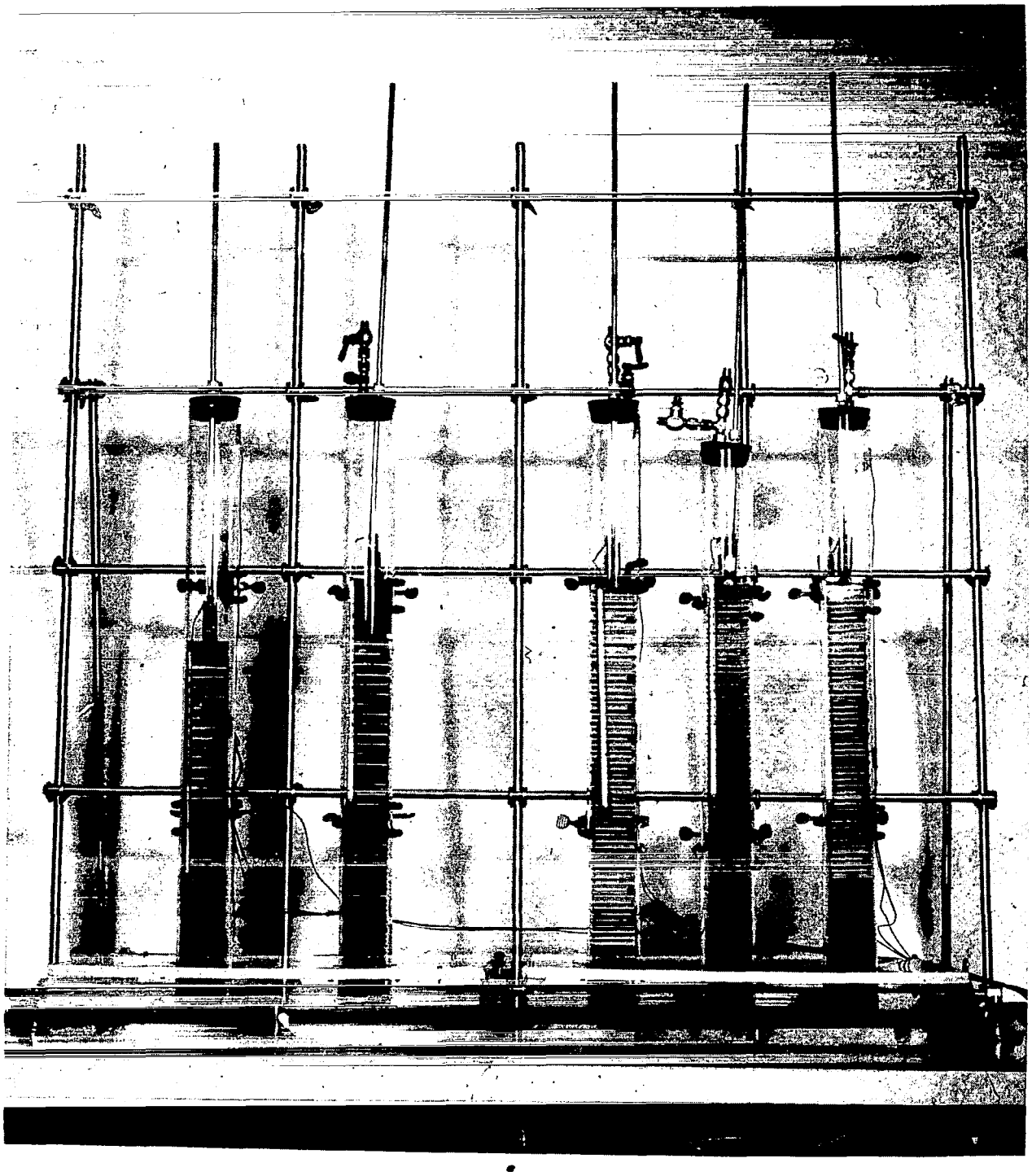

Figure 35 Wicking Apparatus with Samples Installed

a stainless steel rod and clip that passes through the fitting. Also attached to each rod is a thermometer used in recording the temperature in the tubes. The glass tubes are suspended in a Plexiglas reservoir which has a Plexiglas top fitted with soft Neoprene seals that fit around the outside of each glass tube. The seals and the Plexiglas top prevent evaporation and contamination of the liquid contained in the reservoir. The Plexiglas reservoirs are large enough so that the level will remain nearly constant while tests are in progress. The reservoirs are filled with either water or Freon 113, the two liquids under investigation.

The bottom of each tube is submerged below the surface of the liquid in the reservoir, thereby sealing the tube and sample from the atmosphere. The air in the tube is saturated, preventing any net evaporation from the wick during and after the time the liquid has risen to the equilibrium height.

The results of the wicking tests have shown that it can take a long time, i.e., days, for the liquid front in a wicking sample to reach an equilibrium height. Some of the denser porous metal samples did not reach an equilibrium height in 20 days. Similar results have been obtained by other investigators[11]. Generally, after the first few hours of a wicking test, the rate of rise of the liquid front becomes very small and increasingly difficult to see. Because of the small amount of liquid present at the higher levels in the sample, it is quite important to enclose the wick in a saturated-vapor environment to prevent mass transfer. Failure to eliminate the latter would cause a lower than actual value of ℓ_m, the equilibrium height, to be recorded. During tests each apparatus was completely enclosed in a multiwalled cardboard enclosure to keep the entire apparatus at a near constant temperature and to minimize temperature gradients along the length of the wicking samples. As shown in Figure 36, each enclosure had a Plexiglas front for viewing the samples during a test.

During earlier tests it was found that the temperature gradient along each tube could amount to as much as 4°F. This not only caused errors in estimating surface tension but also caused condensation to form on the inside of each tube, making the reading of the liquid level in each sample difficult. To remedy this, thermocouples were attached to the outside of three of the tubes, at the top, middle, and bottom. Thermocouples were also placed in each of the two liquid reservoirs. After the enclosure described above was installed, the temperature gradient along each tube decreased to less than 1°F, and condensate no longer formed in the tubes.

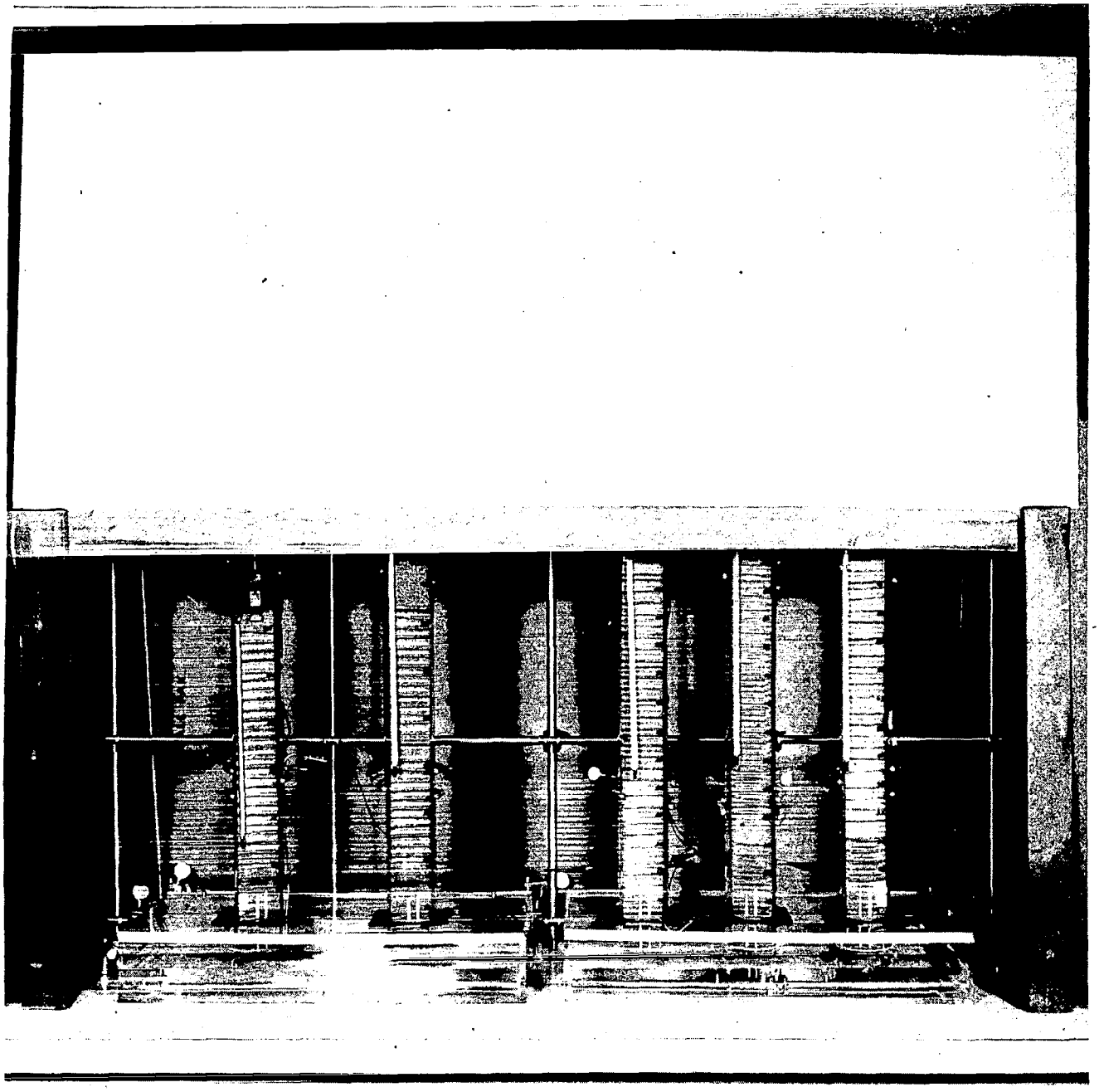

Figure 36 Wicking Apparatus with Insulating Enclosure

Due to the surface finish and the opacity of the materials tested, it was found that it was not possible to visually observe the liquid front in a given wick. Early in the experimental investigations various methods of measuring the position of the liquid front were tried, the best one being that of attaching litmus paper to the wick and noting when the paper was first wet. Other methods tried were the use of dyes and fluorescent liquids irradiated with ultraviolet light.

The litmus paper method was eventually refined by adding a small amount of potassium hydroxide to the water to increase the response of the litmus paper. Tests were made to find the smallest amount of basic material that could be added to the water and still cause pink litmus paper attached to a wick to turn to a vivid blue. It was found that a solution 0.03 per cent by weight of KOH was adequate for this result. This wicking liquid can be treated as being essentially pure water, due to the very small amount of KOH used. Figures 37 and 38 show that the interfacial properties of aqueous solution of 0.03 per cent of KOH differ insignificantly from those of pure water.

The litmus paper in the form of thin strips was held against the surface of the porous sample by a Plexiglas ladder. The ladder and the sample were held together by rubber bands placed around the assembly at various points. A picture of a wick sample both with and without the ladder is shown in Figure 39. The Plexiglas ladder shown in the sketch below, was made by machining rectangular grooves into a 1/8-inch thick sheet of acrylic plastic, resulting in lands about 0.08-inch wide for holding the strips of litmus paper. The first ladders had a land pitch of 0.5 inch, but later the pitch was set at 0.3 inch. On a sample 20 inches long there were 66 strips of litmus paper approximately 0.1 inch wide, one under each land. The grooves in each Plexiglas ladder were 0.08 inch deep, making the ladder very flexible. When rubber bands were wrapped around it and the sample, the ladder conformed to the local irregularities of the porous sample, thereby pressing the litmus strips against the sample surface for good contact.

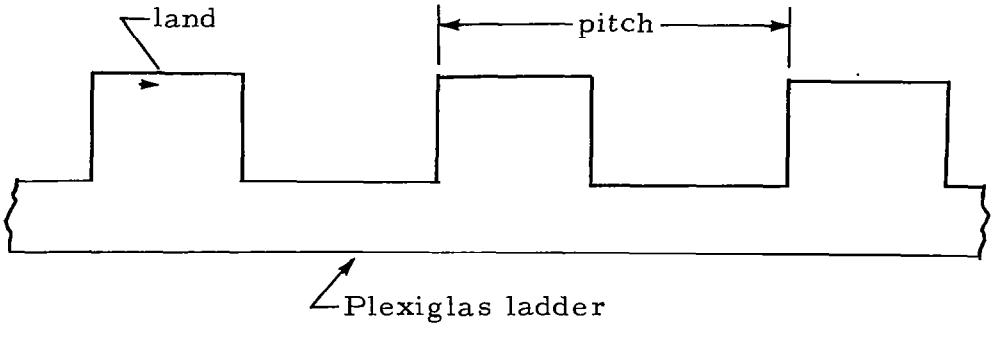

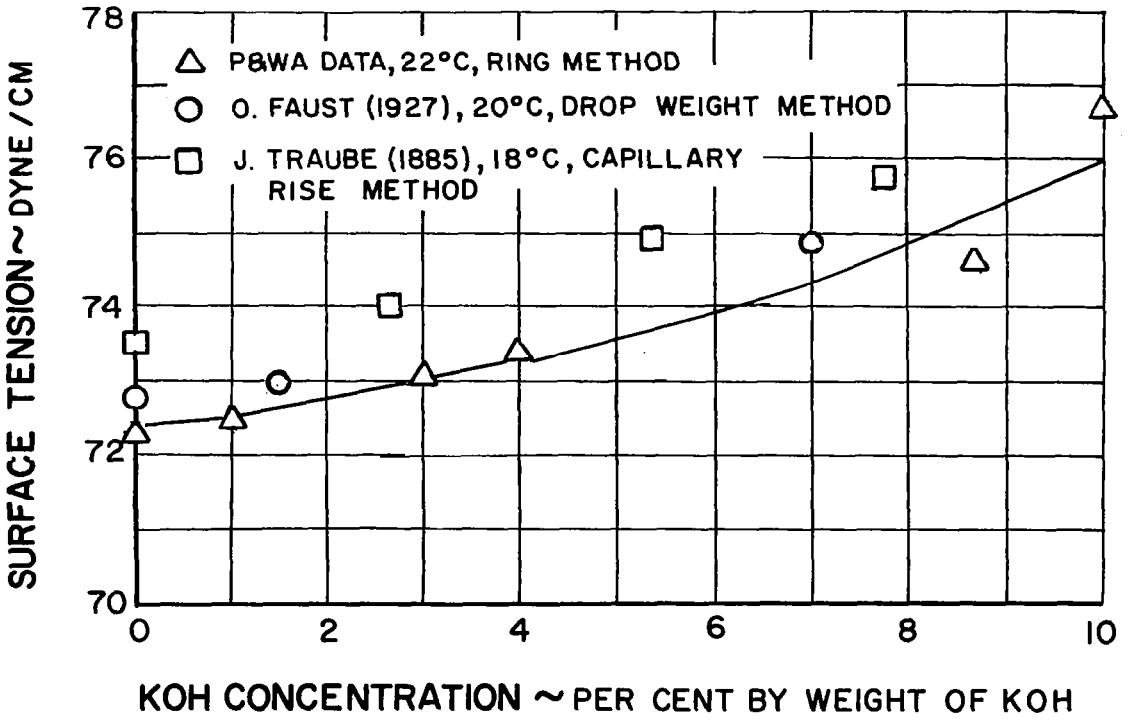

Figure 37 Surface Tension of Aqueous KOH Solutions vs KOH Concentration

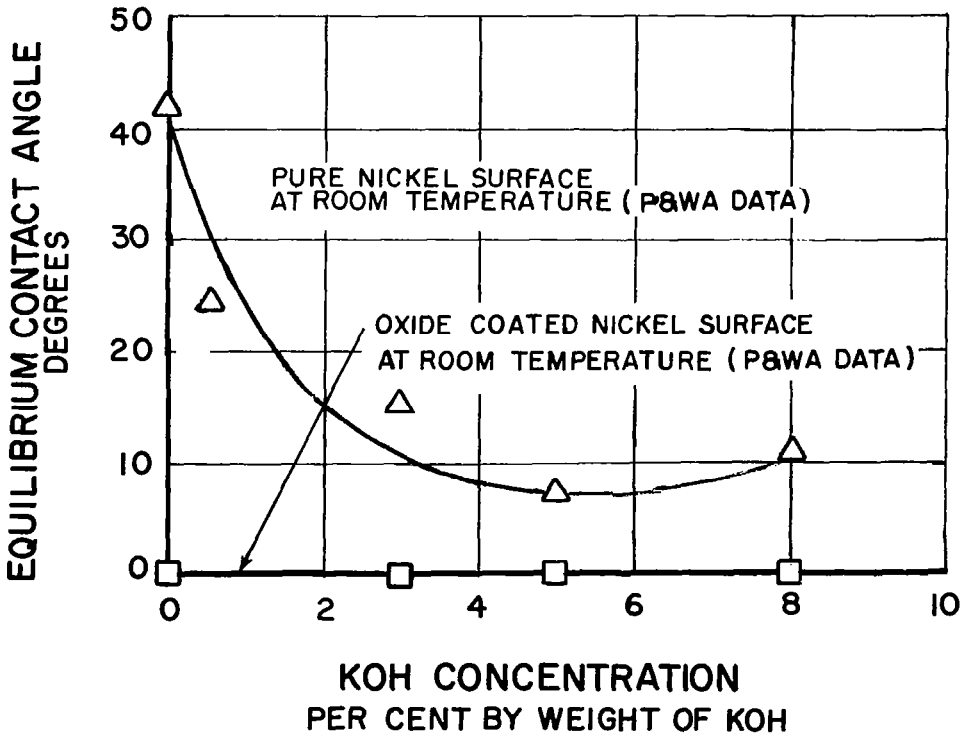

Figure 38 Equilibrium Contact Angle vs Aqueous KOH Concentration for Two Nickel Surfaces

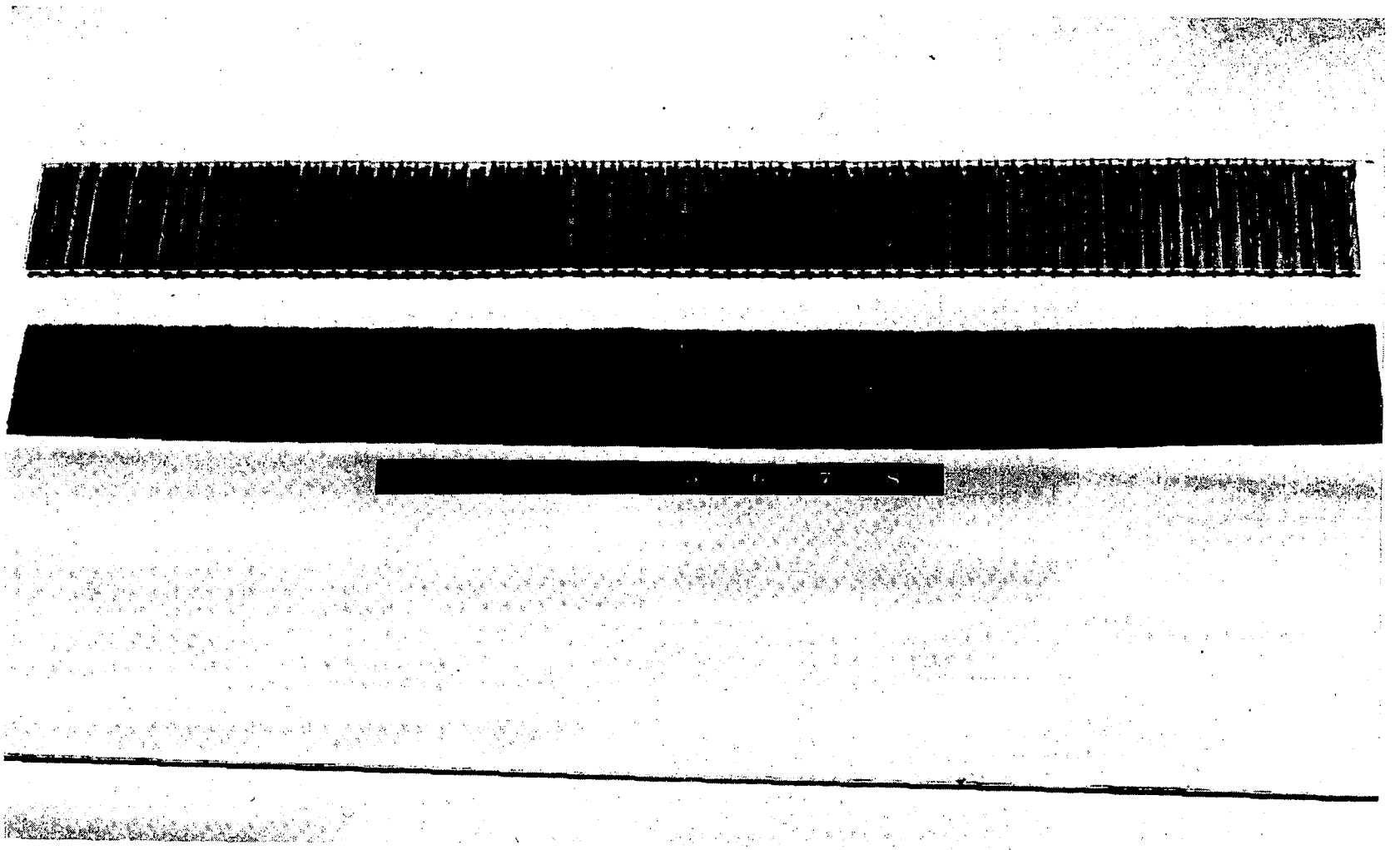

Figure 39 Wicking Samples with and without Litmus Paper

There are two drawbacks to the use of the litmus paper. One is that the litmus paper does not respond instantaneously to the position of the actual liquid front when the front first reaches the level of a given strip. It takes a finite amount of time to wet the paper and to react with the pH indicators in the litmus paper. The measured rate-of-rise curve is then lower than the rate-of-rise curve of the actual liquid front in the sample. However, for elapsed times of an hour or longer, this difference was found to be negligible.

The other drawback is the fact that each strip is separated by a finite distance of 0.22 inch. Thus the finest division for measuring the height of the liquid front is this spacing. It was felt that any closer spacing would introduce too much litmus paper, which in itself is an excellent wick and might influence test results. However, with moderate wicking heights of 6 inches, this error of -0.22 inch +0.08 inch amounts to an uncertainty of only -3.7 per cent +1.3 per cent in measured values of maximum wicking rise, ℓ_m.

Two wicking rise stands were built in order to test up to eleven wicking samples at a time. The samples varied in length from about 4 to 16 inches depending on the individual wicking capability. Each wick sample was sintered to a backup plate to simulate the actual construction in a vapor-chamber fin application.

C. Wicking Rise Test Procedure

The procedure involved in observing the liquid front in a wicking sample consisted of placing strips of pink litmus paper every 0.30 inch along the vertical length of the sample. In the tests involving water the wicking liquid as explained in the last section was actually an aqueous solution of 0.03 per cent potassium hydroxide, essentially having the same surface chemistry characteristics as pure water. The liquid front which is difficult to visually observe in the sample itself, was located by noting when each successive litmus paper started to turn blue.

The same technique was utilized during the wicking tests in which Freon 113 was used, except that blue litmus paper was substituted for the pink. Nothing was added to the Freon, for it was found that the blue litmus paper turned a very visible darker blue immediately upon coming in contact with Freon 113.

Before any wicking test was begun, each sample was subjected to the following cleaning procedure:

1) Washing the sample in a vapor degreaser and immediately rinsing the sample in distilled water before the condensed vapor re-evaporated,

2) Bathing in a reagent-grade acetone bath,

3) Submerging the sample immediately in distilled water, followed by several distilled water rinsings, and

4) Air-drying the sample in a clean oven at 500°F for at least 2 hours.

This procedure was followed for each sample to try to insure that the wetting characteristics of each sample would stay constant. After a sample was removed and cooled in the atmosphere, it was stored in a clean plastic bag until tested.

At the start of a wicking test, the sample with attached litmus paper was placed into one of the tubes shown in Figure 35, with the end of the sample above the reservoir level. Time was permitted for the air in the tube to come into equilibrium with the liquid so that there was no net mass transfer during the actual wicking test. The lower end of the vertical wicking sample was lowered into the liquid by means of the fitting at the top of the tube, and a stopwatch started. The time, temperature, and level were recorded every time a litmus paper changed color, indicating passage of the liquid front. When the rate of rise slowed to less than 0.3 inch (one litmus paper) per hour, readings were taken every hour. When the rate of rise of the liquid front was less than 0.3 inch for every two hours, readings were taken at two-hour intervals to the end of a test. The wicking run on a sample was terminated when either, 1) the liquid front reached the sample top, 2) a period of two weeks elapsed, or 3) the liquid front failed to rise 0.3 inch (one litmus paper) in 3 days. The height at which the latter occurs is defined as the equilibrium height, ℓ_m.

D. Test Results

At least one wicking rise test was run on each of the samples described in Section IV A. In some cases as many as three wicking tests in water and one in Freon 113 were run on a sample.

The results of the wicking tests in water are shown in Figures 40 to 61 which present the variation of liquid height with time. The only sample listed in Section IV A that is not represented in these figures is Sample H5. This sample was excluded after it was found that it had not been completely oven-dried after the cleaning process, which resulted in erroneous data for the only wicking test run on H5. In all cases the curves shown in these figures represent the particular wicking test that resulted in the largest value of the equilibrium height.

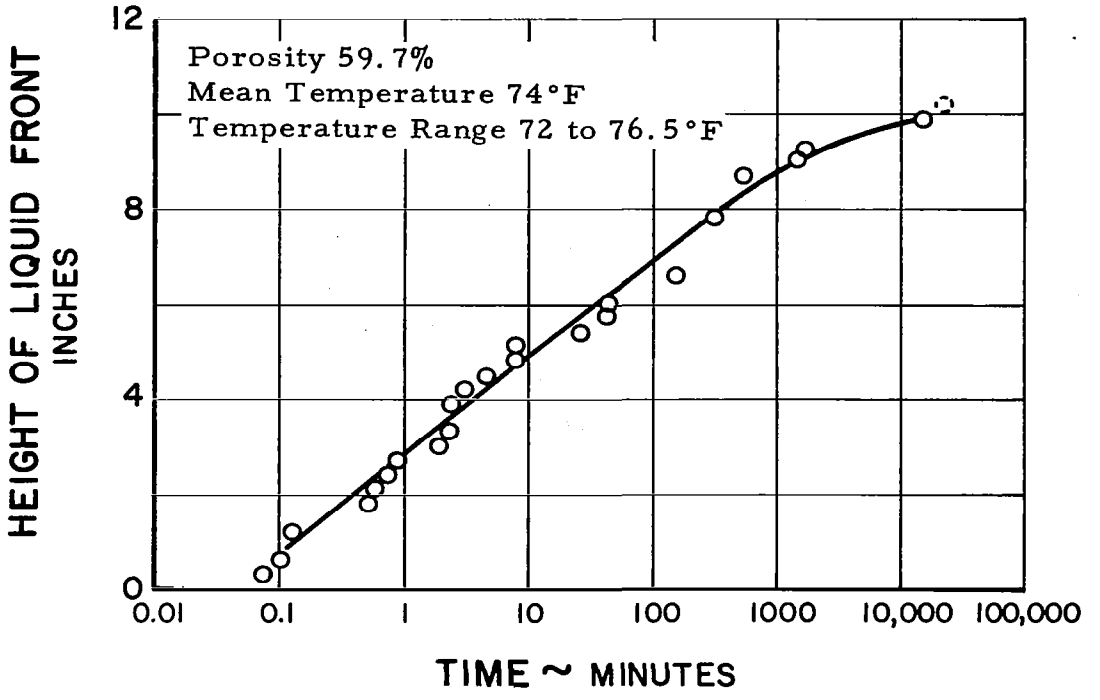

Figure 40 Water Wicking Curve for Sintered Nickel Power Sample M1

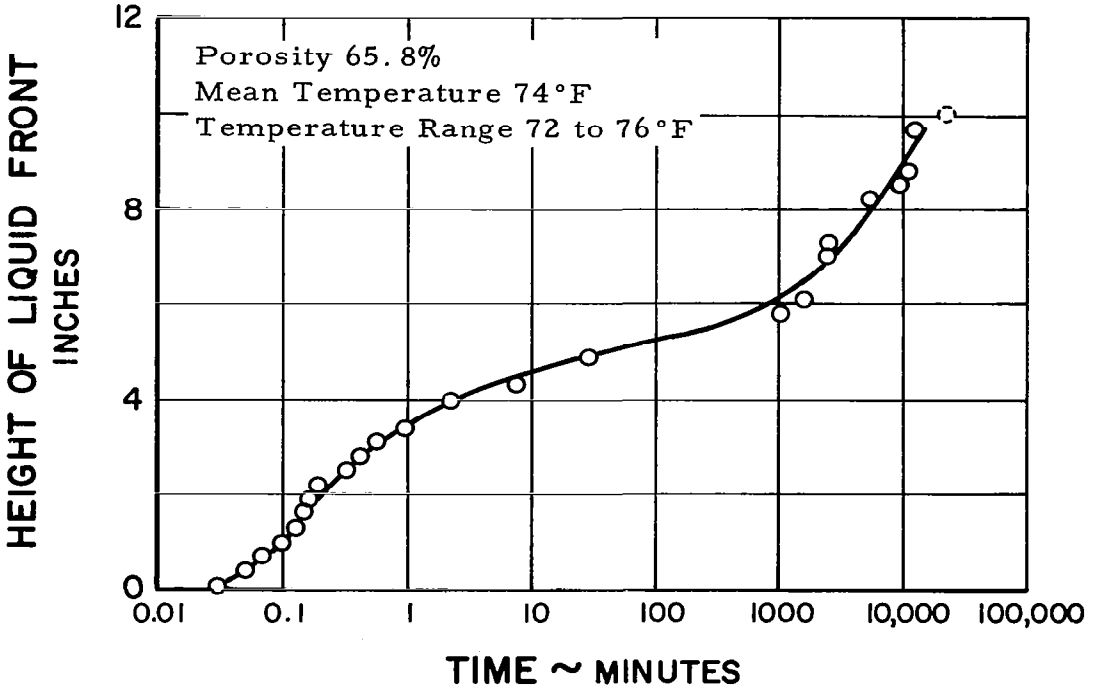

Figure 41 Water Wicking Curve for Sintered Nickel Power Sample M2

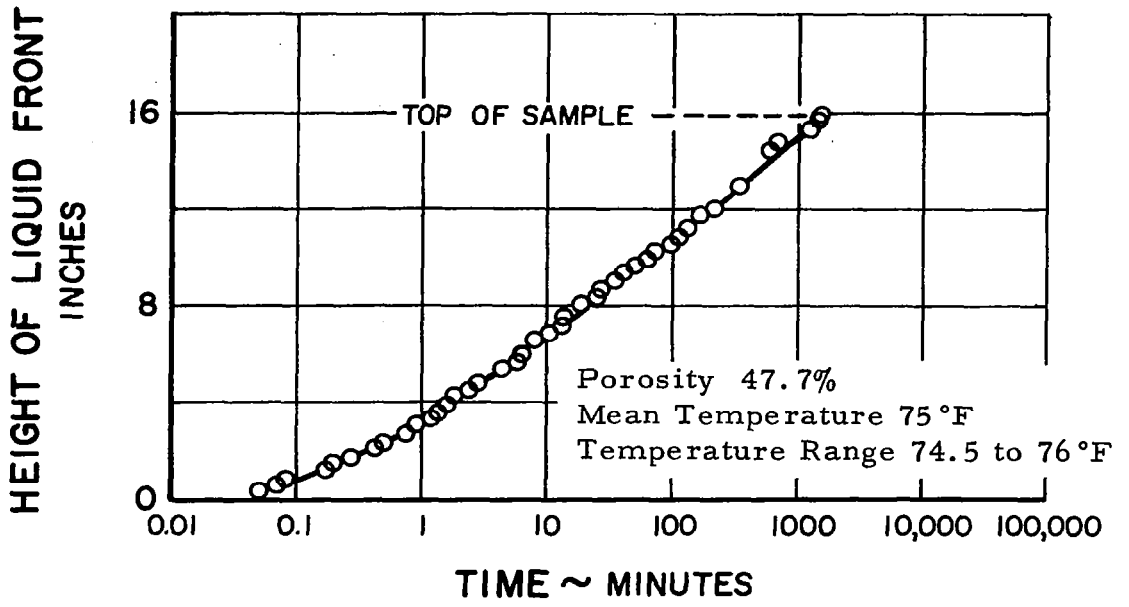

Figure 42 Water Wicking Curve for Sintered Nickel Power Sample M3

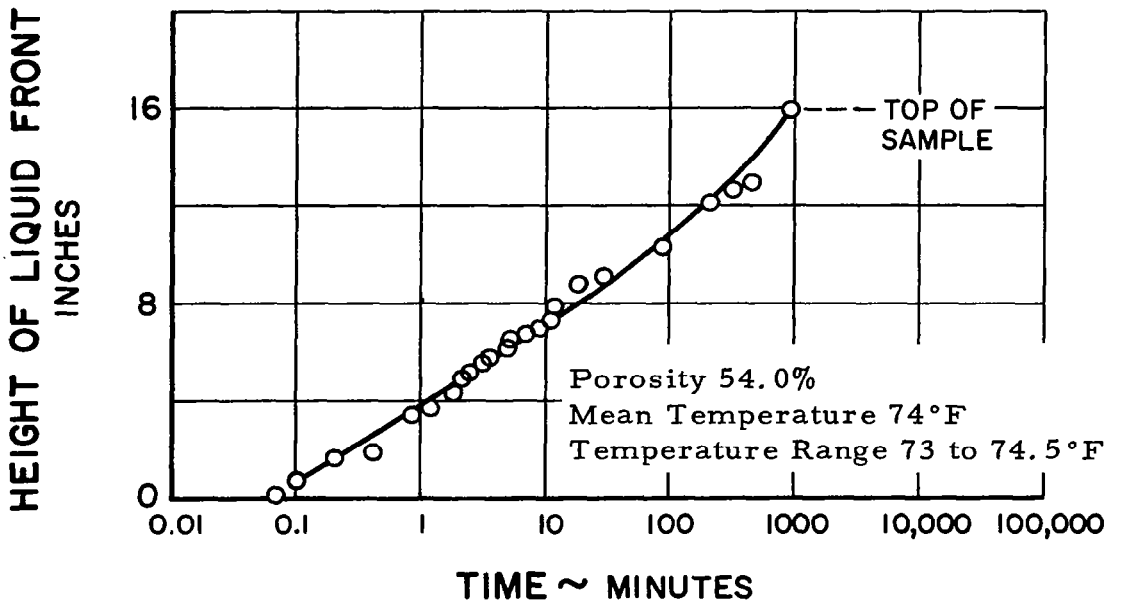

Figure 43 Water Wicking Curve for Sintered Nickel Power Sample M4

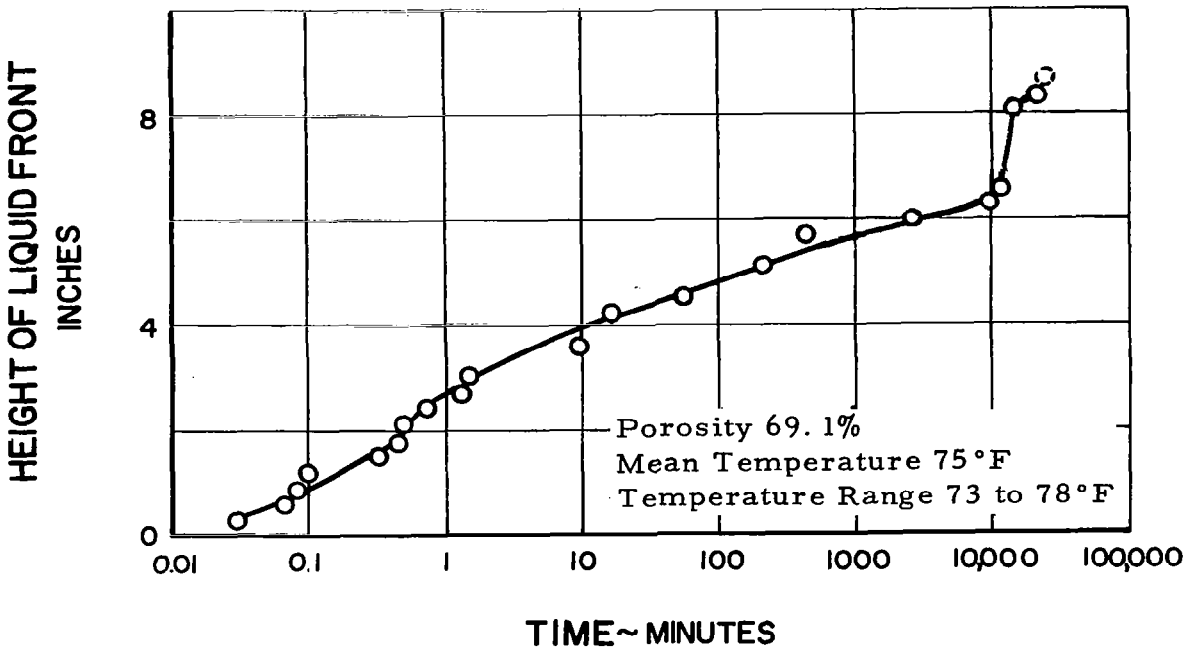

Figure 44 Water Wicking Curve for Sintered Nickel Power Sample M5

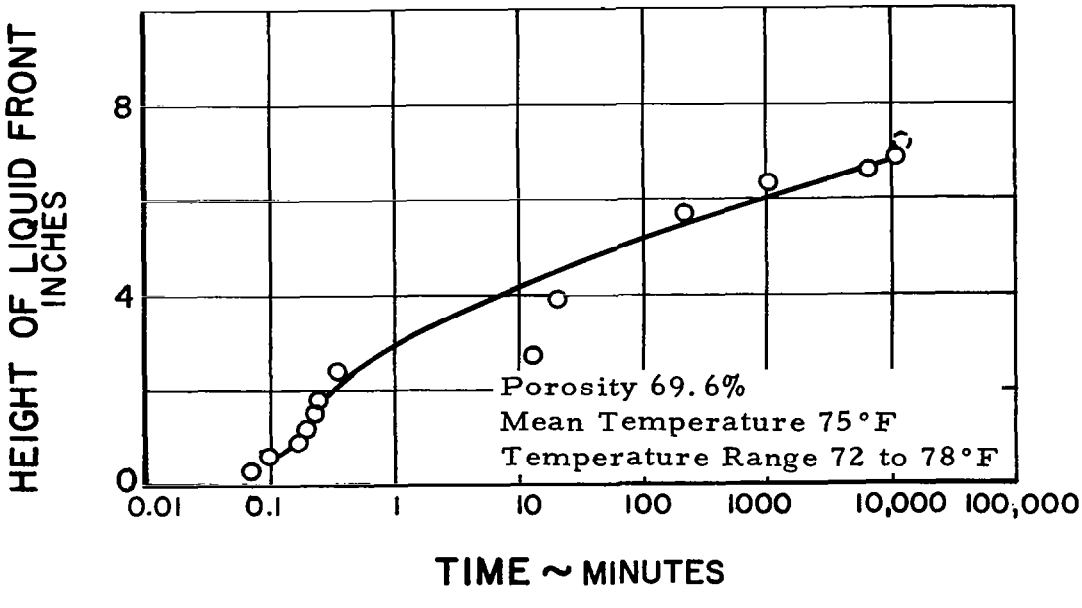

Figure 45 Water Wicking Curve for Sintered Nickel Power Sample M6

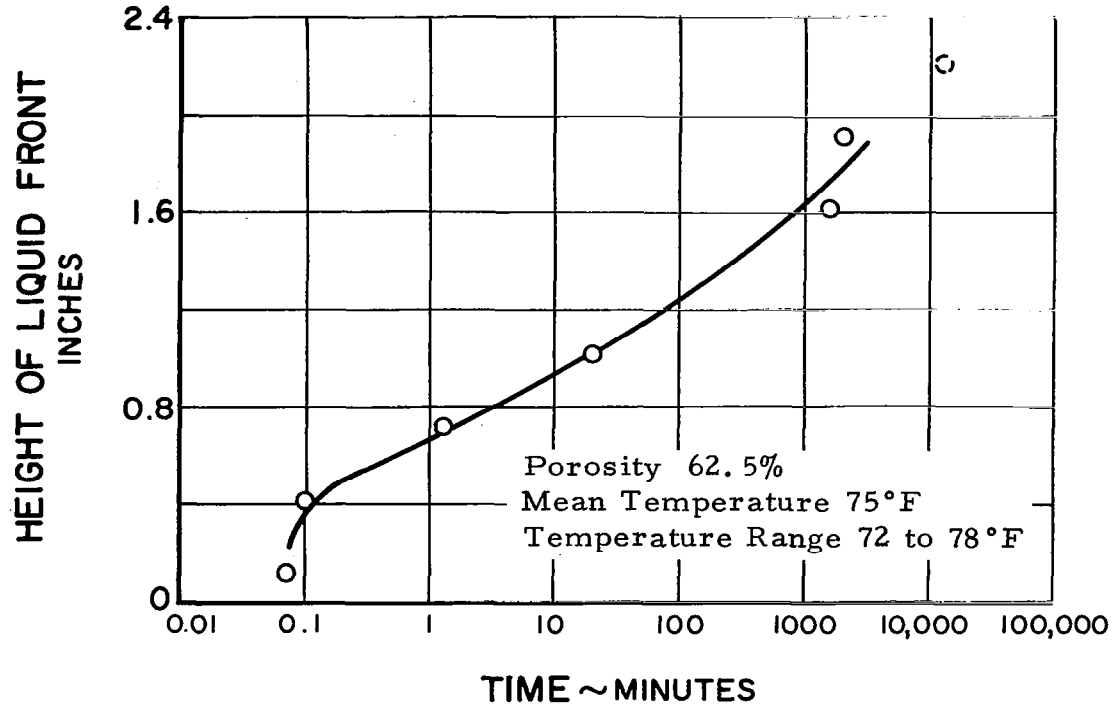

Figure 46 Water Wicking Curve for Sintered Nickel Screen Sample M7

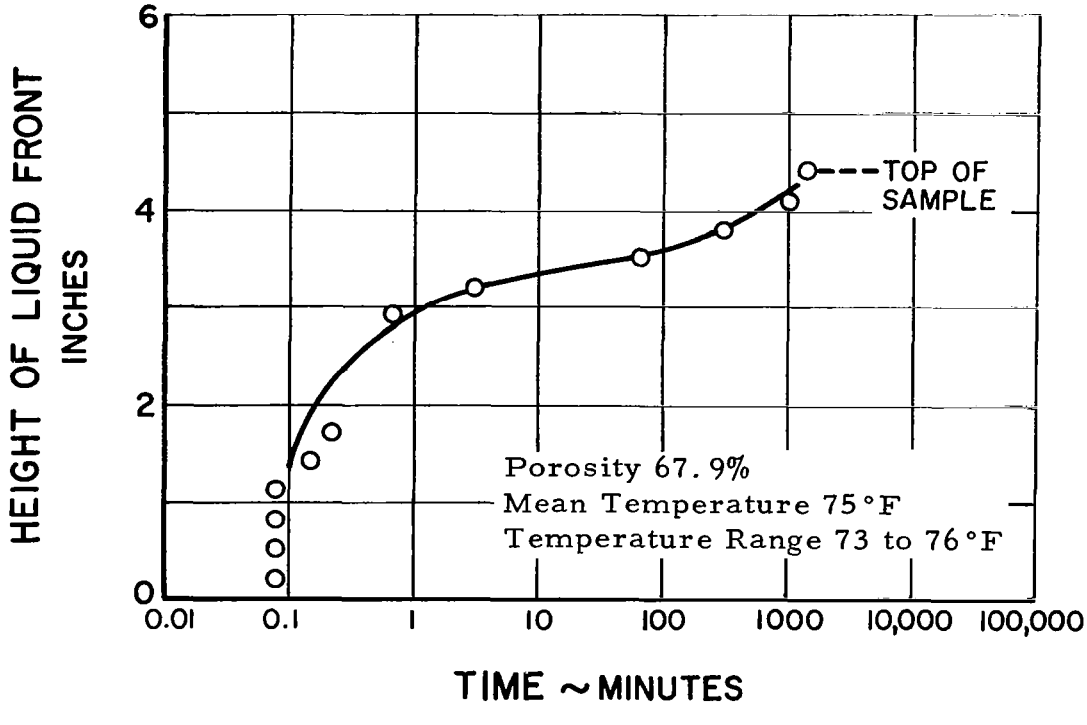

Figure 47 Water Wicking Curve for Sintered Nickel Screen Sample M8

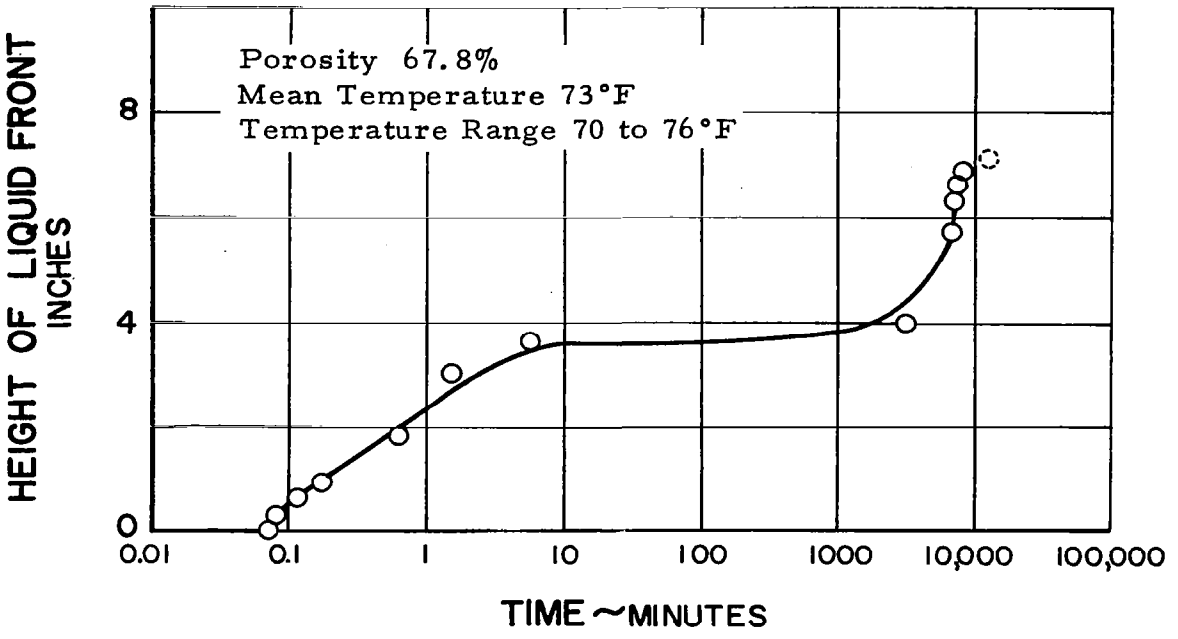

Figure 48 Water Wicking Curve for Sintered Nickel Screen Sample M9

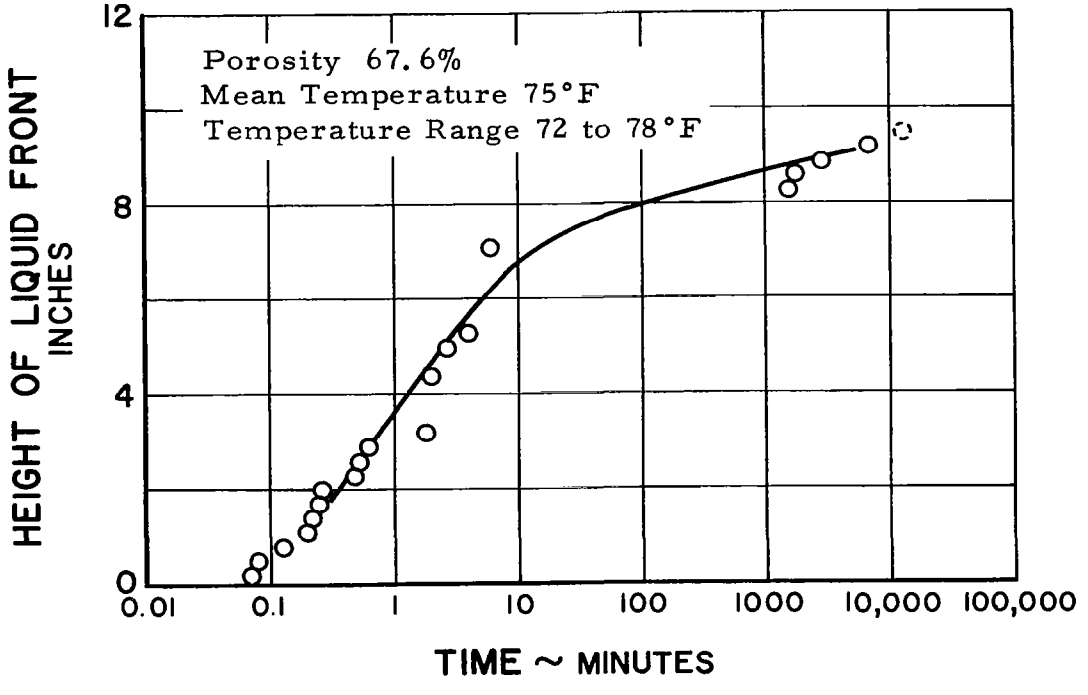

Figure 49 Water Wicking Curve for Sintered Nickel Screen Sample M10

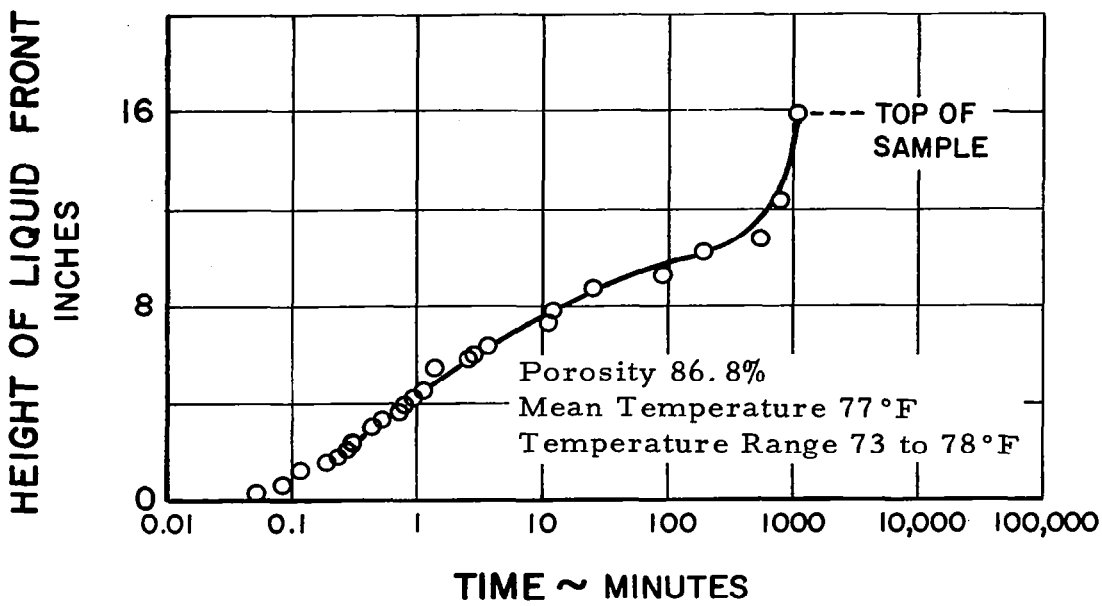

Figure 50 Water Wicking Curve for Sintered Nickel Fiber Sample H1

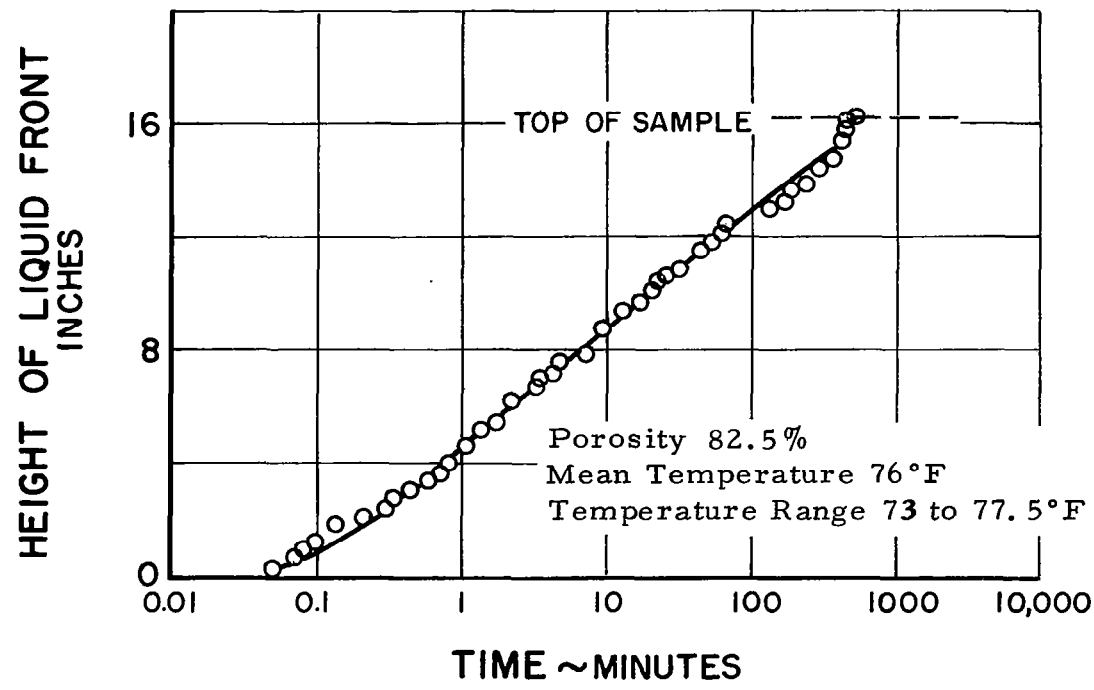

Figure 51 Water Wicking Curve for Sintered Nickel Fiber Sample H2

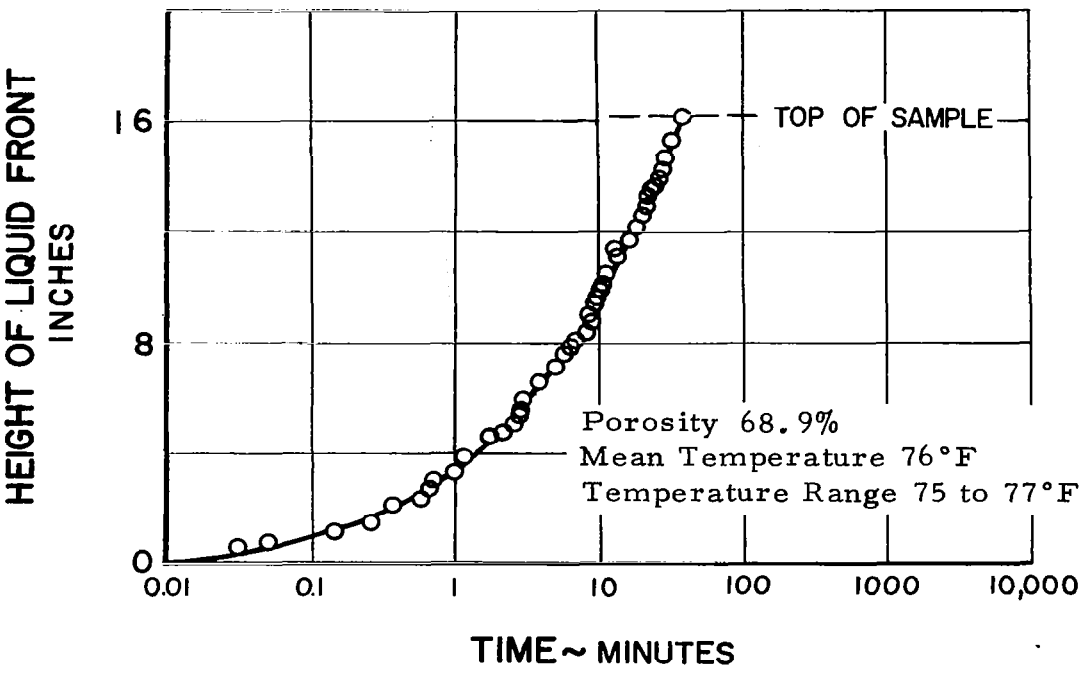

Figure 52 Water Wicking Curve for Sintered Nickel Fiber Sample H3

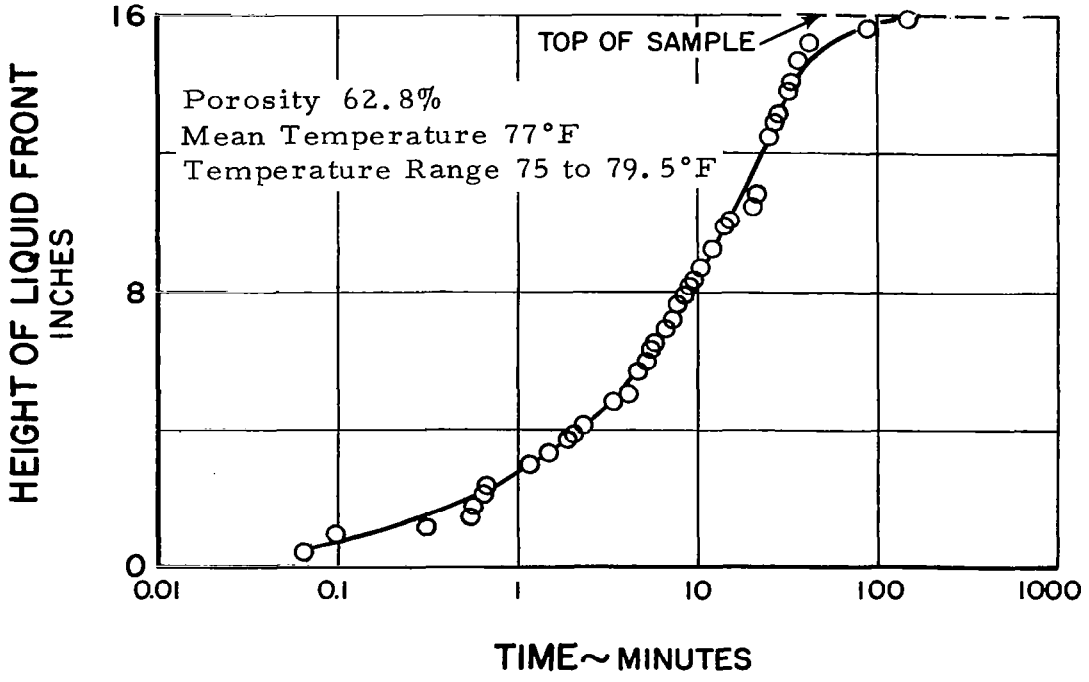

Figure 53 Water Wicking Curve for Sintered Nickel Fiber Sample H4

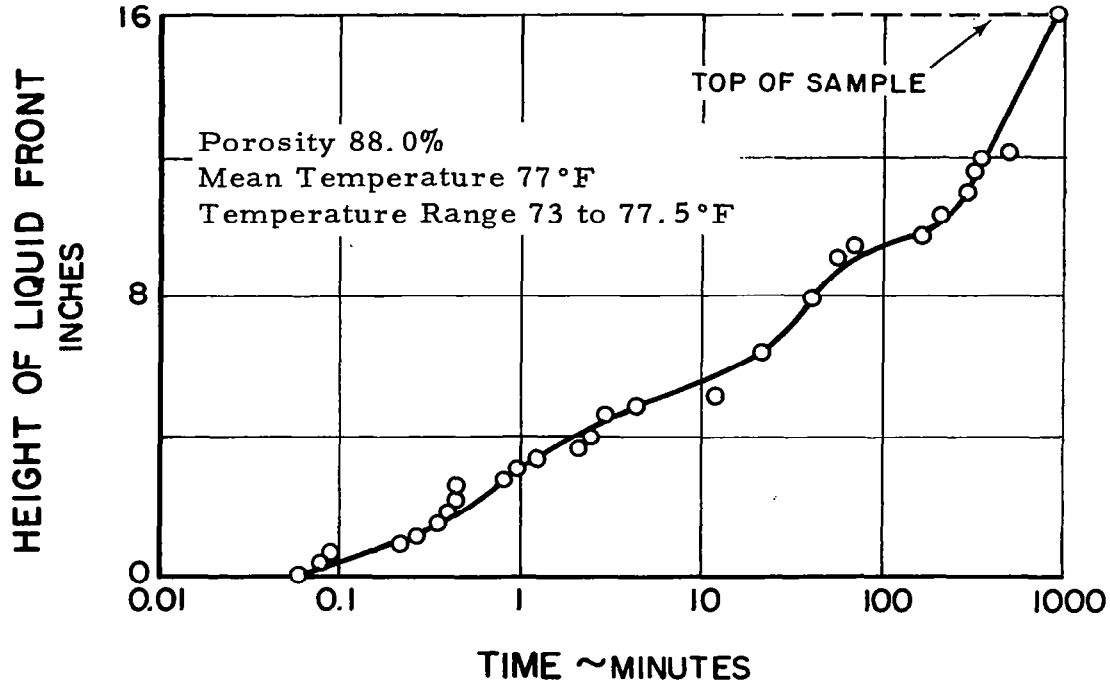

Figure 54 Water Wicking Curve for Sintered Nickel Fiber Sample H6

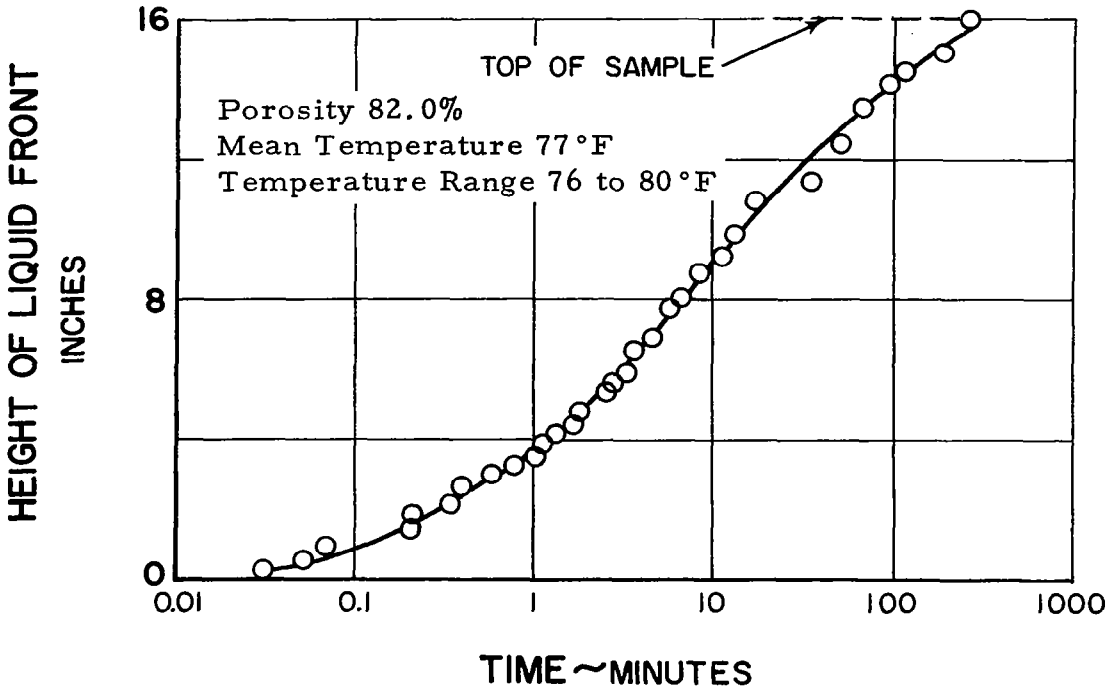

Figure 55 Water Wicking Curve for Sintered Nickel Fiber Sample H7

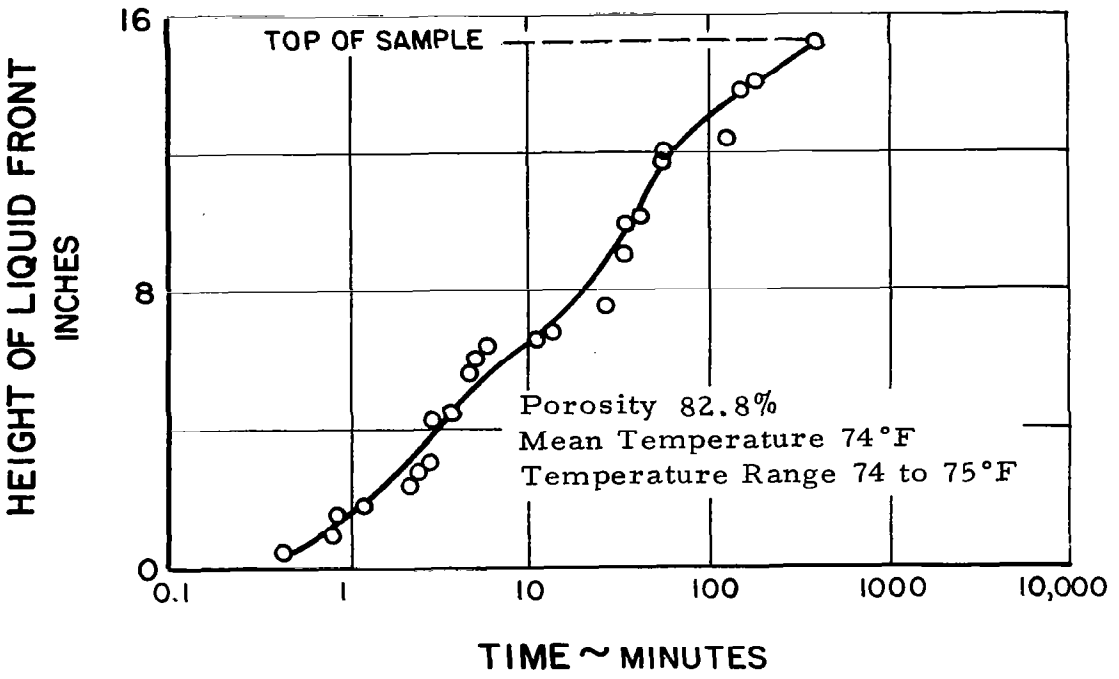

Figure 56 Water Wicking Curve for Sintered Nickel Fiber Sample H8

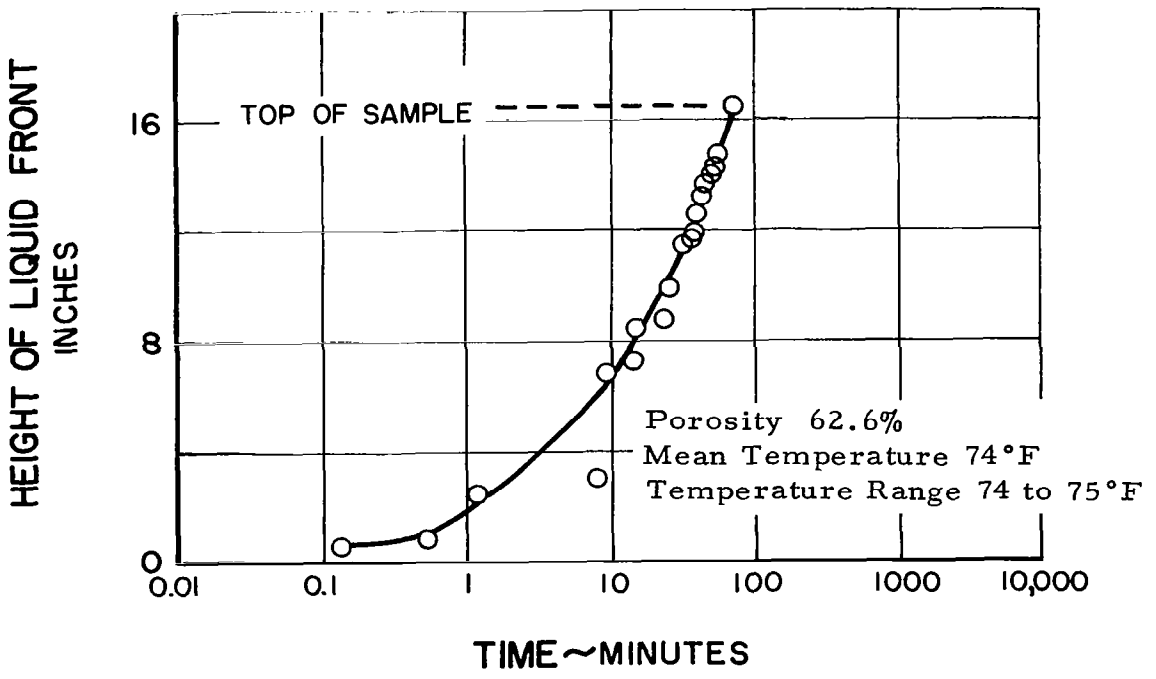

Figure 57 Water Wicking Curve for Sintered Nickel Sample H9

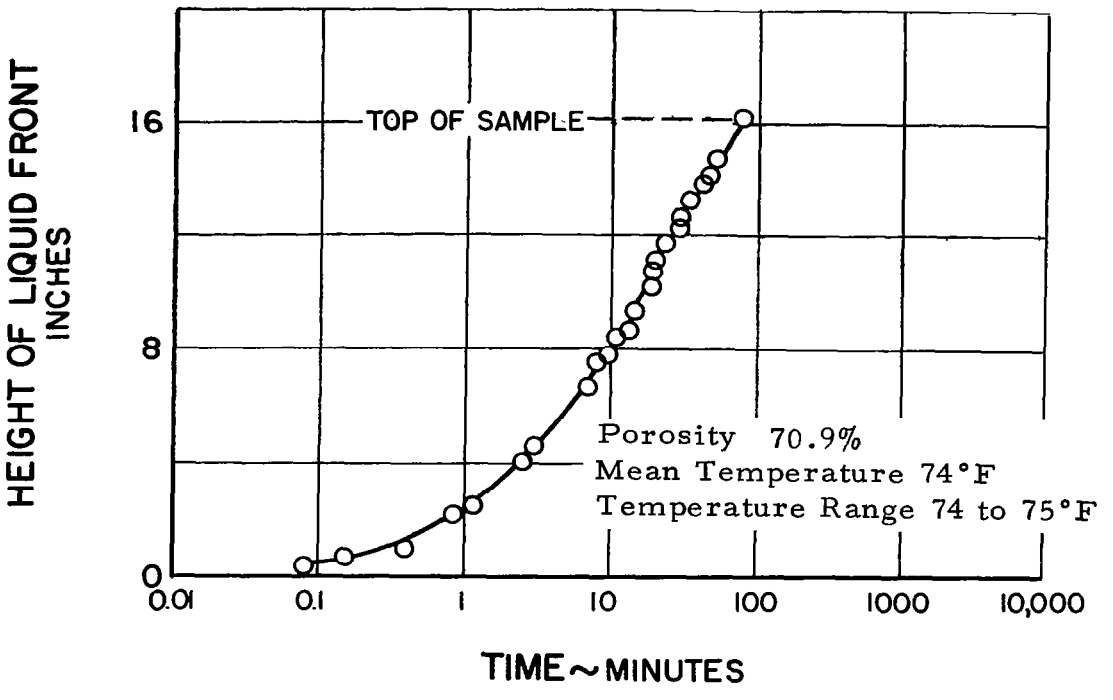

Figure 58 Water Wicking Curve for Sintered Nickel Fiber Sample H10

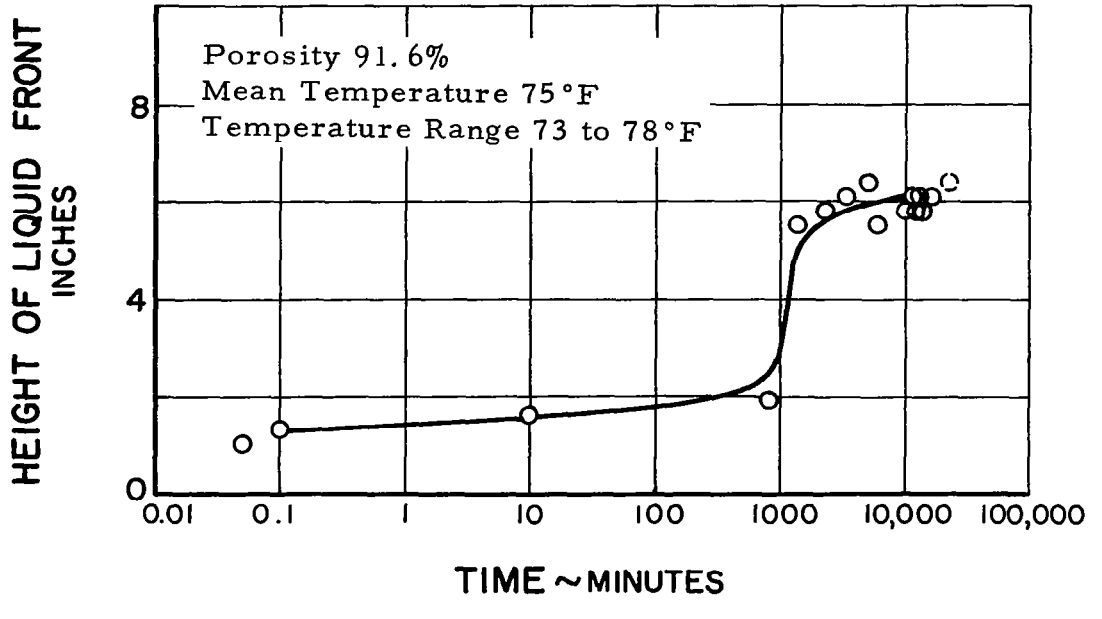

Figure 59 Water Wicking Curve for Sintered Stainless Steel Fiber Sample H11

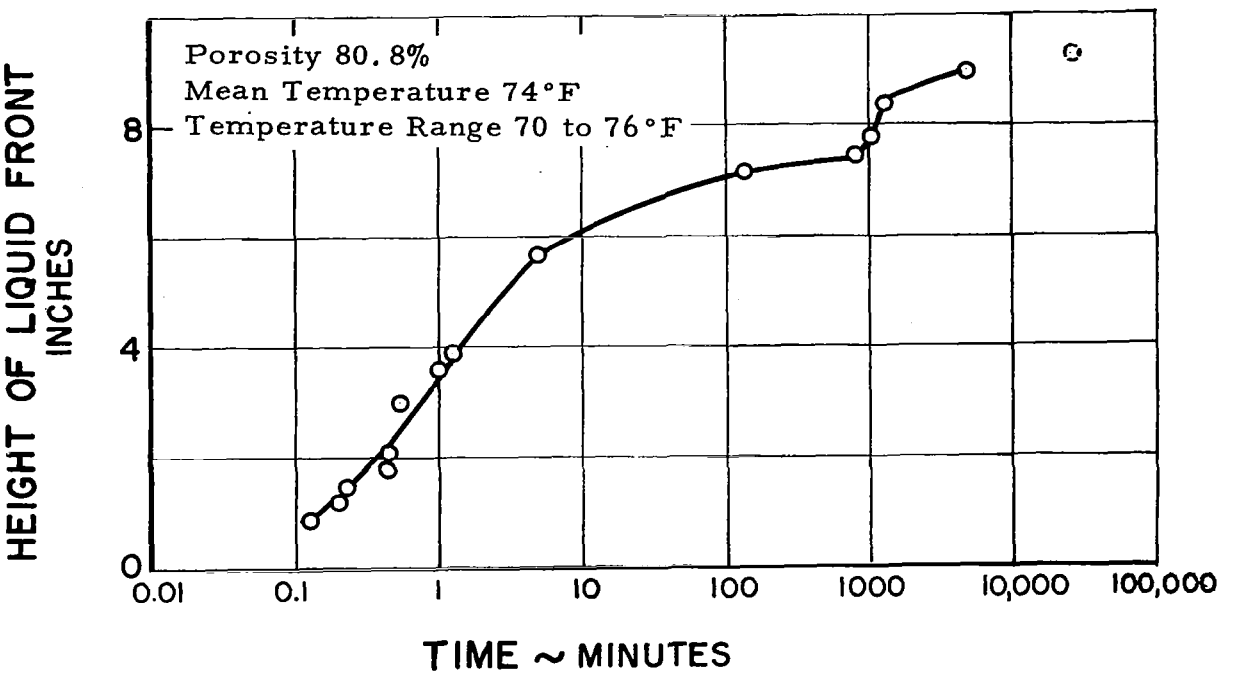

Figure 60 Water Wicking Curve for Sintered Stainless Steel Fiber Sample H12

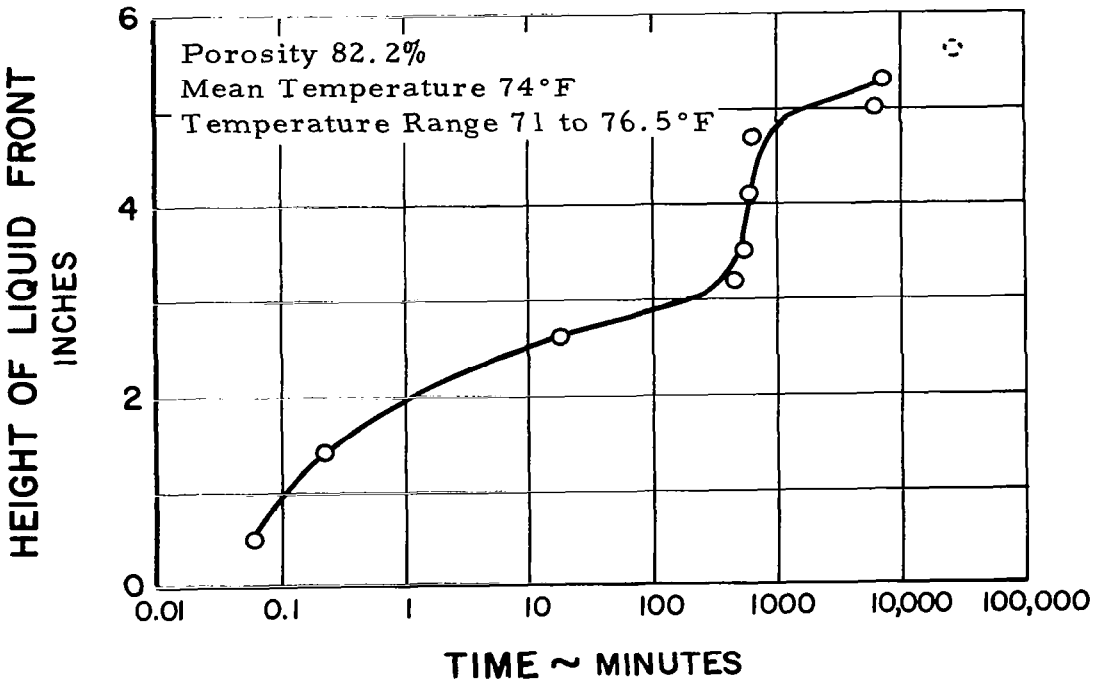

Figure 61 Water Wicking Curve for Sintered Stainless Steel Fiber Sample H13

Representative wicking samples were chosen from those that had the largest value of ℓ_m with water. These samples, M1, M4, M6, H1, H2, H3 and H6, were then recleaned and prepared for wicking tests with Freon 113. The rate of rise results for four of these samples are shown in Figures 62 to 65. Although the equilibrium height was obtained for the other three samples, their rate of rise curves are not shown since the liquid reservoir height varied during the test. This variation was due to evaporation of the Freon 113 over weekends.

Because of the relatively long time required for the liquid front to reach equilibrium in a sample, all of the plots shown in Figures 40 to 65 have logarithmic time scales. As shown in these figures this equilibrium time can exceed 10,000 minutes.

In a number of the tests the samples proved to be too short, as the liquid front rose to the top. This occurred with samples M3, M4, M8, H1, H2, H3, H4, H6, H7, H8, H9 and H10 in the tests involving water. Unfortunately, wicks longer than 16 inches could not be obtained from all of the wick manufacturers.

In tests where the liquid front did not progress to the top of the samples (samples M1, M2, M5, M6, M7, M9, M10, H11, H12, H13 with water and all the tests involving Freon 113), the height of the first litmus paper above the liquid front and the time at which the test was terminated are indicated by a dotted circle. The solid circle just below the dotted circle indicates the last litmus paper to be wetted. This solid circle represents the equilibrium height of the sample except for the test on Sample M4 in Freon 113 (see Figure 63). This test was discontinued before the equilibrium height (as defined in Section V C) was reached. In the test on Sample H11 in water (see Figure 59) the observed height of liquid fluctuated with time near the final equilibrium height. This was perhaps due to a combination of difficulty in observing the height and to small temperature variations causing non-equilibrium conditions to exist.

No attempt was made to fit an analytical model to any of the rate of rise curves shown in Figures 40 to 65. This is because these curves do not present the true rate of rise of the liquid front in the sample, but are dependent on the speed with which the individual litmus paper strips respond to the presence of liquid front in the sample, especially at times near zero. Thus, the response time is the only reasonable explanation that can be offered for the large changes in slope shown in the wicking curves for Samples M5, M9, M10, H1, H11, and H13 with water. However, this response time should not affect the final measured value of ℓ_m.

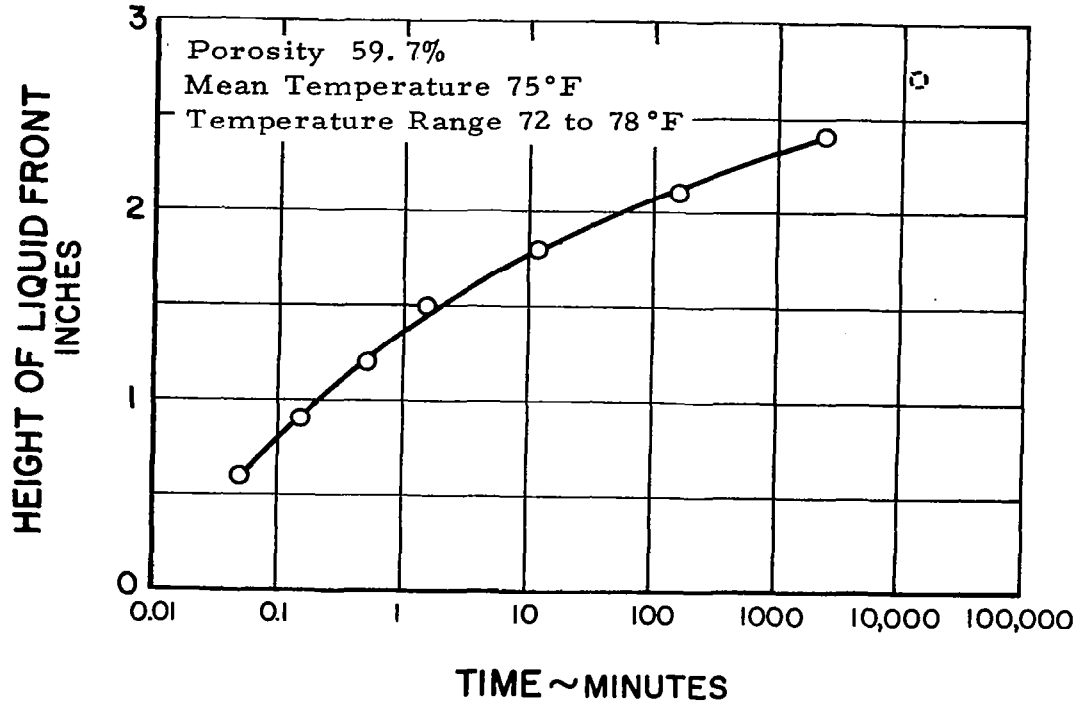

Figure 62 Freon 113 Wicking Curve for Sintered Nickel Powder Sample M1

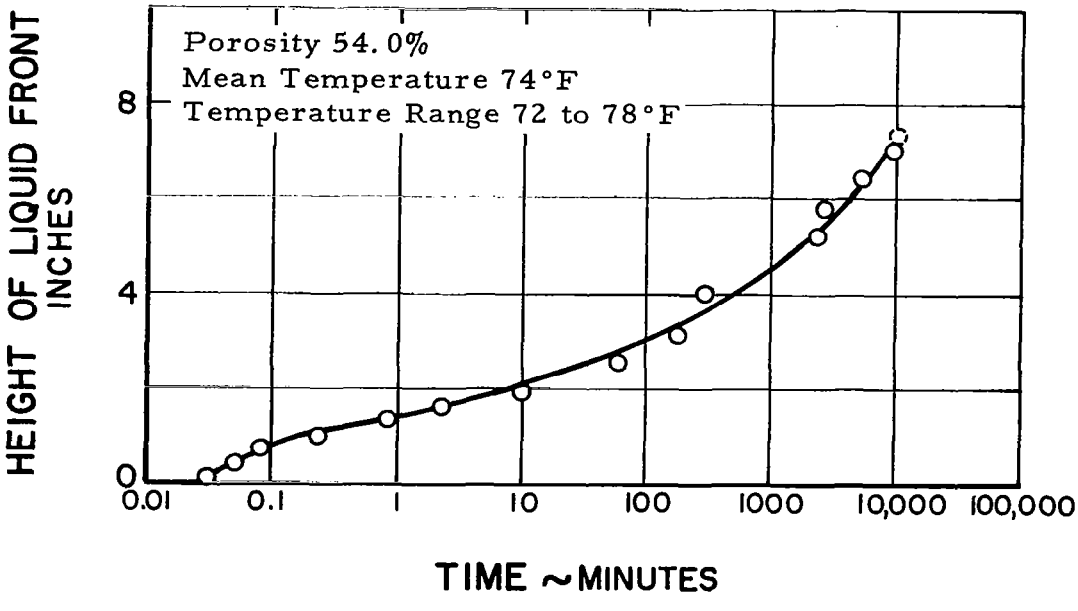

Figure 63 Freon 113 Wicking Curve for Sintered Nickel Powder Sample M4

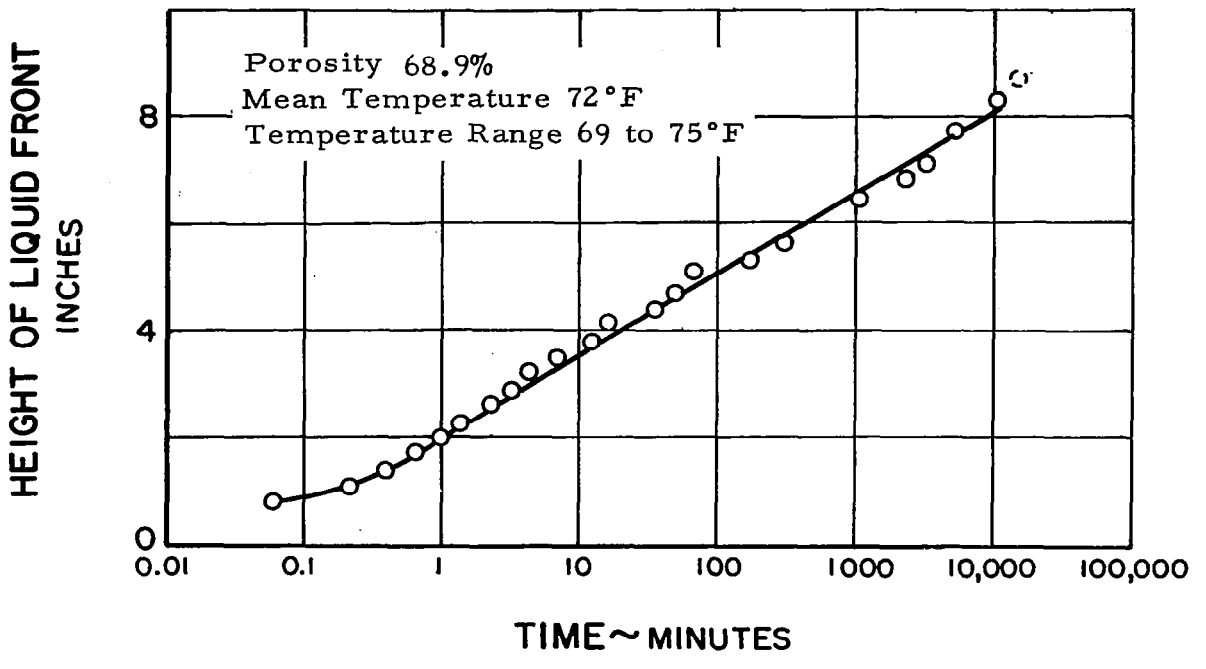

Figure 64 Freon 113 Wicking Curve for Sintered Nickel Fiber Sample H3

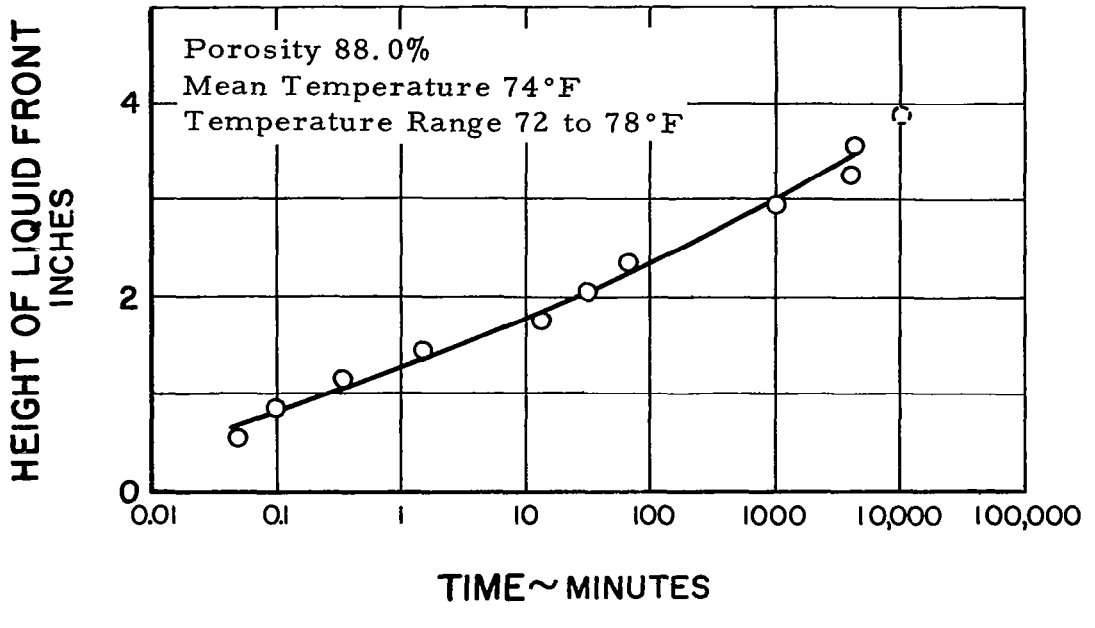

Figure 65 Freon 113 Wicking Curve for Sintered Nickel Fiber Sample H6

The wicking characteristics of the porous materials under investigation are summarized in Table 7. The final equilibrium heights for the wicking tests utilizing water and Freon 113 are listed. The values listed show that the capillary forces in the sintered screen samples are relatively weak, while those associated with the sintered fiber and powder samples can be quite high, due presumably to the finer pore structure obtainable in the latter groups.

TABLE 7

Wicking Characteristics of Porous Materials

Sample No.	(ℓ_m) water inches	(ℓ_m) Freon 113 inches
M1	9.9	2.4
M2	9.7	--
M3	>15.9	--
M4	>16.0	>7.0
M5	8.4	--
M6	6.9	2.0
M7	1.9	--
M8	>4.4	--
M9	6.9	--
M10	9.2	--
H1	>15.9	4.2
H2	>16.1	4.9
H3	>16.1	8.2
H4	>16.0	--
H6	>16.0	3.6
H7	>16.0	--
H8	>15.2	--
H9	>16.4	--
H10	>16.2	--
H11	6.1	--
H12	9.0	--
H13	5.3	--

Temperature: approx. 75°F

The difference between equilibrium heights for the two liquids can be explained in terms of the density, surface tension, and contact angle. As shown earlier, the minimum radius of curvature that a wick can support is given by

$$R_{min} = \frac{2 g_o \sigma}{\rho_L g \ell_m} \tag{81}$$

where R_{min} = minimum radius of curvature, and it is assumed that the meniscus is a segment of the surface of a sphere
σ = surface tension
ρ_L = density of the liquid
g_o = proportionality constant in Newton's second law
g = local acceleration of gravity

The radius of the pore in which the minimum radius occurs is

$$r_p = R_{min} \cos \phi \tag{82}$$

where ϕ is the contact angle between the liquid and the solid material of the wicking sample.

If it is assumed that the minimum radius of curvature occurs in the same size pores in both the water wicking tests and the Freon 113 wicking tests, then Equations (81) and (82) can be combined to arrive at an expression relating the equilibrium heights, given by

$$\frac{(\ell_m)_W}{(\ell_m)_F} = \left(\frac{\sigma_W}{\sigma_F}\right)\left(\frac{(\rho_L)_F}{(\rho_L)_W}\right)\left(\frac{(\cos\phi)_W}{(\cos\phi)_F}\right) \tag{83}$$

where the subscripts w and F refer to water and Freon 113 respectively.

If the contact angles associated with water and Freon 113 are assumed to be equal, and values of fluid properties are substituted, then Equation (83) becomes

$$\frac{(\ell_m)_W}{(\ell_m)_F} = 5.94 \tag{84}$$

However, when the experimental values tabulated in Table 7 are used to calculate the equilibrium height ratio, the resulting values listed in Table 8 are less

than those given by Equation (84). This would indicate that the contact angles in the water tests and the Freon 113 tests are not equal.

TABLE 8

Comparison of Water and Freon 113 Wicking Tests

Sample No.	$\left[\frac{(\ell_m)_w}{(\ell_m)_F}\right]$ measured	ϕ_w (calculated), $\phi_F = 0$ Eq. 83 degrees	$(\ell_m)_w$ (calculated), Eq. (84) inches
M1	4.1	46	14.3
M6	3.4	55	12.0
H1	>3.8	<50	24.9
H2	>3.3	<57	29.2
H3	>1.96	<70.8	48.7
H6	>4.4	<42	21.4

Freon 113 itself is an excellent solvent, which means that it has a contact angle of zero or near zero in a relatively clean wick. If it is assumed that $\phi_F = 0°$, the contact angle of water in the wicking samples can be calculated using Equation (83) and the experimental values of the equilibrium height ratio. These calculated water contact angles which are listed in Table 8 show that the contact angle with water could have been as high as 55 degrees in some of the wicking materials.

Contact angle data given in Figure 38 shows that the contact angle formed between water and a clean pure nickel surface is about 42 degrees, while that formed between water and a clean nickel oxide surface is zero degrees. If the assumption used above that the minimum pore sizes are equal in both the water and Freon 113 tests is correct, then the non-zero value of ϕ_w listed in Table 8 results from 1) a wick that was not truly clean, or 2) a wick in which the nickel was not completely oxidized. As outlined in Section V C , every effort was made to keep the samples clean. Also, each sample was air dried several times in an oven at 500°F for two hours, and appeared to be well oxidized (evidenced by a dark color and a dull finish) after each oven exposure. Thus no answer can be given as to which of the reasons, 1) or 2) above, was responsible for the apparent non-zero contact angles tabulated in Table 8.

Based on the Freon 113 data, the water equilibrium height that would have occurred had both fluid contact angles been zero can be calculated from Equation (84). These values are listed in Table 8 and can be seen to be significantly higher

than the experimental values given in Table 7. However, to evaluate each wicking material for use in a vapor-chamber fin experimental model, only the experimentally determined values of ℓ_m listed in Table 7 should be used.

This is the most realistic approach to take because the wicking material that is used in the fin will be made and treated in the same way that the wicking samples were. Under these conditions, the experimentally determined value of ℓ_m for a given fluid is the quantity that should be used in any fin design calculations.

E. Summary

To obtain data on the minimum liquid-vapor interfacial radius of curvature that a wick would support, tests were conducted to determine the final equilibrium height to which a liquid would rise in a wicking material. The wicking materials were chosen from the porous material samples listed in Section IV. Two liquids, water and Freon 113, were used in the wicking rise tests.

In general it was found that the time necessary to reach an equilibrium height can be quite long, i.e., in the order of months. In some of the tests conducted, a true equilibrium height was not reached, and the test was terminated when the liquid front velocity fell below 0.3 inch in 3 days.

In the tests involving water, it was found that capillary forces in the best wicking materials caused the water to rise rapidly to the top of the sample (16 inches). In poorer wicking samples the water front height was as low as 1.9 inches.

Wicking rise tests involving Freon 113 yielded equilibrium heights lower than those utilizing water, due primarily to the lower surface tension of Freon 113. Comparison of tests involving both liquids, showed that despite the oxidation and cleaning procedures followed, the contact angle in the water wicking tests could have been as high at 55 degrees.

VI. PERMEABILITY TESTS

A. Objective

The object of the permeability tests was to determine the wick friction factor K_1 for several of the porous materials described in Section IV, and, in particular, to determine the dependency of K_1 on flow rate, temperature, fluid properties and time.

The wick friction factor range of the metal wicks used in this study is compared to those of other porous materials in Table 9.

As defined in Equation (25), K_1 is the reciprocal of permeability, or

$$K_1 = \frac{1}{\text{permeability}} \tag{85}$$

with the units of $(\text{length})^{-2}$.

TABLE 9

Flow Resistance of Various Porous Media

Substance	Wick Friction Factor $1/ft^2 \times 10^{-8}$
cork board	0.62 to 2.8 *
hair felt	0.77 to 1.1 *
cigarette	0.84 *
metal wicks (P&WA data)	0.80 to 61
sand (loose beds)	5.2 to 47 *
Fiberglas	18 to 39 *
soils	66 to 3,200 *
bituminous concrete	40 to 9,300 *
sandstone (oil sand)	310 to 1,900,000 *
agar-agar	2,100 to 47,000 *
leather	7,700 to 9,800 *
black slate powders	7,700 to 19,000 *
brick	4,200 to 190,000 *
silica powder	18,000 to 72,000 *
limestone, Dolomite	21,000 to 470,000 *

* Scheidegger, A.E., The Physics of Flow through Porous Media, Macmillan, 1960, p 87

K_1 can be measured by passing fluid at a known rate of flow through a rectangular wicking sample of known size. The pressure drop across the sample can be measured, and K_1 can then be calculated from the expression

$$K_1 = \left(\frac{A_T}{\Delta x}\right)\left(\frac{\rho_L}{\mu_L}\right)\left(\frac{\Delta P_f}{w_L}\right) \tag{86}$$

where A_T is the total cross-sectional area of the sample perpendicular to the liquid flow direction, Δx is the length of the sample, ρL and μL are the liquid density and viscosity, ΔP_f is the pressure drop across the length of the sample, and w_L is the liquid flow rate.

As mentioned in Section III D , K_1 is dependent on the geometry and dimensions of the passages in the wicking material.

At the low rates of liquid flow encountered in the vapor-chamber fin, Darcy's law[7] for laminar flow through porous media will apply, meaning that K_1 should be independent of the flow rate and liquid properties and therefore of liquid temperature.

The permeability investigations of Ginwala, Blatt, and Bilger[11] show that in their work K_1 is initially constant with time, but increases in magnitude after a certain amount of flow has passed through the wicking material. This phenomenon seems best explained by assuming that tiny gas bubbles are present in the liquid in the wick. If these bubbles stick in the matrix of the wicking material, they might decrease the effective flow area in the wick and increase K_1. The same thing could have been true if foreign particles were present in the liquid. The permeability apparatus described in the next section was designed to eliminate these problems.

B. Description of Permeability Apparatus and Test Specimens

Each test specimen of wicking material was 2 inches wide and 3 inches long in the flow direction. The porous material was approximately 0.1 inch in height and was bonded to a backup plate 0.025 inch thick made of the same material as the wick sample. Figure 66 shows a cross-section of a wick sample normal to the flow direction. The flow entrance and exit sections were cut by the electrochemical machining process (described in Section IV C) to prevent any wick material distortion.

A schematic drawing of the permeability apparatus is shown in Figure 67. The apparatus consisted of a closed loop fluid system with a mechanical pump which forced

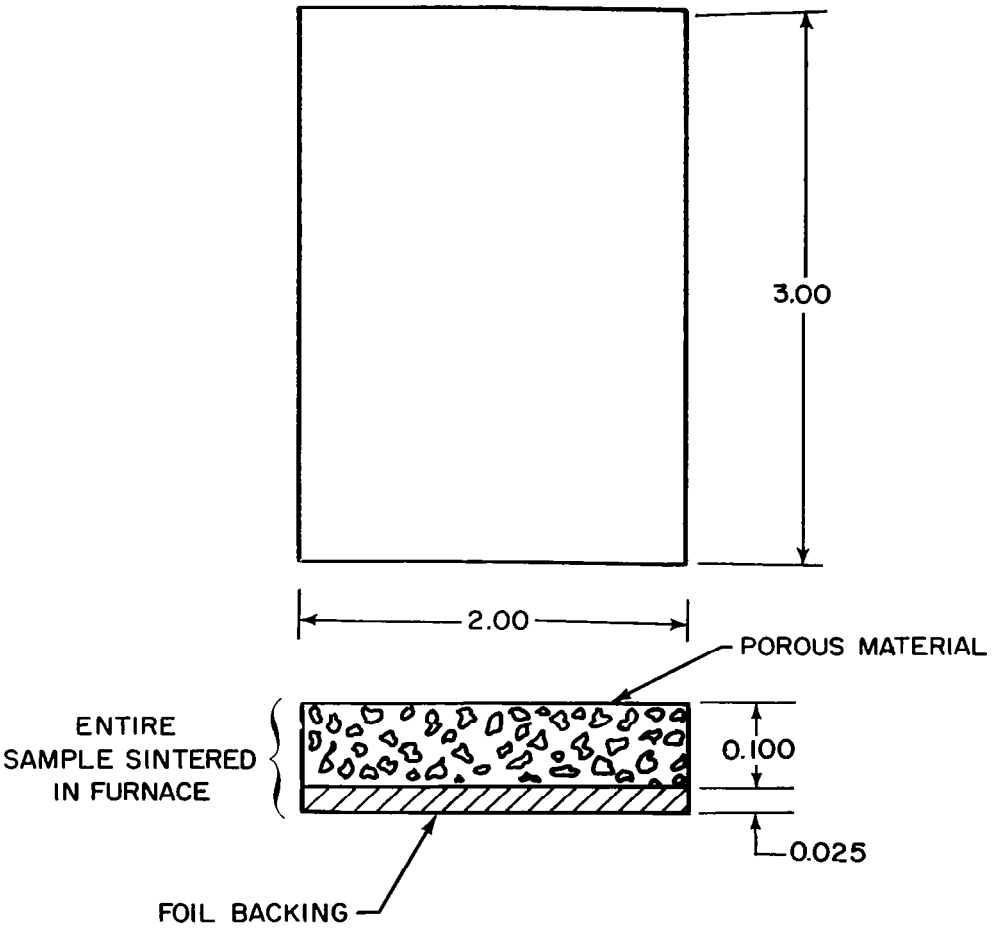

Figure 66 Dimensions of Permeability Samples

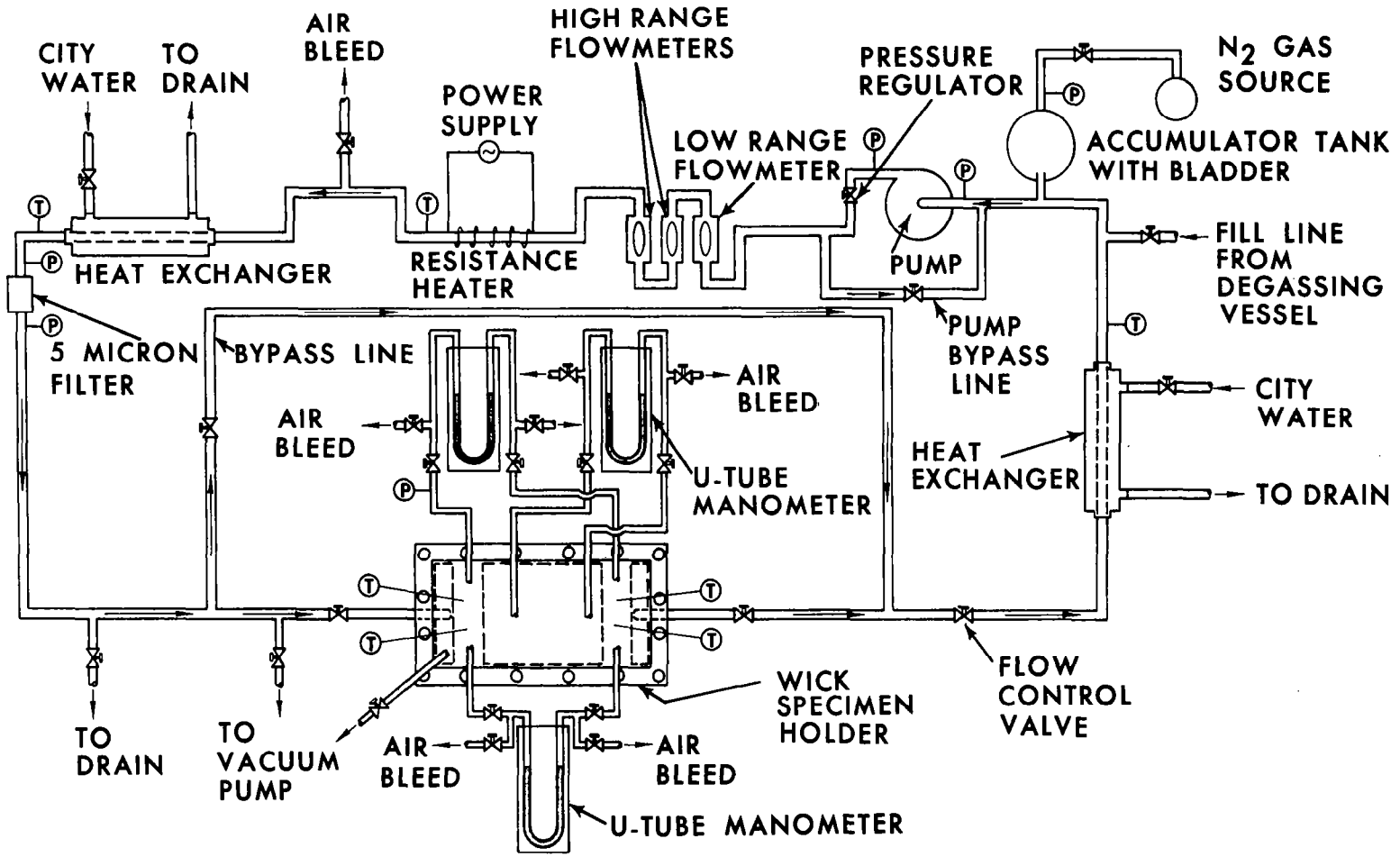

Figure 67 Schematic Diagram of Permeability Apparatus

a liquid through the wick. The wick was enclosed by gaskets in a sample holder so that the fluid flowed through the wick.

The tubing was 1/4 inch 316 stainless steel tubing, chosen for its corrosion-resistant properties. The valves used throughout the system were made of 316 stainless steel also. The filter was made of 316 stainless steel sintered powder metal and had a five-micron filter rating. The filter prevented microscopic foreign material from lodging in the wick test sample. The heaters and coolers used were constructed of stainless steel material to prevent corrosion in the system.

The accumulator tank was a standard 2 1/2-gallon high pressure hydropneumatic transfer barrier accumulator. During operation, the working fluid was only in contact with the Buta-N bladder or the stainless steel inserts and fittings associated with the bladder. Any desired pressure level could be set in the system, and yet a separation could be maintained between the pressurizing gas and the working fluid. This separation of the gas and liquid prevented the gas from dissolving in the liquid, thus maintaining a gas-free system.

The pump for the system was a sealless positive-displacement gear pump. This type of pump prevented leakage of air into the system and working fluid leakage from the system. The impeller gears were made of Teflon and the housing material of stainless steel. The drive between motor and pump was coupled magnetically through a solid wall.

Photographs and a sketch of the wick sample holder are shown in Figures 68, 69, and 70. The holder was constructed of 316 stainless steel and contained the necessary fittings for measuring the temperature of the working fluid and the pressure drop of the fluid through the wick. The system was designed to allow for wick holder removal while preventing the leakage of air into the system. Upon installation of the wick holder, the holder assembly could be evacuated to minimize the transfer of entrapped air in the holder to the working fluid. Gasket material of neoprene was used to prevent leakage of the fluid around the wick sample.

The manometers chosen for measuring the pressure drop through the wick sample were of the thirty-inch U-tube variety. Readings to the nearest 0.1 inch and estimates to the nearest 0.05 inch of fluid differential could be made. These manometers contained air bleeds in each leg for removal of entrapped gas in the lines. Manometer taps (see Figure 70) were located on the wick holder to obtain a pressure drop measurement within the wick, thus removing any entrance or exit effects. Two other manometers measured the pressure drop across the entire wick sample.

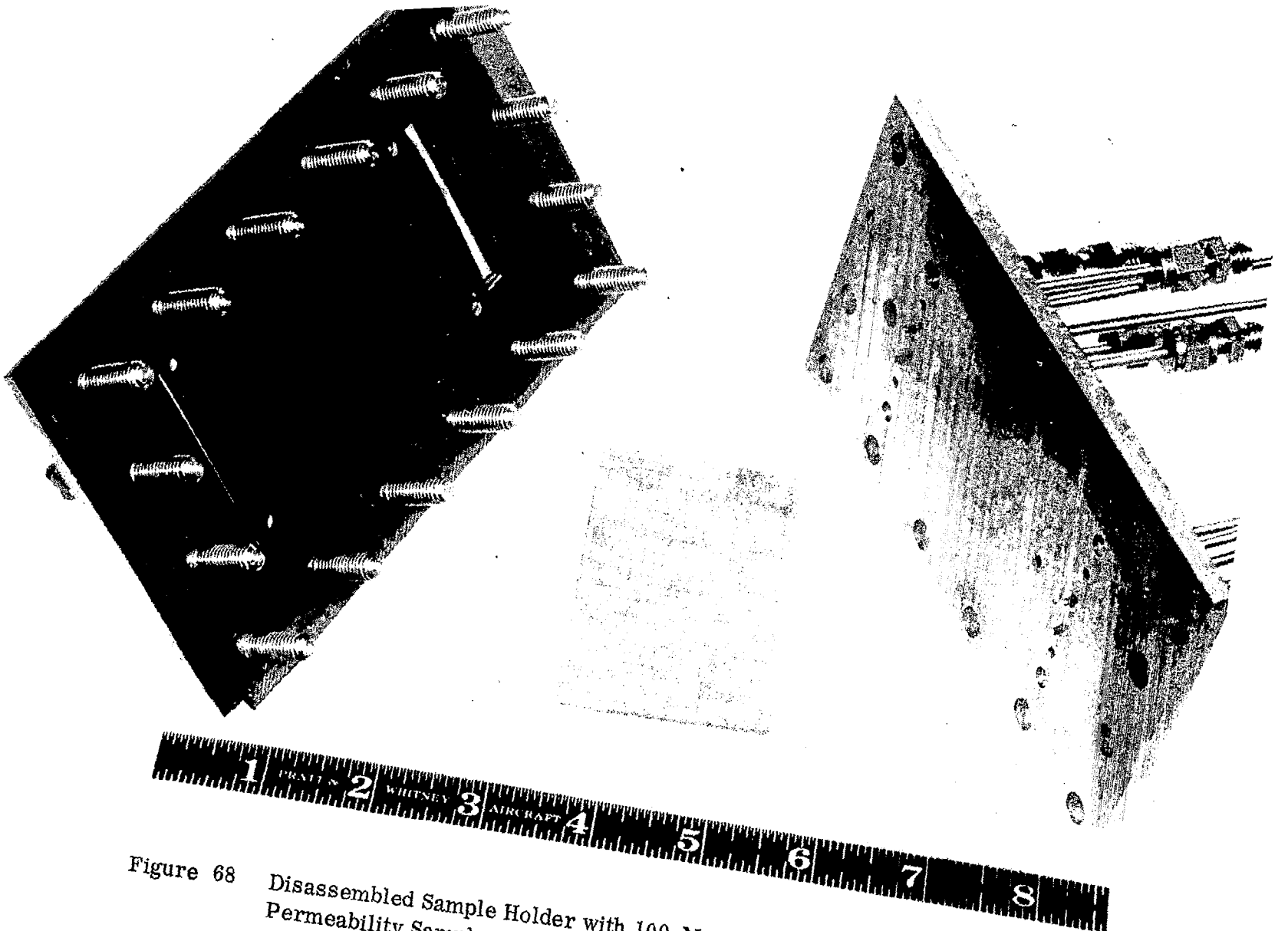

Figure 68 Disassembled Sample Holder with 100-Mesh Sintered Screen Permeability Sample M 8

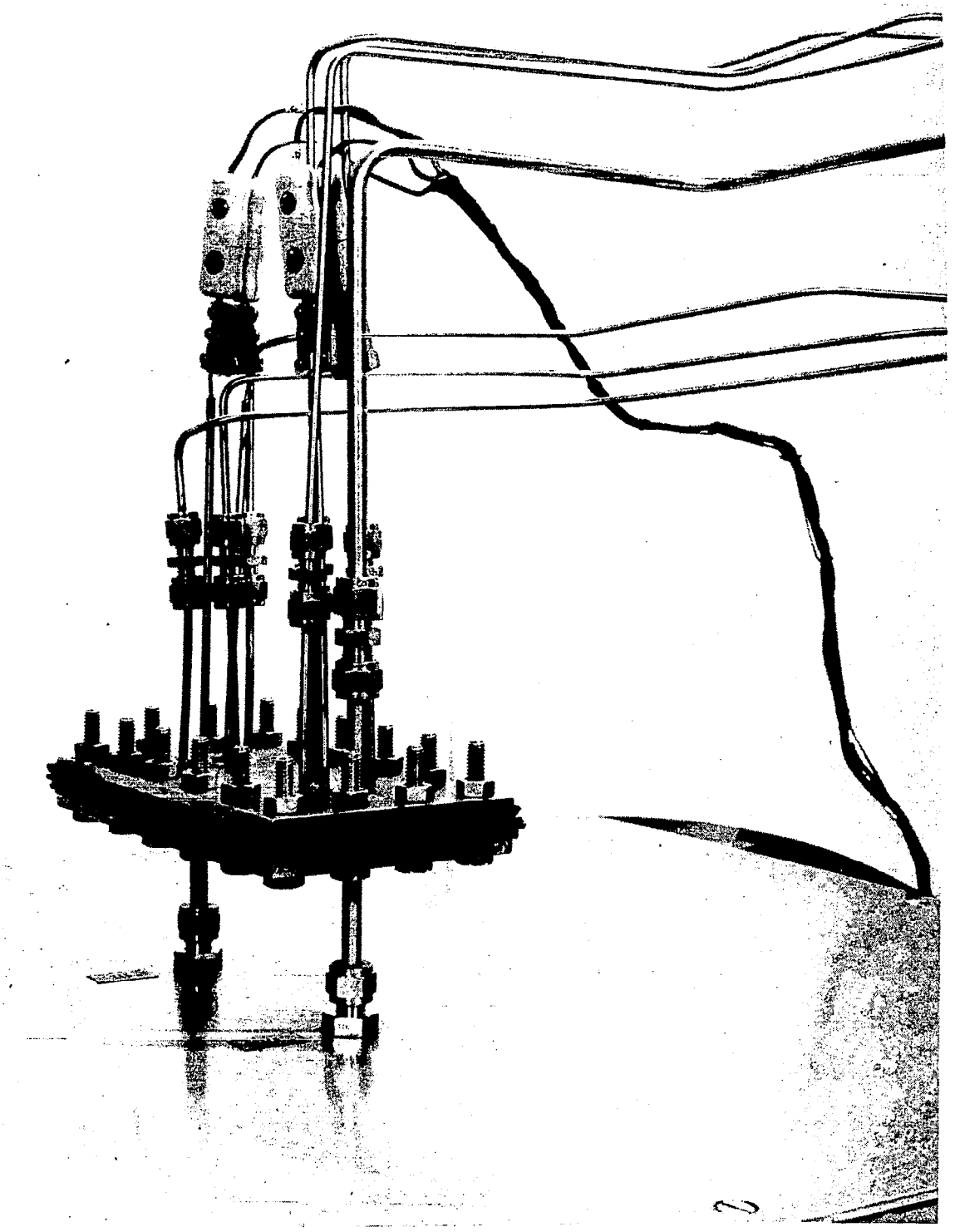

Figure 69 Sample Holder for Permeability Apparatus

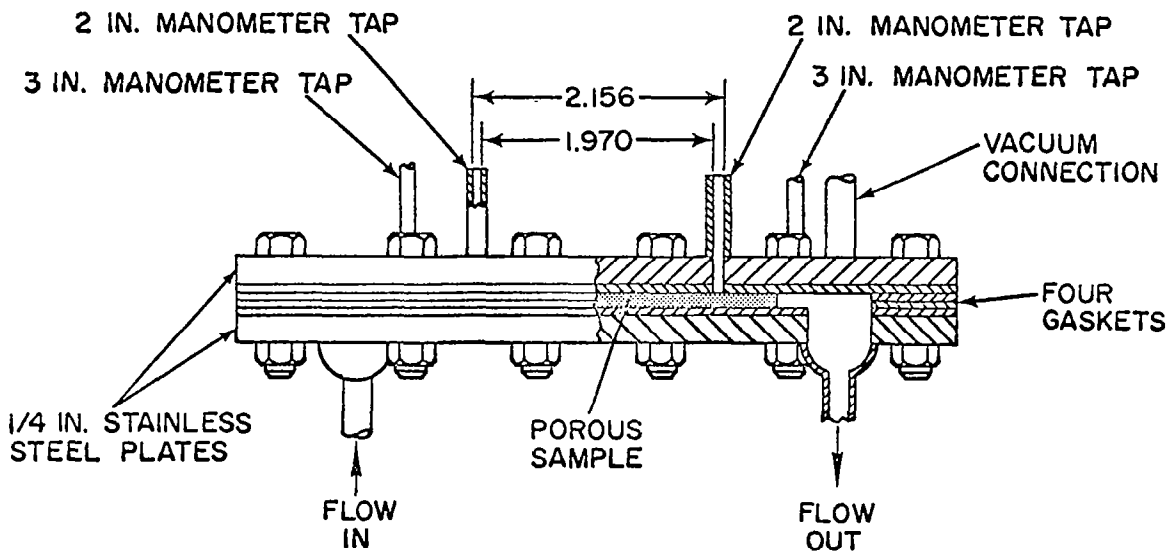

Figure 70 Sketch of Wick Permeability Sample Holder Showing Pressure Taps

Each manometer fluid was chosen both for its specific gravity and its immiscibility with the test liquid. When water was the test liquid, the manometer fluid used was acetylene tetrabromide (specific gravity 2.962 at 70°F) to measure the higher pressure drops, and diphosgene (specific gravity 1.6175 at 79°F) to measure the lower pressure drops. When Freon 113 (specific gravity 1.572 at 75°F) was used as the working fluid, two different solutions of thallium malonate-thallium formate (specific gravities 2.0151 and 3.6437 at 75°F) were used to cover the pressure-drop range.

The flowmeters chosen for flow measurement were Fisher-Porter Tri-Flat variable-area meters. Three meters were selected to cover the flow ranges. The ranges for these meters were 0.2 to 1.4 lb_m/hr, 0.5 to 15 lb_m/hr and 1.5 to 18 lb_m/hr for water; and 0.3 to 1.8 lb_m/hr, 1.0 to 18 lb_m/hr, and 2.0 to 25 lb_m/hr for Freon 113.

Temperature measurements were made with chromel-alumel thermocouples connected to a Honeywell Brown Electronik readout instrument. The accuracy of this system is estimated to be ±2°F. Pressure measurements were made using Bourdon-tube type gages with a maximum scale reading of 30 psig. Scales were in 0.2 psi increments and readings could be estimated to the nearest 0.1 psi. These gages had bleed ports for removal of entrapped gases in the lines. Experimental pressures were in the range of 3 to 15 psig.

Also included in the permeability apparatus was a means of ensuring that the working liquid was not saturated with gas. In preliminary tests, deaerating the liquid was done in the closed loop of the permeability apparatus by raising the liquid temperature with a resistance heater, causing the solubility of the liquid to decrease. The gas expelled from the liquid was collected and bled from a high point of the apparatus. The liquid was then cooled to ambient temperature, and was in a partially deaerated state.

Previous experimenters found that K_1 increased with time for a fixed flow rate and theorized that air, previously absorbed in the liquid, became trapped in the wick as bubbles. The trapped air blocked some flow passages and increased both the pressure drop and the apparent friction factor K_1. With deaerated liquid, the tendency to form bubbles should be reduced. In order to determine the capabilities of the apparatus to provide values of K_1 independent of time, the preliminary tests were performed with water flowing through a stainless steel sintered fibrous metal wick. These tests indicated that during a run of 15-1/2 hours at a constant flow rate of 12.9 lb_m/hr, K_1 increased 25 per cent. Since other investigators[11] found that for water saturated with gas the flow through wicks was practically stopped during an endurance run, the deaerating method appeared to be an effective solution of the problem. However, this method of deaerating the liquid in the closed loop is limited in effectiveness because all of the fluid in the apparatus cannot be deaerated. The fluid in the pressure gage lines, U-tube lines, and the accumulator tank (see Figure 67) is not deaerated because it does not flow in the closed loop.

In an effort to make K_1 constant with time, an additional deaerating apparatus was made. This apparatus was separate from the permeability apparatus, and its purpose was to supply completely deaerated liquid for filling the permeability apparatus. This new apparatus was simply an air-tight vessel made from stainless steel and equipped to heat and boil about five gallons of liquid. Figure 71 shows the vessel in front of the permeability apparatus during filling. Although the filling procedure is explained in more detail below, the basic approach was as follows. The test liquid was put into the vessel and brought to a boil. The gas was expelled from the liquid due to the high temperature and bled from the vessel. This deaerated liquid was then passed into the evacuated permeability system. The degree of gas saturation of the water in the permeability apparatus after filling with liquid from this vessel was estimated to be less than 20 per cent.

Liquid treated in this way yielded no gas when it was passed through the deaerating section of the permeability system loop. Hence, a definite improvement in

decreasing the degree of gas saturation was made by the addition of the deaerating vessel. After filling the system with water from the new vessel, an endurance test run with the same sample and flow rate resulted in no increase of K_1 for a period of 25 hours. Thus the time-dependency of K_1 found by other investigators appears to have been due to the presence of dissolved gas in the test liquid.

C. Test Procedure for Permeability Apparatus

1. Filling of Permeability Apparatus

The following procedure describes the filling of the permeability apparatus using the deaerating vessel shown in Figure 71. Because the permeability accumulator tank holds about 2-1/2 gallons of liquid in reserve, this filling procedure was only necessary after five or six samples were tested.

1) The permeability apparatus was drained of any fluid. This involved taking the apparatus apart at several locations and draining low points.

2) Nitrogen gas was passed through the apparatus to evaporate any remaining fluid.

3) A vacuum pump was attached to the apparatus so that the entire system (without the wick holder) and the tubing connecting the apparatus to a closed liquid outlet valve on the deaerating vessel were evacuated to a pressure no greater than 1 mm of Hg.

4) The deaerating vessel was filled with the test liquid, and the liquid was then brought to its saturation temperature. During this heating process the valve at the top of the vessel was opened for expelling both gas, which was expelled from the test liquid, and test liquid, which drained out because of its expansion. Eventually only test fluid vapor came from the top valve on the vessel and a pressure could be built up in the vessel by closing the valve. A pressure between 2 and 5 psig was maintained by turning the heater on and off as a control.

5) With a pressure less than 1 mm of Hg in the permeability apparatus and a pressure of about 5 psig in the vessel, the liquid outlet valve on the vessel was opened to begin filling of the permeability system. During the process of filling, the evacuation was continued at the highest point of the apparatus. When the test fluid in liquid

Figure 71 Wick Permeability Apparatus with Degassing Equipment in Place

form appeared at the high point, the vacuum pump was disconnected from the apparatus. A half hour or more was required after initially opening the liquid valve to fill the apparatus. After the pressure of the apparatus became the same as the pressure in the vessel, the apparatus was valved off from the vessel. To fill the system with liquid usually required two-thirds of the contents of the vessel.

2. Wick Permeability Testing Procedure

The wick permeability testing procedure was as follows:

1) The permeability apparatus (except for the sample holder) was filled with deaerated liquid as described above.

2) Measurements of the wick dimensions necessary for evaluating K_1 were made.

3) The wick was cleaned using the same procedure as for the wicking rise samples (Section V C).

4) The wick and sample holder were assembled as shown in Figure 70.

5) The sample holder was filled with deaerated liquid from the rest of the permeability apparatus by evacuating the holder to at least 1 mm of Hg and then opening the inlet and outlet sample holder valves. The evacuation was discontinued when the holder was full of liquid.

6) The U-tubes were bled, using the positive pressure in the permeability apparatus.

7) The test program performed with the permeability apparatus included the evaluation of K_1 for 13 different wicks, evaluation of K_1 at various flow rates for 12 wicks, the evaluation of K_1 at various temperatures for three wicks, the evaluation of K_1 for long testing periods for two wicks, and the evaluation of K_1 using a different test fluid for four samples.

D. Test Results

The permeability results obtained with water on thirteen samples selected from those listed in Section IV A are presented in Table 10 and Figures 72 to 78 in terms of the wick friction factor K_1.

The porosity values listed in Table 10 for the samples tested may be slightly smaller than the porosity values given in Section IV for the respective samples. This is the result of a slight compressing of the softer permeability samples when being installed between the gaskets of the wick holder. A slight deflection of the gaskets on the top and bottom of the sample was necessary to prevent any leaks, and on the softer porous materials the pressure associated with the gasket deflection caused some compressing. The effect of compression has been accounted for in the porosity and permeability results presented in this section, by using the sample dimensions measured after each permeability test.

TABLE 10

Wick Friction Factor for Porous Material Samples

Test Fluid: Water

Sample No.	Porosity, %	Wick Friction Factor $K_1 \times 10^{-8}$, $1/ft^2$
H1	83.6	21.2
H2	81.4	27.6
H3	68.9	61.3
H6	86.9	30.2
H11	88.7	1.70
H12	80.7	4.75
H13	81.8	0.80
M2	64.5	3.4
M4	54.0	11.5
M6	69.6	3.1
M7	62.5	1.4
M8	58.5*	6.1
M10	65.1	12.0

* Significant amount of change in porosity due to compression

In the range of flow rates encountered in the vapor-chamber fin, Darcy's law [7] for flow through porous media applies, meaning that K_1 as given by Equation (86) should be independent of flow rate. Figures 72 to 75 show K_1 vs flow rate per unit area (i.e., the flow rate w_L divided by the cross-sectional area A_T) for different sintered screen samples, sintered powder samples, and sintered fiber samples. These figures demonstrate that for a certain range of flow rate per unit area, K_1 is independent of flow rate.

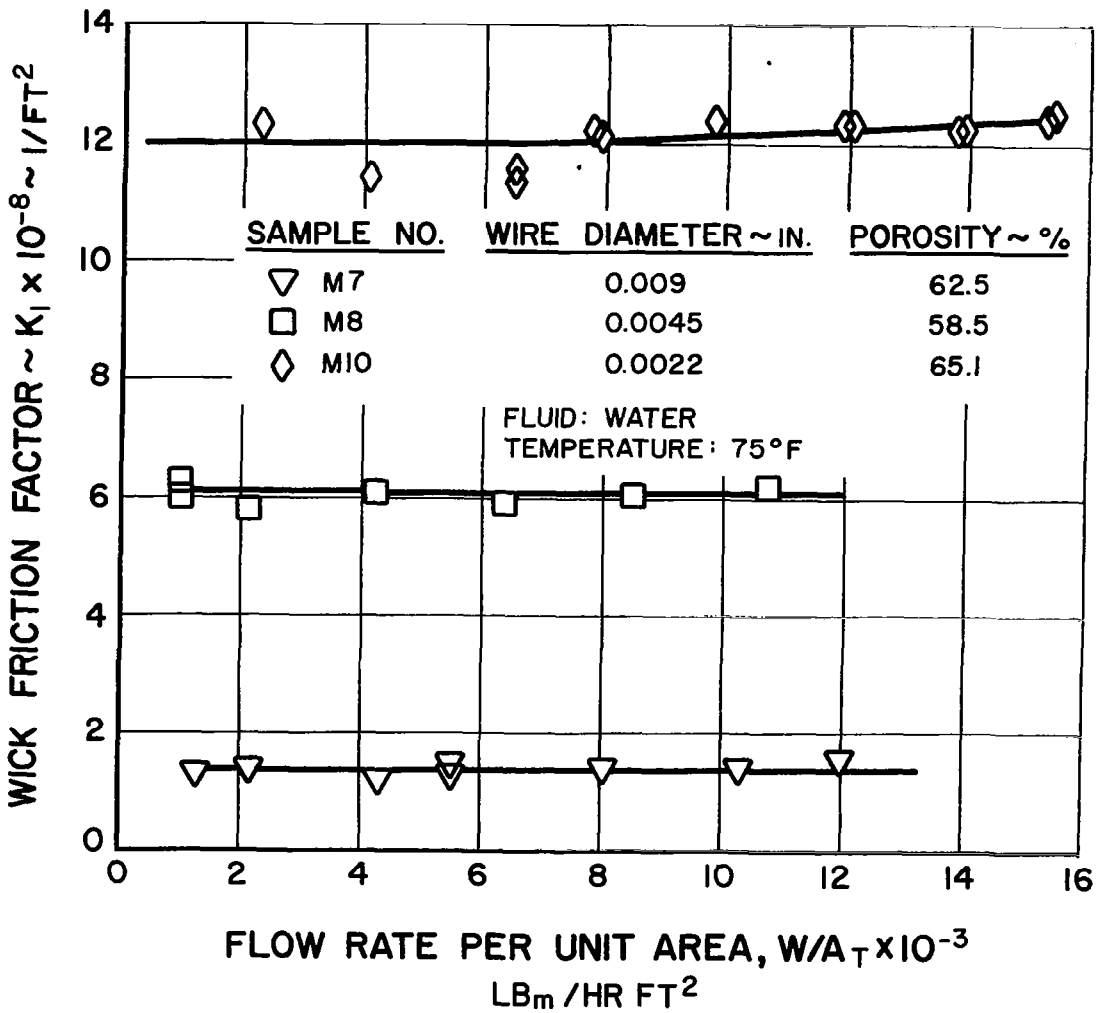

Figure 72 Wick Friction Factor vs Flow Rate per Unit Area for Sintered Nickel Screen Samples

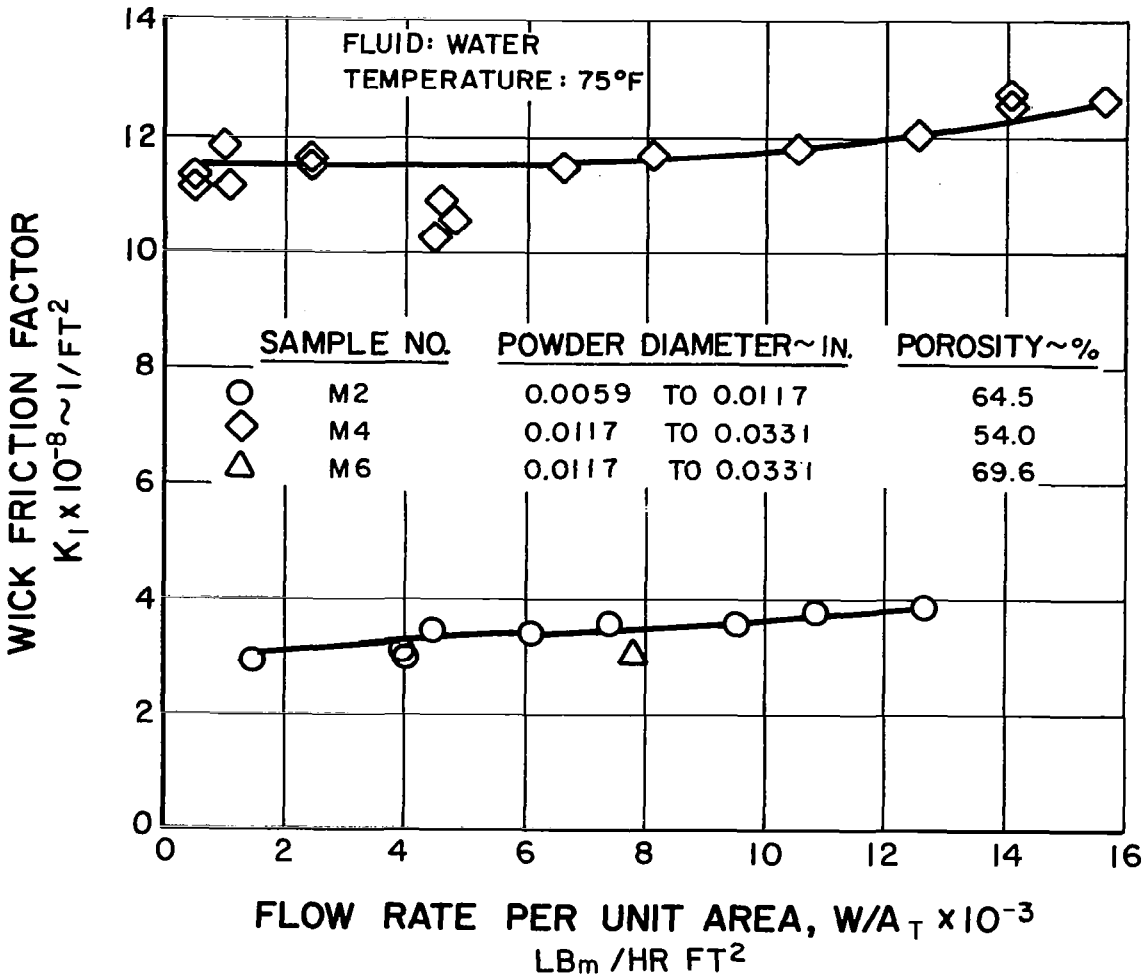

Figure 73 Wick Friction Factor vs Flow Rate per Unit Area for Sintered Nickel Powder Samples

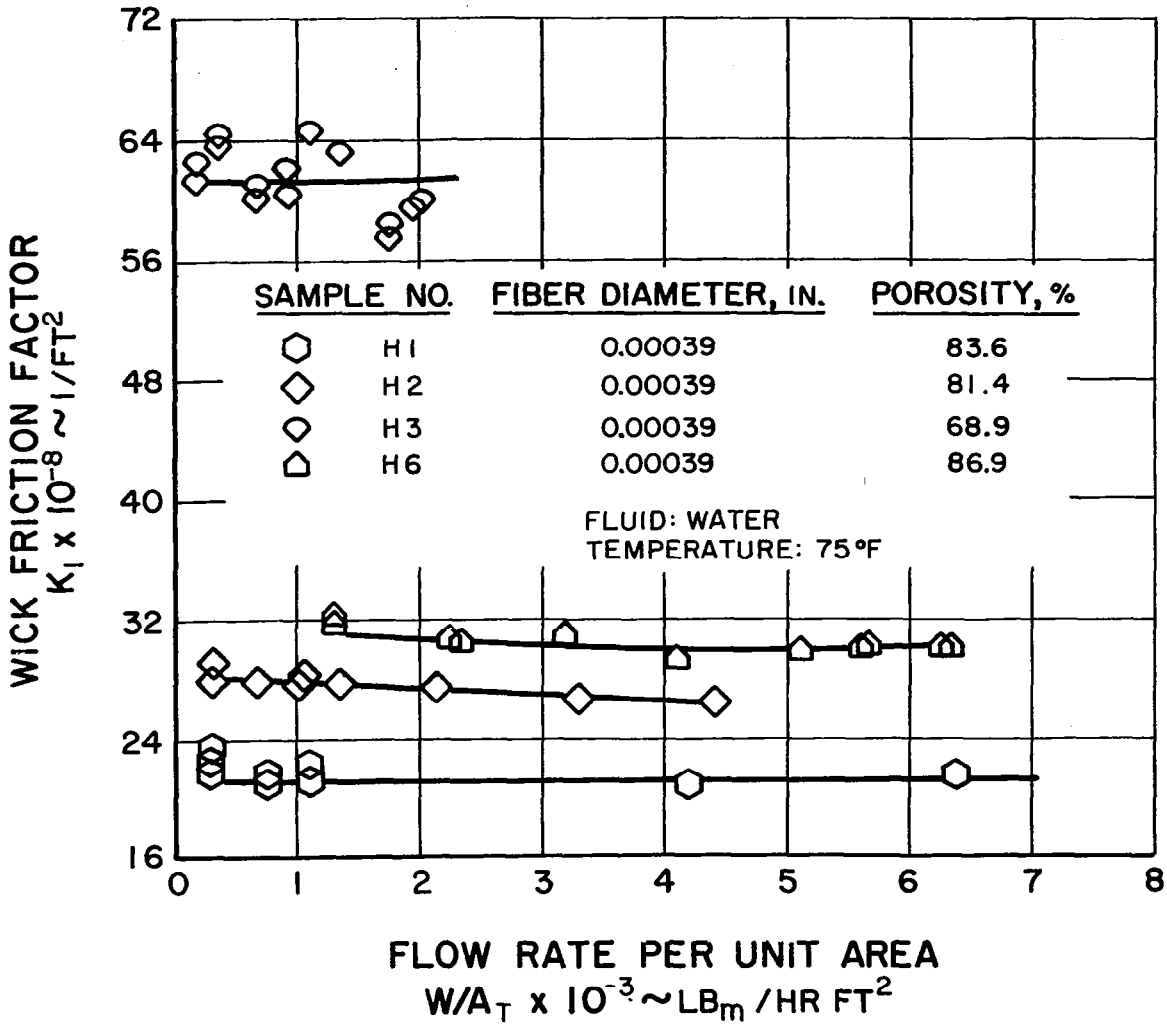

Figure 74 Wick Friction Factor vs Flow Rate per Unit Area for Sintered Nickel Fiber Samples

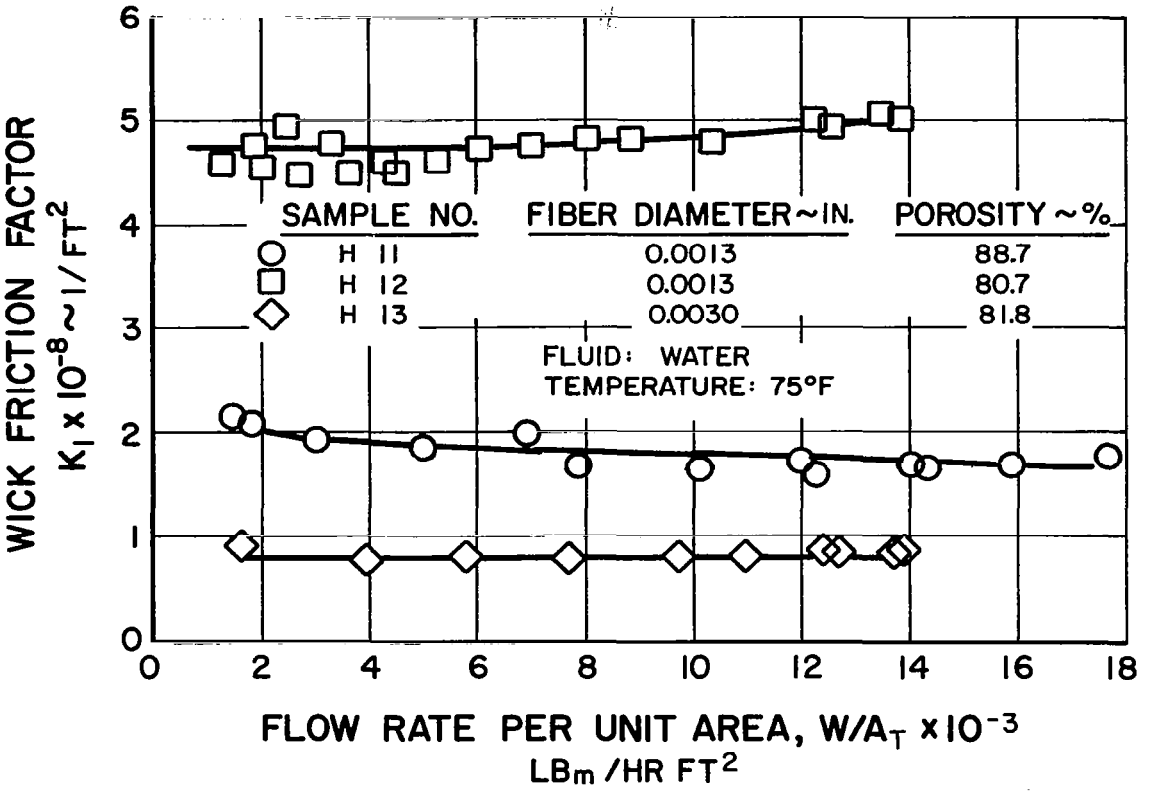

Figure 75 Wick Friction Factor vs Flow Rate per Unit Area for Sintered 430 Stainless Steel Fiber Samples

In interpreting these figures it should be noted that the points given at very low rates of flow per unit area become inaccurate for either or both of two reasons. First, the instrument for measuring flow rate for flow rates per unit area less than 1 x 10^3 $lb_m/hr\ ft^2$ (experimental flow of 1.4 $\frac{lb_m}{hr}$) becomes increasingly inaccurate as flow rate decreases. Second, the inaccuracy in measuring the pressure drop for samples with relatively low values of K_1 becomes greater at low flows because of the small pressure drops. These two reasons account for the scatter of points at the lower flow rates per unit area.

The data presented in Figure 72 for three sintered screen samples, demonstrates the independency of K_1 on flow rate over most of the range of flow rates per unit area tested. In Figure 73, in which data for sintered powder samples is presented, the value of K_1 for sample M4 remains constant from 1 x 10^3 to 9 x 10^3 $lb_m/hr\ ft^2$, but then K_1 increases slightly from 9 x 10^3 to 15 x 10^3 $lb_m/hr\ ft^2$. This increasing K_1 indicates that the Darcy flow regime has been exceeded. Within the Darcy flow regime friction is the only cause of pressure drop, but at higher flow rates inertia effects resulting in drag forces start to enter as a pressure drop component, causing K_1 to increase. This upward trend of K_1 at flow rates per unit area above 9 x 10^3 $lb_m/hr\ ft^2$ is also present in Sample M10 of Figure 72, Sample M2 of Figure 73, and Sample H12 of Figure 75. All of the samples tested over the flow rates per unit area of about 1 x 10^3 to 9 x 10^3 $lb_m/hr\ ft^2$ resulted in values of K_1 having very little or no dependency on flow rate.

Figure 76 is a plot of wick friction factor vs fluid temperature of several different samples for tests with water. In the temperature range of 75 to 160°F the friction factor remained constant while the liquid viscosity changed by a factor greater than two. This shows that, in the range tested, K_1 as given in Equation (86) is independent of the variation of fluid properties with temperature.

Figure 77 is a plot of wick friction factor versus time for wick Sample H12 with deareated water and M2 with aerated water. Over a test time of 84 hours there was no change in the value of K_1 for Sample H12 with deaerated water as the test fluid. Over a test time of 53 hours, the value of K_1 increased 18 per cent for Sample M2 with aerated water as the test fluid. This trend was experienced by other investigators[11] with test liquids which had not been deaerated. For all permeability test data presented previously in this report, deaerated test fluid was used. Thus, it is expected that the results presented are constant with respect to time.

Figure 78 is a plot of wick friction factor versus flow rate per unit area for four different samples with two different test fluids, water and Freon 113.

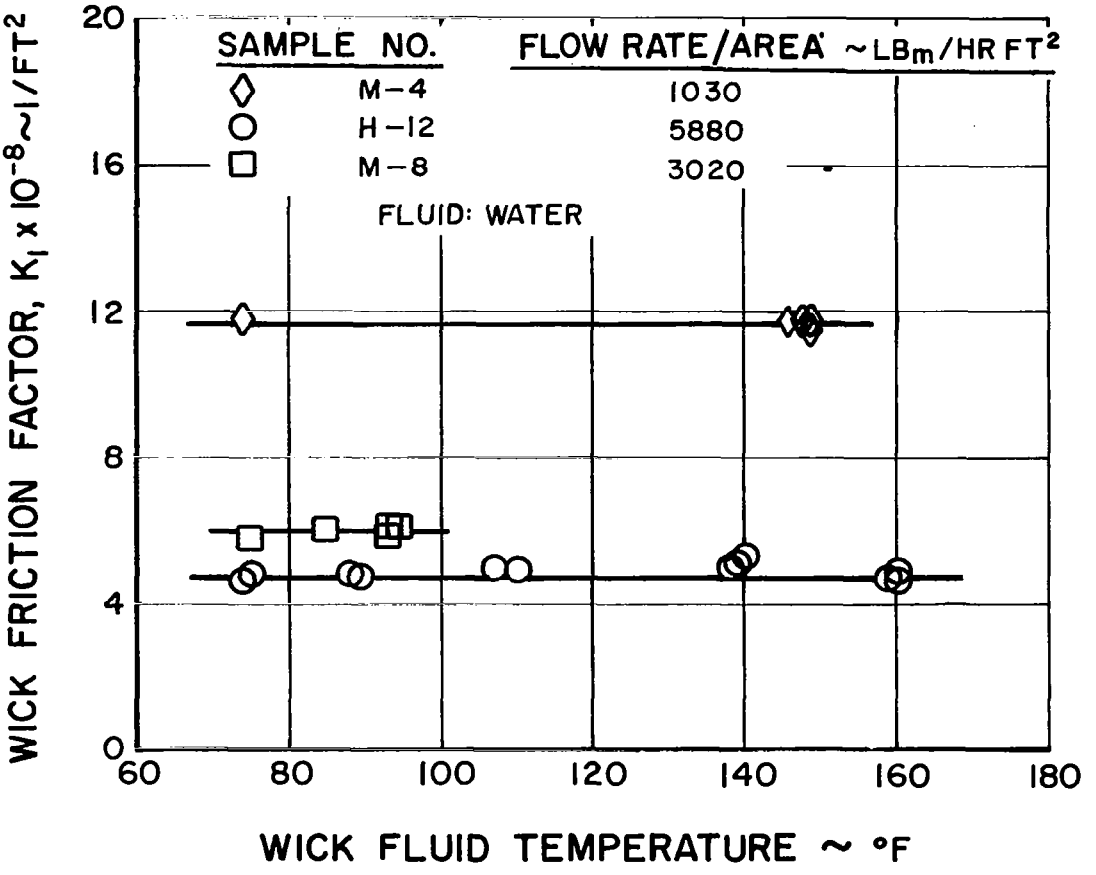

Figure 76 Wick Friction Factor vs Temperature for Sintered Metal Wicks

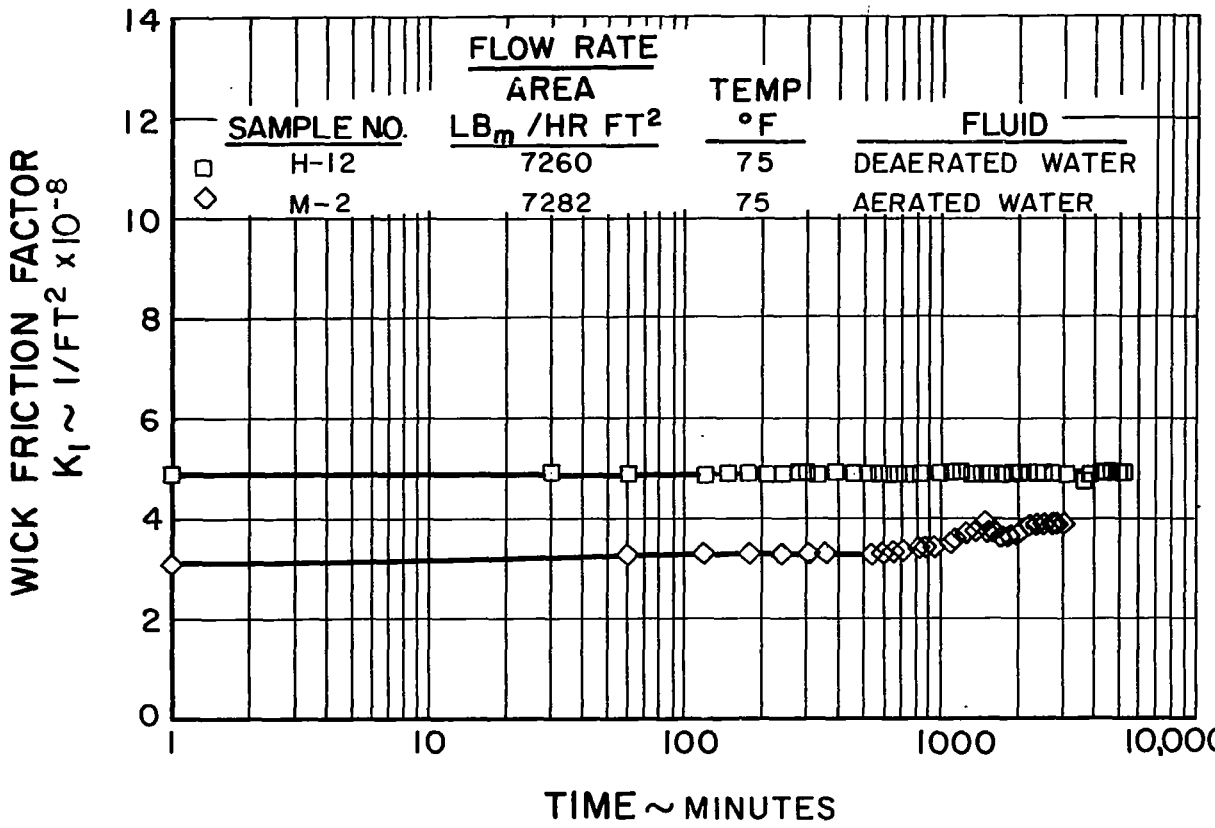

Figure 77 Permeability Duration Runs Using Aerated and Deaerated Water for Two Sintered Metal Wicks

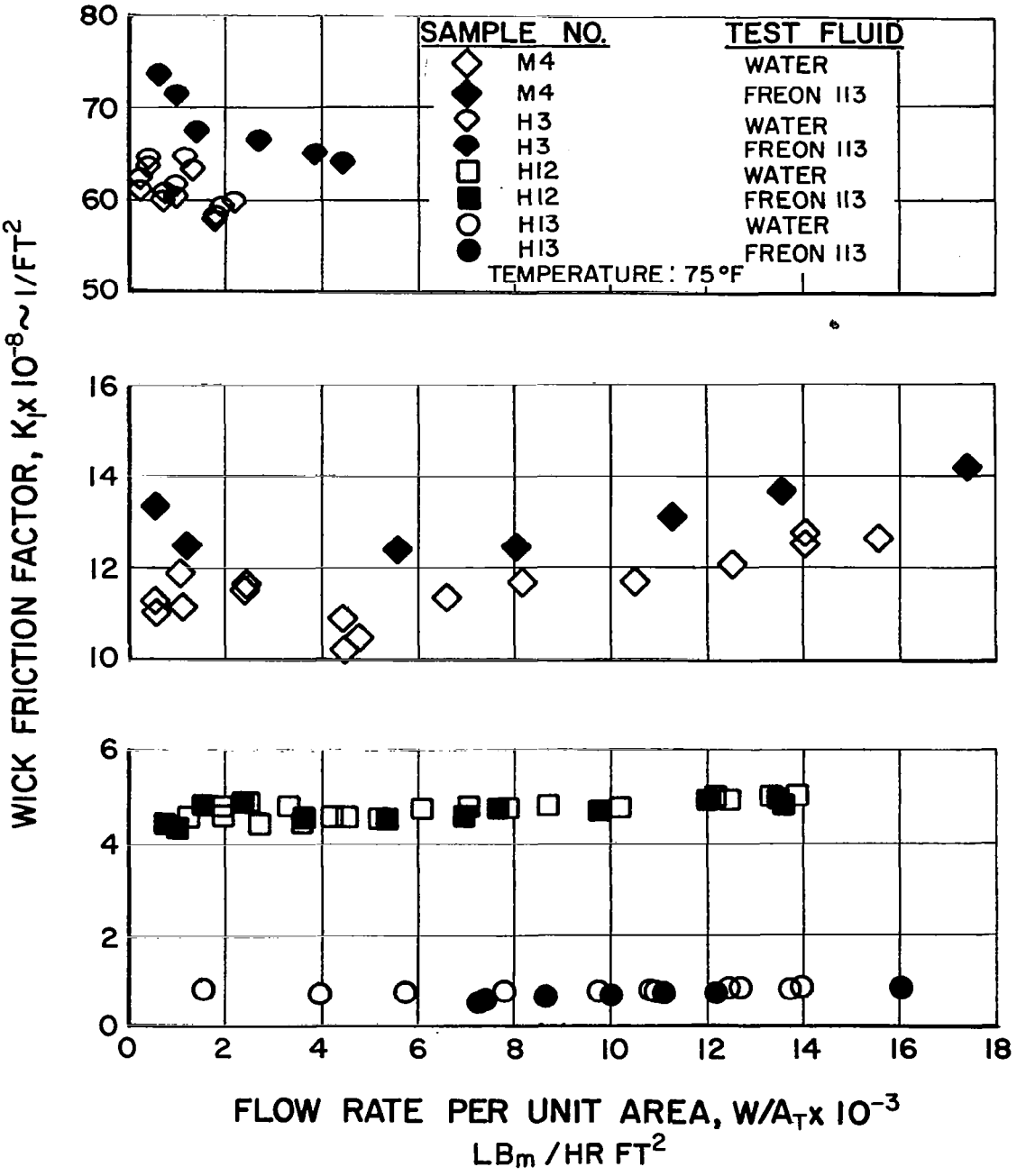

Figure 78 Wick Friction Factor vs Flow Rate per Unit Area with Test Fluids Water and Freon 113 for Sintered Metal Wicks

In general the variation of the Freon 113 data points from the average value of K_1 obtained from the water results was within the probable uncertainty discussed in the next section. Larger variations than expected occurred for only three Freon 113 data points on Sample H-13 in the Darcy flow regime. As Darcy's law implies, K_1 seems to be independent of the test fluid properties for flow within the Darcy flow regime.

E. Accuracy of Permeability Results

To determine K_1 as defined in Equation (86), pressure-drop data was taken for two lengths of each sample: the entire sample length of about three inches, and an internal length of about two inches. The nominal three-inch dimension of the sample was measured within ±1 per cent. However, the electrochemically-cut entrance and exit sections of the wicks were not always perpendicular to the nominal three-inch dimension, and for some samples an angle of 10 degrees from the perpendicular existed, caused by the cutting process. Because this discrepency might have caused a slight flow maldistribution at the sample entrance and exit, data from both lengths was compared in Figure 79, demonstrating a usual variation of less than ±3 per cent. The nominal two-inch dimension is fixed by the construction of the pressure taps in the sample wick holder, as shown in Figure 70. The actual measurement was 2.06 inches for the center-to-center distance.

The probable uncertainty of K_1 determined with water in the permeability apparatus is summarized in Table 11. The table includes the expected accuracy of all parameters used in calculating K_1 from Equation (86). All of the results of K_1 presented in this report were calculated using pressure drops measured from the two inner pressure taps, except where the pressure differential between these taps read below two inches of manometer fluid. For this latter case the pressure drops between the outer set of pressure taps (3 inches center-to-center distance) was used. The data from the inner set of pressure taps was preferentially used in comparing the different samples to eliminate end effects. From Table 11 the expected accuracy of K_1 presented in this report may be expressed by dividing the samples into two groups. For samples with $K_1 < 4.0 \times 10^8$ $1/ft^2$ the probable uncertainty of the K_1 results are within 9.8 per cent for flow rates per unit area above 4.4×10^3 $lb_m/hr\ ft^2$, and within 5.3 per cent for flow rates per unit area above 7.3×10^3 $lb_m/hr\ ft^2$. For the samples with $K_1 > 4.0 \times 10^8$ $1/ft^2$, the probable uncertainty of K_1 is within 9.8 per cent for flow rates per unit area above 1.4×10^3 $lb_m/hr\ ft^2$, and within 5.3 per cent for flow rates per unit area above 4.1×10^3 $lb_m/hr\ ft^2$. All experimental data obtained for water except one point was within the probable uncertainty range from the mean line through the data.

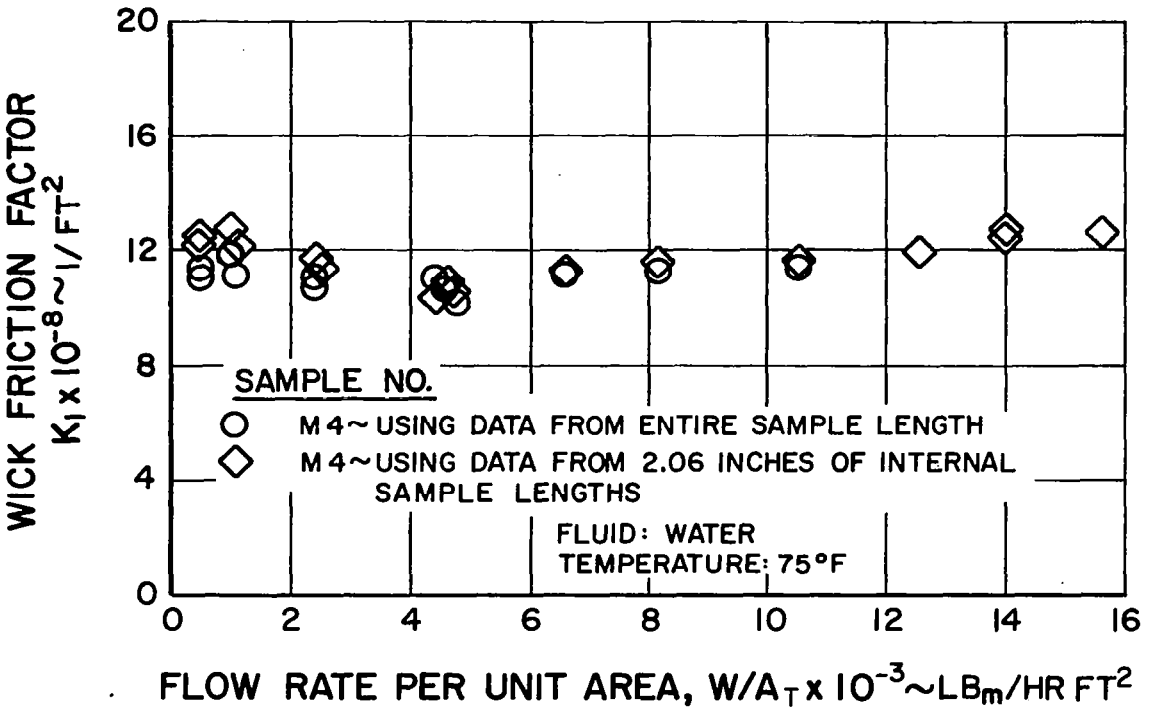

Figure 79 Wick Friction Factor for Sample M4 vs Flow Rate Using an Internal and External Sample Length

F. Summary

The wick friction factor K_1 of each of thirteen of the samples listed in Section IV was measured and was found to range from 0.80×10^8 $1/ft^2$ for a high-porosity sintered fiber sample to 61.3×10^8 $1/ft^2$ for a low-porosity sintered fiber sample.

The wick friction factor values were determined in a range of flow rates where K_1 was independent of the flow rate, i.e., in the Darcy flow regime.

The wick friction factor values were found to be independent of temperature.

The wick friction factor was found to be independent of time if the test fluid was deaerated. However, an increase of K_1 with time was found if the test fluid was aerated.

The value of K_1 appeared to be independent of the test fluid properties as determined from tests on samples using both water and Freon 113.

TABLE 11

Accuracy of Wick Friction Factor, K_1

Parameter or Dimension	Accuracy of 3-Inch Results			Accuracy of 2-Inch Results		
	Magnitude	Uncertainty	Per cent Uncertainty	Magnitude	Uncertainty	Per cent Uncertainty
density (H_2O at 75°F) lb_m/ft^3	62.2	$<\pm 0.1$	$<\pm 0.16\%$	62.2	$<\pm 0.1$	$<\pm 0.16\%$
viscosity (H_2O at 75°F) $lb_m/ft\ sec \times 10^3$	0.616	± 0.01	$\pm 1.78\%$	0.616	± 0.01	$\pm 1.78\%$
length, Δx inches	3.00[1]	± 0.020	$\pm 0.67\%$	2.060	$<\pm 0.01$	$<\pm 0.48\%$
cross-section area, A_c $(inches)^2$	0.20[1]	± 0.002	$\pm 1.00\%$	0.20[1]	± 0.002	$\pm 1.00\%$
flow rate	Flowmeter Reading					
flowmeter No. 1						
0.41 lb_m/hr	10.5	± 0.1	$\pm 1.68\%$[2]			
1.24 lb_m/hr	18.8	± 0.1	$\pm 2.25\%$[2]	Same As Accuracy of 3" Results		
flowmeter No. 2						
1.24 lb_m/hr	5.0	± 0.25	$\pm 7.24\%$[2]			
3.84 lb_m/hr	9.5	± 0.25	$\pm 3.81\%$[2]			
12.2 lb_m/hr	22.0	± 0.1	$\pm 1.15\%$[2]			
pressure drop	U-Tube Reading			U-Tube Reading		
0.056 psi	2.50"	± 0.05"	$\pm 2.00\%$	0.79"	± 0.05"	$\pm 6.32\%$
0.111 psi	5.00"	± 0.05"	$\pm 1.00\%$	1.57"	± 0.05"	$\pm 3.18\%$
0.666 psi	30.0"	± 0.05"	$<\pm 0.50\%$			

TABLE 11 (Cont'd)

Parameter or Dimension	Accuracy of 3-Inch Results			Accuracy of 2-Inch Results		
	Magnitude	Uncertainty	Percent Uncertainty	Magnitude	Uncertainty	Percent Uncertainty
pressure drop	U-Tube Reading					
0.666 psi	9.4"	±0.05	±0.53%	9.4"	±0.05"	±0.53%
2.12 psi	30.0"	±0.05	±0.50%	30.0"	±0.05"	±0.50%
wick friction factor, K_1						
for all flows from 0.41 lb_m/hr to 12.2 lb_m/hr and for ΔP of 0.056 psi to 2.12 psi			±7.75%[3]			±9.75%[3]
for flows 3.84 lb_m/hr and ΔP 0.111 psi			±4.26%[3]			±5.27%[3]

[1]The exact magnitude varied slightly in different samples

[2]These uncertainties take into account the instrument accuracy and the calibration error

[3]These uncertainties are obtained from the square root of the sum of the uncertainties squared for the parameters in Equation (86)

VII. DISCUSSION OF CAPILLARY PUMPING PARAMETER

A. The Capillary Pump

The porous material of a wick acts as a liquid pump because of the action of capillary forces. These forces are produced by the interaction of the liquid-vapor interface in the wick and the internal solid surface of the wick itself. Whenever the capillary forces bring about any movement of the liquid in the wick, frictional forces arise that oppose the liquid motion.

A capillary pump can be evaluated by calculating the maximum flow rate that it can achieve. This was essentially done in deriving the analytical model of the vapor-chamber fin in Section III. However, to eliminate the complication of mass addition along the length of the wick, the following capillary pump model will be considered to illustrate what this output depends upon.

Shown in Figure 80 is a rectangular piece of wicking material acting as a capillary pump. The material has a total flow area of A_T and a flow length of Δx.

At the front face, a wetting liquid is being evaporated at such a rate that the wicking material is providing a maximum flow. If this is true, then the pres-

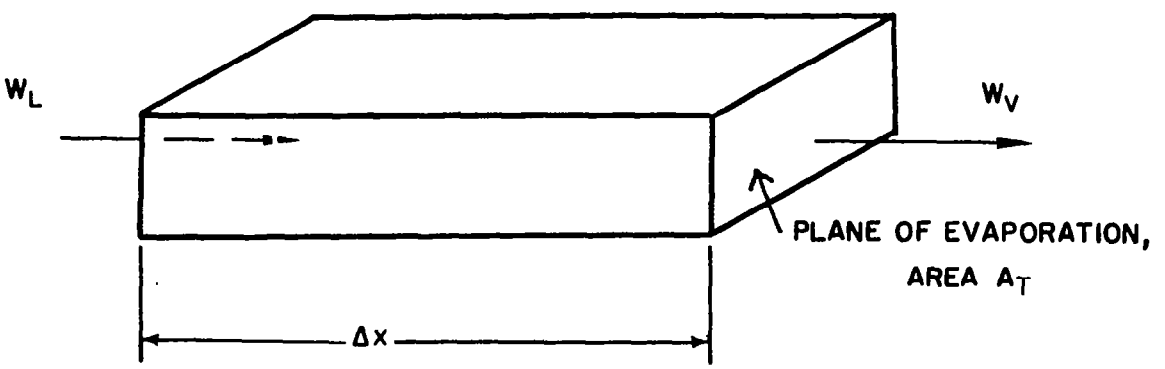

Figure 80 Model of a Capillary Pump

sure drop $(\Delta P)_\sigma$ across the liquid-vapor interface at the plane of evaporation is given by the Laplace-Young equation

$$(\Delta P)_\sigma = \frac{2\sigma}{R_{min}} \tag{87}$$

where σ is the fluid surface tension and R_{min} is the minimum radius of curvature of the liquid-vapor interface that the wick can support. It has been assumed that the menisci are segments of the surface of a sphere. The pore radii producing the curvature in Equation (87) will be equal to R_{min} only if the contact angle is zero.

The pressure drop given in Equation (87) must be balanced by the frictional pressure drop caused by the flow of liquid through the wick, so that

$$(\Delta P)_\sigma = (\Delta P)_f \tag{88}$$

Combining Equation (88) with Equation (87) and the definition of the wick friction factor, Equation (25), yields an expression for $(w_L)_{max}$, the maximum flow rate that the capillary pump pictured in Figure 84 can produce, or

$$(w_L)_{max} = \left(\frac{2\rho_L \sigma}{\mu_L}\right)\left(\frac{A_c}{\Delta x}\right)\left(\frac{1}{K_1 R_{min}}\right) \tag{89}$$

where K_1, the wick friction factor, is a constant for flow in the Darcy regime. Thus, given a wick size and a fluid, the maximum output of the capillary pump depends on the parameter

$$\frac{1}{K_1 R_{min}} \tag{90}$$

As discussed in Section III D, K_1 is dependent only on the pore geometry in the wick. However R_{min} is a function of the pore geometry in the wick, the wick material, and the liquid. The parameter in (90) shows that any evaluation of a capillary pump must include both a consideration of the liquid and the wick itself.

In Section V it was shown that R_{min} for a given wick could be determined from

$$R_{min} = \frac{2 g_o \sigma}{\rho_L g \ell_m} \tag{91}$$

where ℓ_m is the maximum height to which a liquid will rise in a vertical sample of the wick when exposed to a gravity field, g.

By combining Equations (91) and (89) the maximum capillary pump output is given by

$$(w_L)_{max} = \left(\frac{\rho_L \sigma}{\mu_L}\right)\left(\frac{g \rho_L}{g_o \sigma}\right)_{WR} \left(\frac{A_T}{\Delta x}\right)\left(\frac{\ell_m}{K_1}\right) \tag{92}$$

where the subscript WR refers to the conditions under which ℓ_m was determined. Equation (92) can be used to express the amount of energy "pumped" by multiplying both sides by the latent heat of vaporization.

Hereafter, the term ℓ_m/K_1 will be referred to as the capillary pumping parameter. It should be emphasized that this parameter is a function of the liquid, the wick geometry, and the wick material. Equation (92) shows that ℓ_m/K_1 is a significant parameter for comparing the pumping capabilities of various wicking materials of the same size with the same liquid.

B. Experimental Capillary Pumping Parameter Results

Values of the capillary pumping parameter for both water and Freon 113 are listed in Table 12. Also tabulated are values of porosity, wick friction factor, and equilibrium heights taken from the experimental data in Sections IV, V, and VI.

From Table 12 it can be seen that the capillary pumping parameter for Freon 113 is lower than that of water for each sample tested.

Although K_1 is independent of liquid properties, ℓ_m is not. Values of ℓ_m with Freon are lower than those with water for a given sample, for the reasons given in Section V D , which results in lower values of ℓ_m/K_1.

The values of ℓ_m/K_1 in Table 12 show that sintered fiber samples form the best capillary pumps, followed by sintered powder samples. The sintered screen samples demonstrated the lowest potential as capillary pumps.

TABLE 12

Capillary Pumping Parameter

Sample No.	Type	Porosity, %	$(\ell_m)_w$, inches	$(\ell_m)_f$, inches	K_1, $1/ft^2$	$(\ell_m/K_1)_w$, ft^3	$(\ell_m/K_1)_f$, ft^3
M1	powder	59.7	9.9	2.4	-	-	-
M2	"	65.8	9.7	-	3.40×10^{8}	2.38×10^{-9}	-
M3	"	47.7	>15.9*	-	-	-	-
M4	"	54.0	>16.0*	>7.0	11.5 "	> 1.16 "	$> 0.508 \times 10^{-9}$
M5	"	69.1	8.4	-	-	-	-
M6	"	69.6	6.90	2.0	3.10 "	1.85 "	0.543 "
M7	screen	62.5	1.9	-	1.40 "	1.14 "	-
M8	"	67.9	> 4.4	-	6.10 " **	> 0.604 " **	-
M9	"	67.8	6.9	-	-	-	-
M10	"	67.6	9.2	-	12.0 "	0.640 "	-
H1	fiber	86.8	>15.9*	4.2	21.2 "	> 0.625 "	0.165 "
H2	"	82.5	>16.1*	4.9	27.6 "	> 0.486 "	0.148 "
H3	"	68.9	>16.1*	8.2	61.3 "	> 0.219 "	0.112 "
H4	"	62.8	>16.0*	-	-	-	-
H5	"	91.8	-	-	-	-	-
H6	"	88.0	>16.0*	3.6	30.2 "	> 0.442 "	0.099 "
H7	"	82.0	>16.0*	-	-	-	-
H8	"	82.8	>15.2*	-	-	-	-
H9	"	62.6	>16.4*	-	-	-	-
H10	"	70.9	>16.2*	-	-	-	-
H11	"	91.6	6.1	-	1.70 "	2.99 "	-
H12	"	80.8	9.0	-	4.75 "	1.58 "	-
H13	"	82.2	5.3	-	0.80 "	5.54 "	-

* Indicates that water wicked to top of sample used in wicking-rise test

** Values may have been significantly affected by the sample being compressed during permeability test (see Table 10)

Also shown by the tabulation of the capillary pumping parameter in Table 12, is that Sample H13, having the largest value of ℓ_m/K_1, would serve as the best capillary pump, followed by H11 and M2. The table indicates that a good capillary pump cannot be chosen on the basis of wicking ability alone, for consideration of frictional forces is equally important. For example, the best material, H13, has one of the lowest values of ℓ_m for water, but it also has by far the lowest value of K_1.

The values of porosity listed in Table 12 are the same as those listed in Table 4 and not those listed in Table 10. The difference between the two tables of porosity is due to the fact that some samples were compressed while being installed in the permeability rig, thus resulting in the slightly lower values listed in Table 10.

C. Effects of Gravity on Capillary Pumping

It should be noted that, although ℓ_m/K_1 is a measure of capillary pump output, it does not include the effect of gravity or head. If an application involves a condition in which a capillary pump must work against gravity, consideration must be given to both the value of ℓ_m/K_1 and ℓ_m itself. For instance if a capillary pump material is to be used in a situation where liquid must be transported by the material over a vertical distance of 10 inches, a material must be chosen that has a value of ℓ_m greater than 10 inches, as well as a high value of ℓ_m/K_1.

This separate consideration of ℓ_m in a gravity situation cannot be neglected in the case of the vapor-chamber fin. In the analysis of the one-dimensional model of the vapor chamber fin in Section III, it was shown that the maximum total rate of heat rejection can be obtained from the following equation

$$Q_{max} = \left(\frac{2\rho_L h_{VL}\sigma}{\mu_L}\right)\left(\frac{\delta b}{x_m}\right)\left(\frac{g\rho_L}{g_o\sigma}\right)_{WR}\left(\frac{\ell_m}{K_1}\right) \qquad (93)$$

where gravity is neglected.

If Equation (93) is modified to include the effect on the liquid in the wick as it flows against gravity, Q_{max} is given by

$$Q_{max} = \left(\frac{2\rho_L h_{VL}\sigma}{\mu_L}\right)\left(\frac{\delta b}{x_m}\right)\left(\frac{g\rho_L}{g_o\sigma}\right)_{WR}\left(\frac{\ell_m}{K_1}\right) - 2\sin\theta\left(\frac{h_{VL}\rho_L^2}{\mu_L}\right)(\delta b)\left(\frac{\ell_m}{K_1}\right)\left(\frac{1}{\ell_m}\right) \qquad (94)$$

where θ is the angle at which the fin is inclined. Equation (94) shows that, for

a given fluid and fin size, to maximize the value of Q_{max} for $\sin\theta > 0$, a wicking material must be chosen on the basis of a large value of ℓ_m/K_1 and also a large value of ℓ_m. However, large values of both of these qualities do not occur simultaneously in any of the samples studied. As the experimentally determined values in Table 12 show, a high value of ℓ_m/K_1 seems to imply a low value of ℓ_m. This might be expected since a porous material that has a large pore size will be characterized by low capillary forces (small value of ℓ_m), but a large pore size is indicative of low frictional forces for a given flow rate (small value of K_1), all of which results in a large value of ℓ_m/K_1 but a low value of ℓ_m. Section VII D contains a more detailed discussion of the effect of pore size on the capillary pumping parameter.

D. Capillary Pump Pore Sizes

Some idea of the structure of the porous materials can be obtained by comparing the pore size distribution, wick rise and permeability data.

The most direct way to get the pore size or sizes of a given capillary material would be by direct measurement. Such a process is obviously not feasible and would result in data difficult to interpret, so that some indirect method of measuring the pore sizes in a material must be used.

The mercury intrusion method of measuring pore size was discussed in Section IV. Pore diameters were shown to be given by the equation

$$D = \frac{4\ \sigma\ \cos\phi}{P} \tag{95}$$

where

- D = diameter of pore
- P = pressure required to force mercury into a pore of diameter D
- σ = surface tension of mercury
- ϕ = contact angle between mercury and the wick matrix material

The median pore diameter, D_{med}, was then defined as the pore size at which 50 per cent of the connected pore space is filled with mercury. Values of D_{med} taken from experimental data of Section IV are listed in Table 13.

An equivalent pore diameter, D_K, can be calculated from the wick friction data presented in Section VI. For a given flow rate of liquid through the wicking material, the resulting pressure drop ΔP over a given sample length Δx can be expressed in terms of the Poiseuille equation for flow in a tube, to get

$$\frac{\Delta P}{\Delta x} = \frac{32\,\mu_L\,u_L}{D_K^{\,2}} \tag{96}$$

where μ_L is the liquid viscosity, u_L is the average liquid flow velocity through the pores of the material and D_K is the equivalent diameter defined by this equation. As defined here, D_K is a variable that contains the effects of tortuosity, interconnectiveness of the pores, and an average pore shape factor and size.

The above expression can be combined with Equation (86) and the continuity equation to obtain

$$D_K = \left(\frac{32}{F_{AR} K_1} \right)^{1/2} \tag{97}$$

where K_1 is the wick friction factor, defined by Equation (25). The free flow area ratio, F_{AR}, is given by Equation (72). In effect, Equation (97) represents the porous material as a bundle of straight parallel tubes of equal size.

The values of D_K listed in Table 13 are based on values of K_1 from the mean line through data taken using water as the test fluid. These values show that the actual numerical agreement between D_K and D_{med} is reasonably good at least for the fibrous wicks. This is somewhat surprising, for the two methods are physically quite different, one using frictional data and the other surface-effect data. While each method should be consistent within itself, it would not be expected that values of pore size calculated by the two methods would agree so closely. This correspondence may mean that in the flow region in which K_1 was determined, the effects of tortuosity, interconnectiveness of the pores, and the pore shape factor combine in such a way that the assumption of straight parallet equal-sized tubes made for Equation (97) is an acceptable simplification.

Also listed in Table 13 is the equivalent capillary pore diameter computed from the wicking data of Section V, using the equation for capillary rise in a tube of diameter D_C, with a contact angle of zero degrees

$$D_C = \frac{4\,g_o\,\sigma}{\rho_L\,g\,\ell_m} \tag{98}$$

TABLE 13

Effective Pore Sizes

Sample No.	Type	Measured Median Pore Diameter, D_{med}	Equivalent Frictional Pore Diameter, D_K	Equivalent Capillary Pore Diameter, D_C	
		microns	microns	Water microns	Freon microns
M1	Powder	-	-	117	81
M2	Powder	>70	116	120	-
M3	Powder	-	-	< 73	-
M4	Powder	~80	69.2	< 73	<28
M5	Powder	-	-	138	-
M6	Powder	>80	117	168	96
M7	Screen	-	184	609	-
M8	Screen	>100	91.3*	< 263	-
M9	Screen	-	-	169	-
M10	Screen	~50	61.7	126	-
H1	Fiber	43.8	41.0	< 73	46
H2	Fiber	35.0	36.4	< 72	40
H3	Fiber	26.5	26.5	< 72	23
H4	Fiber	-	-	< 73	-
H5	Fiber	-	-	-	-
H6	Fiber	40.7	33.6	< 73	54
H7	Fiber	-	-	< 73	-
H8	Fiber	-	-	< 77	-
H9	Fiber	-	-	< 71	-
H10	Fiber	-	-	< 72	-
H11	Fiber	>80	140	190	-
H12	Fiber	>70	88.1	129	-
H13	Fiber	>80	213	219	-

* Value may have been significantly affected by the sample being compressed during permeability test (see Table 10)

where ℓ_m is the equilibrium height to which the liquid (water or Freon 113) will rise in a vertical sample.

The discrepancy between the values of D_C for water and Freon 113 for a given sample can be explained by assuming that the contact angles for each liquid were different. Table 8 gives estimates of the water contact angle assuming the contact angle for all Freon 113 tests was equal to zero degrees.

The agreement between the values D_C and the values of D_{med} and D_K in Table 13 is reasonably good except in the case of the screen Samples, M7, M8, M10, powder Sample M4, and fiber Samples H6 and H12. This is curious since it would be expected that for a given material, D_C would be smaller than D_{med}. The latter is a measure of the most populous pore size, while D_C is calculated from the equilibrium height, ℓ_m, which should be a measure of some smaller pore size in the wicking material.

The agreement between these three diameters is particularly good for the fiber samples. It appears from this agreement for these samples that the actual liquid levels recorded in the wicking tests were characterized by a pore size close to D_{med}. If the smaller pores in the wick are considered to be interconnected only by median-size pores, the value of ℓ_m would be expected to depend on the median pore size rather than some smaller size since, during a wick rise test, liquid would be unable to bridge the median pores to reach smaller pores. Such a situation would result in equilibrium heights characterized by D_{med}. Figure 81 is a plot showing the percent variation of D_C from D_K for the wicks tested. This plot shows that, except for the screen samples, D_C was within ± 60 per cent of D_K for both the water and Freon 113 results. Also, D_K was found to be close to D_{med} for the two groups of powder and fiber samples. The large difference between D_C and D_K for the screen samples might be caused by one or both of two factors: 1) D_K may be much smaller than D_C because of a large tortuosity for liquid flow in the wick, or 2) a regular occurrence of large pores in all of the flow passages of the screens due to the stacking of the screen layers might prevent the liquid from rising in a wicking rise test as high as it would in a more homogeneous porous material. The resulting value of D_C may be larger than D_K. The smaller discrepancies of D_C and D_K for fiber and powder samples might be caused by three similar factors: 1) D_K may be smaller than D_C because of the tortuosity for liquid flow in the wick, 2) D_C may be smaller than D_K because smaller pores may be more important in wick rise tests, or 3) D_C may be larger than D_K because of a nonhomogeneous distribution of large pores preventing the liquid in the wicking rise tests from rising as high as it would in an homogeneous material.

Figure 82 shows a plot of ℓ_m/K_1 vs D_K for samples tested in water with porosity as a parameter. This plot is intended to show that, in a very general way, ℓ_m/K_1 seems to increase with pore size for the samples tested.

An explanation of the trends shown in Figure 82 can be given if the assumption is made that D_C is equal to D_K. This assumption is based on the agreement between values of these two diameters shown in Table 13 for the powder and fiber samples. Using this assumption, Equations (97) and (98) can be combined to yield an expression for ℓ_m/K_1 as follows

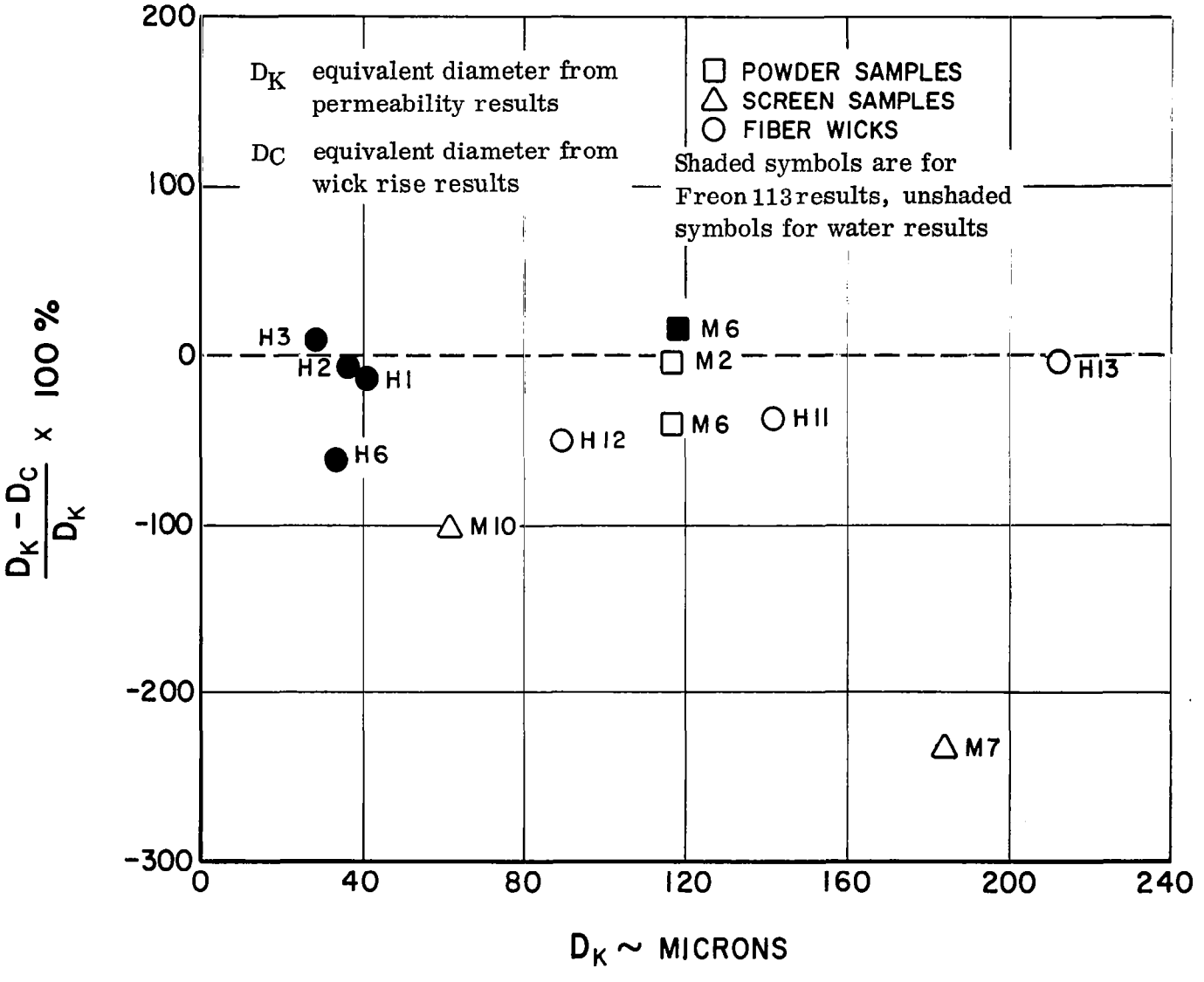

Figure 81 Comparison of Diameters Obtained from Permeability and Wick Rise Tests

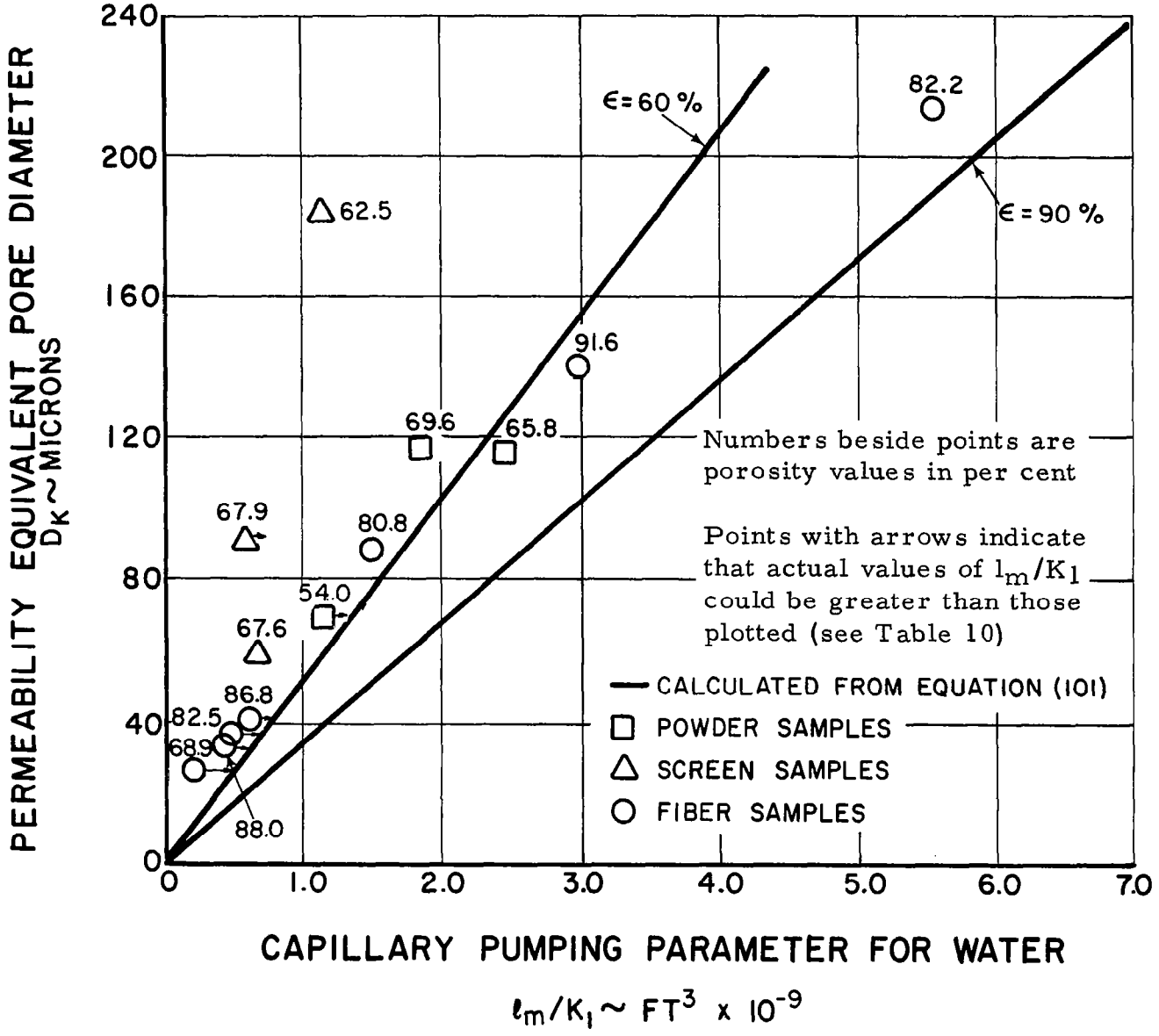

Figure 82 Permeability Equivalent Pore Diameter vs Capillary Pumping Parameter for Porous Materials

$$\frac{\ell_m}{K_1} = \frac{g_o}{8g} \frac{\sigma}{\rho_L} F_{AR} D_K \quad (99)$$

But as shown in Section IV, the free-flow area ratio can be expressed as

$$F_{AR} = \epsilon \quad (100)$$

if it is assumed that the wicking material is isotropic. Using Equation (100), Equation (99) becomes

$$\frac{\ell_m}{K_1} = \frac{g_o}{8g} \frac{\sigma}{\rho_L} \epsilon D_K \quad (101)$$

In effect Equation (101) reduces a wick to an equivalent capillary tube. For such a situation the capillary forces are inversely proportional to the diameter of the tube, (i.e. $\ell_m \sim 1/D_K$) whereas the frictional forces are inversely proportional to the diameter squared, (i.e. $K_1 \sim 1/D_K{}^2$) which leads to the linear dependence of ℓ_m/K_1 on the diameter shown in Equation (101).

Equation (101) is plotted in Figure 82 for values of ϵ equal to 60 and 90 per cent. The data is in fair agreement with these plots. The points representing the sintered-screen samples lie the furthest from these two curves as would be expected from the previous discussion of Figure 81.

Thus Figure 82 shows that the capillary pumping parameter increases with increasing equivalent pore diameter. However, the plot shown in Figure 82 includes the parameter for frictional and capillary forces, and not gravity forces. As pointed out in Section VII C , the evaluation of a wicking material for use in a gravity situation must include a consideration of the ℓ_m of the material as well as ℓ_m/K_1.

E. Summary

The maximum output of a capillary pump was found to be dependent on the capillary pumping parameter ℓ_m/K_1 when zero net body forces are considered. Experimentally determined values of the capillary pumping parameter are presented for thirteen samples. In applications involving a condition in which a capillary pump works against gravity, consideration must be given to both the value of the capillary pumping parameter and ℓ_m, the equilibrium height of liquid in the vertical wick.

Effective pore diameters were computed from mercury porosimeter data, permeability data, and wick rise data. The capillary pumping parameter was found to increase almost linearly with the median pore diameter of the wick.

VIII. BOILING STUDIES

A. Boiling in Wicks

The limitation on fin operation due to boiling occurring in the evaporator wick was discussed in Section III B. A separate test program was performed to study the process of evaporation and boiling of a liquid in a wick.

A number of investigators have studied boiling at wick covered surfaces, but none of their researches are directly applicable to the heat transfer process in the evaporator section of the vapor-chamber fin. Allingham and McEntire[12] obtained boiling coefficients for a tube embedded in water-saturated ceramic fiber wicking material. However, because their data was taken at relatively low temperatures (120-160°F) and low heat fluxes (1000 - 10,000 Btu/hr ft^2), no conclusion can be drawn about peak heat fluxes. Critical heat flux data for a wick covered surface was obtained by Costello and Redeker[13], but because of the path taken by the vapor generated at their heater surface, little correlation can be made between their experimental model and the evaporator of the vapor-chamber fin.

The later work of Costello and Frea[14] is perhaps the most germane to the problem of boiling in the fin. By wrapping a cylindrical electric heater in wicking material they were able to obtain pool-boiling critical heat fluxes as high as 1.2×10^6 Btu/hr ft^2 in water, with a 50°F difference between the heater temperature and the saturation temperature of the liquid. The data of Costello and Frea is both gravity-dependent and geometry-dependent, because the vapor produced was not vented through the wicking material, but rose through an opening in the wick above the heater. Thus, the question of the ability of the wick to support the flow of vapor from and liquid to a region of the heated surface was not conclusively answered. However, the extremely high value of the critical heat flux obtained in their studies was very encouraging.

B. Objective

The objective of the tests was to determine the following boiling heat transfer characteristics while boiling from a wick-covered planar surface:

1) The variation of heat flux, q, with ΔT_{sat}, the temperature at the liquid-wick-solid interface minus the saturation temperature, and

2) The maximum heat flux that can be sustained before film boiling occurs.

The two objectives above were to be determined as functions of wick material, boiling fluid (water or Freon 113), wick orientation with respect to gravity, degree of wick submergence, and surface modification.

Three classes of wicking materials were studied: sintered metal screens, sintered metal powders, and sintered metal fibers. The results are interpreted to determine limitations on boiling from a wick-covered planar surface. The following sections contain a description of the apparatus used to accomplish these objectives and the results obtained from the test program.

C. Description of Boiling Apparatus

1. Overall Design

Figure 83 shows a diagram and Figure 84 a photograph of the boiling test setup, which includes the primary tank containing the test sample, the sample heater, and the guard heater; the auxiliary tank with a heater, and a liquid heater located between the primary and auxiliary tanks. A sketch of the stainless steel primary tank is shown in Figure 85, and a photograph of the interior is shown in Figure 86. The flat test sample to be evaluated was bonded to a resistance heater mounted on copper busbars. The top side of the heater was coated with an electrical insulator (aluminum oxide). The bottom of this heater was firmly pressed against insulating blocks by means of busbar adjusting screws. The insulating blocks, two of which had a Nichrome guard heater sandwiched between, rested on a Textolite platform which was mounted in the stainless steel primary tank. A Plexiglas cover and Neoprene gasket were used to prevent spillage during the tests in which the primary tank was tilted. The overall dimensions of the inside of the primary tank were 10 3/4 x 2 1/4 x 5 3/4 inches.

The auxiliary tank was 3.5 by 2 by 0.5 ft and was made of stainless steel. The purpose of this secondary tank was to provide a large liquid-vapor surface, so that the change in liquid height with time, as the primary tank fluid boiled away, was limited to a negligible amount. In this way, the degree of wick submergence was kept constant during a test. A heater was provided in the secondary tank to preheat the liquid before entering the primary tank.

A fixture was built for tilting the primary tank to determine the effect of wick orientation with respect to gravity on heat transfer coefficients. The

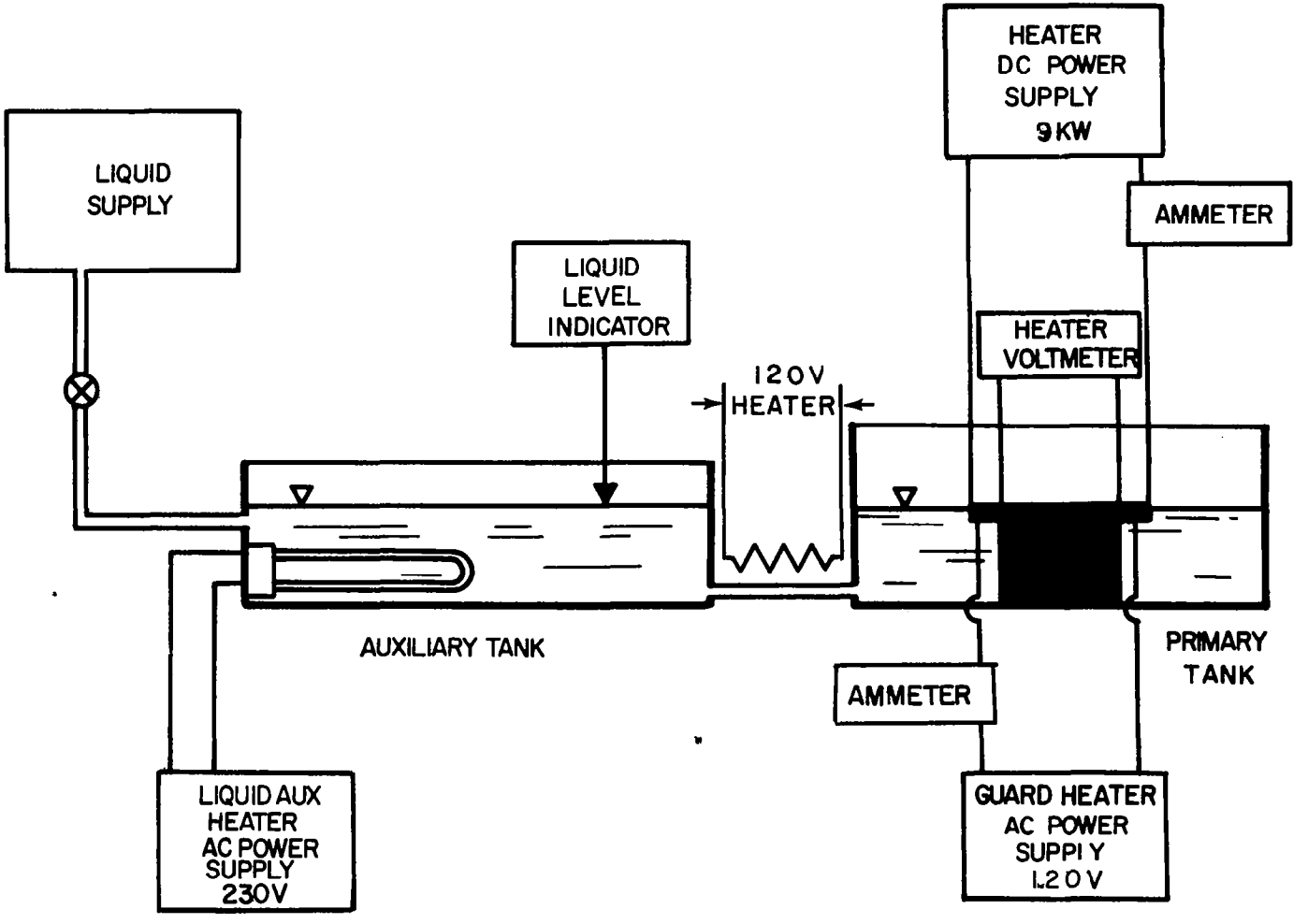

Figure 83 Schematic Diagram of Boiling Test Setup

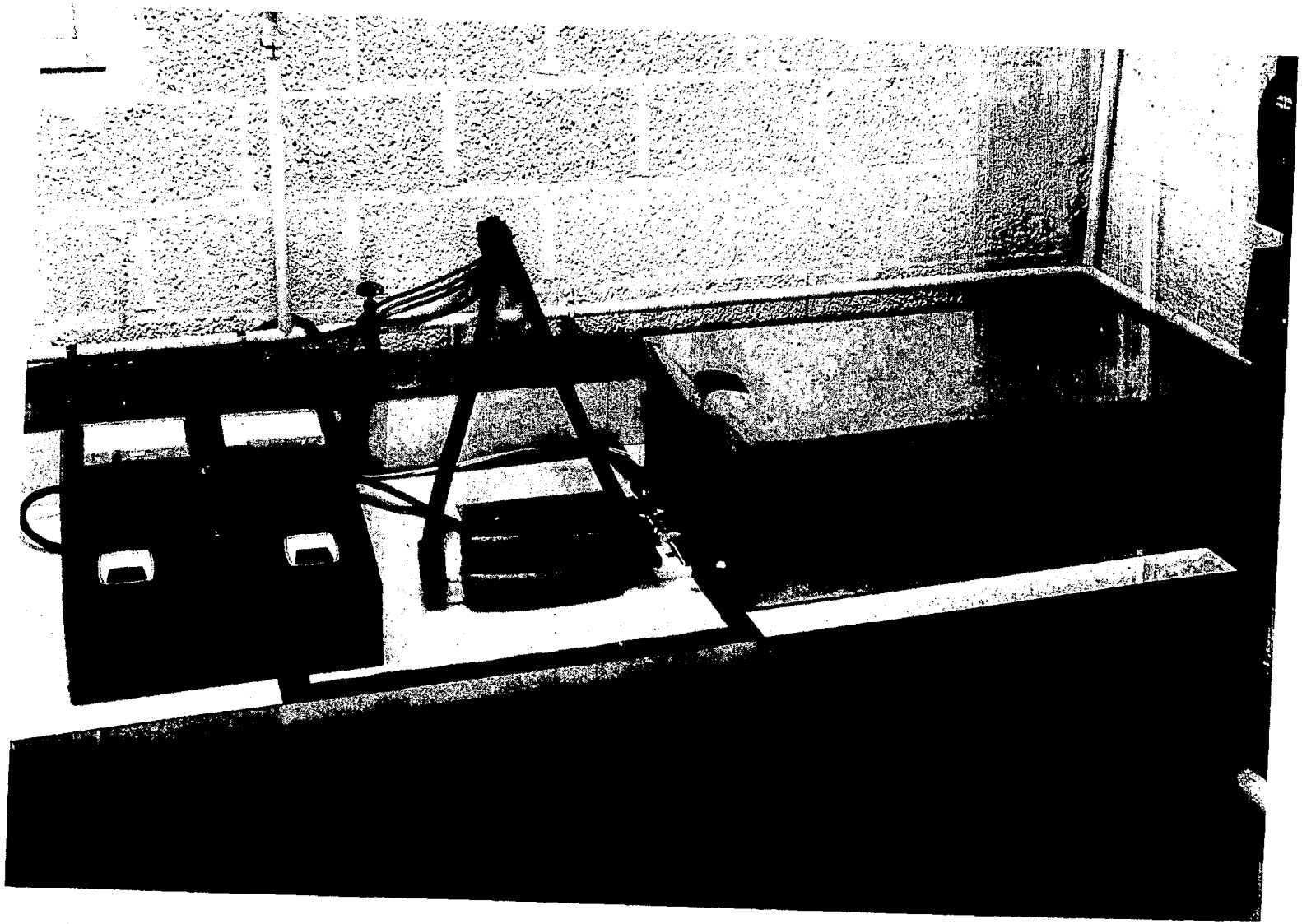

Figure 8 4 Wick Boiling Experimental Test Setup Showing Control Panel, Primary Tank, and Secondary Tank

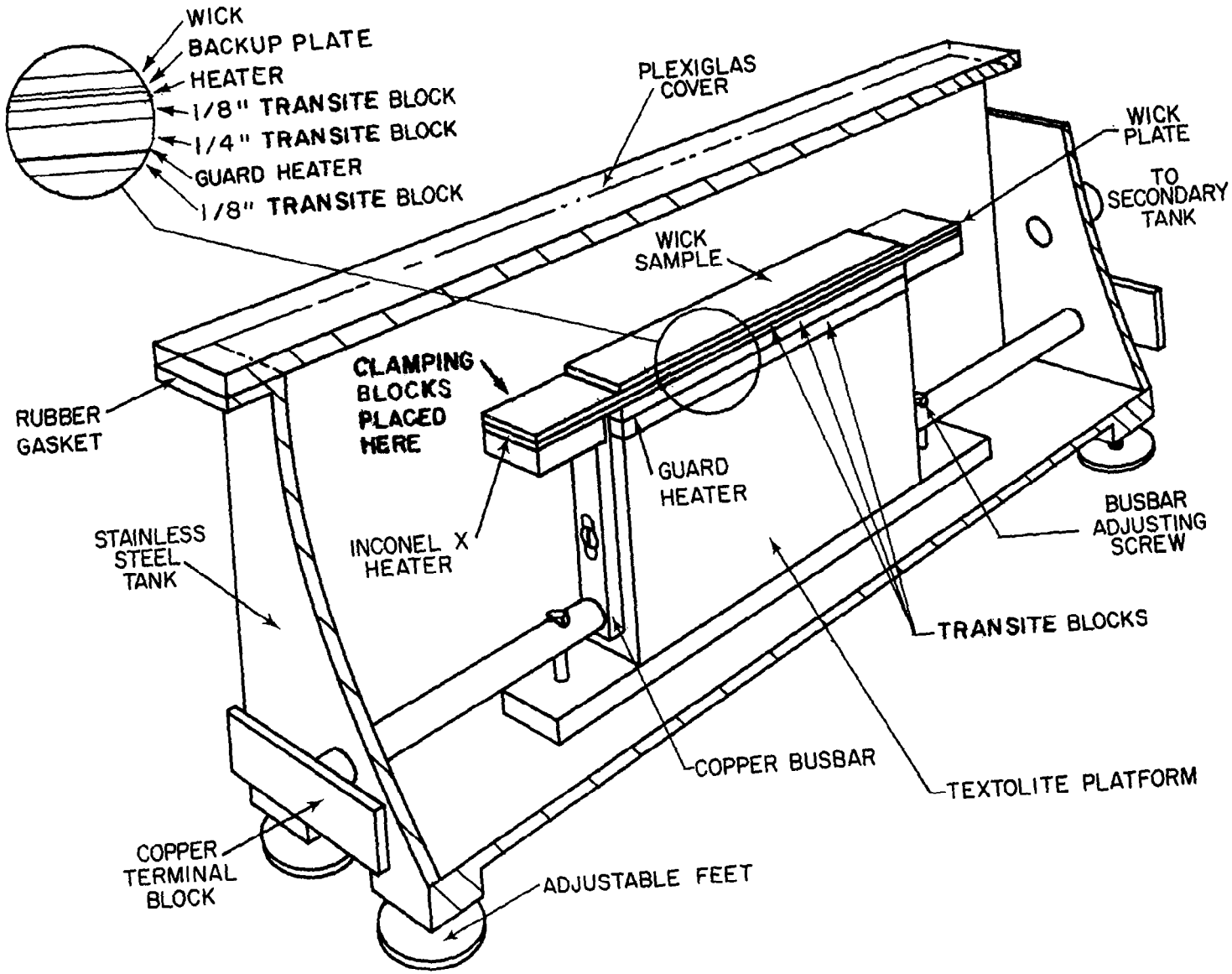

Cutaway View of Boiling Test Apparatus

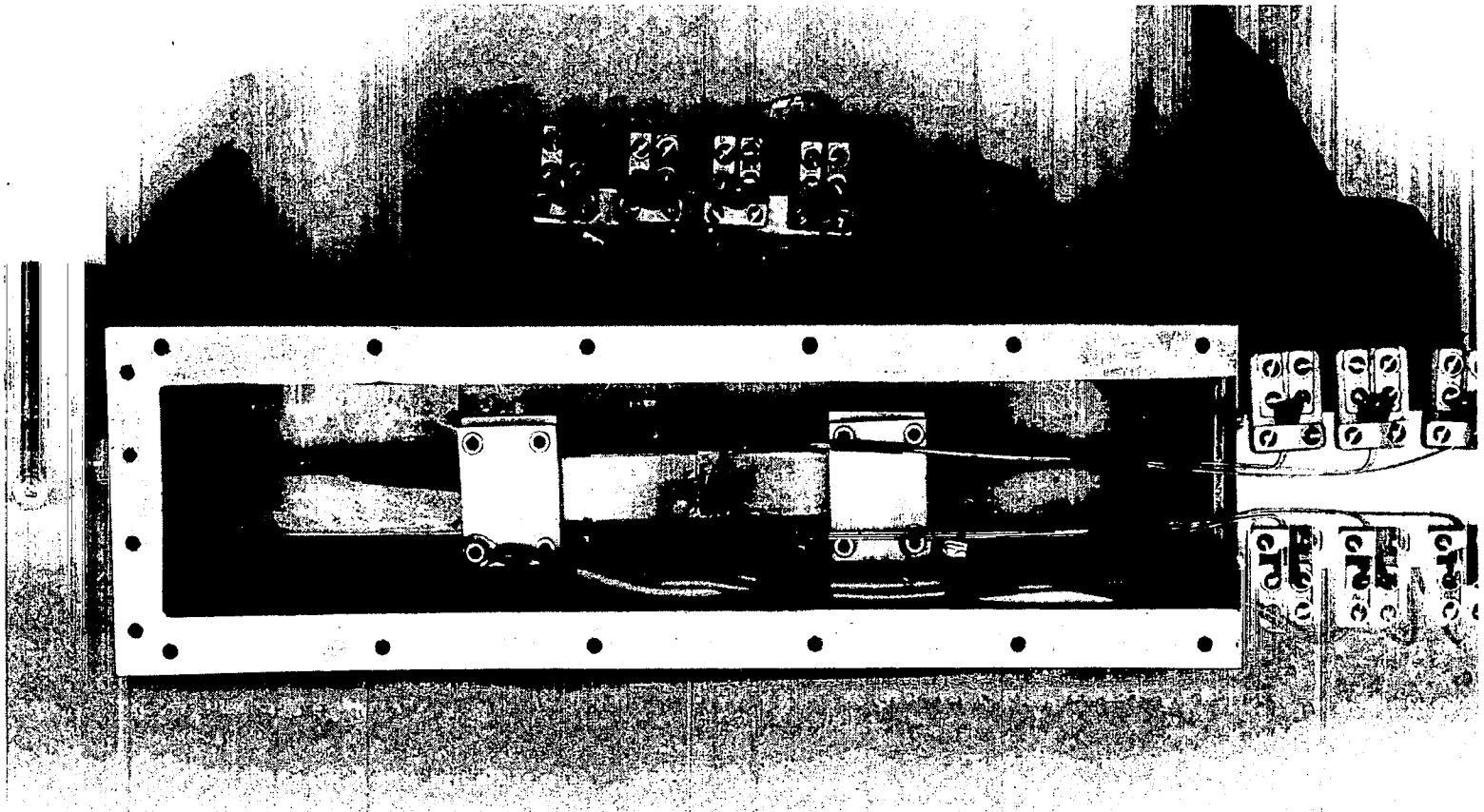

Figure 86 Top View of Primary Tank with Flat-Plate Sample Installed

fixture consisted of two steel plates hinged together at one end and connected by supporting rods on the other end. The tank, which was bolted to one of the plates, could be tilted up to 90 degrees by varying the length of the rods. Figure 87 shows the tank operating at a 45-degree angle.

2. Sample-Heater Assembly

The wick boiling samples consisted of a piece of porous nickel or stainless steel 2 7/8 by 5/8 by approximately 0.1 inch thick bonded to a backup plate of the same material. The exact thickness of each wick used in the boiling tests is given in the table below. The samples were cut from the wicks used in the wick rise tests by electrochemical machining. Since a wick boiling sample was small in size, there should have been little resistance to liquid flow in the wick. Hence, for tests in which the sample was horizontal with respect to the surface of the water, failure should have been due to the onset of film boiling rather than the wicking inability of the sample.

Wick Thickness of Samples Used in Boiling Tests

Wick Sample	Mean Thickness, Inches
M2 - sintered nickel powder	0.111
M7 - sintered 50-mesh nickel screen	0.106
M9 - sintered 150-mesh nickel screen	0.080
H6 - sintered nickel fiber	0.101
H11 - sintered stainless steel fiber	0.098
H13 - sintered stainless steel fiber	0.100

The heater was made of Inconel X for the nickel samples, and stainless steel for the stainless samples. This material selection reduced differential expansion between the heater and sample which could break the sample-heater bond. The top side of the heater was plasma arc-sprayed with a 0.002-inch coating of aluminum oxide. A thin layer of epoxy bonded the coated surface to the sample backup plate. A 1/8 inch Transite block was placed under the heater and held in place by two 1/8-inch wide layers of epoxy along the side edges of the heater and blocks. Figure 88, which is a photograph of a completed sample, shows these edges of epoxy; and Figure 85 shows a schematic of sample-heater construction. This type of sample-heater construction had the following advantages:

a. The aluminum oxide coating provided the electrical resistance necessary to prevent current leakage across the sample, while the thermal conductivity (10 Btu/hr ft°F) remained quite high for an electrical insulator. Hence, the temperature drop across the aluminum oxide was negligible for the heat fluxes of interest (10,000 Btu/hr ft^2 to 150,000 Btu/hr ft^2).

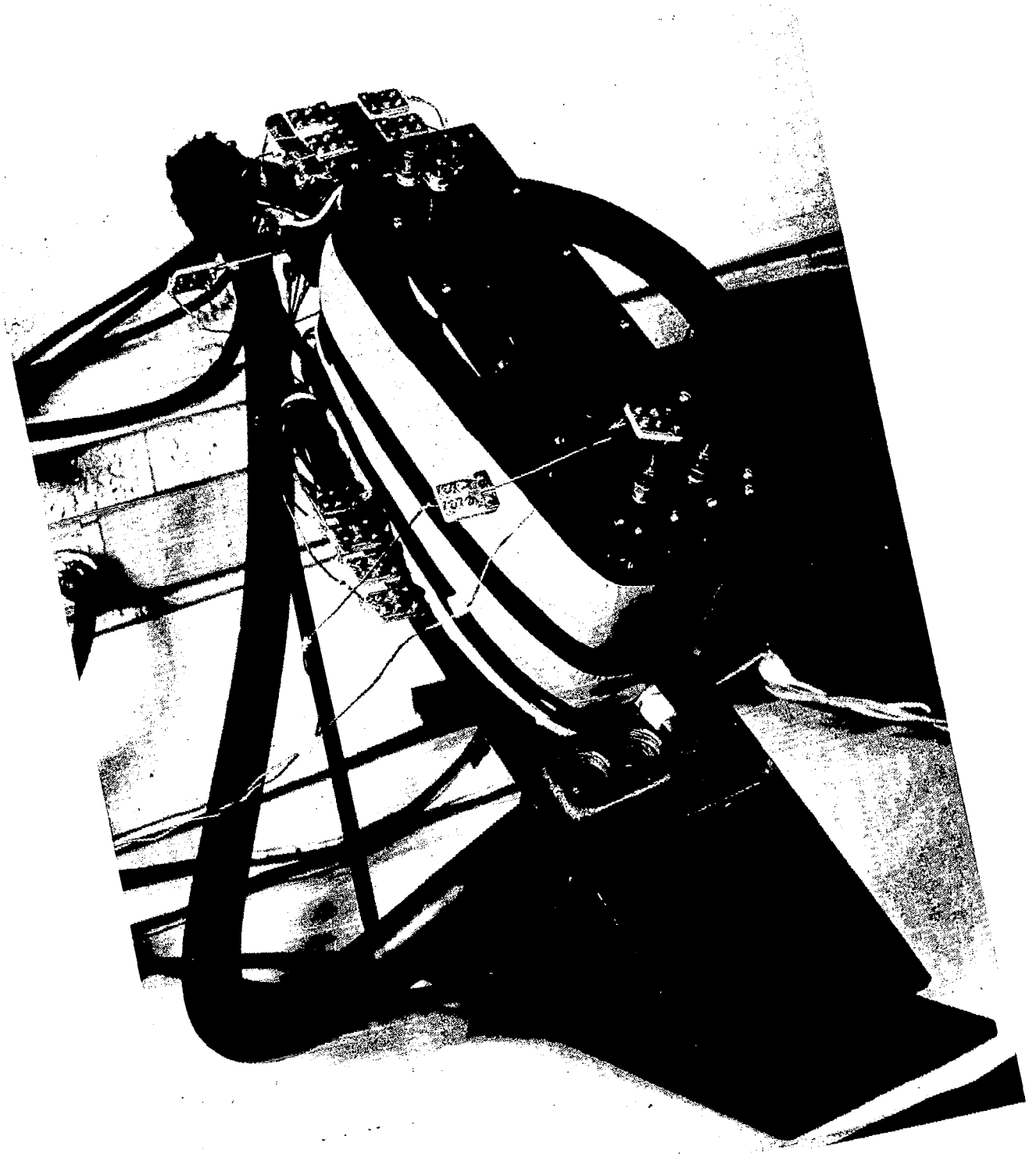

Boiling Apparatus during 45-Degree Angle Test

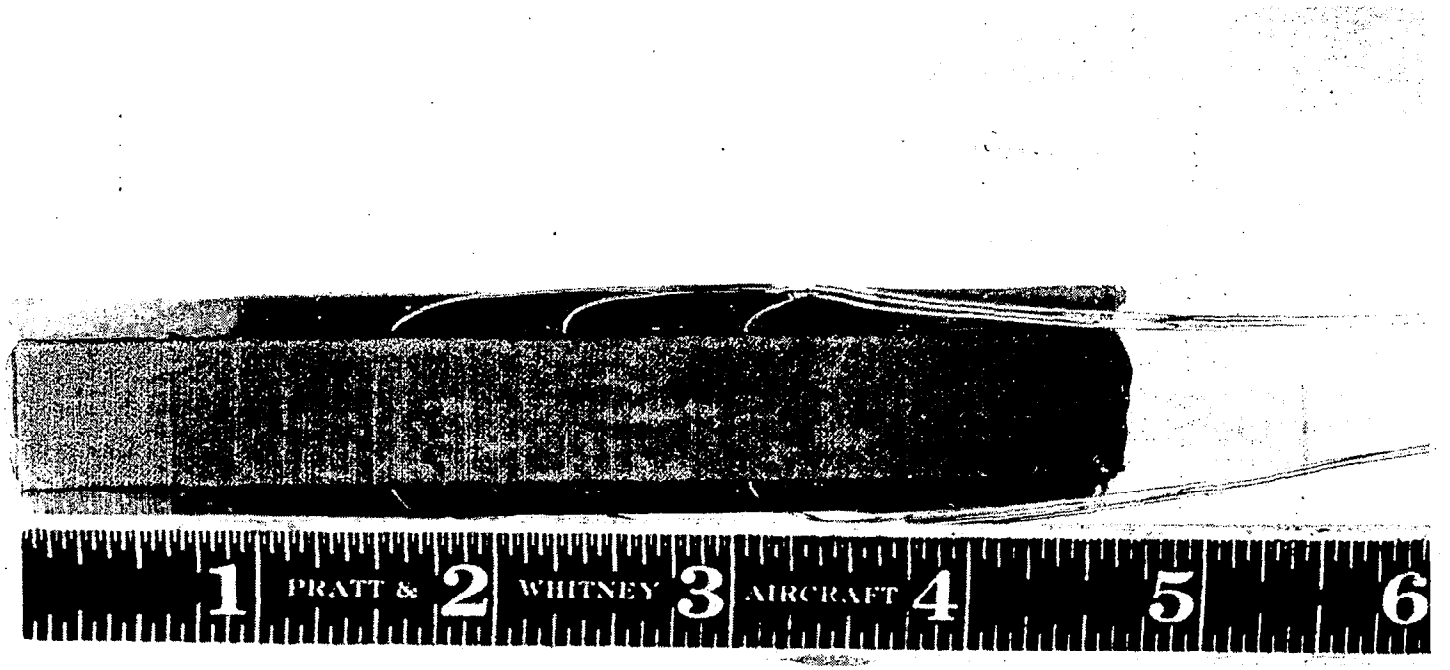

Figure 88 Boiling Test Sample M9, 150-Mesh Sintered Nickel Screen

b. The epoxy bond between the heater and sample maintained good thermal contact.

c. The epoxy edge prevented boiling heat transfer losses from the edges of the sample backup plate and heater. Edge boiling could also inhibit the flow of liquid to the wick surface. The edge of the wick was not covered with epoxy.

d. The Transite prevented boiling from the bottom of the heater. The Transite was held in place by the epoxy on the edges of the assembly rather than by epoxy on the underside of the heater. The epoxy could have decomposed if used on this surface, since the bottom surface of the heater was at the highest temperature of any surface in the boiling apparatus.

3. Instrumentation

Six chromel-alumel thermocouples were located in the underside of the sample backup plate. In addition two thermocouples were located in the vapor region above the sample, and two immersed in the liquid. Also, two sets of thermocouples were located at different planes in the Transite block on top of the guard heater to enable the control of this heater. For each test point, the guard heater was adjusted until the two sets of thermocouples read approximately the same, thus minimizing heat losses from the underside of the heater through the Textolite platform. Figure 89 shows the location of thermocouples installed on each sample and of the thermocouples used to regulate the guard heater. Figure 88 shows six thermocouples installed on a 150-mesh sintered screen sample. The six thermocouple wires installed on the sample were enclosed in sheaths of 0.020-inch outside diameter which were welded in 0.020-inch grooves on the underside of the sample backup plate. The thermocouple wires (0.0025 inch in diameter) were welded to the bottom of the grooves, and the grooves filled with epoxy. Hence, the temperature being measured was at a distance of 0.002 or 0.005 inch from the liquid-wick-solid interface, since the sample backup plates were either 0.022 or 0.025 inch thick.

Other instrumentation included a voltmeter to measure the voltage drop across the sample heater, and two ammeters to measure the current through the sample and guard heaters.

Table 14 presents a summary of the instrumentation used in the boiling rig with the maximum error value of each instrument.

4. Power Supplies

Power for the boiling rig is supplied by a 12 KVA rectifier with a three-phase 480-volt input and a controllable DC output of up to 750 amperes at 12 volts, or 1500 amperes at 6 volts. Power for both the guard heater and the heater located between the primary and auxiliary tanks is controlled by 120-volt input powerstats. The secondary tank heater is a 5 KW 230-volt resistance type, controlled by a powerstat.

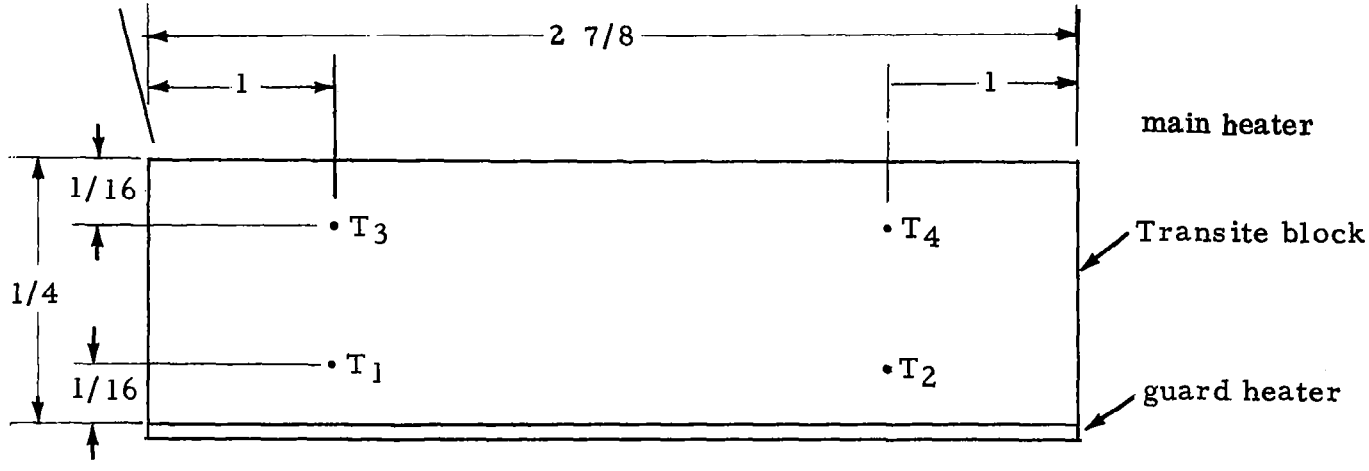

a) Guard Heater Thermocouples (elevation view)

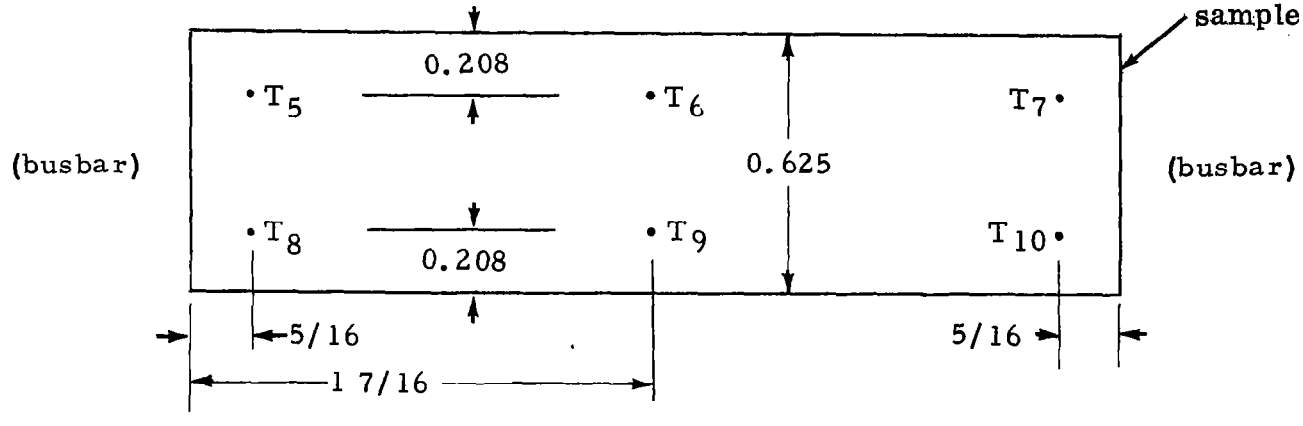

b) Sample Thermocouples (top view)

dimensions in inches

Figure 89 Location of Thermocouples for Sample and Guard Heater

TABLE 14

Boiling Test Instrumentation

Instrument	Number and Measured Quantity	Location	Range of Meter	Range of Tests	Maximum Error
voltmeter	1, heater voltage, E	across heater	0-7.5v	0.5-4v	0.025v
ammeter	1, heater current, I	before heater	0-1000 amps	75-600 amps	5 amps
ammeter	1, guard heater current, I_g	before guard heater	0-30 amps	2 -10 amps	0.25 amps
C-A thermocouple	4, guard heater, T_1, T_2 block temp. T_3, T_4	(see Figure 92)	0 - 800°F	100-650°F	1.5°F
C-A thermocouple	6, sample temp. T_5, T_6, T_7, T_8, T_9, T_{10}	(see Figure 92)	0 - 800°F	100-650°F	1.5°F
C-A thermocouple	2, primary inlet temp. T_{11}, T_{12}	inlet tube to primary tank approx. 1 inch from tank wall	0 - 800°F	100-200°F	1.5°F
C-A thermocouple	2, vapor temp. T_{13}, T_{14}	1/2 inch above sample, 1/2 inch from either end, half way across in width direction	0 - 800°F	200-220°F	1.5°F
C-A thermocouple	2, primary tank water temp. T_{15}, T_{16}	adjacent to Textolite platforms, 1/2 inch from sample ends, immersed in water 3/4 inch	0 - 800°F	100-200°F	1.5°F
C-A thermocouple	1, busbar temp. T_{17}	probe for busbar temperature at any location	0 - 800°F	100-650°F	1.5°F

D. Test Procedure

The boiling tests were started by filling the secondary tank with the test fluid to the approximate level desired in the primary tank. The hose clamp in the line connecting the two tanks was opened, allowing the fluid to flow from the secondary tank through the heater to the primary tank. The heater was adjusted to fill the primary tank with fluid at the desired temperature. Fine adjustments of the liquid level in the primary tank to change the degree of liquid saturation in the wick sample could be made by altering the adjustable feet on the primary tank or the level of liquid in the secondary tank.

Power was supplied to the primary heater, and the input varied to obtain the desired heat fluxes at which data was to be taken. At each test point the guard heater was adjusted by means of a 120V powerstat until the temperatures of the top two Transite-block thermocouples read approximately the same as the bottom two (indicating neglible heat loss from the bottom of the heater through the Textolite block). The temperatures were recorded after stabilizing to a point where there was no change over a three-minute period. The heater voltage and current and the guard heater current were also recorded. Adjustments in the liquid level could be made between data points, if necessary. (The decrease in water level due to boil-off was 0.018 inch for a 10-minute run at a heat flux of 300,000 Btu/hr ft^2.)

As power input was increased and sample temperature rose above the saturation temperature, vapor bubbles formed at nucleation sites within the wick. Further increase in sample temperature resulted in the formation of larger and more numerous bubbles until for some cases the sample was finally blanketed with vapor, indicating film boiling conditions. At the onset of film boiling, as evidenced by a sharp rise in sample temperature, the test was terminated. In other cases, the test was terminated when the temperature limitation (about 450°F) of the epoxy bond was indicated by any guard heater thermocouple.

E. Calculation Procedure for Heat Flux and ΔT_{sat}

The heat flux of the heater was computed from the measured current and voltage drop across the sample, and the area of the sample. In order to determine the sample heat flux, the heat flux value of the heater was adjusted for heat loss by using a calibration curve for rig heat loss.

The wall temperature at the liquid-wick-solid interface can be calculated using the equation

$$T_{wall} = T_m - \frac{Q}{A}\frac{\Delta x}{K_B} \qquad (102)$$

where T_m = measured temperature of backup plate
Q/A = sample heat flux
Δx = backup plate thickness from thermocouple locations to the liquid-wick-solid interface (0.002 or 0.005 inch depending upon the sample)
K_B = thermal conductivity of the backup plate

The temperature at the liquid-wick-solid interface minus the fluid saturation temperature, ΔT_{sat}, is calculated as follows:

$$\Delta T_{sat} = T_{wall} - T_{sat} \tag{103}$$

where T_{sat} is the fluid saturation temperature.

The test data of ΔT_{sat} vs q presented in the next section is based on averages of T_{wall} calculated from the several measured temperatures.

F. Test Results

The following sections contain a discussion of the test results obtained from the study on boiling from wick covered surfaces. The effects of liquid level (degree of submergence), orientation, surface modification by grooving the wick surface, fluid properties and wick structure are shown by comparing mean lines drawn through the data points for each set of data. All tests were run at atmospheric pressure. Boiling heat transfer data was obtained for an Inconel flat plate in the horizontal position in order to have a reference with which to compare the results of wick boiling tests. Flat plate data is shown in Figure 90, a plot of heat flux versus ΔT_{sat}. Table 15 presents an outlined description of the boiling tests.

1. Effect of Degree of Submergence for Wick in Horizontal Position

The effect of water level, or degree of submergence, is demonstrated in Figure 91 for a sintered 150-mesh nickel screen tested in a horizontal position. The degree of submergence is the ratio of the thickness of wick that is submerged to the total thickness of the wick. The boiling characteristics of the sample did not change significantly as the degree of submergence changed from 100 per cent to 25 per cent. As shown in Figure 91, the two curves representing 100 per cent submergence are not similar. The difference is due to the fact that this sample was rebonded to the heater between Tests No. 1 and 5, and indicates that boiling heat transfer characteristics of a wick covered surface depend strongly on the physical handling of the sample. During these tests, it was determined, by visual observation, that all vapor bubbles emanated from the edge surface with none going through the top surface. In the case of 100 per cent submergence the liquid could be seen on the top and no bubbles were observed emanating from the top.

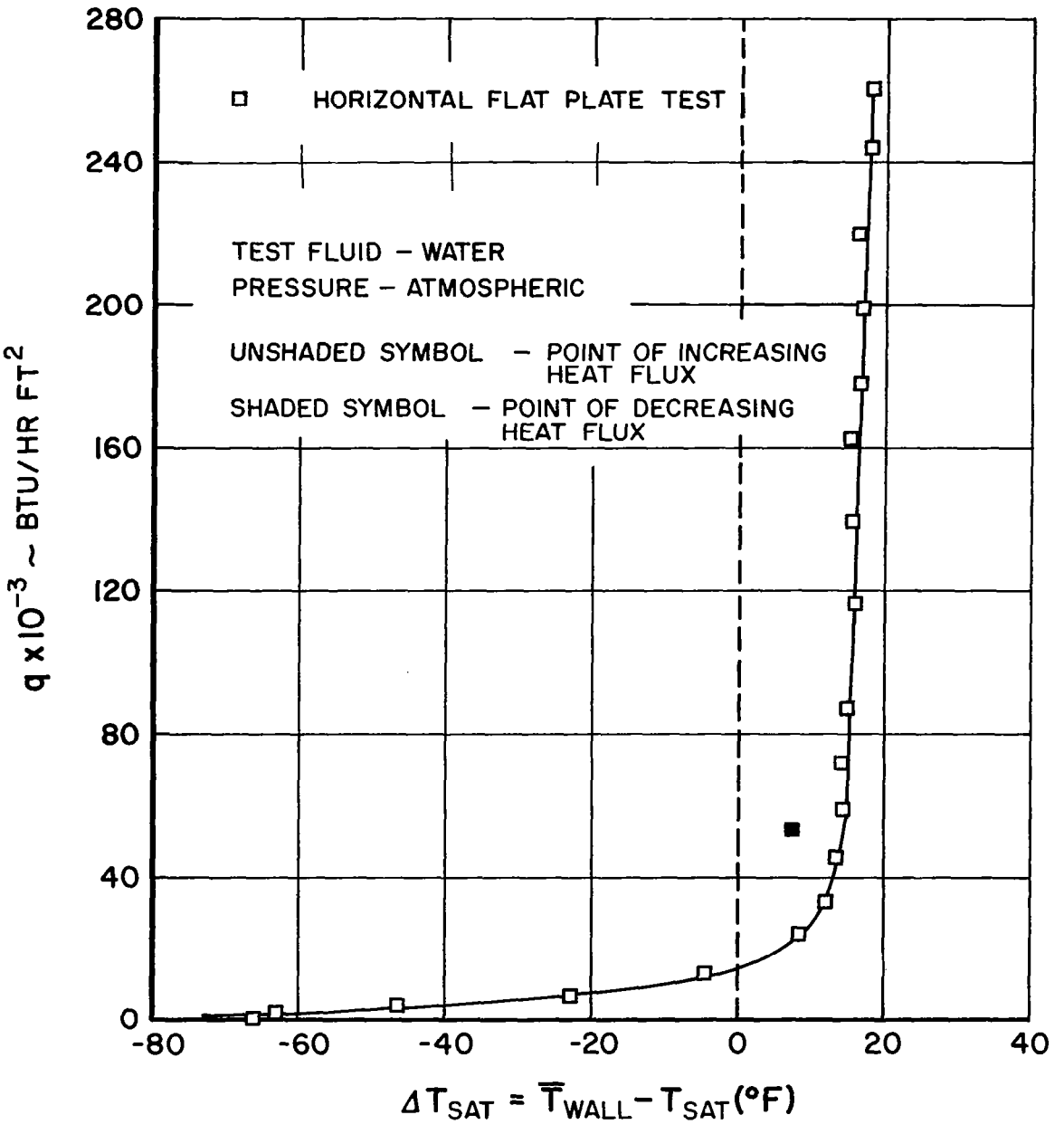

Figure 90 Heat Flux vs ΔT_{sat} for Horizontal Flat Plate

TABLE 15

Summary of Boiling Tests

Test No.	Results Shown In Figure No.	Sample	Test Fluid	Orientation (Angle to (Horizontal - Deg.)	Degree of Submergence (%)	Range of Fluid Bulk Temp	Maximum Thermocouple Temperature Variation From Mean Reading ΔT at q, ΔT - °F and q - Btu/Hr Ft^2	Comments
0	94, 110	flat plate	water	0	100	$q \leq 262,000$ $T \approx 140 \rightarrow 193$	2.5 at 224,000	uniform boiling on surface
1	95	sintered 150-mesh nickel screen - M9		0	100	$q \leq 89,000$ $T \approx 145 \rightarrow 196$	23 at 15,000; 42 at 69,000; 27 at 89,000	all vapor evolution through sides, non-uniform temperature distribution due to preferred paths of vapor escape
2	96			24	5/8" of wick end submerged	$q \leq 48,000$ $T \approx 111 \rightarrow 151$	2 at 19,000; 5 at 48,000 for TC's at submerged end - only one TC used at other end	
3	96, 111			45	1/4" of wick end submerged	$q \leq 41,000$ $T \approx 97 \rightarrow 144$	0 at 16,000; 5 at 41,000 for TC's at submerged end - only one TC used at other end	liquid appeared to be oscillating (period 1 sec) liquid near the wick surface one instant and away from it the next - no vapor bubbles were observed
4	96			90	3/8" of wick end submerged	$q \leq 33,000$ $T \approx 98 \rightarrow 168$	1 at 10,000; 5 at 33,000 for TC's at submerged end - only one TC used at other end	
5	95, 110			0	100	$q \leq 43,000$ $T \approx 126 \rightarrow 166$	10 at 11,000; 45 at 43,000	
6	95			0	50	$q \leq 35,000$ $T \approx 112 \rightarrow 132$	14 at 9,000; 47 at 28,000	same as test no. 1
7	95			0	25	$q \leq 43,000$ $T \approx 134 \rightarrow 145$	3 at 10,000; 47 at 36,000; 34 at 43,000	
8	97,110	sintered 50-mesh nickel screen - M7		0	100	$q \leq 90,000$ $T \approx 151 \rightarrow 189$	5 at 16,000; 12 at 90,000	same as test no. 1
9	97	same as test no. 8 with 5 layers of screen removed		0	100	$q \leq 58,000$ $T \approx 96 \rightarrow 180$	2 at 11,000; 25 at 58,000	vapor evolution through top surface at discrete sites - some through sides
10	98, 100 109, 110	sintered nickel powder - M2		0	100	$q \leq 129,000$ $T \approx 118 \rightarrow 185$	$\simeq 4$ at $\leq 80,000$; 18 at 117,000; 43 at 129,000	vapor evolution predominantly through top surface, some through sides - due to nonuniformities in wick structure. One end of sample had higher limiting heat flux than other end, as shown in figure 93for tests no. 11 & 12. Not shown for test No. 10 since does not change trend of curve appreciably
11	98			0	50	$q \leq 93,000$ $T \approx 121 \rightarrow 181$	2 at 22,000; 5 at 67,000; 29 at 93,000	

TABLE 15 (Cont'd)

Test No.	Results Shown In Figure No.	Sample	Test Fluid	Orientation (Angle to) (Horizontal - Deg.)	Degree of Submergence (%)	Range of Fluid Bulk Temp	Maximum Thermocouple Temperature Variation From Mean Reading ΔT at q, ΔT - °F and q - Btu/Hr-Ft^2	Comments
12	98	sintered nickel powder - M2	water	0	25	$q \leq 93,000$ $T \approx 133 \rightarrow 178$	2 at 22,000; 8 at 79,000; 56 at 93,000	same as tests no. 10 & 11
13	98			90	100	$q \leq 77,000$ $T \approx 131 \rightarrow 212$ $q > 77,000$ $T = 212$	1 at 23,000; 8 at 77,000; 13 at 93,000	same as test no. 10 through 12
14	99, 111			45	1/4" of wick end submerged	$q \leq 74,000$ $T \approx 99 \rightarrow 131$	1 at 41,000; 4 at 74,000 - TC's at submerged end; 1 at 41,000; 5 at 74,000 - TC's at other end	fluid motion in the wick that decreased as the distance from the tank liquid level increased was observed - could not determine whether motion was due to an oscillating interface or vapor bubbles
15	99			90	1/2" of wick end submerged	$q \leq 39,000$ $T \approx 94 \rightarrow 133$	0 at 19,000; 5 at 39,000 - TC's at submerged end; only 1 TC used at other end	
16	100	sintered nickel powder - M2 - with 2 grooves lengthwise along face		0	100	$q \leq 180,000$ $T \approx 95 \rightarrow 191$	3 at 30,000; 11 at 180,000	q of 10,000 - 20,000 vapor evolution from wick surface and grooves - as q increased vapor evolution predominantly from grooves - at max q (180,000) sample nearly obscured due to vigorous boiling
17	101, 108, 110	sintered nickel fiber - H6		0	100	$q \leq 103,000$ $T \approx 123 \rightarrow 193$	1 at 21,000; 3 at 103,000	vapor evolution through top surface
18	101	sintered nickel fiber H6 with 2 grooves cut lengthwise along face		0	100	$q \leq 180,000$ $T \approx 104 \rightarrow 182$	1 at 15,000; 6 at 180,000	vapor evolution predominantly from grooves - some from sides
19	101			0	50	$q \leq 128,000$ $T \approx 119 \rightarrow 184$	2 at 30,000; 7 at 128,000	vapor evolution from grooves and sides
20	103			45	1/2" of wick end submerged	$q \leq 20,000$ $T \approx 99 \rightarrow 117$	2 at 7,000; 2 at 20,000 - TC's at submerged end; only 1 TC used at other end	same as tests no. 14 & 15
21	103			90	1/2" of wick end submerged	$q \leq 21,000$ $T \approx 114 \rightarrow 135$	1 at 14,000; 4 at 21,000 - TC's at submerged end; 1 at 14,000; 0 at 21,000 TC's at other end	
22	104, 110	sintered stainless steel fiber - H11		0	100	$q \leq 141,000$ $T \approx 111 \rightarrow 185$	1 or 2 at 105,000; 10 at 141,000	
23	104			0	50	$q \leq 58,000$ $T \approx 103 \rightarrow 171$	1 at 17,000; 6 at 58,000	vapor evolution predominantly through top surface - some through sides
24	104			0	25	$q \leq 71,000$ $T \approx 98 \rightarrow 174$	<2 at $<71,000$	

TABLE 15 (Cont'd)

Test No.	Results Shown In Figure No.	Sample	Test Fluid	Orientation (Angle to) (Horizontal - Deg.)	Degree of Submergence (%)	Range of Fluid Bulk Temp	Maximum Thermocouple Temperature Variation From Mean Reading ΔT at q, ΔT - °F and q - Btu/Hr-Ft^2	Comments
25	105	sintered stainless steel fiber - H13	water	0	100	$q \leq 74,000$ $T \approx 118 \rightarrow 183$	1 at 11,000; 2 at 38,000; 2 at 74,000	at q = 49,000 all vapor evolution was through top surface; at q = 74,000 some vapor also evolved through sides
26	105			0	50	$q \leq 49,000$ $T \approx 115 \rightarrow 171$	2 at 11,000; 3 at 49,000	at q = 20,000 all vapor evolution was through top surface; at q = 28,000 some vapor also evolved through sides
27	105			0	25	$q \leq 78,000$ $T \approx 120 \rightarrow 177$	1 at 11,000; 4 at 78,000	vapor evolution through top surface - possibly some through sides
28	105, 106 109, 110			0	100	$q \leq 132,000$ $T \approx 140 \rightarrow 195$	2 at 23,000; 19 at 132,000	vapor evolution predominantly through top surface - some at sides
29	106			45	100	$q \leq 70,000$ $T \approx 104 \rightarrow 210$	3 at 20,000; 6 at 70,000	vapor evolution through top surface
30	106			90	100	$q \leq 32,000$ $T \approx 95 \rightarrow 149$	1 at 12,000; 4 at 32,000	same as test no. 28
31	107, 111			45	1" of wick end submerged	$q \leq 74,000$ $T \approx 100 \rightarrow 141$	only 1 TC used at submerged end; 4 at 18,000; 1 at 74,000 - TC's at other end	same as test nos. 14 and 15
32	107			90	1" of wick end submerged	$q \leq 27,000$ $T \approx 97 \rightarrow 139$	only 1 TC used at submerged end; 2 at 17,000; 3 at 27,000 - TC's at other end	
33	108	smooth Inconel flat plate	Freon 113	0	100	$q \leq 44,000$ $T \approx 78 \rightarrow 117$ $q > 44,000$ $T = 117$	4 at 18,000; 3 at 114,000	boiling over entire surface
34	108	roughtened Inconel flat plate		0	100	$q \leq 37,000$ $T \approx 79 \rightarrow 117$ $q > 37,000$ $T = 117$	4 at 23,000; 4 at 112,000	boiling over entire surface
35	108, 109	sintered nickel powder - M2		0	100	$q \leq 37,000$ $T \approx 75 \rightarrow 117$ $q > 37,000$ $T = 117$	9 at 23,000; 28 at 37,000; 120 at 61,000	vapor evolution across top surface
36	108, 109	sintered nickel fiber - H6		0	100	$q \leq 76,000$ $T \approx 81 \rightarrow 111$	2 at 32,000; 8 at 73,000; 22 at 76,000	same as test no. 35
37	108, 109	sintered stainless steel fiber - H13		0	100	$q \leq 78,000$ $T \approx 76 \rightarrow 111$	6 at 19,000; 35 at 51,000; 113 at 78,000	same as test no. 35

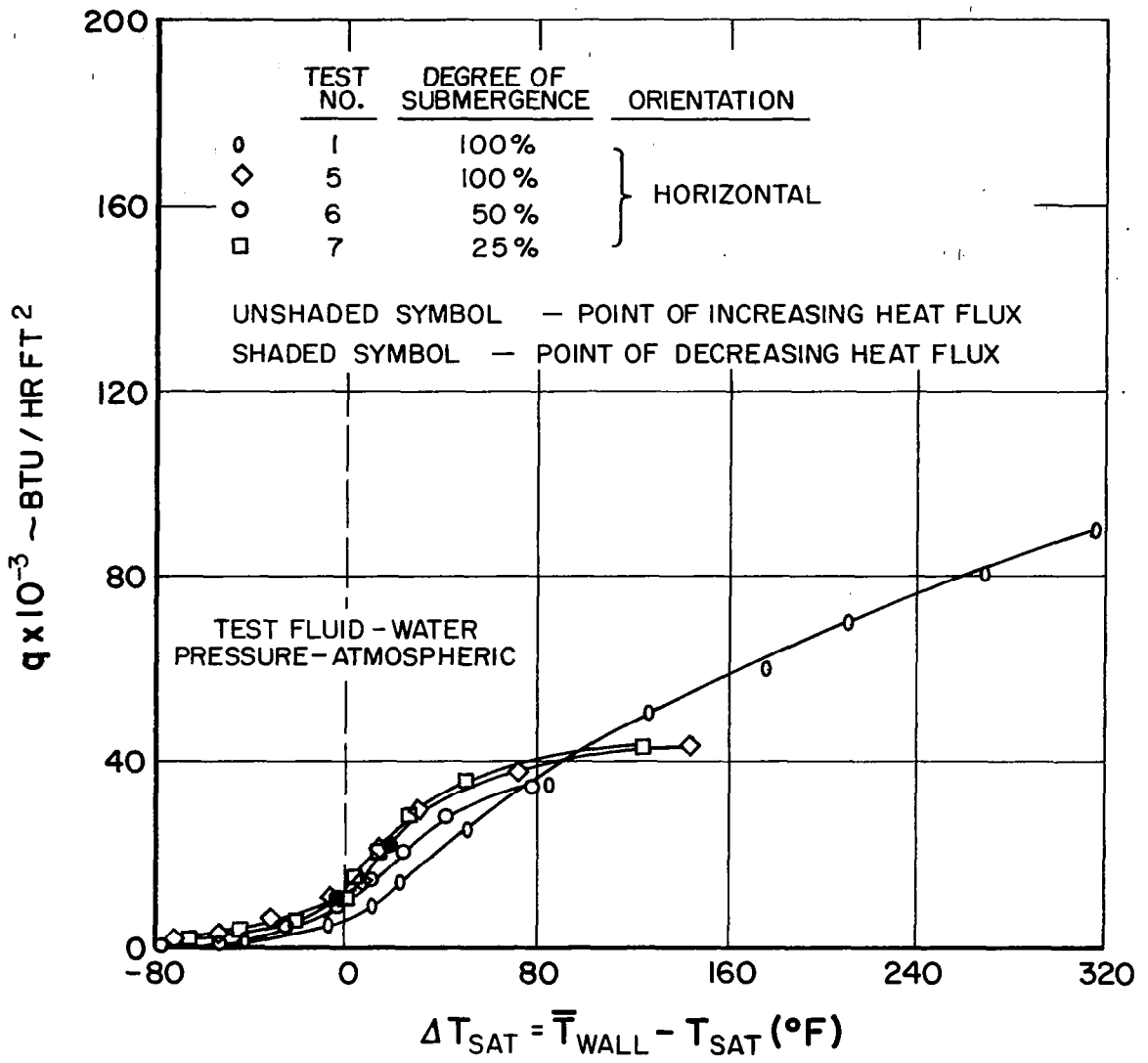

Figure 91 Heat Flux vs ΔT_{sat} for Sintered 150-Mesh Nickel Screen Wick (Sample M9) in Horizontal Position

Figures 94, 97, 100 and 101 show curves of heat flux vs ΔT_{sat} for several other wick samples, with degree of submergence as a parameter. These curves indicate that for both a sintered metal powder wick (Figure 94) and sintered metal fiber wicks (Figures 97, 100, and 101) a decreasing water level results in a reduced heat transfer rate for a given ΔT_{sat}. Hence, the boiling heat transfer coefficient for these samples decreases as the degree of submergence decreases. During these tests, nucleation sites were observed scattered across the surface of the wick and vapor evolution occurred at the face of the sample, rather than at the edges, as occurred with the sintered 150-mesh nickel screen.

Some of the data shown in Figure 97 was obtained using a sample with 2 grooves cut lengthwise along the face. A sketch of this sample is shown in Figure 98. The presence of the grooves did not alter the result that heat flux at a particular ΔT_{sat} decreased as degree of submergence decreased.

2. Effect of Thickness of a Sintered Metal Screen Wick

The effect of wick thickness for a sintered metal screen was determined in two tests on a sintered 50-mesh nickel screen sample. These were a horizontal, 100 per cent submergence test on a 0.106-inch thick sample made of 7 screen layers, and a horizontal 100 per cent submergence test on the same sample with the top 5 screen layers removed. During the first test, no bubbles were observed leaving the top surface of the sample. Instead, as in the 150-mesh screen sample test, the vapor bubbles left the wick only at preferred sites along the edges of the sample. On the other hand, in the test with only 2 layers of screen, vapor bubbles were seen escaping from the top surface of the sample at discrete sites. The results of these tests are shown in Figure 93. The boiling heat transfer coefficient of the 2-layer thick sample is significantly higher than that of the 7-layer thick sample, probably due to the ease of vapor escape rather than to any difference in nucleation within the wick.

3. Effect of Inclination With End of Wick Submerged

The object of these tests was to determine if the orientation of gravitational forces affect the boiling characteristics of a wick covered surface. To accomplish this, tests were made in which a sample was inclined to the horizontal, with a section of the wick, from 1/4 to 1 inch, submerged in the liquid. The liquid wicked up the sample due to capillary forces and was vaporized. The results of these tests are shown in Figures 92, 95, 99 and 103, for four test samples.

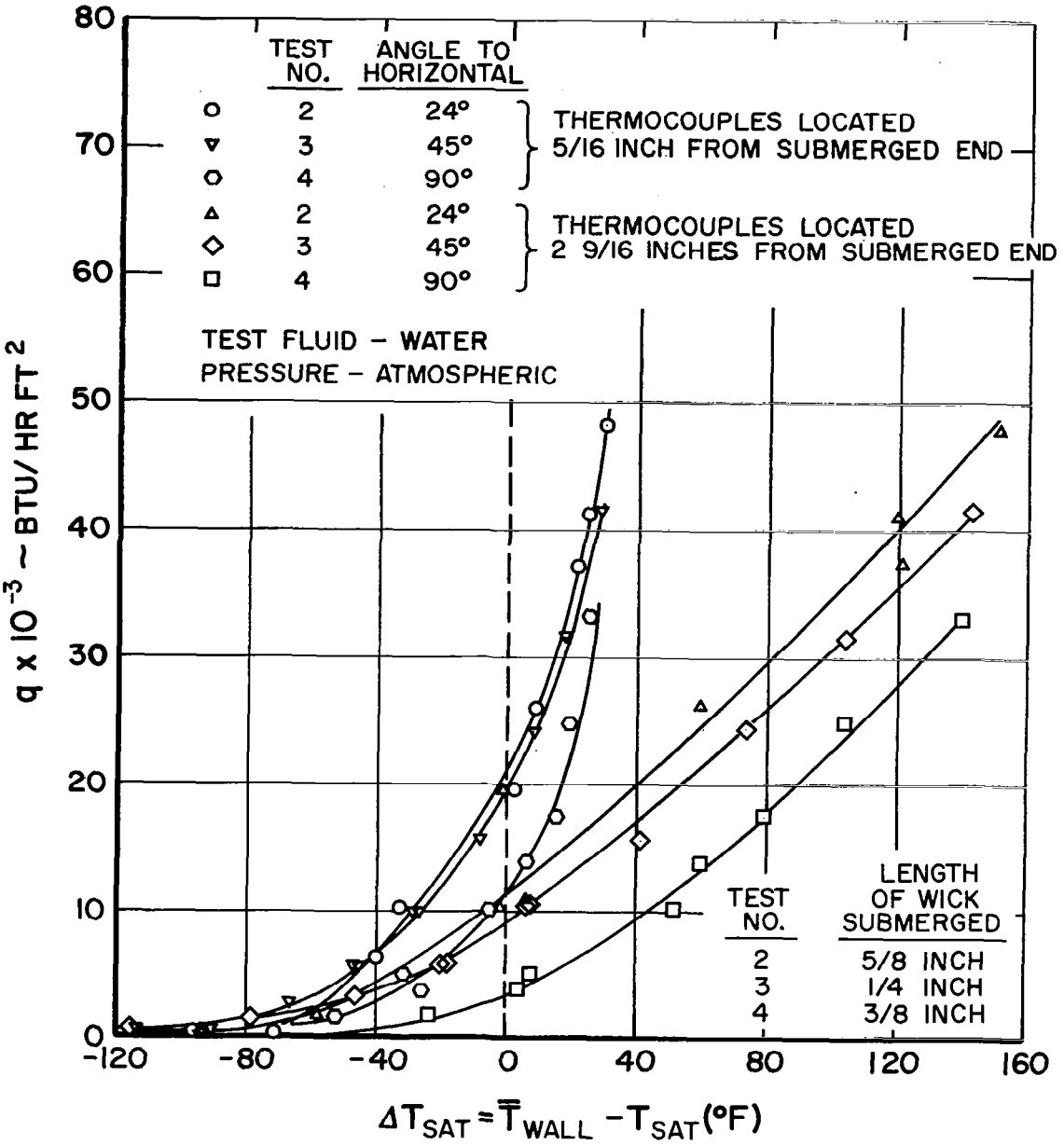

Figure 92 Heat Flux vs ΔT_{sat} for Sintered 150-Mesh Nickel Screen Wick (Sample M9) at Angles to Horizontal

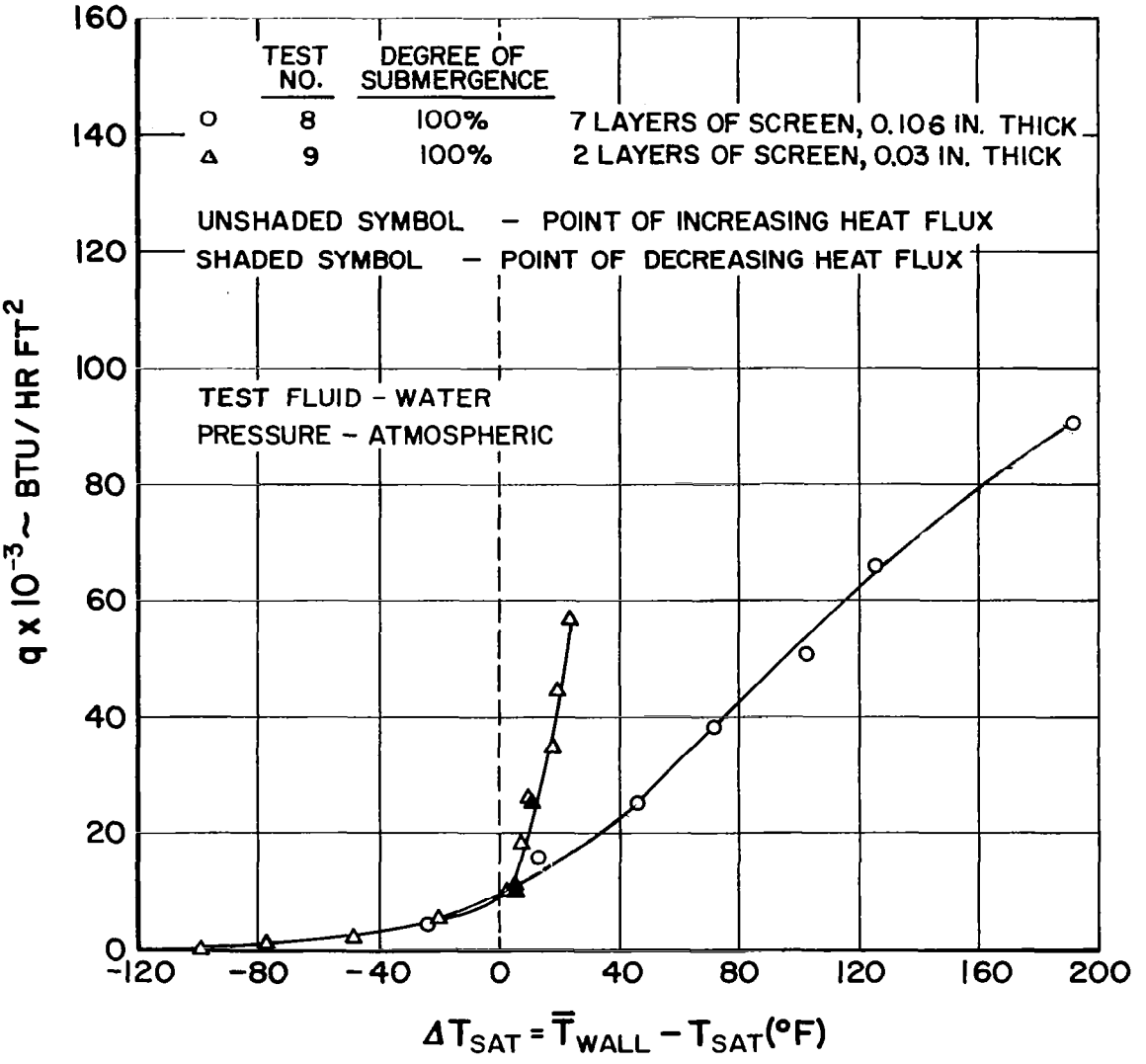

Figure 93 Heat Flux vs ΔT_{sat} for Sintered 50-Mesh Nickel Screen Wick (Sample M7)

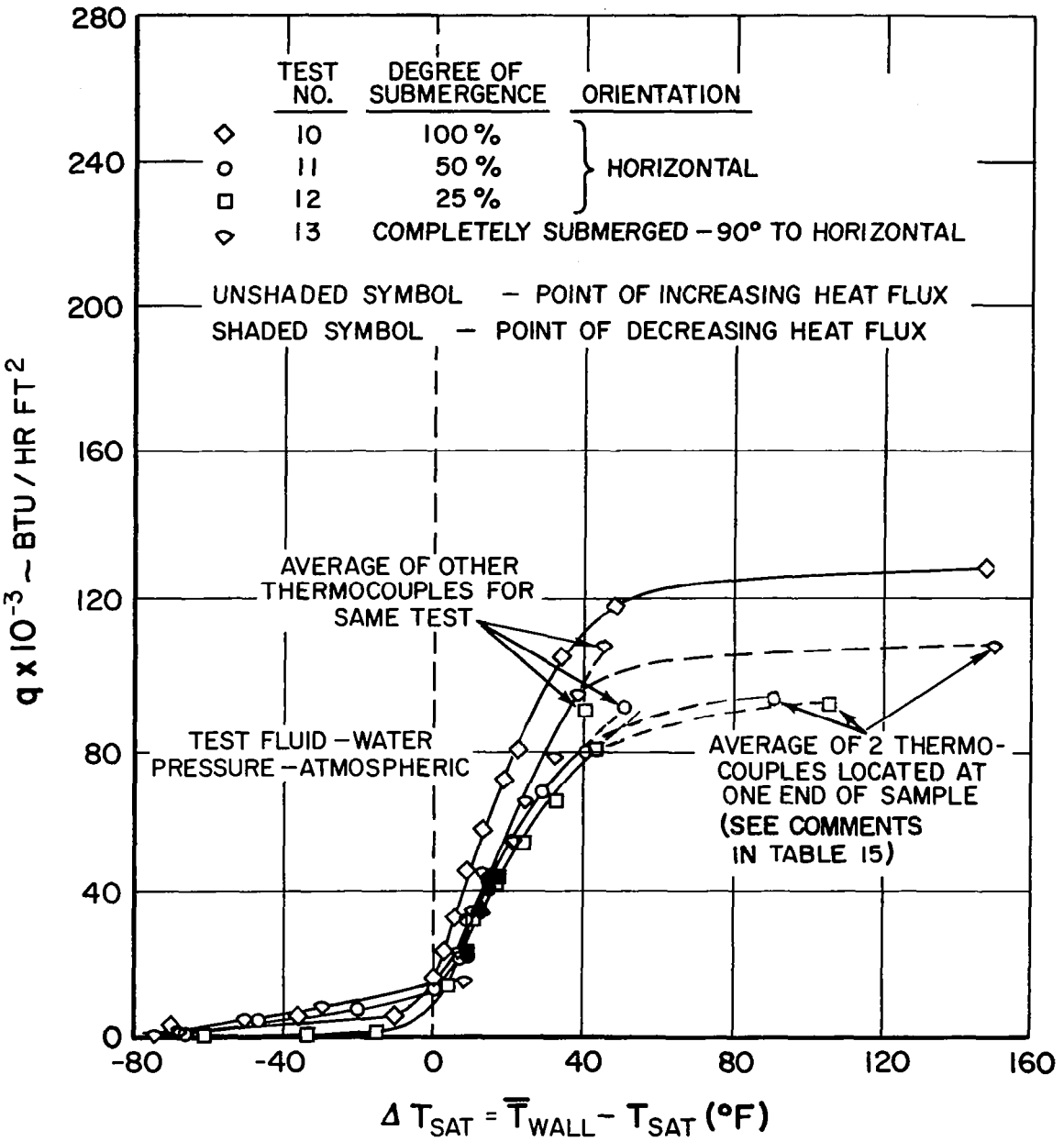

Figure 94 Heat Flux vs ΔT_{sat} for Sintered Nickel Powder Wick (Sample M2) in Horizontal Position and Completely Submerged in Vertical Position

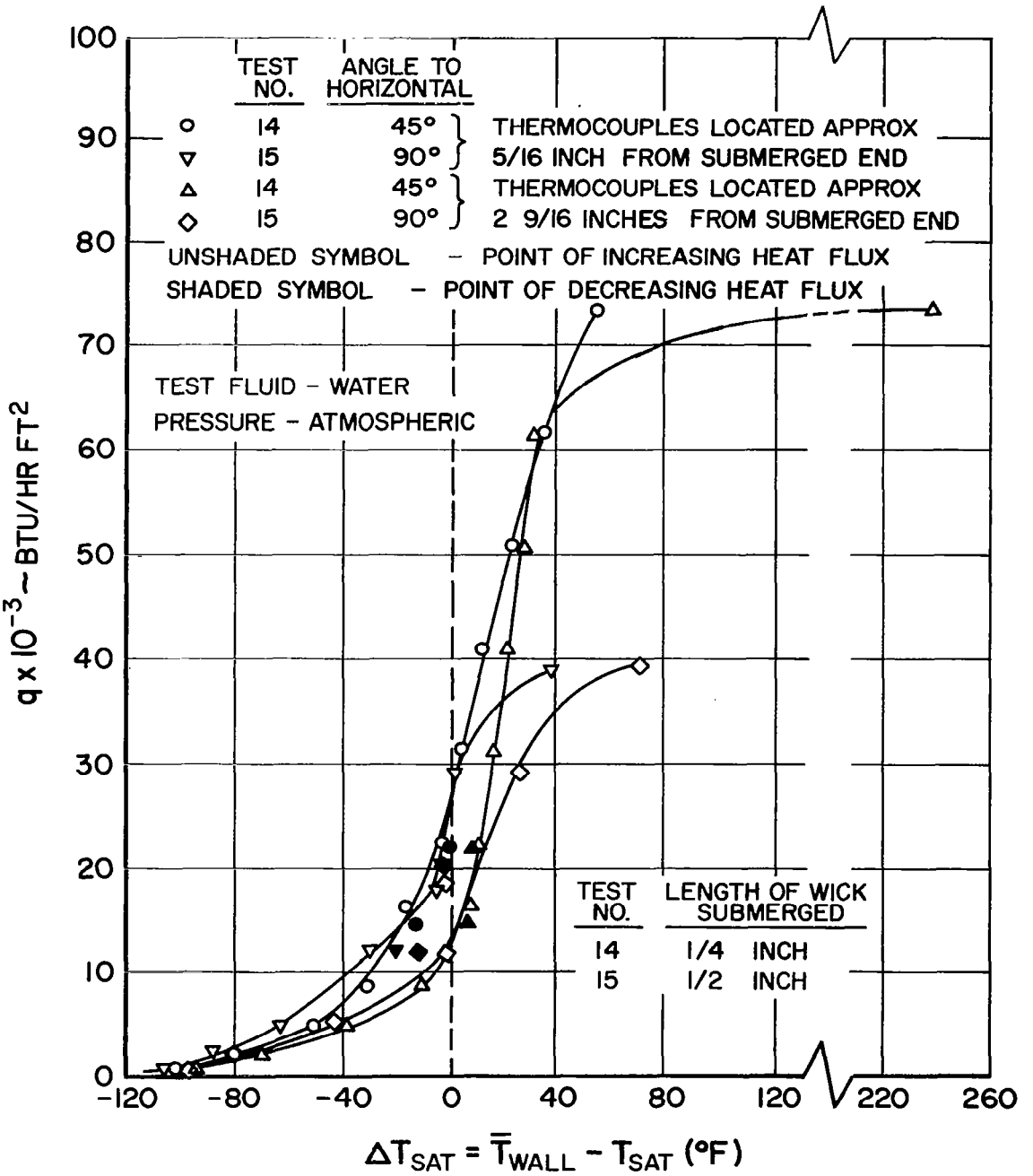

Figure 95 Heat Flux vs ΔT_{sat} for Sintered Nickel Powder Wick (Sample M2) with Partial Submergence at Angles to Horizontal

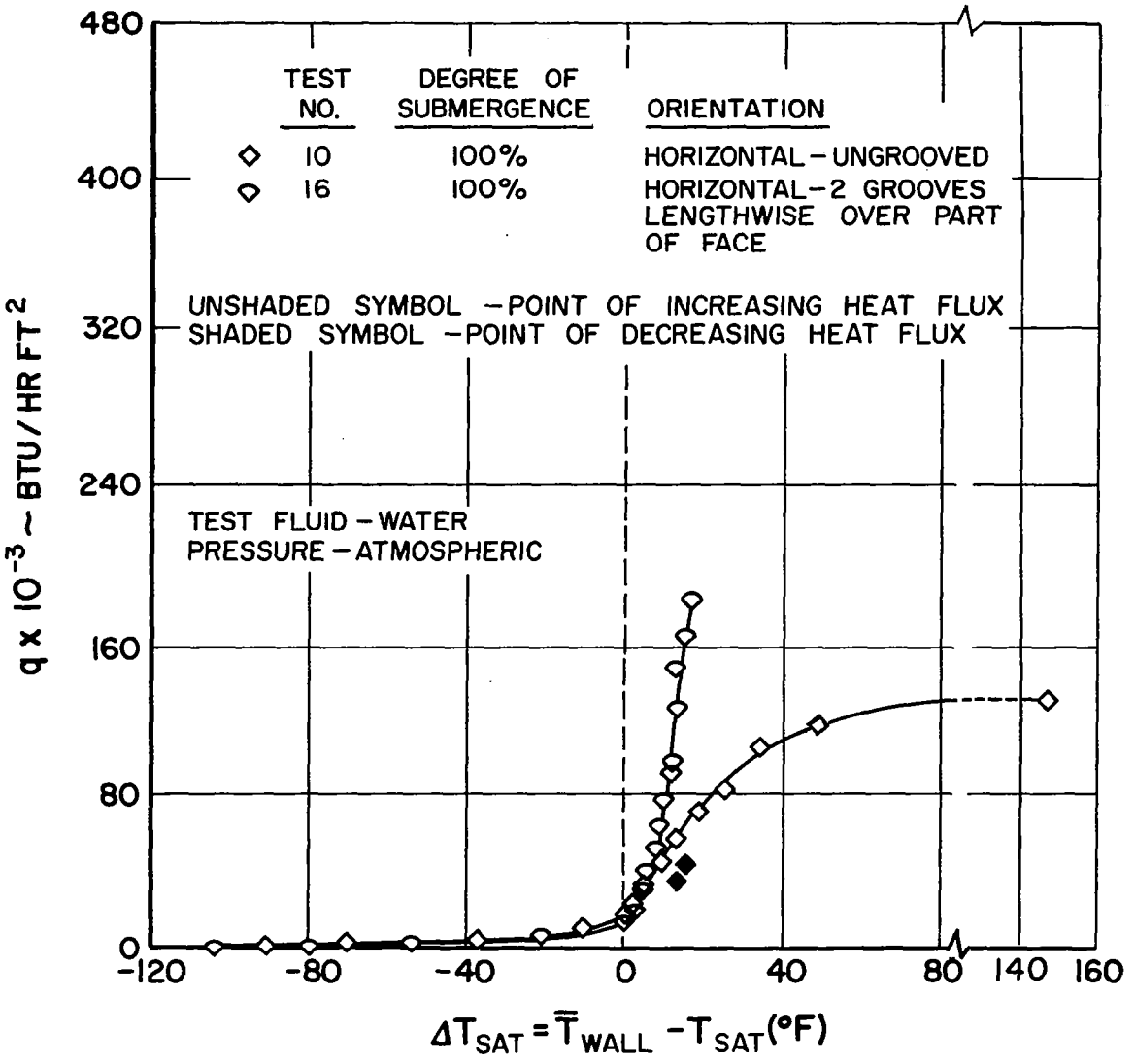

Figure 96 Heat Flux vs ΔT_{sat} for Grooved and Ungrooved Sintered Nickel Powder Wicks (Sample M2)

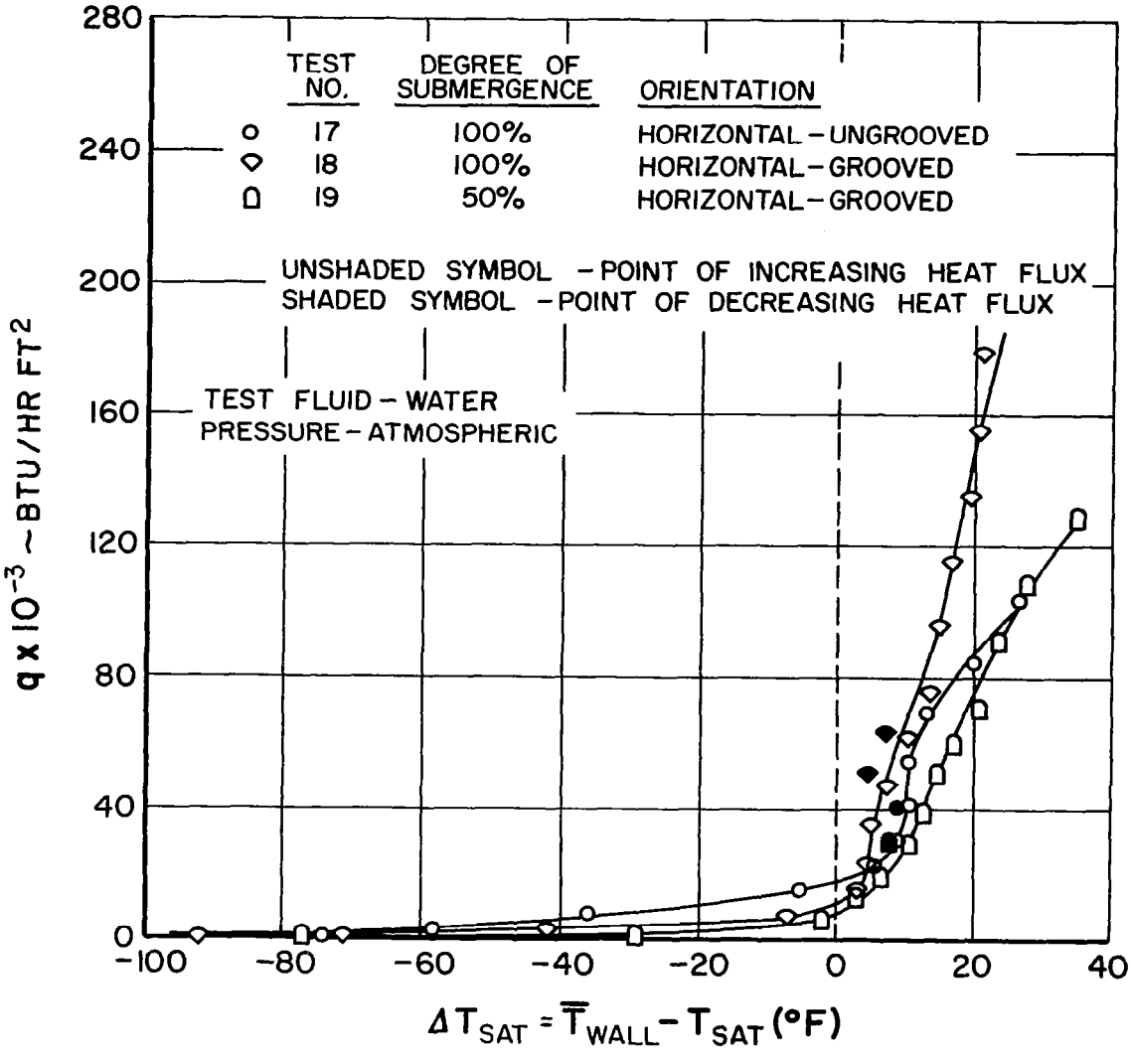

Figure 97 Heat Flux vs ΔT_{sat} for Sintered Nickel Fiber Wick (Sample H6) in Horizontal Position

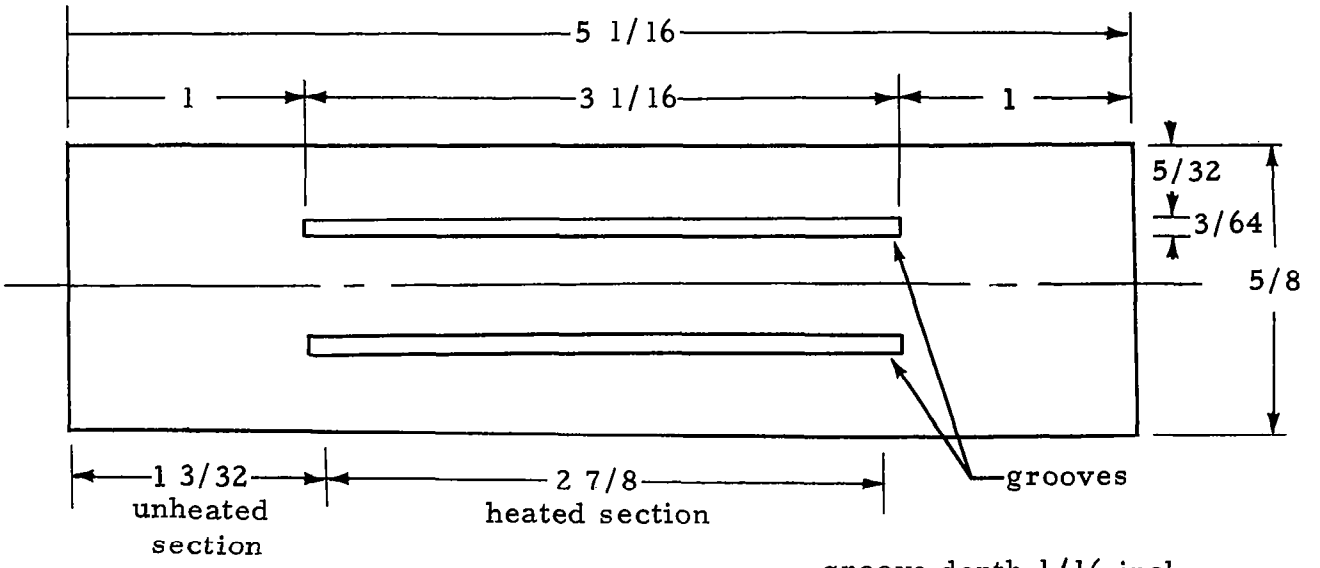

unheated end sections are crushed under clamping blocks (see Figure 85) and do not function as wicks

groove depth 1/16 inch
nominal sample thickness 0.10 inch

all dimensions in inches

Figure 98 Dimensions of Grooved Samples

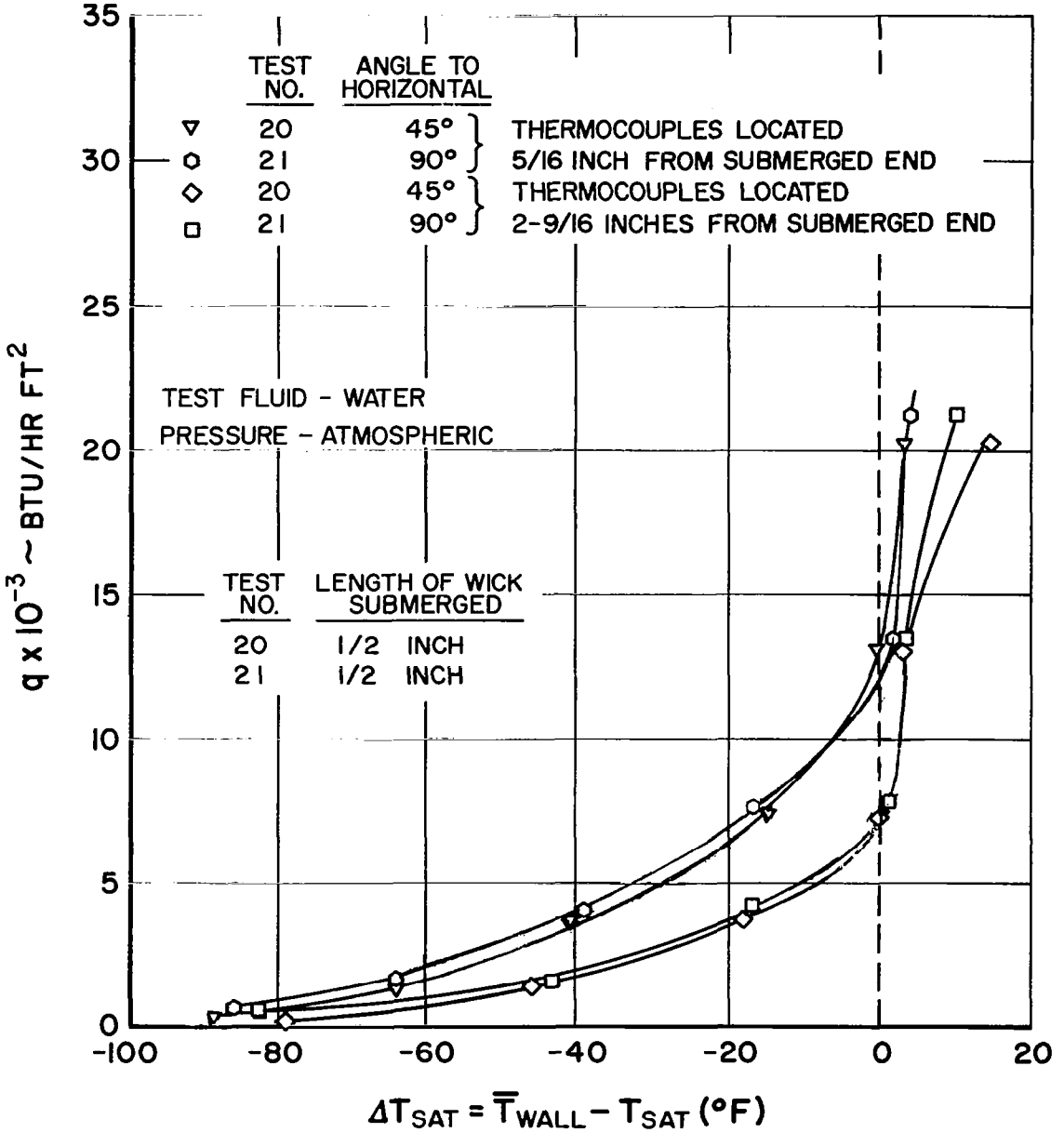

Figure 99 Heat Flux vs ΔT_{sat} for Grooved Sintered Nickel Fiber Wick (Sample H6) at Angles to Horizontal

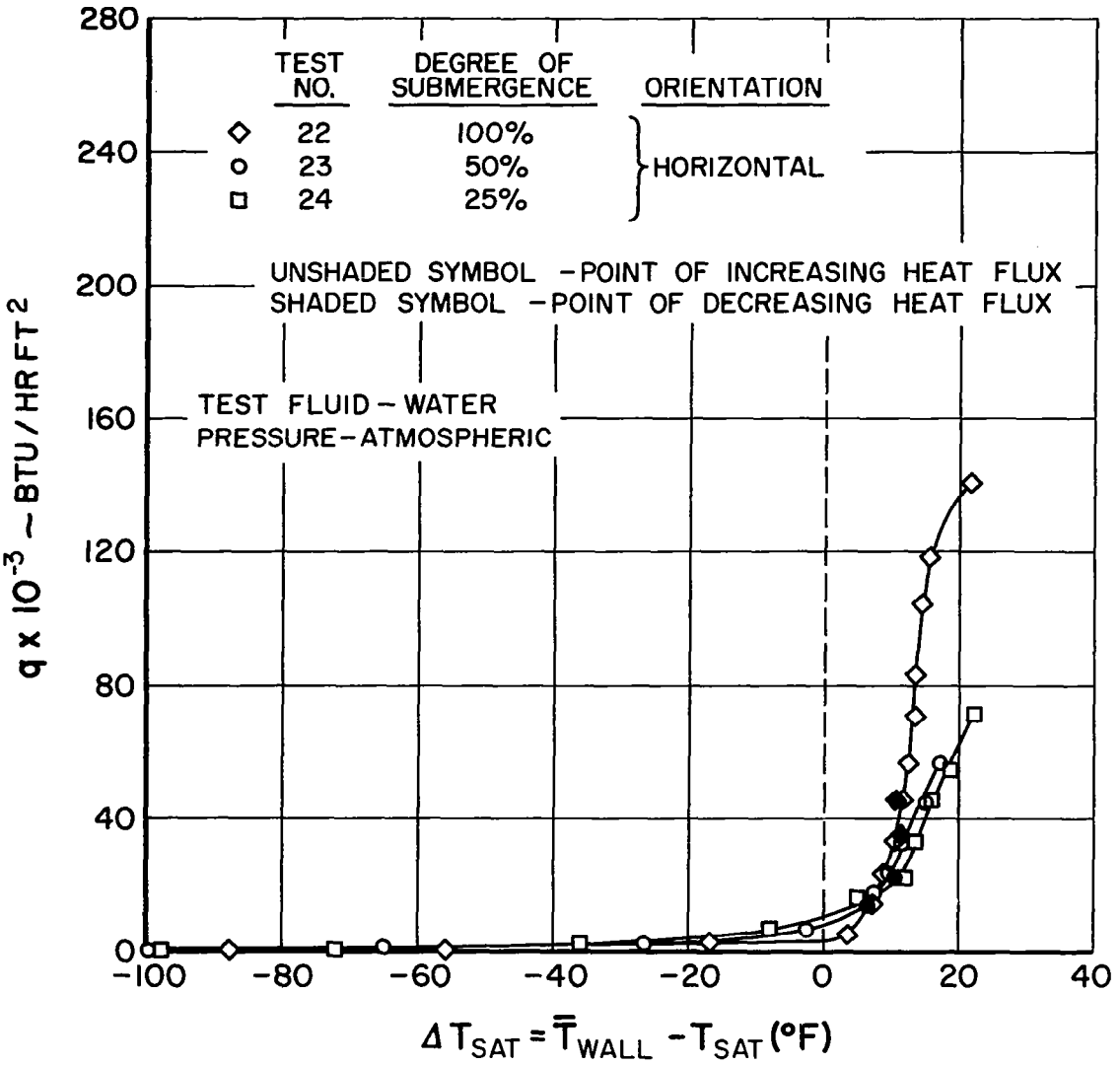

Figure 100 Heat Flux vs ΔT_{sat} for Sintered Stainless Steel Fiber Wick (Sample H11)

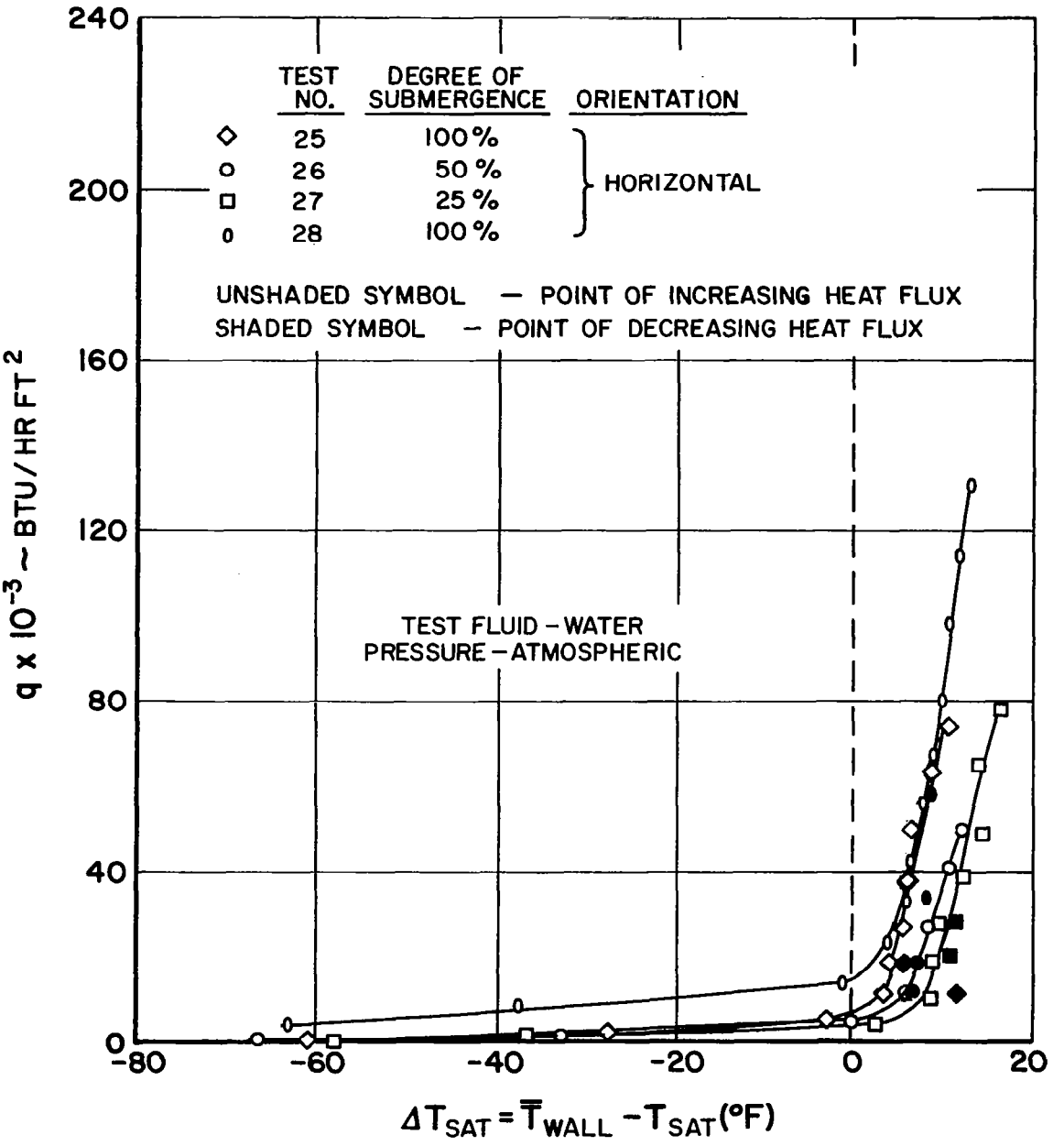

Figure 101 Heat Flux vs ΔT_{sat} for Sintered Stainless Steel Fiber Wick (Sample H13) in Horizontal Position

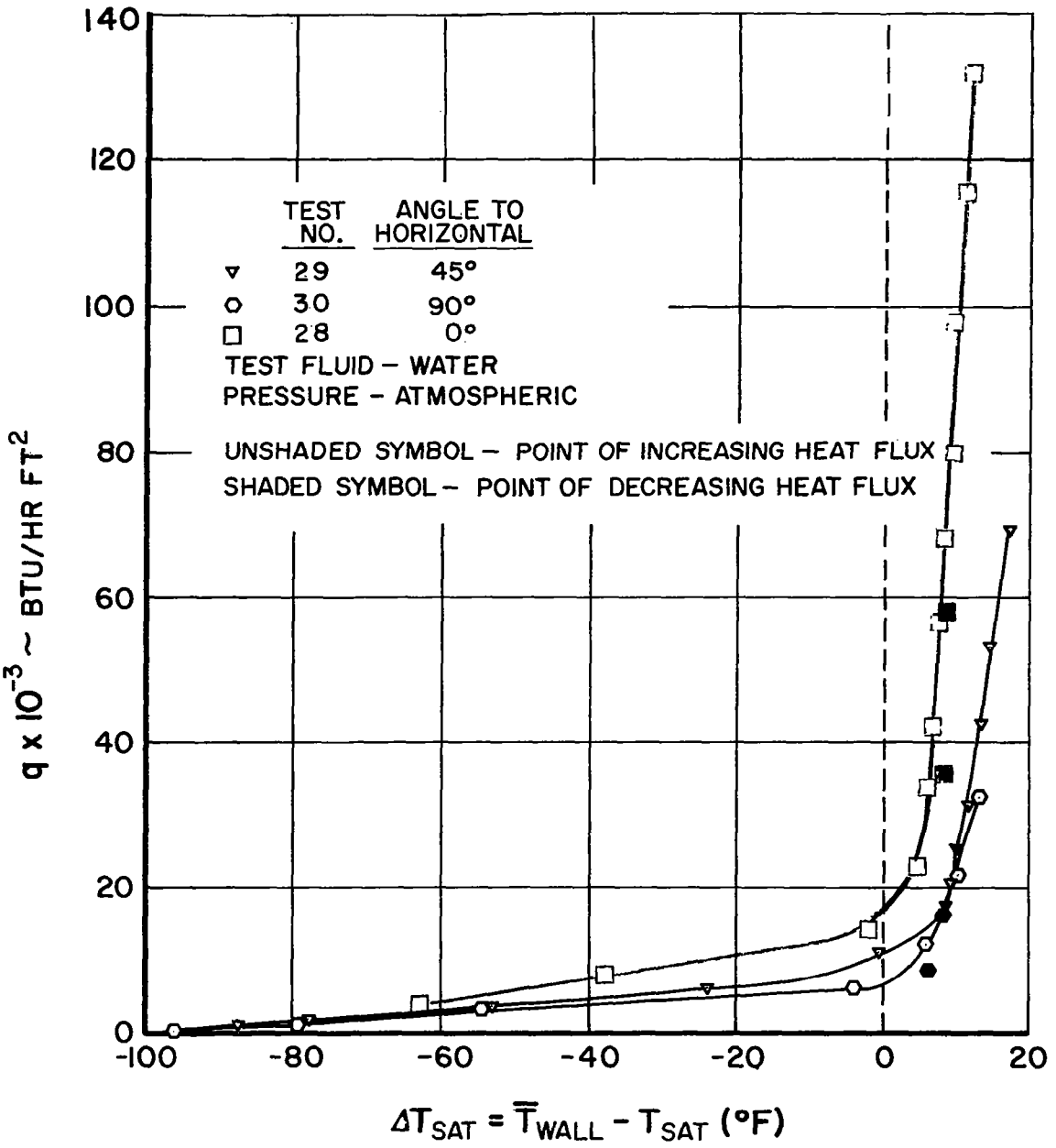

Figure 102 Heat Flux vs ΔT_{sat} for Sintered Stainless Steel Fiber Wick (Sample H13) Completely Submerged at Angles to Horizontal

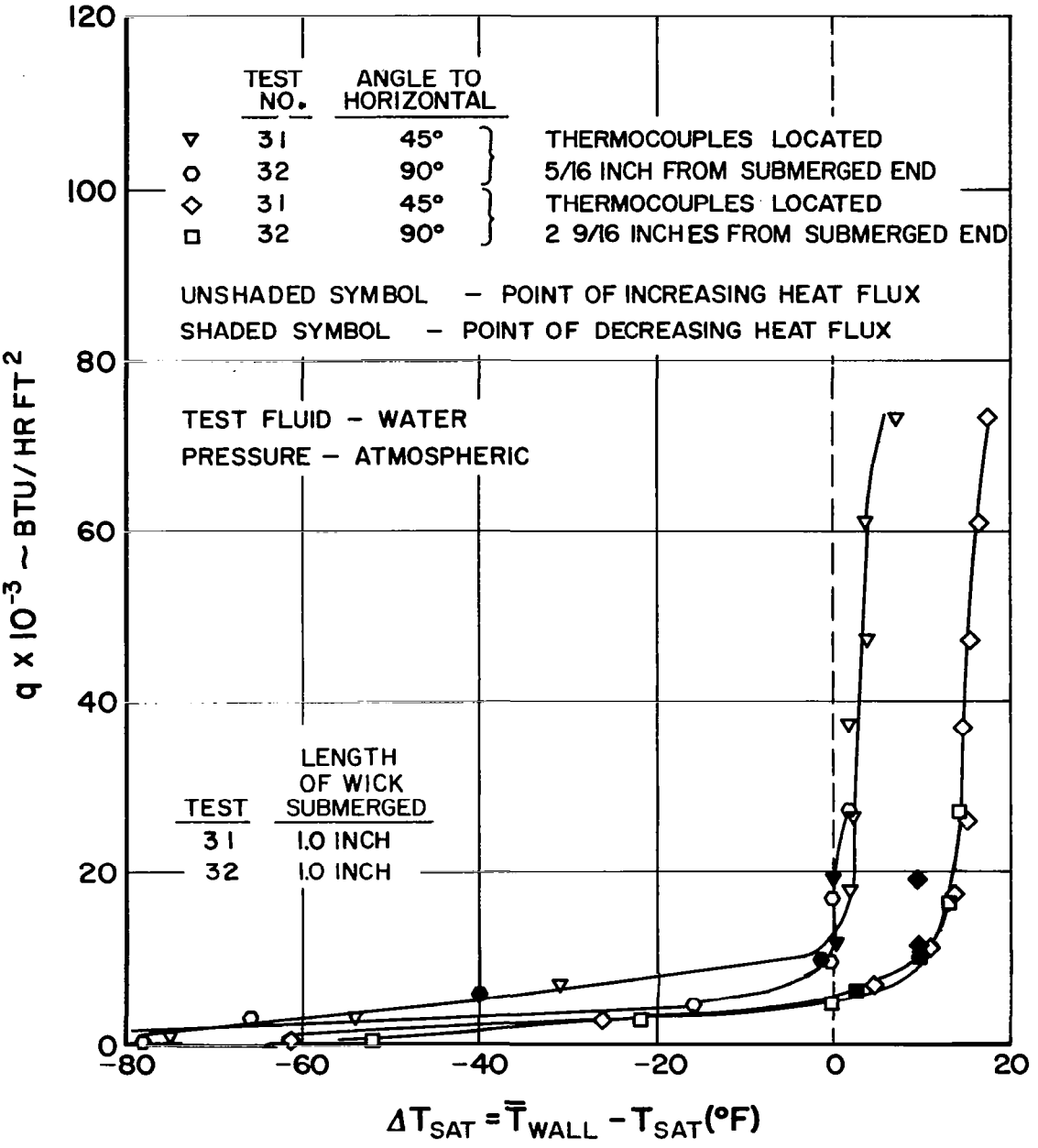

Figure 103 Heat Flux vs ΔT_{sat} for Sintered Stainless Steel Fiber Wick (Sample H13) Partially Submerged at Angles to Horizontal

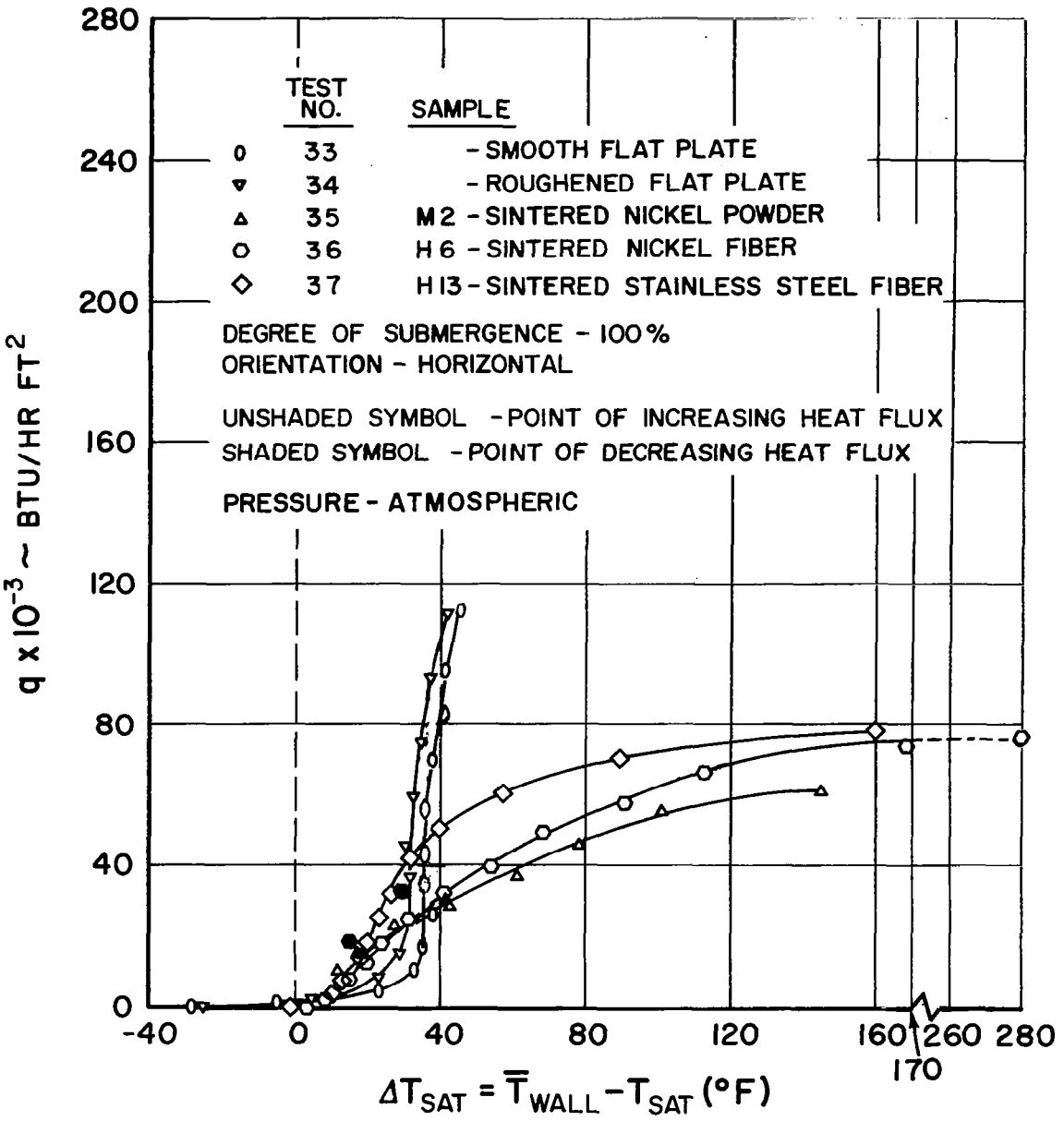

Figure 104 Results of Wick Boiling Tests with Test Fluid Freon 113

Each figure shows a plot of heat flux, q, versus ΔT_{sat} based on sample temperatures calculated at two locations; from an average of the thermocouples located closest to the surface of the test fluid (Thermocouples No. 5 and 8 - Figure 89), and an average of the thermocouples located farthest from the surface of the test fluid (Thermocouples No. 7 and 10 - Figure 89). In some cases, the lower thermocouples were located below the liquid surface.

Figure 92 is a graph of heat flux vs ΔT_{sat} for the sintered 150-mesh nickel screen. It is shown that ΔT_{sat} at the location farthest from the liquid surface is greater than that at the location nearest the liquid surface for a given average heat flux. The temperature variation is probably due to gravity forces and escaping vapor opposing the flow of fluid in the wick. The test fluid has to flow by capillary wicking about an additional 2 1/4 inches beyond the lower thermocouples to reach the thermocouples located farthest from the test fluid. It is likely that only the smallest pores near the top of the wick are filled with liquid, resulting in the wick containing considerable vapor at this point. This causes a higher resistance to heat transfer, and thus a higher sample temperature. A possible contributing cause for capillary pumping failure of the large pores in the upper region of the wick is that vapor generated in the lower regions probably has difficulty in escaping from the wick, thus causing a greater resistance for liquid flow to the upper region. This is somewhat substantiated by the observation in the horizontal-orientation fully-submerged test on the same sample (Test No. 1) that the vapor only escaped through the wick sides. Gravity effects may also be seen by comparing the temperature of the sample at the end farthest from the water for the three tests shown in Figure 92. This temperature can be seen to become progressively higher as the angle is increased and the component of gravity force opposing the flow increased.

Figures 95, 99, and 103 show curves of heat flux versus ΔT_{sat} for three different samples inclined both 45 degrees and 90 degrees to the horizontal with one end submerged in the water tank. These curves are for sintered nickel powder, sintered nickel fiber and sintered stainless steel fiber wicks, respectively. In all cases the average thermocouple reading at the top of the sample was higher than at the lower end of the sample. However, no appreciable difference was noticed between the 45-degree angle test and the 90-degree angle test, except for the sintered nickel powder sample at heat fluxes greater than 25,000 Btu/hr ft^2 (see Figure 95). It should be noted that for the other two samples there is no data at the two different angles for heat fluxes greater than 25,000 Btu/hr ft^2. The results of these tests can be explained in the same manner as those of the sintered 150-mesh nickel screen. That is, the additional capillary force needed to overcome gravity effects causes

some of the larger pores to fail as capillary pumps. The lower limiting heat flux of sample M2 in the 90-degree inclined case as compared to the 45-degree inclined case was probably due to increased effects of gravity at higher heat fluxes, because of the greater requirements of the wick to overcome the frictional pressure loss. The frictional pressure loss effects are compounded at a higher heat flux since both greater amounts of vapor exist and a higher liquid flow is required.

For all of the samples tested at an inclination, the tests on the same samples in the fully submerged horizontal position indicated lower ΔT_{sat} at the higher heat fluxes than the average of the upper thermocouples did for the inclined cases at the same heat flux. This can be expected, since for the horizontal cases the liquid has to wick, at most, one-half of the sample width (5/16 inch), rather than a large fraction of sample length (2 5/8 inches).

4. Effect of Inclination With Wick Fully Submerged

Figure 94 contains the results of a test on a sintered nickel powder wick (M2) in a vertical position and completely submerged. This curve can be compared to the curve contained in the same figure with the sample in a horizontal position and completely submerged. The latter case produced both a lower ΔT_{sat} for a given heat flux in the boiling regime and a higher limiting heat flux. Figure 102 shows a similar effect of inclination on ΔT_{sat} at a given heat flux for a sintered stainless steel fiber wick when fully submerged. The most likely explanation for these results is that the vapor can more easily escape from the wick surface in a horizontal position.

5. Effect of Grooves Cut in Wick

Figures 96 and 97 are graphs of heat flux versus ΔT_{sat} for both grooved and ungrooved wicks oriented horizontally. Figure 96 shows the effect of grooving a sintered nickel powder wick, and Figure 97 the effect of grooving a sintered nickel fiber wick. In both cases it can be seen that grooving the wick both reduces the degree of wall superheat required for a given heat flux and increases the limiting heat flux. As shown in Figure 96 the limiting heat flux for an ungrooved sintered nickel powder wick is about 130,000 Btu/hr ft^2, while that for a grooved sample is greater than 180,000 Btu/hr ft^2. The grooved wicks have 2 slots cut lengthwise along the face which measure 2 7/8 inch long, 3/64 inch wide and 1/16 inch deep. Figure 98 is a drawing of a grooved wick, showing the location of the grooves. The improved performance of the grooved samples was probably due to smaller resistance for vapor escape offered by the grooves.

6. Effect of Fluid Properties

To determine the effect of fluid properties on boiling from a wick-covered surface, tests were made with several samples in a horizontal position at 100 per cent submergence with Freon 113 as the test fluid. The results of these tests are shown in Figure 104, and are replotted in Figure 105 to allow for a comparison of tests on the same sample with both water and Freon 113 as test fluids. The results of the tests shown on Figure 105 demonstrate that invariably a higher heat flux was obtained at a given ΔT_{sat} when water was used as the test fluid. The limiting heat flux was also significantly higher when water was used as the test fluid as shown in the table below.

Sample	Test Fluid Water	Test Fluid Freon 113
sintered nickel powder wick (M2)	128,000 Btu/hr ft^2	63,000
sintered nickel fiber wick (H6)	>104,000	75,000
sintered stainless steel fiber wick (H13)	>132,000	80,000

As a means of analytically comparing the values of limiting heat flux found experimentally with water and Freon 113 as the test fluids, the following critical heat flux correlation, proposed by Rohsenow and Griffiths[15], was used:

$$\frac{q_{\text{critical}}}{\rho_v h_{VL}} = 143\, g^{1/4} \left(\frac{\rho_L - \rho_v}{\rho_v} \right)^{0,6} \qquad (104)$$

where q = heat flux
ρ_L = liquid density
ρ_v = vapor density
h_{VL} = heat of vaporization
g = acceleration due to gravity

While this correlation is for a bare surface, rather than a wick-covered surface, it allows a means of comparison of critical heat flux for various

fluids based on physical properties. Assuming vapor density to be small compared to liquid density, from Equation (104) the critical heat flux for Freon 113 divided by the critical heat flux for water is

$$\frac{\left(q\right)_{\substack{\text{critical}\\ \text{Freon 113}}}}{\left(q\right)_{\substack{\text{critical}\\ \text{water}}}} = \frac{h_{VL\,\text{Freon 113}}}{h_{VL\,\text{water}}} \left(\frac{\rho_{L\,\text{Freon 113}}}{\rho_{L\,\text{water}}}\right)^{0.6} \left(\frac{\rho_{v\,\text{Freon 113}}}{\rho_{v\,\text{water}}}\right)^{0.4} \tag{105}$$

which reduces to

$$\frac{\left(q\right)_{\substack{\text{critical}\\ \text{Freon 113}}}}{\left(q\right)_{\substack{\text{critical}\\ \text{water}}}} \approx \frac{1}{4} \tag{106}$$

when saturation properties at atmospheric pressure are substituted.

Although the ratio of peak heat fluxes obtained from the data was greater than this ratio, the analytical prediction that Freon 113 has a lower critical heat flux was verified.

7. Effect of Wick Structure

In addition to determining the boiling heat transfer characteristics of a wick-covered surface, it is further necessary to evaluate and classify the performance of wicking materials. To accomplish this, comparisons were made between the boiling heat transfer characteristics of a flat plate, sintered screen wicks, a sintered metal powder wick, and sintered metal fiber wicks.

A graph of heat flux versus ΔT_{sat} for several samples tested horizontally at 100 per cent submergence with Freon 113 as the test fluid is presented in Figure 104. A comparison of the curves shows that the sintered metal fiber wicks (H13 and H6) as boiling surfaces are better than the sintered metal powder wick (M2), but not as good as smooth or roughened flat plates, when the distance the liquid has to travel is insignificant.

Figure 106 allows the same type comparison as Figure 104, only with water used as the test fluid. Included in Figure 106 are results of tests on three different sintered fiber wicks, one sintered powder wick, and two different

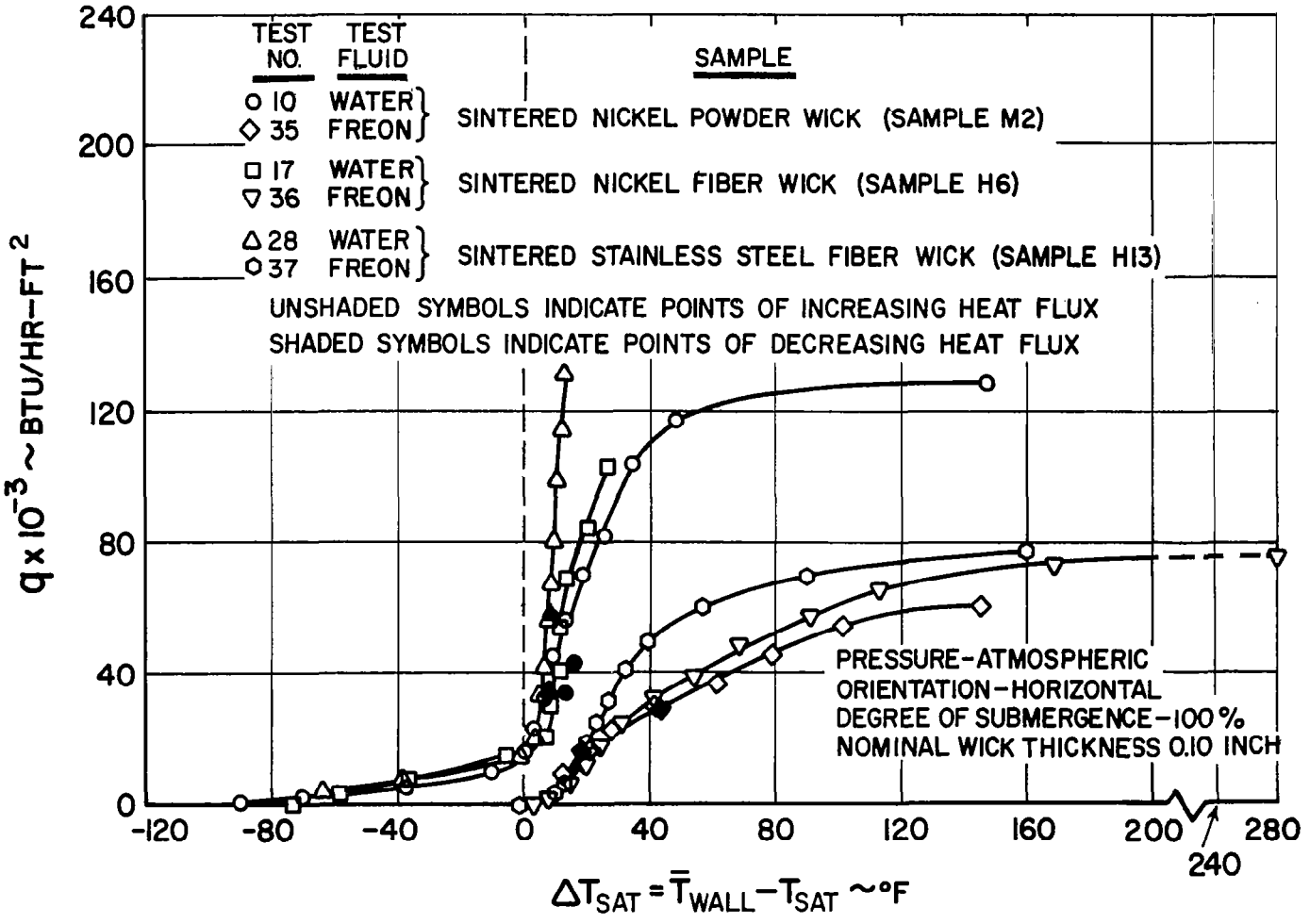

Figure 105 Comparison of Wick Boiling Characteristics of Three Samples Tested in Water and Freon 113

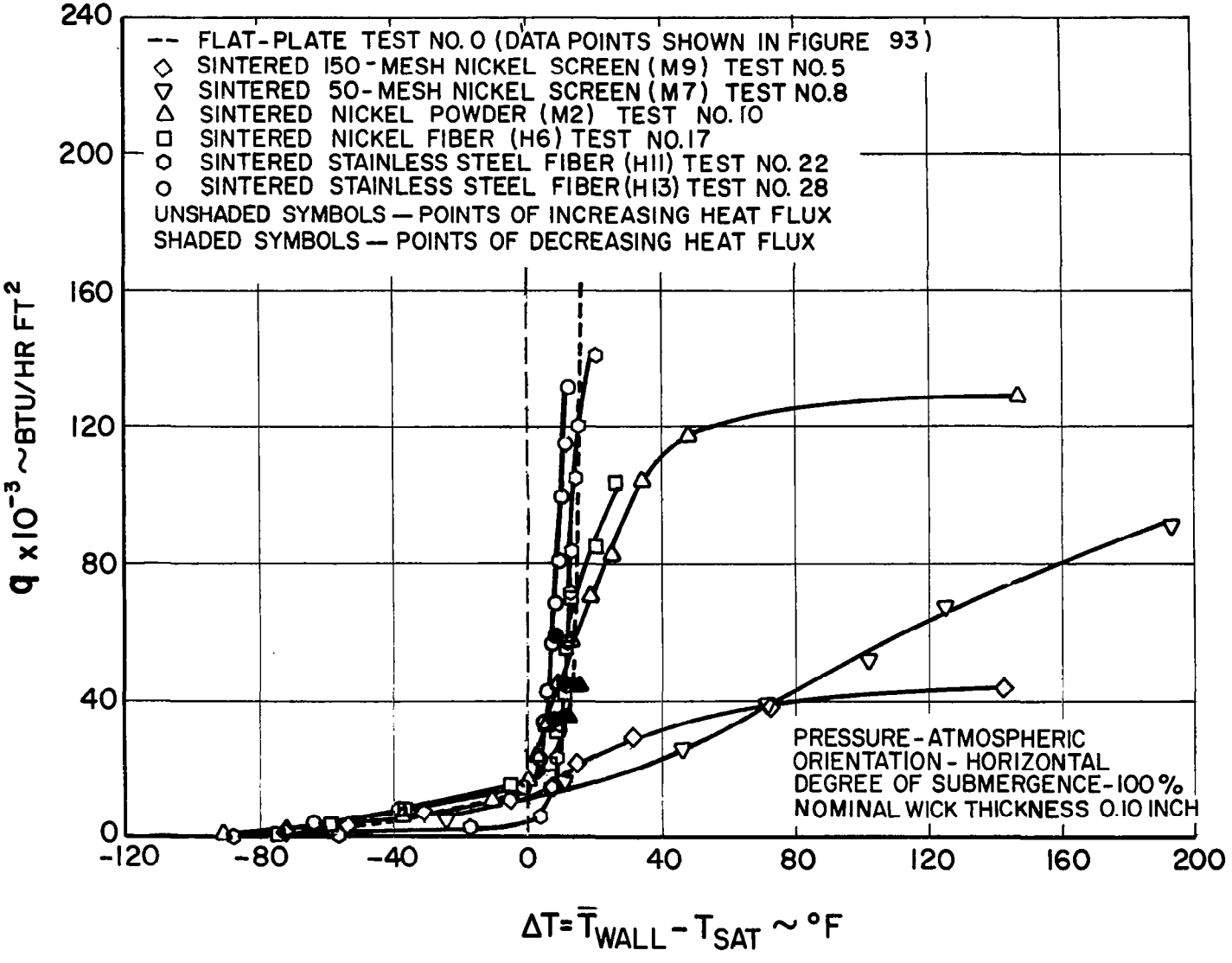

Figure 106 Results of Wick Boiling Test with Water as Test Fluid

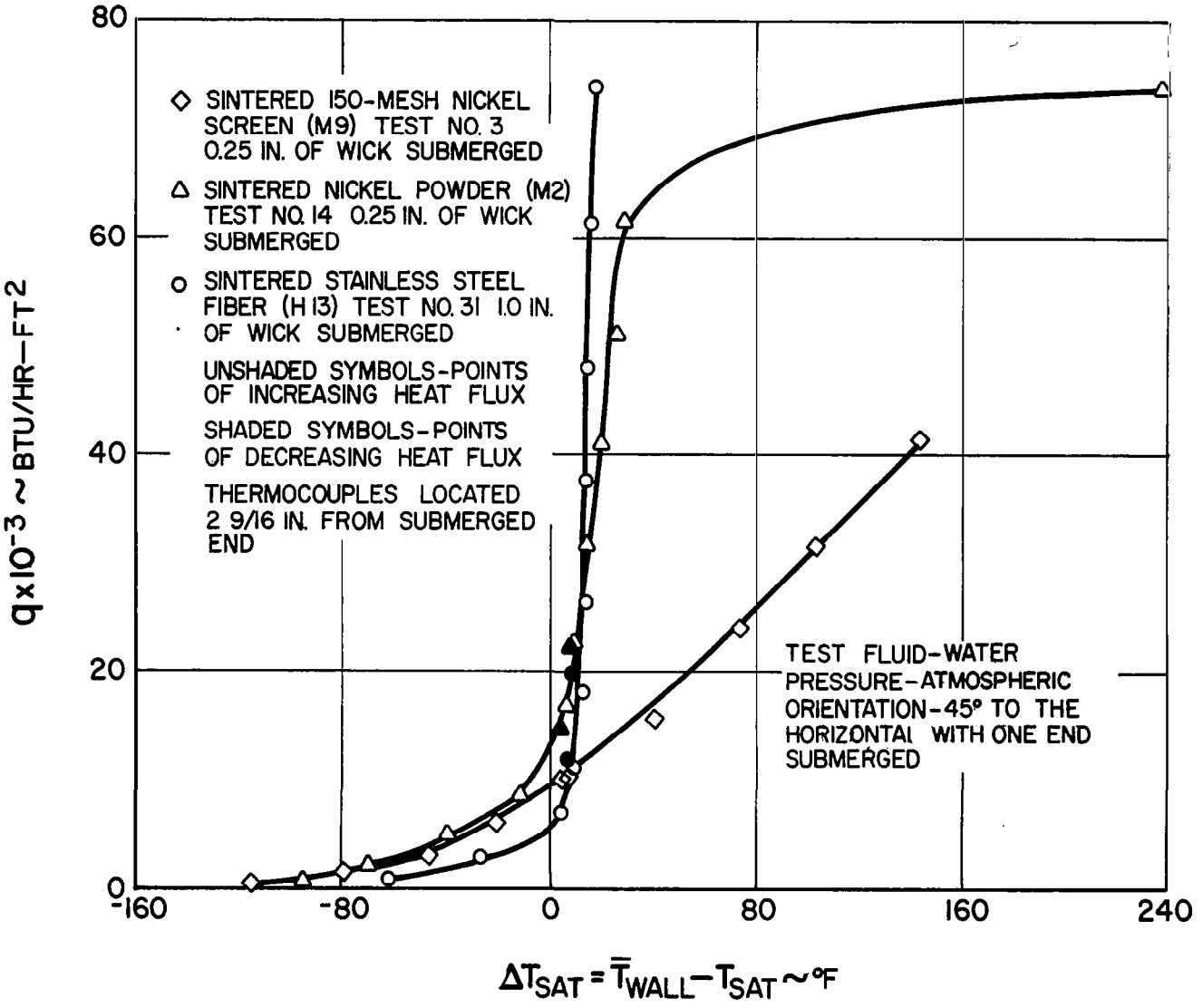

Figure 107 Comparison of Sample Boiling Characteristics When Fluid Wicks up Sample

screen wicks. The three sintered metal fiber wicks have the best boiling characteristics, followed by the sintered metal powder wick, and then the two sintered screen wicks. With water as the test fluid, two of the sintered metal fiber wicks (H13 and H11) perform as well as the flat plate (see dashed line Figure 106), contrary to the results of the tests with Freon 113 as the test fluid and H13 as the test sample. Probably H11 and H13 would have shown poorer performance than the flat plate when tested in water if a higher heat flux had been obtained. The poorer performance of H13 compared to the flat plate when tested in Freon 113 may be attributed to vapor blanketing of the wick sample (i. e. limiting heat flux being attained) at lower heat fluxes than with water.

In order to compare the boiling characteristics of several wick materials when the test fluid has to be wicked through the length of the sample, some of the results of tests with the sample inclined at an angle of 45 degrees to the horizontal, with a section submerged in the water, were replotted in Figure 107. This figure presents curves of heat flux versus ΔT_{sat}, where the sample temperatures used in the calculation of ΔT_{sat} are averages of the temperatures measured by the thermocouples located farthest from the liquid surface (Nos. 7 and 10 - Figure 93). Results are shown for the sintered 150-mesh nickel screen wick (M9), a sintered nickel powder wick (M2), and a sintered stainless steel fiber wick (H13). This figure shows that the sintered stainless steel fiber wick had the best boiling characteristics, such as a low ΔT_{sat} (18°F) for a given heat flux (74, 000 Btu/hr ft^2) and a relatively high limiting heat flux (> 74, 000 Btu/hr ft^2). The sintered nickel powder sample had fairly good boiling heat transfer characteristics (i. e. low ΔT_{sat}) up to a heat flux of about 62, 000 Btu/hr ft^2. The limiting heat flux for this sample was about 74, 000 Btu/hr ft^2. The sintered 150-mesh nickel screen exhibited the poorest performance, with a very high degree of wall superheat (144°F) for a low heat flux (41, 500 Btu/hr ft^2). The ΔT_{sat} for this sample increased gradually as heat flux increased, with no sudden break in the curve. This was probably due to the inability of the vapor to escape readily, as was previously discussed.

In order to see if the limiting heat fluxes in these inclined tests were associated with failure of the wicks as capillary pumps, Equation (50) was rewritten as follows:

$$\sigma \left(\frac{\rho}{\sigma}\right)_{WR} \ell_m = \frac{q' \mu_L x_E^2}{2 h_{VL} \delta \rho_L g_o} K_1 - \rho_L \sin \theta \, x_E \qquad (107)$$

where, in this case, q' and x_E are the evaporator heat flux and length, respectively.

The term on the left is the capillary pump capability and the terms on the right are the frictional loss and gravitational head loss, respectively.

The experimentally determined values of ℓ_m from the wick rise tests, and K_1, from the permeability tests, listed below, and the other known values were substituted in the above equation to solve for the predicted limiting heat flux.

Sample	K_1 (ft^{-2})	ℓ_m (inch)
sintered 150-mesh nickel screen wick (M9)	9.0×10^8 *	6.9
sintered-nickel powder wick (M2)	3.4×10^8	9.7
sintered stainless steel fiber wick (H13)	0.8×10^8	5.3

* estimated value based on interpolation of values for samples M8 and M10

The results of the calculation are presented below:

Sample	Predicted Value of Limiting Heat Flux-Btu/hr ft^2
sintered 150-mesh nickel screen wick	0.2×10^6
sintered-nickel powder wick	1.2×10^6
sintered stainless steel fiber wick	4.6×10^6

The only sample that experimentally exhibited a definite limiting heat flux was the sintered nickel powder wick, and this value was considerably lower than the calculated value. However, the above analysis assumed liquid flowed through all of the pores, whereas in the boiling tests, vapor was probably present in a considerable fraction of the pores. If considerable vapor were present, the frictional pressure loss would be much higher due both to a reduction in flow cross-sectional area and perhaps an increase in K_1 if the Darcy regime were exceeded.

It appears from inspecting Figure 107 that the sintered fiber sample would attain the highest limiting heat flux, followed by the sintered powder sample. The sintered screen sample did not show a distinct limiting heat flux in the range tested. However, it appears that it would fail before the sintered powder sample. The results of the analysis show the same order in limiting heat flux as that mentioned above. This agreement might only be fortuitous since it is difficult to ascertain the fraction of pores containing vapor in each of the different samples and the effects of boiling on limiting capillary pumping heat flux.

G. Summary and Conclusions

The test results obtained from a study on boiling from a wick-covered surface indicate that:

1. Of the porous materials tested, the sintered metal fiber wicks exhibited the best boiling characteristics in both a horizontal and inclined position. Although the sintered metal screen wicks had the poorest performance, they could be used as a wicking surface at relatively low heat fluxes. However, even at low heat fluxes a relatively high ΔT_{sat} is required. This would be undesirable since either a higher system temperature would be required for the same heat rejection rate and heat transfer area, or a greater heat transfer area would be required for a given heat rejection rate and operating temperature.

2. Vapor in a wick probably causes a significant resistance to the flow of liquid through the wick. For a wick with only one end submerged in liquid, the greater the distance from the liquid surface, the poorer the boiling performance. This can probably be attributed partially to vapor blocking liquid flow up the wick. For fully submerged 50-mesh screen wicks, one seven-layer thick screen and the other two layers thick, the thinner wick showed a lower ΔT_{sat} for a given heat flux when both were in horizontal position. This was definitely attributed to the inability of the vapor to escape normal to the surface in the seven-layer case. A further illustration of how the ease of vapor escape affects ΔT_{sat} was observed in comparing tests on two different samples fully submerged, where the samples were oriented both horizontally and at angles to the horizontal. In this comparison, the horizontal test produced better results which can probably be attributed to easier vapor escape.

3. The greater the degree of submergence in the horizontal position, the better the boiling performance for sintered metal powder and sintered metal fiber wicks. The boiling test performance of a sintered metal screen appeared to be independent of degree of submergence; however, in these tests all vapor escaped through the edges of the wick rather than through the top surface.

4. Grooving a wick that has poor boiling characteristics tends to improve the performance and increase the limiting heat flux. This is concluded from only horizontal testing with full or partial submergence, and further testing would be needed to determine whether this conclusion holds for other cases.

5. In the comparison of tests on samples run both with water and Freon 113 as test fluids, the results showed that much better performance was obtained with water. One correlation indicated that critical heat flux is approximately proportional to vapor density to the 0.4 power, liquid density to the 0.6 power, and the latent heat of vaporization to the 1.0 power. This correlation qualitatively agrees with the test results which indicate that water has a higher critical heat flux than Freon 113.

IX. CONCLUSIONS

A. The simplified analysis indicated that the maximum height to which a liquid will rise in a vertical wick, ℓ_m, and the friction factor, K_1, are the important parameters in determining the capability of a capillary pump in a heat pipe. This theory indicates that the larger the value of the capillary pump parameter, ℓ_m/K_1, the better the capillary pump, when head effects due to gravity are negligible. If an application involves operation at a condition in which a capillary pump must work against gravity, consideration must be given to both the value of ℓ_m/K_1 and of ℓ_m itself. The important fluid properties for capillary pumping were also indicated by the simplified analysis.

B. The experimentally determined capillary pumping characteristics of the three classes of materials indicated that as a class the sintered fiber samples were best, followed by the sintered powder samples. The sintered screen samples demonstrated the lowest potential as capillary pumps.

C. Experiments conducted to determine the heat transfer coefficients and limiting heat transfer rates for boiling indicate that some of these porous materials provide high values of these quantities when adequate paths for vapor escape from within the wick are provided. Other samples which do not provide vapor removal paths result in values of heat transfer coefficients significantly lower than those of a bare flat surface. Three sintered fiber samples were determined to have the best heat transfer characteristics of those tested, followed by a sintered powder sample and sintered screens.

D. The analyses and experimental results indicate that vapor-chamber fins employing suitable wicks can operate at relatively high evaporator heat fluxes and corresponding wick flow rates.

APPENDIX 1

References

1. Grover, G. M., T. P. Cotter, and G. F. Erickson, Structures of Very High Thermal Conductance, J. of Appl. Phys., June 1964, 35, p. 1190

2. Deverall, J. E. and J. E. Kemme, High Thermal Conductance Devices Utilizing the Boiling of Lithium or Silver, Report No. LA-3211, April 9, 1965, Los Alamos Scientific Laboratory, Los Alamos, New Mexico

3. Deverall, J. E. and J. E. Kemme, Satellite Heat Pipe, Report No. LA-3278-MS, April 20, 1965, Los Alamos Scientific Laboratory, Los Alamos, New Mexico

4. Haller, H. C., S. Lieblein, and B. G. Lindow, Analysis and Evaluation of a Vapor-Chamber Fin-Tube Radiator for High-Power Rankine Cycles, NASA TN D-2836, June 1964, NASA Lewis Research Center, Cleveland, Ohio

5. Adamson, Arthur W., Physical Chemistry of Surfaces, Interscience, 1960, pp 4-6

6. Cotter, T. P., Theory of Heat Pipes, Report No. LA-3246-MS, Los Alamos Scientific Laboratory, Los Alamos, New Mexico

7. Scheidegger, Adrian E., The Physics of Flow Through Porous Media, Macmillan, 1960, pp 68-90

8. Fox, H. W., E. F. Hare, and W. A. Zisman, Wetting Properties of Organic Liquids on High Energy Surfaces, J. Phys. Chem, 1955, 59, p. 1098

9. Gorring, R. L. and S. W. Churchill, Thermal Conductivity of Heterogeneous Materials, Chemical Engineering Progress, Vol. 57, No. 7, pp. 53-59, July 1961

10. Carman, P. C., Flow of Gases Through Porous Media, Butterworths, 1956, p. 8

11. Ginwala, K., T. A. Blatt, and R. W. Bilger, Engineering Study of Vapor-Cycle Cooling Components for Space Vehicles, Tech. Doc. Repts. No. ASD-TDR-63-582, Sept. 1963, AF Flight Dynamics Laboratory, Air Force Systems Command, Wright-Patterson Air Force Base, Ohio, pp 120-148

12. Allingham, W. D., and J. A. McEntire, Determination of Boiling Film Coefficient for a Heated Horizontal Tube in Water-Saturated Wick Material, J. Heat Transfer, Feb. 1961, pp 71-76

13. Costello, C. P., and E. R. Redeker, Boiling Heat Transfer and Maximum Heat Flux for a Surface with Coolant Supplied by Capillary Wicking, Chem. Engr. Progress Symp. Series, 1963, No. 41, 59, pp 104-113

14. Costello, C. P., and W. J. Frea, The Role of Capillary Wicking and Surface Deposits in the Attainment of High Pool Boiling Burnout Heat Fluxes, AIChE Journal, May 1964, 10, pp 393-368

15. Rohsenow, W. M., and P. Griffith, Correlation of Maximum Heat Flux Data for Boiling of Saturated Liquids, AIChE - ASME Heat Transfer Symposium, Louisville, Kentucky, March 1955

APPENDIX 2

Nomenclature

Latin-Letter Symbols

A_P	cross-sectional area of pores in wick sample normal to liquid flow
A_T	total cross-sectional area of wick sample normal to liquid flow
b	dimension of vapor-chamber fin element in z - direction
C_L	*specific heat of an incompressible liquid*
D	diameter
D_C	equivalent capillary pore diameter defined by Equation (99)
D_K	equivalent frictional pore diameter defined by Equation (98)
$\bar{D}$	mean pore diameter
F	force
F_{AR}	free flow area ratio, defined as A_P/A_T
g	local acceleration of gravity
g_o	proportionality constant in Newton's second law
h	enthalpy
h_{VL}	latent heat of vaporization
J	proportionality constant relating work energy to heat energy
k	thermal conductivity
K_1	*wick friction factor, defined by Equation (25)*
K_B	thermal conductivity of wick backup plate
ℓ_m	maximum height to which a liquid will rise in a vertical wick sample
M	momentum
N	dimensional liquid parameter, $\frac{\rho_L h_{VL} \sigma}{\mu_L}$
P	pressure
P_a	atmospheric pressure
Q	heat energy per unit time
Q_{max}	maximum fin heat rejection rate
q	time rate of heat transfer per unit area (heat flux)
q'	heat flux in evaporator section
R, R'	radius of curvature of a liquid-vapor interface
R_{min}	minimum radius of curvature at the liquid-vapor interface that a given wicking material will support
R_C	radius of curvature of the liquid-vapor interface in pore C
r	pore radius
$\bar{r}$	mean pore radius
T	temperature
T_M	measured temperature of wick backup plate
T_{sat}	saturation temperature of fluid
T_{wall}	wall temperature at the liquid-wick-solid interface
u	velocity
u_L	average liquid flow velocity in the pores of wick
V	volume of pores
V_T	total volume of wick
w	mass flow rate
W_T	total weight of wick
x_E	total length of evaporator section of vapor-chamber fin
x_M	total length of condensing section of vapor-chamber fin
x_T	total length of condensing and evaporating sections of vapor chamber fin

Greek-Letter Symbols

$\alpha(r)$	pore size distribution function
ΔP	pressure drop
ΔT_{sat}	temperature difference between saturated vapor and the liquid-wick-solid interface
Δx	wick sample length in flow direction
δ	liquid-wick thickness
ϵ	porosity, defined as total void volume divided by total sample volume
θ	angle fin makes with the horizontal, positive when heated section is at elevated end and negative when heated section is at lower end
ϕ	liquid-solid contact angle measured within liquid
μ	absolute viscosity
ρ	density
σ	liquid-vapor surface tension

Superscripts

c	due to convection
k	due to conduction

Subscripts

B	backup plate
d	friction and inertia
e	equivalent
F	pertaining to Freon 113 data
f	due to friction
g	pertaining to gravity
L	liquid
med	median
P	pore, or due to pressure
S	solid
T	total
V	vapor
w	pertaining to water data
WR	pertaining to conditions of wicking rise tests
x	at a given x
x + dx	at a given x + dx
σ	pertaining to capillary effects
1	at point 1
2	at point 2

APPENDIX 3

Derivation of Fin Equation Including Effects of Gravity and Evaporator Section

The model of the vapor-chamber fin shown in Figure 6 is modified by:

1) Including gravity forces (The fin is inclined at an angle θ measured from the horizontal. The angle θ is defined as positive when the heated section is at the elevated end and negative when the heated section is at the lower end.)
2) Including the evaporator pressure drop by assuming the same theoretical model in the evaporator as in the condenser section.

The model used in the second modification can be considered suitable at a low heat flux where heat is conducted through the wick-liquid composite to the liquid-vapor interface where evaporation takes place. At a high heat flux the boiling process in the wick structure is more complicated, and this simplified model may not apply.

With gravity forces included, a gravity force, F_g, is added to the forces acting on the differential element shown in Figure 7. The gravity force is written as

$$F_g = - \frac{g}{g_o} \rho_L \epsilon b \delta \sin \theta \, dx \qquad (3\text{-}1)$$

and acts in the direction of flow for values of θ between 180 and 360 degrees, and opposite to the direction of flow for values between zero and 180 degrees.

The differential momentum equation (28) becomes

$$-2\sigma \frac{dR}{R^2} - \epsilon K_1 \mu_L u_L \, dx - \frac{g}{g_o} \rho_L \sin\theta \, dx = \frac{\rho_L}{g_o} \frac{d}{dx} (u_L)^2 \, dx \qquad (3\text{-}2)$$

The combined energy-continuity equation must be modified to account for the rate of work done by the gravity force on a volume element, and Equation (33) becomes

$$u_L \rho_L \frac{dh_L}{dx} - (h_V - h_L) \rho_L \frac{du_L}{dx} + \frac{q}{\delta \epsilon} - \frac{\rho_L u_L}{J} \frac{g}{g_o} \sin\theta = 0 \qquad (3\text{-}3)$$

where J is the proportionality constant relating work energy to heat energy.

In the condenser section Equation (39) becomes

$$u_L = \frac{q}{h_{VL}\,\delta\,\epsilon\,\rho_L}\,x - \frac{g/g_o \sin\theta}{J\,h_{VL}} \int_o^x u_L\,dx \qquad (3\text{-}4)$$

If gravity forces are neglected

$$u_L = \frac{q}{h_{VL}\,\delta\,\epsilon\,\rho_L}\,x \quad \text{or} \quad du_L = \frac{q}{h_{VL}\,\delta\,\epsilon\,\rho_L}\,dx \qquad (3\text{-}5)$$

from Equation (3-4). For values of θ between zero and 180 degrees, the velocity of the liquid in a gravity field will be less than the value calculated from Equation (3-5). The maximum value of the second term on the right side of Equation (3-4) divided by the first term is approximately $\frac{g}{g_o}\,\frac{x}{2J\,h_{VL}}$, which is much less than one.

Therefore, the gravity term in Equation (3-4) may be neglected, and the expression for liquid velocity is unchanged when gravity forces are present.

Equations (3-2) and (3-5) can be combined to give an energy-continuity-momentum integral equation, valid in the condenser section

$$-\int_{R_{x=o}}^{R_{x=x}} 2\sigma\,\frac{dR}{R^2} - \int_o^x K_1\,\frac{q}{h_{VL}\,\delta}\,\frac{\mu_L}{\rho_L}\,x\,dx - \int_o^x \frac{g}{g_o}\,\rho\sin\theta\,dx = \int_o^x \frac{2q^2}{g_o\,h_{VL}^2\,\rho_L\,\epsilon^2\,\delta^2}\,x\,dx \qquad (3\text{-}6)$$

where x is the distance from the origin shown in Figure 6 to any point in the condenser section.

The velocity of the liquid in the fin may be plotted vs fin length as shown in the sketch below.

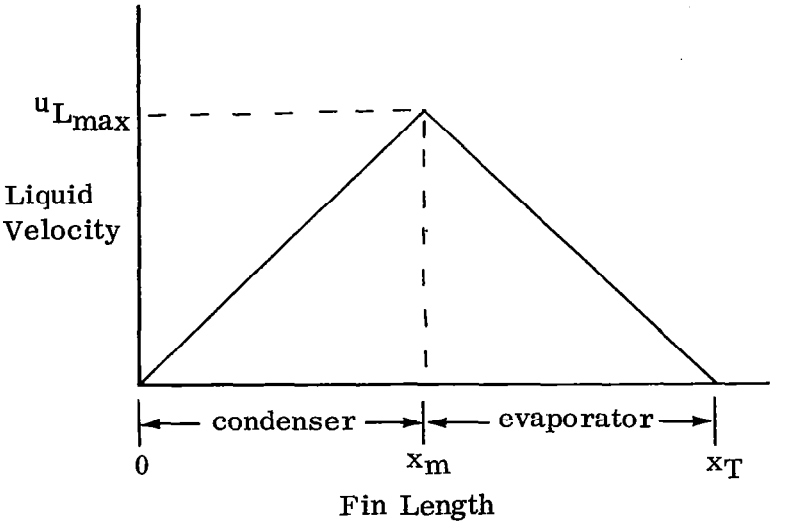

Fin Length

Integration of Equation (3-5) beween $x = 0$ and $x = x_m$ shows that

$$u_{L_{max}} = \frac{q\, x_m}{h_{VL}\, \delta\, \epsilon\, \rho_L} \tag{3-7}$$

and integration using the boundary condition

$$u_{x = x_m} = \frac{q\, x_m}{h_{VL}\, \delta\, \epsilon \rho_L}$$

and $u_{x = x} = u_L$ yields

$$u_L = \frac{q'}{h_{VL}\, \delta\, \epsilon\, \rho_L} (x - x_m) + \frac{q\, x_m}{h_{VL}\, \delta\, \epsilon\, \rho_L} \tag{3-8}$$

where x is a value greater than x_m and q' is the evaporator heat flux.

Since the heat transferred in the evaporator is equal to the heat transferred in the condenser,

$$q\, x_m = -q' (x_T - x_m)$$

$$\text{or } q' = -\frac{q\, x_m}{x_T - x_m} \tag{3-9}$$

Substitution of Equation (3-9) into Equation (3-8) gives an expression for the liquid velocity in the evaporator section

$$u_L = \frac{q\, x_m}{h_{VL}\, \delta\, \epsilon\, \rho_L} \left(\frac{x_T - x}{x_T - x_m} \right) \tag{3-10}$$

Equations (3-2) and (3-10) can be combined to give an an energy continuity-momentum integral equation valid in the evaporator section.

$$-2\sigma \int_{R_x = x_m}^{R_x = x} \frac{dR}{R^2} - K_1 \mu \frac{q}{h_{VL}\, \delta\, \rho_L} \frac{x_m}{x_T - x_m} \int_{x_m}^{x} (x_T - x)\, dx - \frac{g}{g_o} \rho_L \sin\theta \int_{x_m}^{x} dx$$

$$= \frac{q^2}{g_o\, h_{VL}^2\, \rho_L\, \epsilon^2\, \delta^2} \left(\frac{x_m}{x_T - x_m} \right)^2 \int_{x_m}^{x} d\,(x_T - x)^2 \tag{3-11}$$

To evaluate the maximum output of the capillary pump, the liquid radius of curvature must be very large at x = 0 (i. e. $R \to \infty$) and very small at $x = x_T$ (i. e. $R = R_{min}$), with some intermediate value R_i , at $x = x_m$. This assumes that the interface in the evaporator is in the position shown in Figure 5 (a). Integrating Equation (3-6) between $R = R_\infty$ ($x = 0$) and $R = R_i$ ($x = x_m$) yields

$$\frac{2\sigma}{R_i} - K_1 \mu_L \frac{q}{h_{VL}\, \delta\, \rho_L} \frac{x_m^2}{2} - \frac{g}{g_o} \rho_L \sin\theta\, x_m = \frac{q^2}{g_o\, h_{VL}^2\, \rho_L^2\, \epsilon^2\, \delta^2} x_m^2 \tag{3-12}$$

Integrating Equation (3-11) between $R = R_i$ ($x = x_m$) and $R = R_{min}$ ($x = x_T$) yields

$$\left[\frac{2\sigma}{R_{min}} - \frac{2\sigma}{R_i} \right] - K_1\, \mu_L\, \frac{q}{h_{VL}\, \delta\, \rho_L} \frac{x_m\,(x_T - x_m)}{2} -$$

$$\frac{g}{g_o} \rho_L \sin\theta\, (x_T - x_m) = - \frac{q^2}{g_o\, h_{VL}^2\, \rho_L\, \epsilon^2\, \delta^2} x_m^2 \tag{3-13}$$

Addition of Equations (3-12) and (3-13) yields

$$\frac{2\sigma}{R_{min}} - K_1 \mu_L \frac{q}{h_{VL}\delta \rho_L} \frac{x_m x_T}{2} - \frac{g}{g_o} x_T \rho_L \sin\theta = 0 \qquad (3\text{-}14)$$

There are no momentum terms in Equation (3-14) which is expected since the liquid velocity is zero at $x = 0$ and $x = x_T$.

As shown in Equation (47)

$$R_{min} = \left(\frac{2 g_o \sigma}{\rho_L g \ell_m}\right)_{WR}$$

Substituting R_{min} into Equation (3-14) and rearranging terms yields an expression for the maximum total heat input that can be transferred to a vapor-chamber fin as a function of geometry, wick properties and fluid properties.

$$Q_{max} = \left[2\left(\frac{\rho_L h_{VL} \sigma}{\mu_L}\right)\left(\frac{b\delta}{x_T}\right)\left(\frac{g}{g_o} \frac{\rho_L}{\sigma}\right)_{WR} - \left(\frac{2\rho_L^2 h_{VL}}{\mu_L} \frac{g}{g_o}\right)\left(\frac{b\delta}{\ell_m}\right) \sin\theta\right] \frac{\ell_m}{K_1} \qquad (3\text{-}15)$$

Neglecting the evaporator section (i.e $x_T = x_m$) and solving for the maximum total heat transferred to a fin in a horizontal position Equation (3-15) reduces to

$$Q_{max} = 2\left(\frac{\rho_L h_{VL} \sigma}{\mu_L}\right)\left(\frac{b\delta}{x_m}\right)\left(\frac{g}{g_o} \frac{\rho_L}{\sigma}\right)_{WR} \left(\frac{\ell_m}{K_1}\right) \qquad (3\text{-}16)$$

which is identical to Equation (49) in Section III D.